Eruption of Solar Magnetic Flux Ropes and Associated Flaring Activity: Observational Perspectives

A thesis
Submitted in partial fulfillment of
the requirements for the degree of
Doctor of Philosophy
by

Suraj Sahu
(Roll No. 17330034)

Supervisor:
Prof. Bhuwan Joshi
Udaipur Solar Observatory
Physical Research Laboratory
Udaipur 313 001, India

Discipline of Physics
Indian Institute of Technology Gandhinagar
Gandhinagar 382 355, India
February 2023

To

my parents

Declaration

I declare that the thesis entitled **"Eruption of Solar Magnetic Flux Ropes and Associated Flaring Activity: Observational Perspectives"** has been prepared by me under the guidance of **Dr. Bhuwan Joshi, Professor, Udaipur Solar Observatory, Physical Research Laboratory**. The thesis represents my ideas in my own words and where other's ideas or words have been included, I have adequately cited and referenced the original sources. I also declare that I adhered to all principles of academic honesty and integrity and have not misrepresented or fabricated or falsified any idea/data/fact/source in my submission. I understand that any violation of the above will be cause of disciplinary action by the institute and can also evoke penal action from the sources which have thus not been properly cited or from whom proper permission has not been taken when needed. No part of the thesis has formed the basis for the award of any degree or fellowship previously.

Suraj Sahu
01/02/2023

Suraj Sahu

Roll No: 17330034

Registration date: 04 August 2017

CERTIFICATE

It is certified that the work contained in the thesis titled **"Eruption of Solar Magnetic Flux Ropes and Associated Flaring Activity: Observational Perspectives"** by **Suraj Sahu** (Roll no: 17330034), is a record of original research work done by him during the period of study under my supervision and that the thesis has not previously formed the basis for the award to the candidate of any Degree, Diploma or other similar titles and that the thesis represents independent research work on the part of the scholar. I have read this dissertation and in my opinion, it is fully adequate in scope and quality as a dissertation for the degree of Doctor of Philosophy.

Bhuwan Joshi

Dr. Bhuwan Joshi
Professor
Udaipur Solar Observatory
Physical Research Laboratory
Udaipur 313 001, India

Acknowledgements

I would like to start by expressing my sincere and deep gratitude to my PhD adviser, Prof. Bhuwan Joshi for his invaluable guidance, encouragement and support throughout my PhD tenure.

I take this opportunity to express my gratitude to my Doctoral Studies Committee (DSC) members, Dr. Aveek Sarkar, Dr. Girjesh Gupta, and Dr. Vishal Joshi for continuous evaluation of my work and useful suggestions. Also I am grateful to them for examining the thesis.

I express my sincere acknowledgements to Prof. Anil Bhardwaj, Director, Physical Research Laboratory (PRL) for providing the necessary facilities to carry out my research work. I thank the PRL academic committee members for reviewing my research progress and providing invaluable suggestions which helped in improving the quality of the thesis.

I thank all the team members of SDO, RHESSI, GOES, LASCO, BBSO for providing data which I utilized in the thesis.

Finally, this thesis would not have come to reality without the help of a few great people whom I met during my PhD. However, I won't mention their name, because "they know who they are". Also, I would like to thank a few fellows for teaching me lessons for life in some way or other. Last but not least, I thank myself for sustaining the various ups and downs in my PhD life, remembering the famous quote of Swami Vivekananda: "Believe in yourself and the world will be at your feet" as the source of inspiration.

Suraj Sahu

Udaipur Solar Observatory, Udaipur, Rajasthan

01 February 2023

Abstract

The solar eruptive phenomena consist of various forms energetic and explosive activities occurring throughout the solar atmosphere. It is now well-understood that the solar eruptive events usually take the forms of filament eruptions, flares, coronal mass ejections (CMEs), solar jets, etc. The source of origin of these explosive events lies in the complexity of the magnetic configurations permeating the solar atmospheres from the photosphere to corona. The continuous photospheric motions shuffle the coronal magnetic field lines creating entanglement and this results in the storage of free magnetic energy, which ultimately releases drastically to give rise to the numerous explosive activities on the Sun. Usually, an eruptive flare expands and evolves through all the atmosphric layers and the associated radiative signatures span over the entire electromagnetic spectrum. The various ground- and space-based observational resources cover a wide range of spatial, temporal, and spectral domains, which help in understanding the different atmospheric layers through measurements of their physical parameters, viz., temperature, density, pressure, etc. In view of this, it is important to investigate the origin and evolution of the solar eruptive events through multi-wavelength and multi-instrument observational facilities.

It is now well-established that the magnetic flux rope (MFR) is the basic constituent of the solar eruptive phenomena. An MFR is defined as the bundle of field lines that wind around each other and wrap around a common axis. In this thesis, we focus on the exploration of the build-up, activation, eruption, and subsequent evolution of MFRs in the framework of the eruptive flares. Our analyses reveal a number of important observational results related to the physics of MFR with the aid of multi-wavelength data, complemented by the coronal magnetic field modeling techniques. The E(UV) imaging observations are obtained from the Atmospheric Imaging Assembly (AIA) instrument on board the Solar Dynamics Observatory (SDO) spacecraft. The photospheric magnetic field evolution is studied from the data gathered from the Helioseismic and Magnetic Imager (HMI) instrument on board SDO. The imaging and spectroscopic capabilities of Reuven Ramaty High Energy Solar Spectroscopic Imager (RHESSI) are extensively utilized to investigate the thermal and non-thermal energy release processes associated with different stages of the eruptive phenomena through analysis of the X-ray sources. The Large Angle and Spectrometric Coronagraph (LASCO) on board the Solar and Heliospheric Observatory (SOHO) spacecraft provides the white light observations of CMEs. The temporal information about the evolutionary stages of solar flares are obtained from the disk-integrated soft X-ray light curves in the 1–8 and 0.5–4 Å channels of the Geostationary Operational Environmental Satellite (GOES) system. In order to investigate the precise coronal magnetic field structures, we use two different magnetic field extrapola-

tion techniques. For the analysis of small-scale magnetic fields at lower coronal heights, we use the Non-Linear Force-Free Field (NLFFF) extrapolation technique, whereas, the large-scale coronal magnetic structures are investigated through the Potential Field Source Surface (PFSS) method. Both these extrapolation methods are based on the numerical techniques.

We analyze the processes responsible for the build-up and activation of a hot channel in high temperature EUV passbands, located over the polarity inversion line (PIL) of the flaring region within the NOAA active region (AR) 12371 during 2015 June 22. The activated hot channel erupts following the standard flare reconnection scenario giving rise to a major M6.6 flare and associated CME. Prior to the onset of the eruptive flare, the hot channel undergoes a prominent activation phase during which it displays co-spatial hard X-ray (HXR) emission up to energies of 25 keV. We obtain an MFR co-spatial to the hot channel through NLFFF modeling. To our knowledge, this is the first time a developing MFR/hot channel is being detected in direct HXR observations. These distinct, localized HXR sources from the central part of the MFR suggest its build-up and activation through magnetic reconnection among the sheared/twisted field lines representing the MFR magnetic structure. We observe significant changes in the AR's photospheric magnetic field prior to the flare onset, during an extended period of ≈42 hr in the form of rotation of sunspots, moving magnetic features, and flux cancellation along the PIL. During the activation phase of the MFR, it undergoes a slow rise phase (≈14 km s^{-1}) for ≈12 minutes, which is thought to be the result of the ongoing magnetic reconnection occurring at multiple locations within the MFR core field. Suddenly, a fast transition (≈109 km s^{-1} with acceleration ≈110 m s^{-2}) in the kinematic evolution of the MFR is observed, which temporally marks the onset of the impulsive phase of the ensuing M6.6 flare. This sudden transition in the speed of the erupting MFR precisely divides the pre-flare and impulsive phase of the flare. This observation points toward the standard flare reconnection scenario, which entails the inherent feedback process between the early dynamics of the eruption and the strength of the flare magnetic reconnection. The erupting MFR finally blows out the constraining overlying field lines completely to be observed in the coronagraphic images as a CME.

An MFR may form at the base of the convective layer of the Sun due to dynamo mechanism. Buoyancy instability causes the MFR to emerge from the solar interior and overshoot the photosphere to break into the atmosphere. The footpoints of a bundle of emerged MFRs usually become visible in the white light intensity images as sunspot groups, forming the ARs. The various photospheric motions strongly affect the subsequent dynamics of an MFR after its emergence. In view of this idea, we try to explore the efficient coupling between the photospheric and coronal magnetic fields and associated processes through the investigation of a series of homologous eruptive flares. The flares originate from NOAA AR 12017 during 2014 March 28–29 and are of successively increasing intensities (M2.0, M2.6, X1.0). The EUV observations coupled with coronal magnetic field modeling reveal that the eruptive flares are triggered by the eruption of MFRs embedded by a densely packed system of bipolar loops within a small part of the AR. The evolution of photospheric magnetic field over an interval of $\approx$44 hr encompassing the three events undergoes important phases of emergence and cancellation processes together with significant changes near the PILs where the flux ropes lie. In view of this, our observational results point toward the tether-cutting mechanism as the viable triggering mechanism responsible for the eruptions. Between the second and third event, we observe a prominent phase of magnetic flux emergence which temporally correlates with the build-up phase of free magnetic energy in the AR corona. This observation is suggestive of an efficient coupling between the rapidly evolving photospheric and coronal magnetic fields in the form of persistent flux emergence that leads to a continued phase of the build-up of free magnetic energy, which gets released episodically resulting into the three homologous flares of successively increasing intensities.

The homologous eruptive flares in AR 12017 are triggered by the eruption of compact MFRs within the flaring region. The spatial extent of the source region of eruptions is much compact compared to the CMEs produced as a result of the eruptions. Each of the three CMEs developed in the wake of the eruptions gradually attains a large angular width, after expanding from the compact eruption-source site. We analyze this remarkable observation of generation of broad CMEs resulting from compact eruptions. We find these eruptions and CMEs to be consistent with the "Magnetic-Arch-Blowout" (MAB) scenario: each compact-flare blowout-eruption is seated in one foot of a far-reaching magnetic arch, explodes up the encasing leg of the arch, and blows out the arch to make a broad CME.

In summary, our observational results obtained from the multi-wavelength and multi-instrument data, complemented by the coronal magnetic field modeling techniques, are useful to understand the build-up, activation, triggering, and subsequent evolution of MFRs in the framework of the eruptive flares. Our results can be used as important inputs toward the prediction of near-Earth space weather phenomena.

Keywords: Solar coronal mass ejections, Solar flares, Solar magnetic fields, Solar magnetic flux ropes

List of Publications

1. "Hard X-Ray Emission from an Activated Flux Rope and Subsequent Evolution of an Eruptive Long-duration Solar Flare".
   Suraj Sahu, Bhuwan Joshi, Prabir K. Mitra, Astrid M. Veronig, and V. Yurchyshyn, (2020), **The Astrophysical Journal**, 897, 157,
   DOI: https://iopscience.iop.org/article/10.3847/1538-4357/ab962b.

2. "Homologous Compact Major Blowout-eruption Solar Flares and their Production of Broad CMEs".
   Suraj Sahu, Bhuwan Joshi, Alphonse C. Sterling, Prabir K. Mitra, and Ronald L. Moore, (2022), **The Astrophysical Journal**, 930, 41,
   DOI: https://iopscience.iop.org/article/10.3847/1538-4357/ac5cc1.

3. "Evolution of Magnetic Fields and Energy Release Processes During Homologous Eruptive Flares".
   Suraj Sahu, Bhuwan Joshi, Avijeet Prasad, and Kyung-Suk Cho, (2023), **The Astrophysical Journal**, 943, 70,
   DOI: https://iopscience.iop.org/article/10.3847/1538-4357/acac2d.

All of the above publications are attached at the end of this thesis.

Table of Contents

List of Figures

List of Tables

Chapter 1

Introduction

The Sun has immensely dominated the lives and thoughts of humankind from the very beginning of human civilization. Starting from the earliest known civilizations to modern human activities, the Sun continues to influence in numerous ways. As the source of light and warmth, the Sun has naturally astonished the curious and scientific minds. The prolific advancement of science and technology in the last few decades has opened up novel avenues for the exploration of the Sun. Being our closest star, the Sun provides a great opportunity for us to study intricate features of its surface and atmosphere, and derive various physical parameters.

Apart from the benevolent nature of the Sun, there is a dark side of it. Sporadic outbursts of high-energy particles and ejections of magnetised plasma from the Sun can sometimes create severe geomagnetic storms in the near-Earth environment causing disruption of communication systems, power grids etc. The high-energetic particles associated with these outburts may endanger the astronauts traveling in the interplanetary space. As our modern, hi-tech society becomes increasingly vulnerable toward the solar hazards, it is important to study the intrinsic dynamic nature of the Sun and formulate models to enable the forecasting of solar eruptions in the near-Earth environment.

1.1 Solar eruptive phenomena

Solar eruptive phenomena correspond to the numerous transient activities, from small- to large-scales, occurring in the solar atmosphere intermittently. Our solar observing capabilities with various ground- and space-based instruments have enabled us to observe these phenomena majorly in the forms of filament/prominence eruption, solar flare, coronal mass ejection, etc. The synthesis of multi-wavelength and multi-instrument observations has revealed that these eruptive events are guided by the complexity of magnetic

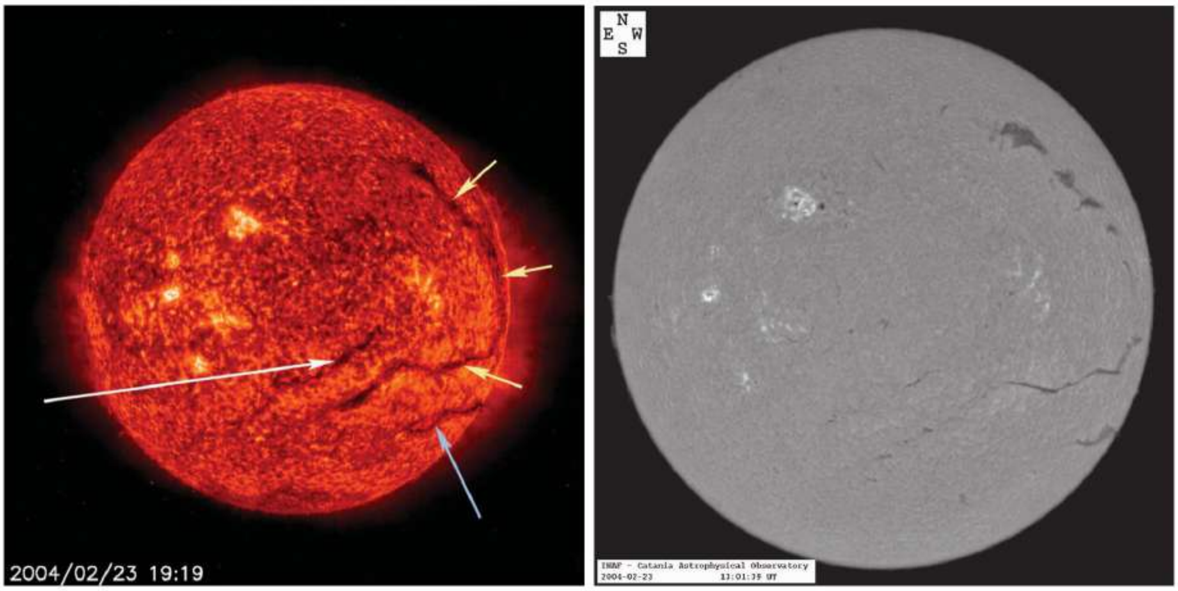

Figure 1.1: left: image of the Sun as observed in the He II 304 Å channel on SOHO/EIT, on 23 February 2004, revealing three dark filaments (indicated by arrows). Right: image of the Sun in Hα on the same day revealing different spatial details of these filaments. Figure is adopted from Parenti (2014).

field in the different layers of the solar atmosphere, which ultimately manifest themselves as ejection of magnetized plasma out into the heliosphere.

1.2 Filament or prominence

Solar filaments are intriguing structures composed of cool, dense plasma suspended in the solar corona upto average height of $\approx$100 Mm above the photosphere. They are termed as "filaments" on the solar disk, where they are observed in absorption in various visible (e.g., Hα), Extreme Ultraviolet (EUV) (e.g., He II) chromospheric spectral lines (Figure 1.1). On the other hand, these structures are described as "prominences" when they are viewed above the solar limb, where they appear as bright features against the dark background of the sky (Figure 1.2). Hence, filament and prominence are the two different terms of the same physical structure (see reviews by Mackay *et al.*, 2010; Parenti, 2014; Gibson, 2018). The existence of cool, dense plasma being suspended in the hotter and rarer corona has been a mystery ever since the first observations of filaments and prominences (Hirayama, 1985; Zirker, 1989; Tandberg-Hanssen, 1995). The magnetic structure of filaments is not fully understood yet, with many observational results and theoretical models differing on the exact nature of the filament's magnetic field. In this regard, the physical processes governing the origin and subsequent evolution

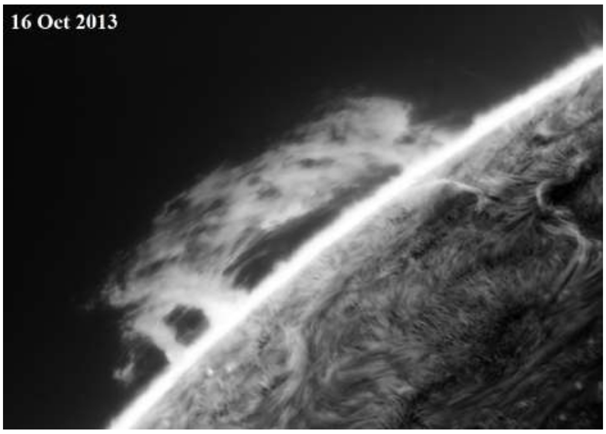

Figure 1.2: processed image of a large solar prominence taken in Hα (6563 Å) using a 150 mm solar telescope with a monochrome camera. Courtesy: `https://cs.astronomy.com/asy/m/sunandmoon/489304.aspx`.

of the prominence plasma and associated magnetic structure remain a contemporary topic of debate.

Filament magnetic structure

Filaments are invariably located above polarity inversion lines (PILs), i.e., lines on the photosphere where the radial component (B_r) of the magnetic field changes sign. Filaments can be found within the activity nest consisting of multiple bipolar sunspot groups (active region filament), at the border of the active regions (ARs) (intermediate filament), and at the quiet regions of the Sun (quiescent filament). A typical filament consists of three basic components: a spine, barbs, and two extreme ends/legs (Figure 1.3). The spine runs horizontally along the top of the filament and is considered to be the main axis of the filament. The barbs are observed to protrude from the side of a filament. In case of prominence, the barbs are seen to extend down from the spine to the lower atmospheric layers. The two extreme ends of a filament are known as 'legs', that terminate in the photosphere in opposite polarity regions. The Hα observations of quiescent filaments reveal that each of these three structural components consist of thin thread-like structures (Martin, 1998; Pécseli and Engvold, 2000). The individual threads are found to have widths of ≈200 km and lifetimes of the order of few minutes, whereas, the filaments as a whole can be stable for few days to few months.

Physical properties of filaments

Temperature of filaments can vary between 7500 to 9000 K and the electron density ranges from 10^9 to 10^{11} cm^{-3} (Parenti, 2014). It is to be noted that the temperature of filaments

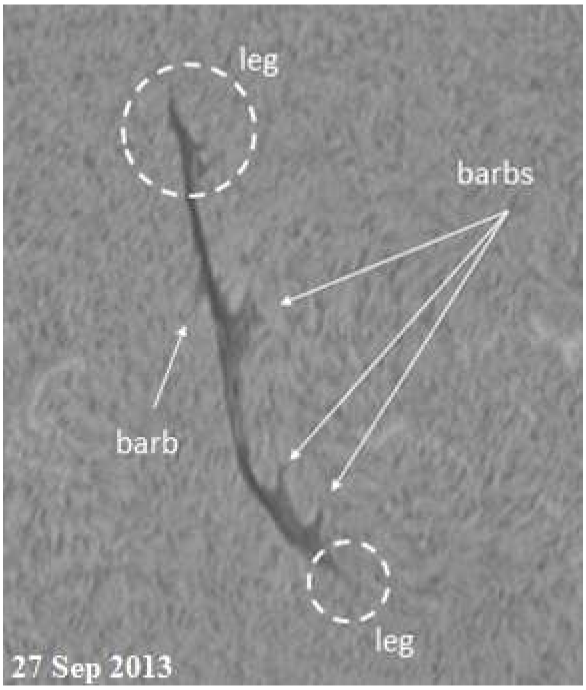

Figure 1.3: Hα image of a filament with its three distinct components. Courtesy: `https://www.stce.be/news/219/welcome.html`.

is ~2 orders lesser than the temperature of ambient corona, while their electron density is ~2 orders higher than the coronal electron density. The pressure within filaments is in the range of ≈0.02–1 dyne cm^{-2}. Considering a cool filament consisting mostly of neutral hydrogen, the mass of a filament can be roughly estimated to be in the range of 10^{12}–10^{15} gm (Labrosse *et al.*, 2010).

1.3 Flare

Solar flares are the most powerful magnetic explosions in the solar system. In tens of minutes to few hours, they can release energy of the order of $\approx 10^{32}$ erg, along with emission of radiation across the entire electromagnetic spectrum, starting from radio to γ wavelength range (Fletcher *et al.*, 2011). The source of the energy which rapidly gets released during a flare is the energy that is previously stored in the magnetic fields due to electrical currents flowing into the corona. The emitted radiation during a flare consists of both thermal and non-thermal components. The thermal signatures of flares include optical, ultraviolet (UV), EUV, soft X-ray (SXR) emissions, whereas, the non-thermal signatures are observed in the hard X-ray (HXR), microwave, and radio wavelength ranges. The non-thermal contribution of the total flare energy originates from the production of highly-accelerated charged particles due to magnetic reconnection observed in the forms of HXR and microwave sources (Benz, 2017). The type II and type III radio bursts can be used as indiret probe to gain information about the restructuring of coronal magnetic field and early development of CME propagation (Cairns *et al.*, 2003; Reid and Ratcliffe,

Table 1.1: Hα classification of solar flares.

Importance class	Corrected Area (A)	
	In millionths of a solar hemisphere*	In square degrees
S	A < 100	A < 2.0
1	$100 \leqslant$ A < 250	$2.1 \leqslant$ A < 5.1
2	$250 \leqslant$ A < 600	$5.2 \leqslant$ A < 12.4
3	$600 \leqslant$ A < 1200	$12.5 \leqslant$ A < 24.7
4	A $\geqslant$ 250	A $\geqslant$ 24.8

$*$ one millionth of the solar hemisphere $\approx 1.5 \times 10^6$ km^2

2014). The charged particles created at the reconnection site travel down to the chromosphere and produce rapid plasma heating by depositing their energy. As a result, the chromospheric plasma gets evaporated and fill the loop arcades formed due to reconnection. In this process, the kinetic energy of charged particles is converted into the thermal energy of the heated evaporating chromospheric plasma material, thus contributing to the total flare energy budget.

1.3.1 Flare classification

Hα classification

In this classification scheme, a flare is characterized by its brightness and spatial extent in the Hα (6563 Å) spectral line. To be considered as a flare, the brightness should exceed the threshold of 150% of the background brightness and the area of flaring region should be more than the ten millionths of the visible solar hemisphere. In this classification scheme, flares are classified with a character (S = subflare, or 1, 2, 3, or 4 for the successive larger flares) that denotes the flare size and a letter (f = faint, n = normal, b = bright) corresponding to subjective estimate of the flaring intensity (see Table 1.1).

GOES classification

In this classification scheme, the flares are categorized according to their SXR flux emission during the flare peaks as measured by the 1–8 Å channel of GOES satellite. The GOES SXR flux is measured in the units of W m^{-2} and plotted on a logarithmic scale conventionally. The flares are classified with a letter (A, B, C, M, and X) corresponding to the powers of 10 (-8, -7, -6, -5, and -4, respectively) of the peak 1–8 Å flux along with a number (between 1–9) that acts as a multiplier (see Table 1.2). For example, if the peak SXR flux in the 1–8 Å channel of a flare is 6.6×10^{-5} W m^{-2}, then the flare is recognized as M6.6 flare.

Table 1.2: GOES SXR classification of solar flares.

Flare class	Peak flux in 1–8 Å (W m^{-2})
A	10^{-8} to 10^{-7}
B	10^{-7} to 10^{-6}
C	10^{-6} to 10^{-5}
M	10^{-5} to 10^{-4}
X	10^{-4} and above

1.3.2 Temporal evolution of solar flares

Solar flare is a multi-wavelength phenomenon. Therefore, in order to understand the different evolutionary aspects of a flare, it is important to analyze its temporal evolution in different wavelength bands. In Figure 1.4, we present the evolution of a typical flare, as it progresses with time.

Pre-flare and precursor phase

Preceding a flare, the initial signs of activity are collectivelly termed as 'pre-flare' activity. This term also covers the 'flare precursor' events, which are small-scale brightenings observed in UV to SXR wavelengths happening ≈tens of minutes before the flare. Spatially resolved intensity curves obtained from the flaring location reveal that flare precursors often occur in the neighborhood of a flaring site (Fárník *et al.*, 1996; Fárník and Savy, 1998; Warren and Warshall, 2001; Fárník *et al.*, 2003). Statistical study conducted with a large data set reveals that the onset of pre-flare activity, in the form of weak SXR emission, precedes the onset of impulsive HXR emission by ≈3 minutes in the vast majority of flares, regardless of their total energy or duration (Veronig *et al.*, 2002). Spectral line broadening has also been observed in the pre-flare phase, indicative of the non-thermal effects such as plasma turbulence (Harra *et al.*, 2009). It has been suggested that the pre-flare brightening may occur as a result of slow magnetic reconnection and provide a trigger for the subsequent large-scale eruption (Moore *et al.*, 2001; Chifor *et al.*, 2007).

Impulsive phase

The primary energy release occurs during the impulsive phase of a flare through a fundamental process called 'magnetic reconnection' (Priest and Forbes, 2002). This phase of flare activity varies from tens of seconds to tens of minutes and is characterized by HXRs, γ-rays, microwaves and white light continuum emission, suggestive of strong

Figure 1.4: schematic representation of temporal evolution of the flare intensity at different wavelength regimes. The various phases of the flares (indicated at the top) show large variation in their duration and depend on the flare under consideration. Figure adopted from Benz (2017).

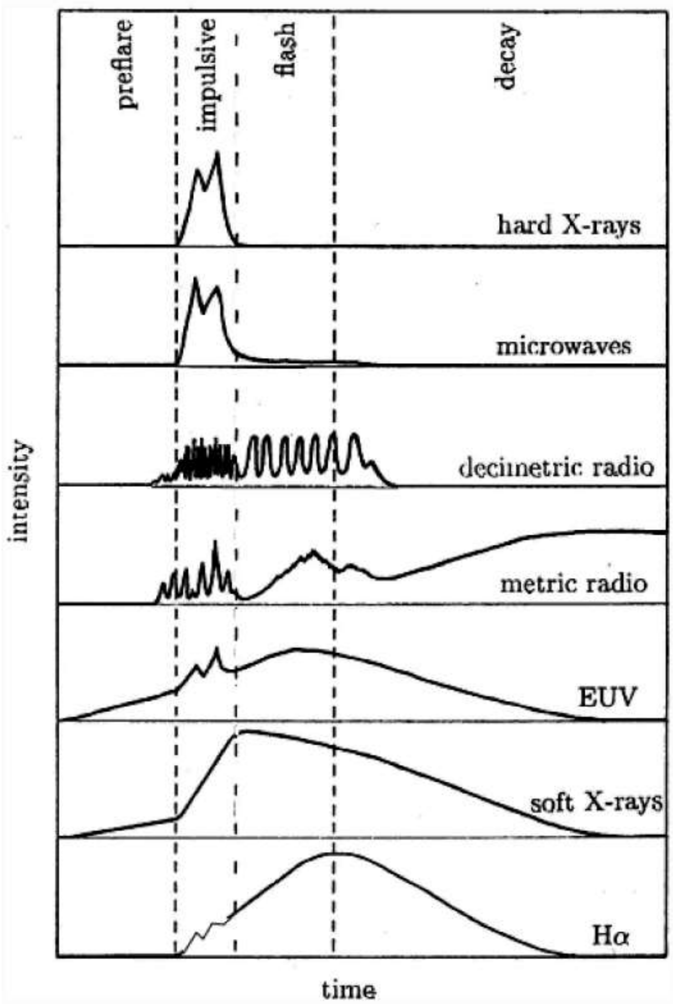

acceleration of charged particles produced due to reconnection. According to the classical non-thermal thick-target model (e.g., Brown, 1971; Lin and Hudson, 1976), electrons are accelerated to ≈100 keV in the corona and then spiral downwards, creating microwaves (Dennis, 1988). After reaching the footpoints of a coronal loop, the electrons interact with the chromospheric plasma and produce HXRs due to Bremsstrahlung process and drive evaporation of heated chromospheric plasma (Figure 1.5). This evaporating thermal plasma fills the post-reconnected loops which emits mostly in EUV and SXRs. Recent observations have revealed that HXR sources can also be found in the corona on top of post-reconnected loops, which mark the precise locations of magnetic reconncetion process (Fletcher *et al.*, 2011; Benz, 2017). The thermal signatures during the impulsive phase can be observed in the form of a pair of elongated brightening (i.e., flare ribbons) along the footpoints of the post-reconnected loops, usually observed in Hα and UV images (Figure 1.6). The flare ribbons gradually move apart from each other with the evolution of the flare (Fletcher and Hudson, 2002; Temmer *et al.*, 2007). The thermal SXR and Hα emissions finally reach their maxima after the impulsive phase, when

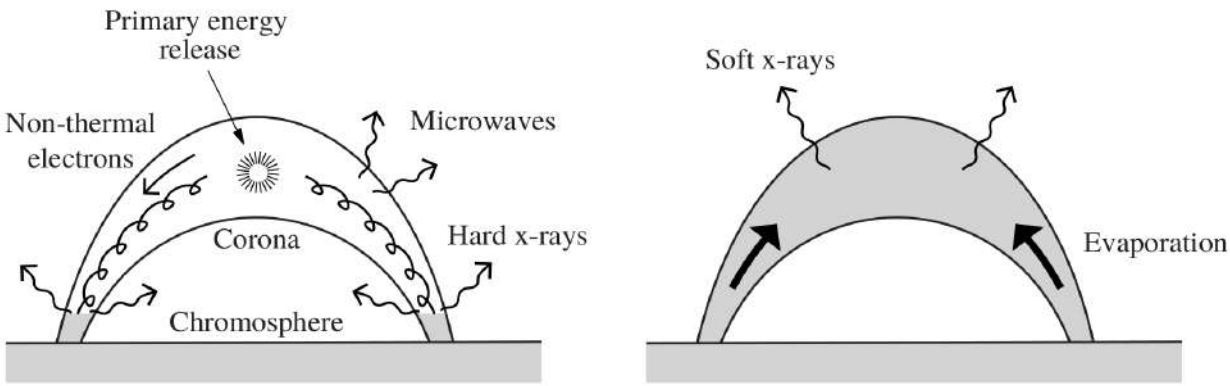

Figure 1.5: the production of microwaves, HXRs, and SXRs according to the non-thermal thick-target model. Figure is taken from Priest and Forbes (2002).

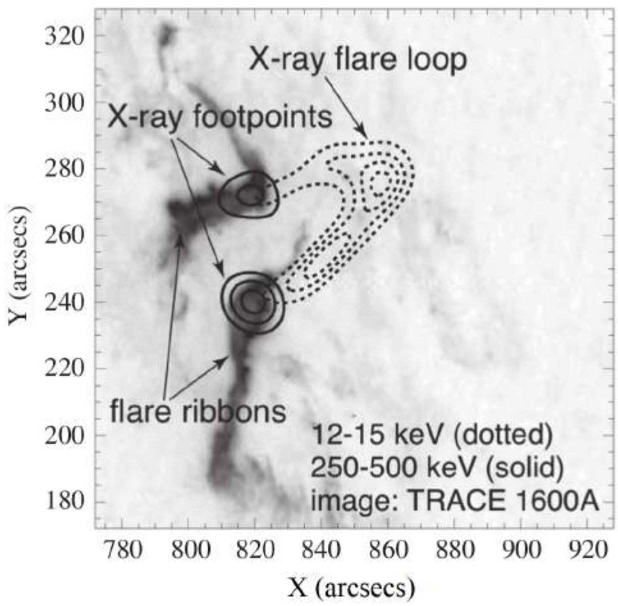

Figure 1.6: X-ray observations from RHESSI at the peak of a typical solar flare, showing a SXR loop linking two HXR footpoints, superimposed on a UV 1600 Å image from TRACE. Figure taken from Krucker *et al.* (2008).

energy is more gently released. The rapid increase in Hα intensity and line width has been termed as 'flash phase' (Benz, 2017). It coincides with the impulsive phase in general, although the Hα intensity may peak later, in comparison to the other intensity curves of different wavelength bands (see Figure 1.4).

Gradual phase

The gradual phase of a flare is identified by its slowly decaying HXR and microwave signatures, with increasing thermal SXR and EUV signatures. As the chromospheric

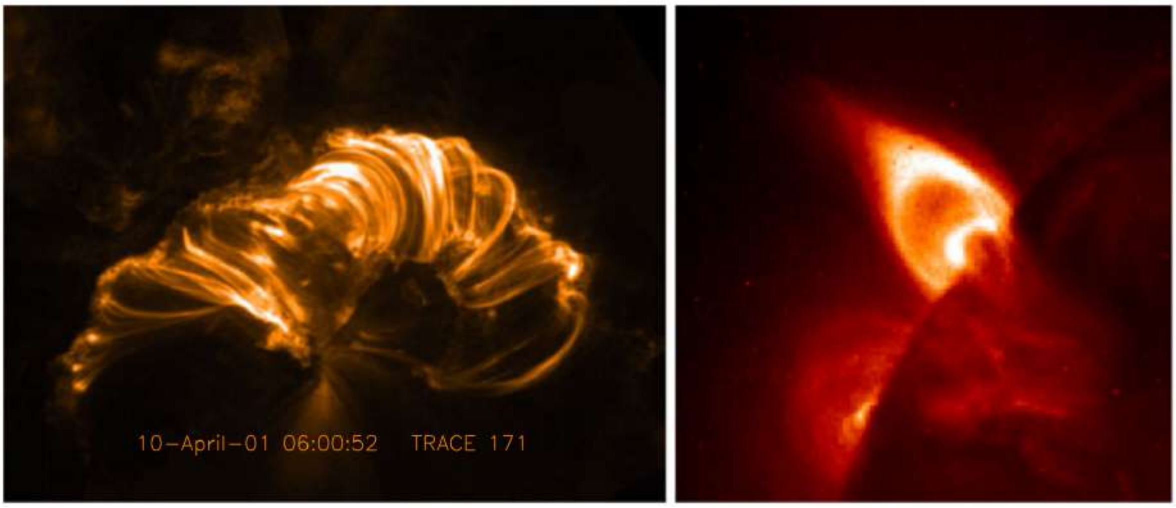

Figure 1.7: left: a flare arcade formed during the gradual phase of the X2.3 flare (SOL2001-04-10T05:26), observed in TRACE 171 Å channel. Right: a large post-flare cusp structure observed several hours after the impulsive peak of SOL1999-03-18T08:31 (M3.3), observed by Yohkoh/SXT. Figure adopted from Fletcher *et al.* (2011).

plasma is rapidly heated by the deposition of energy due to charged particles, it fills the post-reconnected loops, that emit mostly in SXR, EUV bands and gradually appear to grow in size (Figure 1.7; left image). The loop arcades show a gradient in temperature, with the outermost loops being the hottest. The hottest outer loops sometimes exhibit a "cusp" shaped structure observed in X-ray images (Figure 1.7; right image). Later on, as the corona cools, the loop arcade becomes visible in lower temperature emissions, such as EUV and Hα (Schmieder *et al.*, 1995). The gradual phase may last several hours, depending on the magnitude of the flare. In many events, the cooling timescales of the loops point toward an additional energy source during the gradual phase. The origin of this energy source is thought to come from ongoing slow reconnection between the tangled post-flare loops or at locations above them and its associated heating (MacCombie and Rust, 1979; Forbes *et al.*, 1989).

1.3.3 Standard flare model

Solar flares offer a wide variety of temporal and spatial aspects that need to be considered collectively to understand the flare mechanism. Flares triggered by an erupting filament provide some common multi-wavelength signatures, viz., pair of flare ribbons, footpoint HXR sources, formation of post-flare arcades, etc. In order to explain these broad range of flare associated observational signatures, a standard flare model in 2D, also known as CSHKP model (Figure 1.8) has been developed by combining the pioneer-

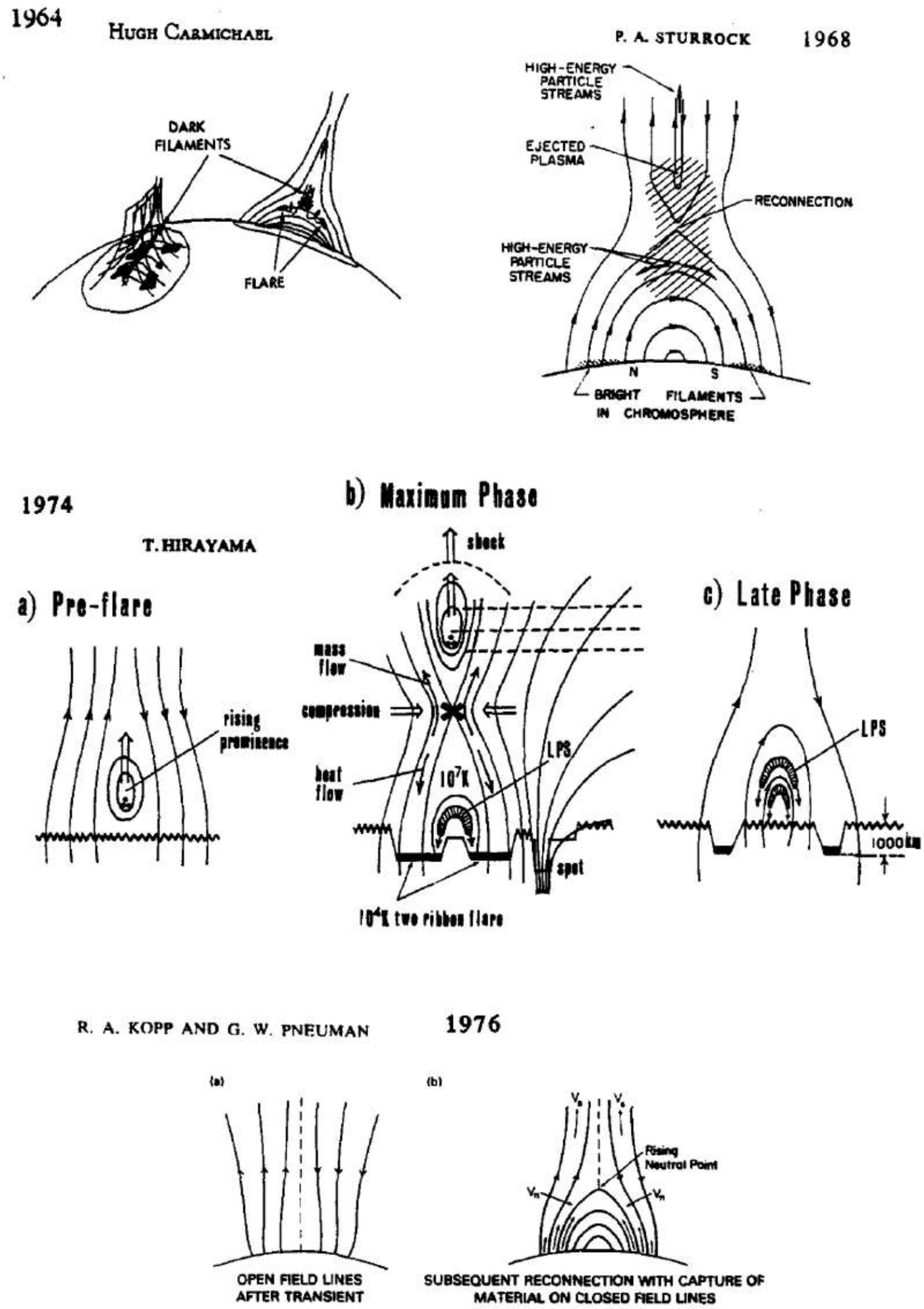

Figure 1.8: The basic coronal magnetic field configurations for eruptive flares first proposed by Carmichael (1964) (upper left), later improved by Sturrock (1966) (upper right), Hirayama (1974) (middle), and lastly by Kopp and Pneuman (1976) (bottom). Figure is taken from Svestka and Cliver (1992).

ing works of Carmichael (1964); Sturrock (1966); Hirayama (1974); Kopp and Pneuman (1976).

Carmichael (1964) first proposed that the flare ribbons and flare loops are coupled and can be formed as a consequence of relaxation of stretched magnetic field in the wake of eruption. Sturrock (1966) identified that the origin of main energy release during a flare is the magnetic reconnection process caused by tearing-mode instability (Tenerani *et al.*, 2015) in the stretched magnetic field. The distinct phases of a flare, viz., pre-flare, main, and late phase were recognized by Hirayama (1974). Pre-flare activities trigger the upward motion of a filament, which stretches the overlying magnetic field lines, creating a 'X' point underneath it. This 'X' point is the location of magnetic reconnection. As the filament rises further up in the corona, the 'X' point also rises resulting in the reconnection at gradually increasing heights. This explains the gradual separation of flare ribbons and increasing height of post-reconnection loops. Kopp and Pneuman (1976) proposed that the post-reconnection loops (i.e., post flare loops) are the result of magnetic reconnection in the magnetic field which were previously torn open by flare outburst. In summary, all these studies provide a common explanation of energy release during a flare caused by reconnection that occurs in a vertical current sheet formed due to the stretching of magnetic field lines enveloping the erupting filament.

1.4 Coronal Mass Ejection (CME)

Coronal mass ejections (CMEs) are large structures containing plasma ($\sim 10^{12}$–10^{13} kg) and magnetic fields ($\sim 10^{21}$–10^{23} Mx) that are expelled from the Sun into the heliosphere (Webb and Howard, 2012). The study of CMEs is important from both the scientific and technological viewpoints. Scientifically they are of interest because they remove built-up magnetic energy and plasma from the solar corona (Low, 1996), and technologically they are of interest because they are responsible for the most extreme space weather effects at the Earth and other planetary bodies throughout the heliosphere (Baker *et al.*, 2008). CMEs exhibit a wide range of shapes and sizes with many structural variations (Gopalswamy, 2006; Chen, 2011).

1.4.1 Observations of CMEs

According to the original definition, CMEs are an observable change in the coronal structure that involves the appearance (Hundhausen *et al.*, 1984) and outward motion (Schwenn, 1996) of a new, discrete, bright, white light feature in the coronagraph field of view. The white light observation of a CME is associated with the 'Thomson Scattering'

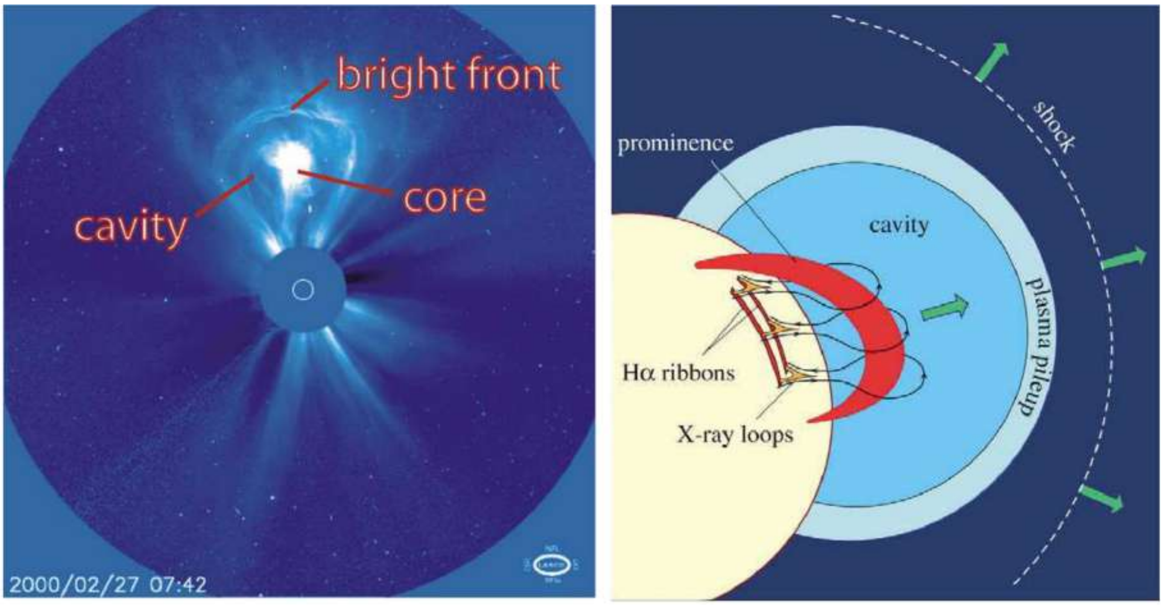

Figure 1.9: left panel: example of the classical three-part structure of a CME observed by LASCO C3 coronagraph. Figure taken from Riley *et al.* (2008). Right panel: A standard model for the "three-part" structure of a CME. Figure adopted from Forbes (2000).

of photospheric radiation by the free electrons contained in the CME core. With the continual observations from various ground- and space-based coronagraphs, a vast data on CME observations are now available.

Remote sensing observations

The remote sensing observations of CMEs reveal their large transient structures in the solar corona. As the coronal density is low compared to photospheric density, the light coming from the photosphere needs to be blocked in order to visualize the corona. The imaging instruments use an artifical occulter (i.e., coronagraph) to block the solar photosphere in order to image the propagation of CME in the corona. The first space-based observation of CMEs was conducted in the early 1970s by the OSO-7 coronagraph (Tousey, 1973). Thereafter, CME observations were made with better quality and longer periods using Skylab (1973–1974; Gosling *et al.*, 1974), P78-1 (Solwind) (1979–1985; Sheeley *et al.*, 1980) and Solar Maximum Mission (SMM) (1980–1989; House *et al.*, 1981). A major advancement in the CME observation was followed by the launch of SOHO (Domingo *et al.*, 1995) in 1995. Thereafter, from 2006 onward, the twin STEREO (Howard *et al.*, 2008) spacecrafts started to provide multi-vantage point observations of CMEs.

Apart from these space-based remote sensing observing facilities of CMEs, several ground-based facilities take CME observations, viz., Mauna Loa Solar Observatory (MLSO) (Koomen *et al.*, 1974; Fisher *et al.*, 1981), Sacramento Peak, New Mexico

(Demastus *et al.*, 1973), Norikura, Japan (Hirayama and Nakagomi, 1974), etc.

In-situ observations

The observation of CME in the heliosphere is taken in the form of its interplanetary counterpart, named as interplanetary coronal mass ejection (ICME) (Dryer, 1994; Zhao and Webb, 2003). The in-situ observations of ICMEs are obtained through the detection of their magnetic field signatures, temperature characteristics, chemical compositions, etc.

CME catalogs

Several "manual" catalogs were constructed using the CME observations from P78/Solwind[1], SMM C/P[2], and LASCO[3] coronagraphs. Recently, these catalogs have been augmented by additional on-line catalogs of CMEs detected by automatic methods. One is the CACTus CME catalog (Robbrecht *et al.*, 2009), which uses the data from STEREO COR2 coronagraphs that are near 1 AU solar orbits. The other catalogs, viz., SEEDS (Olmedo *et al.*, 2008) and ARTEMIS (Boursier *et al.*, 2009) are based on automated detection of CMEs in the LASCO C2 coronagraph observed in the range of 2–6 $R_\odot$.

Basic characteristics of CMEs

Many CMEs exhibit the classical "three-part" structure: a bright leading arc/front followed by a darker, low density cavity, and bright core of dense material as seen in white light coronagraphs (see Figure 1.9). The bright leading front is due to plasma that piles-up ahead of the erupting material. With the expansion of the CME in the heliosphere, one often finds a cavity behind the bright front, where the magnetic field is probably higher compared to the leading edge of CME. The bright core corresponds to the erupting filament plasma, where the brightness originates from the radiation scattered by the dense filament material. CMEs travel in the interplanetary medium with a wide range of speeds that span in the range of ≈30–2500 km s^{-1}, with an average value of ≈300–500 km s^{-1} (Yashiro *et al.*, 2004). Majority of the CMEs show constant velocity or moderate acceleration during its lifetime (Gopalswamy, 2010, 2016).

1.5 Magnetic flux rope (MFR)

Flares and CMEs are considered to be the most energetic and large-scale solar eruptive phenomena that generally occur together though not always (Kahler, 1992; Yashiro *et al.*,

[1]`https://lasco-www.nrl.navy.mil/solwind/fits/`
[2]`https://smm.hao.ucar.edu/smm/smmcp_catalog.html`
[3]`https://cdaw.gsfc.nasa.gov/CME_list/`

2006). The dark cavity and bright core observed in the three-part structure of a CME are thought to be the evidences of 'magnetic flux rope' (MFR) or 'flux rope', which is considered to be the basic component of the solar eruptive phenomena.

An MFR is defined as a helical magnetic structure with the field lines coherently wrapping around the main axis at least one turn between its two ends anchored to the photosphere (Low, 2001; Gibson and Fan, 2006; Cheng *et al.*, 2017). The bright core of a CME in white light observations usually corresponds to the cool filament/prominence material located at the bottom part of its magnetic skeleton, whereas, the dark cavity corresponds to the cross section of the MFR upper magnetic structure, devoid of sufficient plasma material, when observed edge-on (Gibson *et al.*, 2006a; Riley *et al.*, 2008). In the 2D 'standard flare model' (CSHKP model), the pre-eruptive configuration is considered to be a filament, which is modelled to be a helical MFR. However, the mechanisms responsible for the build-up and activation of MFR are not incorporated in this model. In the following, we present a few observational evidences of MFRs detected in the solar atmosphere.

1.5.1 Filament

Filaments are magnetic structures composed of relatively dense, cool plasma suspended in the tenuous, hot corona (see Section 1.2). The magnetic structure of filaments is assumed to be twisted MFRs (van Ballegooijen and Martens, 1989; Aulanier *et al.*, 1999) or sheared arcades (Antiochos *et al.*, 1994; Aulanier *et al.*, 2006b). These kind of magnetic configurations are composed of magnetic dips, which can support the filament plasma material against the solar gravity by providing magnetic tension in the upward direction (Martin, 1998; Mackay *et al.*, 2010). It is also possible that the dips of MFRs remain devoid of sufficient plasma material. In this case, the MFRs can be observed as filament channels in the chromospheric spectral lines and they are found to lie over the PIL of the decaying ARs (Aulanier and Schmieder, 2002; Chen *et al.*, 2014b).

1.5.2 Coronal cavity

Extended, tunnel-like structures above the photospheric neutral lines that are usually observed as dark ellipses in the white light images at the solar limb, embedded in bipolar helmet streamers (Figure 1.10), are known as coronal cavities. A prominence is usually found to lie at the base of the cavities in an embedded fashion. It has been proposed that the coronal cavity corresponds to MFR magnetic structure, i.e., the whole or lower part of the cavities is manifested as the MFR cross section (i.e, upper part of MFR magnetic skeleton devoid plasma) (Low and Hundhausen, 1995). Essentially, the coronal cavities

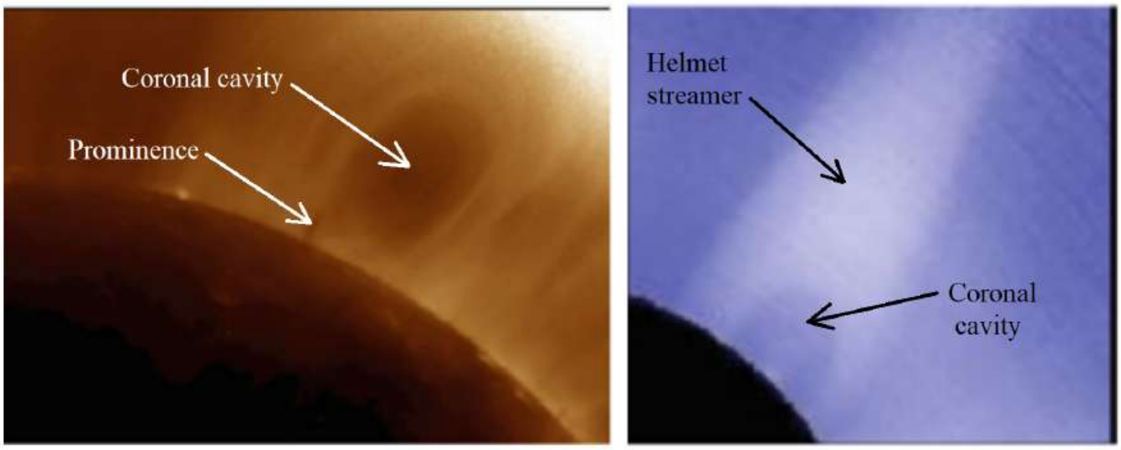

Figure 1.10: left: processed image of a coronal cavity encompassing a prominence observed by SDO/AIA 193 Å channel. Right: image of a helmet streamer surrounding a coronal cavity observed in white light by Mauna Loa Solar Observatory MK4 coronameter. Figure adopted from Gibson (2015).

are coronal limb counterparts to filament channels observed on the solar disk (Gibson *et al.*, 2006b). Coronal cavities are commonly observed in the white light passband of ground-based coronagraphs, such as Mark IV coronameter at the Mauna Loa Solar Observatory (MLSO). They can also be observed in the EUV passbands of the Atmospheric Imaging Assembly (AIA) instrument on-board the Solar Dynamics Observatory (SDO) space-satellite. A coronal cavity typically exists in the low corona for several days to months before eruption and eventually erupts as part of a CME.

1.5.3 Coronal sigmoid

The source regions of solar eruptions often consist of closely-packed hot coronal loops of S (or inverse S) shaped structure as observed in SXR or EUV emissions, are known as 'sigmoid' (Manoharan *et al.*, 1996; Rust and Kumar, 1996; Gibson *et al.*, 2002; Joshi *et al.*, 2017a) (Figure 1.11). The sigmoids are believed to be important precursors of solar eruptions (Hudson *et al.*, 1998; Gibson *et al.*, 2006a; Savcheva *et al.*, 2012b; Kawabata *et al.*, 2018). Based on their life-time, the sigmoids are categorized as transient and persistent ones. The transient sigmoids are sharper and brighter compared to the persistent ones. The persistent sigmoids appear more diffuse and could consist of highly non-potential sheared loops (Pevtsov, 2002; Green *et al.*, 2007). The bright emission from a sigmoid is originated due to heating in a current sheet at the interface layer between the sheared core fields and the ambient coronal magnetic fields (Kliem *et al.*, 2004; Gibson *et al.*, 2006b).

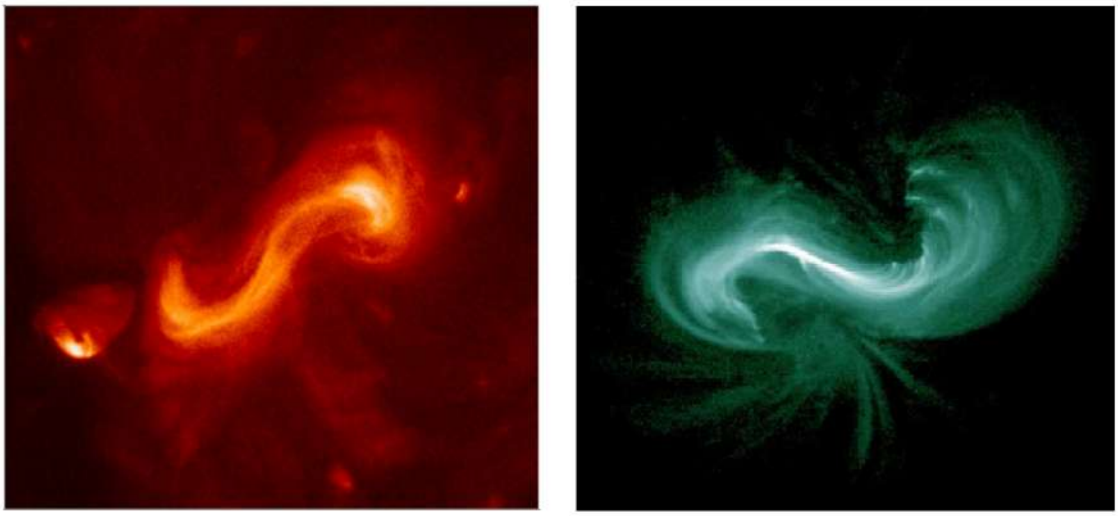

Figure 1.11: left: Hinode/XRT image of a sigmoid taken at 06:41 UT on 2007 February 12 (Savcheva *et al.*, 2012a). Right: SDO/AIA 94 Å image of a sigmoidal structure located within NOAA AR 12158 observed at ≈17:10 UT on 2014 September 10 (Duan *et al.*, 2017).

McKenzie and Canfield (2008) analyzed a coronal sigmoid of persistent category and found that the overall S-shape of the sigmoid arises due to the existence of two separate J-shaped sheared loops spatially linked to each other at their ends. The studies by Green and Kliem (2009) and Liu *et al.* (2010) have revealed that two oppositely directed, sheared J-shaped loops can form a continuous S-shaped structure resulting into a sigmoid through the tether-cutting reconnection. Moreover, some recent results obtained from the Non-Linear Force-Free Field (NLFFF) extrapolation of the coronal magnetic field have revealed that the core field of the sigmoids is comprised of twisted MFR structure enveloped by highly sheared fields (Savcheva and van Ballegooijen, 2009; Jiang *et al.*, 2013; Cheng *et al.*, 2014b).

1.5.4 Hot channel

Hot channel is the observational manifesation of MFRs detected in high temperature EUV coronal passbands. They were first observed as bright blob of hot plasma structures in the AIA 131 Å (temperature ≈11 MK) images (Cheng *et al.*, 2011). Their study revealed that the hot channel/MFR formed during the impulsive phase of the flare of their analysis. However, the hot channel appeared as a dark cavity (i.e., dimming) in the other low temperature (0.05 MK≤T≤2 MK) EUV passbands (e.g., 171, 211 Å, etc.; see Figure 1.12). Later on, other studies by Zhang *et al.* (2012) and Cheng *et al.* (2013) on the exploration of hot channel structures revealed that they existed prior to the eruption as a

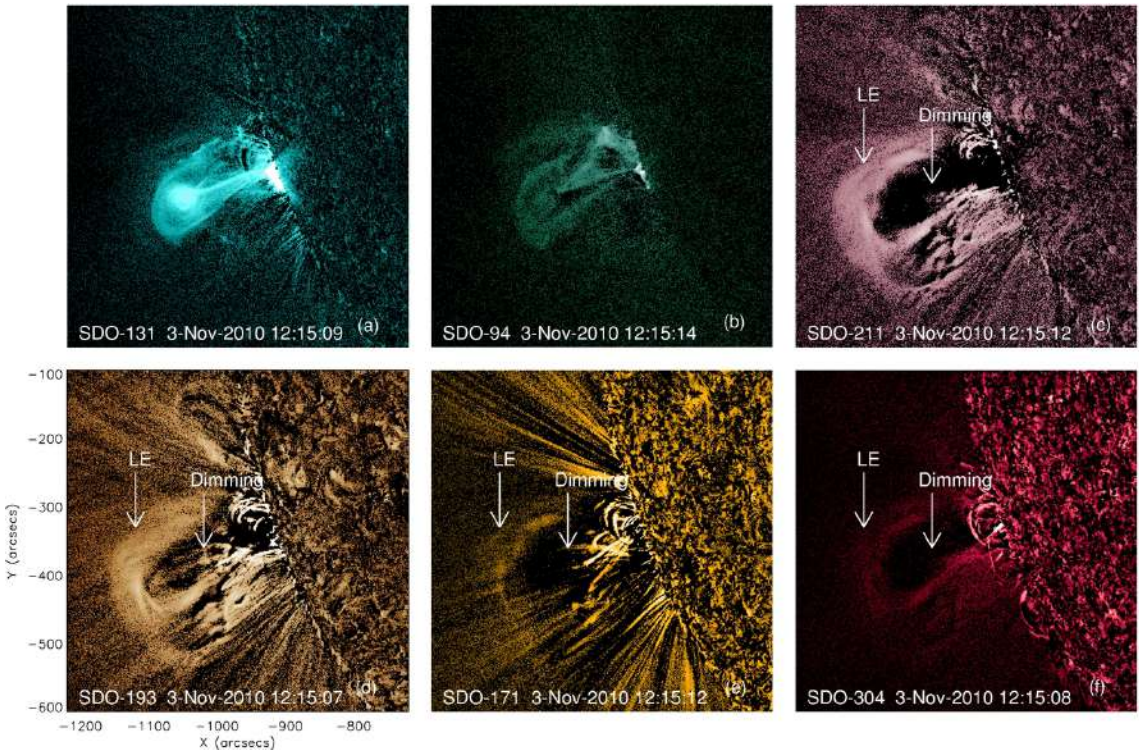

Figure 1.12: AIA base-difference images of the solar eruption on 2010 November 3 at six EUV passbands (131 Å (∼11 MK), 94 Å (∼7 MK), 211 Å (∼2 MK), 193 Å (∼1 MK), 171 Å (∼0.6 MK), and 304 Å (∼0.05 MK)). All images are at ∼12:15 UT subtracting the corresponding base images at ∼12:00 UT. The leading edge (LE) of the eruptive structure and dimming features are indicated by the arrows. We note that the eruption imitates hot channel structure in the hotter (≥7 MK) passbands. Figure adopted from Cheng *et al.* (2011).

writhed channel-like structure. The two elbows of the hot channel were inclined to the opposite directions and the middle portion was concave toward the surface when seen off the solar limb (see Figure 1.13).

Subsequently, further exploration of the hot channel structure was conducted and it was found that they existed prior to the flare/CME onset (Chintzoglou *et al.*, 2015; Joshi *et al.*, 2015; Zhou *et al.*, 2016; Joshi *et al.*, 2017b; Mitra and Joshi, 2019). Cheng *et al.* (2012) estimated the differential emission measure (DEM) of the hot channels. Their study revealed that the temperatures of hot plasma within these structures are observed to cover a broad range of ≈6.5≤log(T)≤7.3. Cheng *et al.* (2014a) identified that the hot channel is capable of evolving smoothly from the inner to the outer corona retaining its coherence. This is morphologically consistent with the CME cavity as seen in the white light coronagraphic images. Nindos *et al.* (2015) conducted a statistical study and concluded that almost half of the major CME producing flares, contain a hot blob or hot

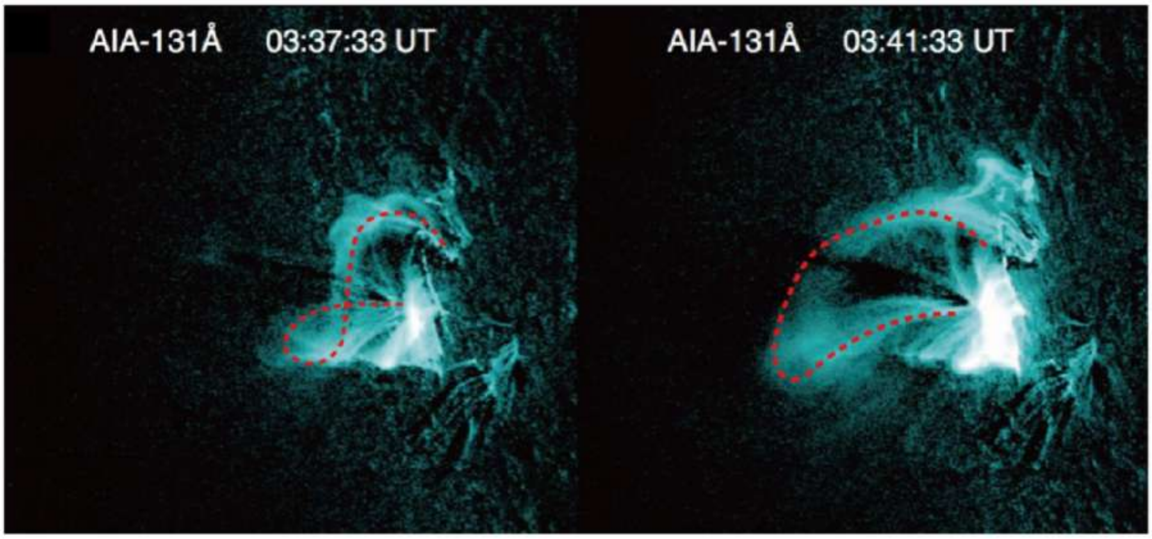

Figure 1.13: AIA 131 Å images showing the pre-existence (left) and eruption (right) of a hot channel-like MFR. The axes of the hot channel are indicated by red dashed lines in both panels. We note clear writhed axis of the hot channel in the left panel. Figure taken from Zhang *et al.* (2012).

channel-like structure. The MFR appears as a hot blob or a hot channel when observed along the parallel or perpendicular to its axis, respectively.

It is widely believed that the filaments, filament channels, prominences, coronal cavities, sigmoids, hot channels, etc. can be reconciled under the banner of MFR. They are basically the different observational evidences of MFR, based on a wide temperature domain and spatial extensions.

1.6 Formation of MFR

The MFR is the basic constituent of the solar eruptive phenomena. There are two prevailing theories regarding the appearance of MFR prior to its eruption. One assumption is that the MFR emerges into the corona from the convective layer through magnetic buoyancy. On the other hand, it can also form in the corona through reconnection and eventually it erupts. We discuss these two scenarios in the following.

1.6.1 Bodily emergence from sub-photospheric layers

The emergence of magnetic flux from the solar interior into the overlying atmosphere is considered to be the driver of a vast range of phenomena unified under the term solar activity (Cheung and Isobe, 2014; Schmieder *et al.*, 2014). It is generally believed that the concentration of magnetic field occurs below the solar convection zone in the tachocline region. A part of the global kinetic energy of solar rotation gets transformed into magnetic energy (forming toroidal magnetic field) by means of solar dynamo process with the aid of solar differential rotation. It has been shown that a horizontal toroidal magnetic field embedded in a magnetically stratified solar interior may be subjected to various instabilities, which ultimately result in the formation of arched flux tubes (Newcomb, 1961; Hughes and Cattaneo, 1987). At this point, magnetic buoyancy becomes important dynamically and its effect drives the transportation of buoyant flux tubes from the solar interior layers to the solar surface, forming Ω-shaped loops, and progressively the ARs (Zwaan, 1987; Fan, 2001; Moreno-Insertis, 2007; Fan, 2009; Leake *et al.*, 2013). An AR is an extended bipolar configuration formed by the coalescence of small emerging flux tubes. A numerical simulation carried out by Manchester *et al.* (2004) modelled the emergence of an MFR from the interior layers below photosphere upto the corona. The MFR was initially located at the convection zone. The early evolution of the MFR occurred through buoyant rise of its middle portion due to reduction of density, which ultimately rose upto coronal heights. A few observational studies also revealed evidences in support of the emergence of MFR from below the photosphere to the corona. The study by Lites (2005) revealed a concave-up geometry in the photosphere beneath an active region filament observed between two opposite polarities. This configuration might arise due to bodily rise of flux rope into the atmosphere resulting into the formation of a massive low-lying filament in the concave field geometry below the rope axis. Later, Okamoto *et al.* (2009) found emergence of a helical flux rope from below the photosphere along the PIL below a pre-existing prominence through Hinode/SOT observations. The 'Magneto-convection' process in the convective zone has important consequences on the MFR emergence process from the interior layers. The convective motions provide undulations in the emerging horizontal field to create Ω-loops and U-loops (Cheung and Isobe, 2014). The U-loops naturally have concave-up geometry. The studies by Bernasconi *et al.* (2002) and Pariat *et al.* (2004) further confirmed the frequent appearance of U-loops in the emerging ARs.

1.6.2 Formation through magnetic reconnection

A model for the formation of MFRs in the solar atmosphere was initially proposed by van Ballegooijen and Martens (1989). This model takes into account both the magnetic reconnection and associated photospheric flux cancellation processes, unified as 'flux cancellation' model (Figure 1.14). According to this model, reconnection among sheared magnetic fields in the vicinity of PIL leads to the formation of helically twisted magnetic structure (i.e., MFR) (Figure 1.15). The lower parts of these helical field lines

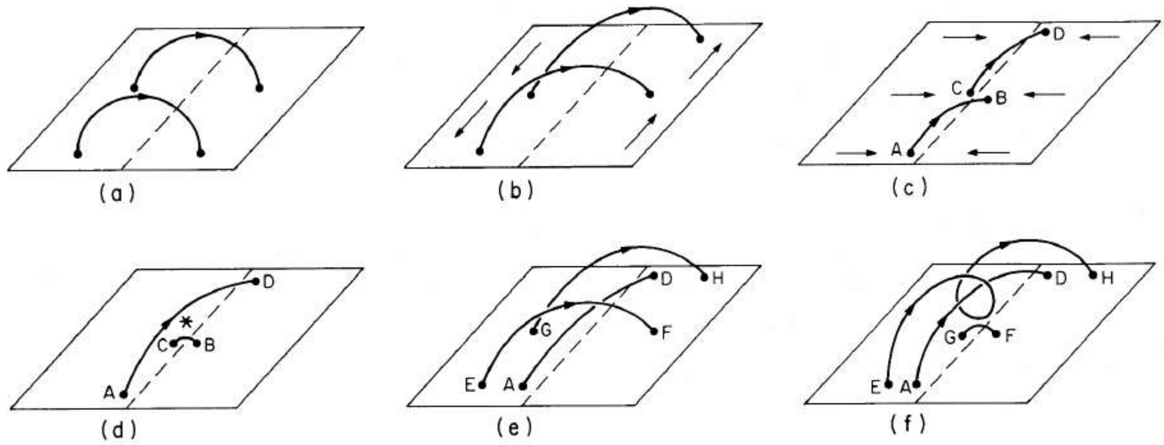

Figure 1.14: flux cancellation in a sheared magnetic field. The rectangle represents the solar photosphere and the dashed line is the PIL separating two opposite magnetic polarities. Panel (a): initial potential field configuration. Panel (b): sheared magnetic field lines are produced by the flows parallel to the PIL. Panel (c): magnetic shear is increased further due to flows toward the PIL. Panel (d): reconnection between sheared loops produces long loop AD and a short loop CB, which subsequently submerges. Panel (e): overlying loops EF and GH are pushed to the PIL. Panel (f): reconnection produces the helical loop EH and a shorter loop GF, which again submerges. Figure is adopted from van Ballegooijen and Martens (1989).

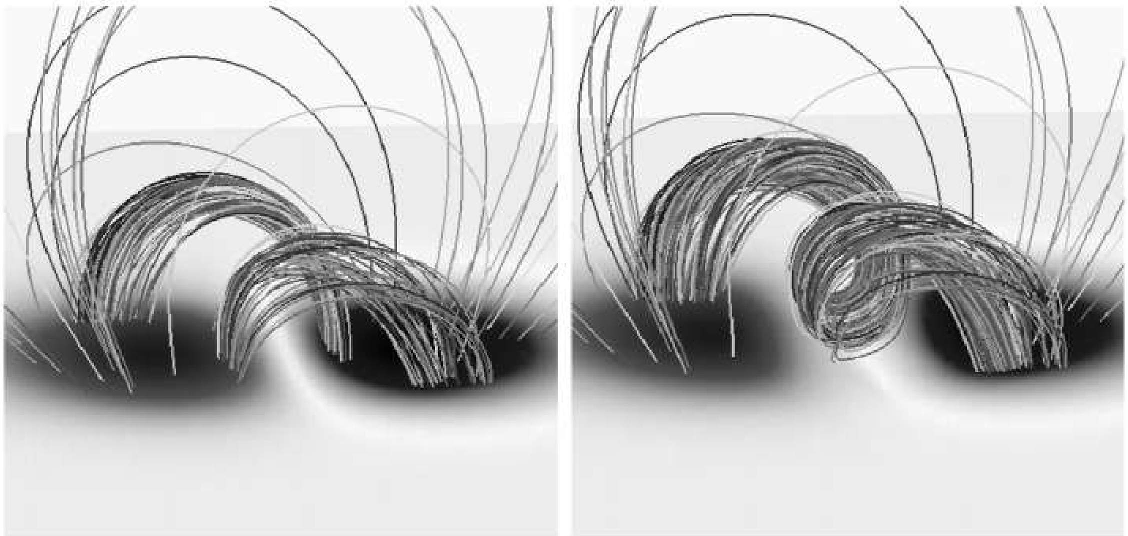

Figure 1.15: sheared magnetic field lines (left panel) evolve into a helically twisted magnetic structure (right panel) as a result of 'flux cancellation' along the PIL. Figure is adopted from Amari *et al.* (1999).

can support the prominence plasma against gravity. At the photosphere, converging flows push the sheared field lines closer to each other and force them to reconnect. The reconnection produces smaller loops which ultimately get neutralized at the PIL due to their small radius of curvature, while the larger loops gradually develop the twisted structure due to reconnection at progressively higher atmospheric heights. Numerical simulations by Amari *et al.* (1999, 2003, 2010) further support and demonstrate the idea put forward by van Ballegooijen and Martens (1989).

1.7 Triggering mechanisms for solar eruptions

Large-scale solar eruptions essentially involve eruption of MFR and associated magnetized plasma. Therefore, it is important to understand the mechanisms responsible for the triggering of an eruption. In this section, we discuss a few representative reconnection-based models for the triggering of solar eruptive phenomena.

Tether-cutting model

The general consensus of removal of overlying magnetic field by means of slow magnetic reconnection in low corona during the solar eruptions led to the development of the 'tether-cutting' model (Moore and Roumeliotis, 1992; Moore *et al.*, 2001). The intial magnetic configuration considered in this model is a single bipolar core field. These bipolar fields are low-lying and strongly sheared, which are enveloped by less-sheared near-potential magnetic arcades (Figure 1.16). Initially, the strongly sheared core fields undergo reconnection, which result in the formation of large twisted flux rope structure connecting the far ends of the core field and small loops that shrink downward. This also results in an outward imbalance for the core field that expands outward and distends the overlying field lines. As this process continues, the overlying field lines are stretched by the erupting flux rope. Below the erupting MFR, a current sheet forms, which facilitates further reconnection and ensuing flare ribbons observed at the footpoints of the post-reconnected loops. This mechanism also speeds up and strengthens the erupting flux rope due to the outflow produced from magnetic reconnection. The ultimate fate of this eruption process can have two possibilities. Either the erupting flux rope ejects out of the initially closed bipole, opening the envelope field (Figure 1.16, lower right panel) forming the core of the resulting CME, or the eruption is arrested and confined within the closed bipole (Figure 1.16, lower left panel). It has been proposed that there are two likely factors which determine the path the eruption takes. First is the flux content of the sheared core relative to the envelope field and second is the height at which the reconnection begins (Moore *et al.*, 1997, 1999).

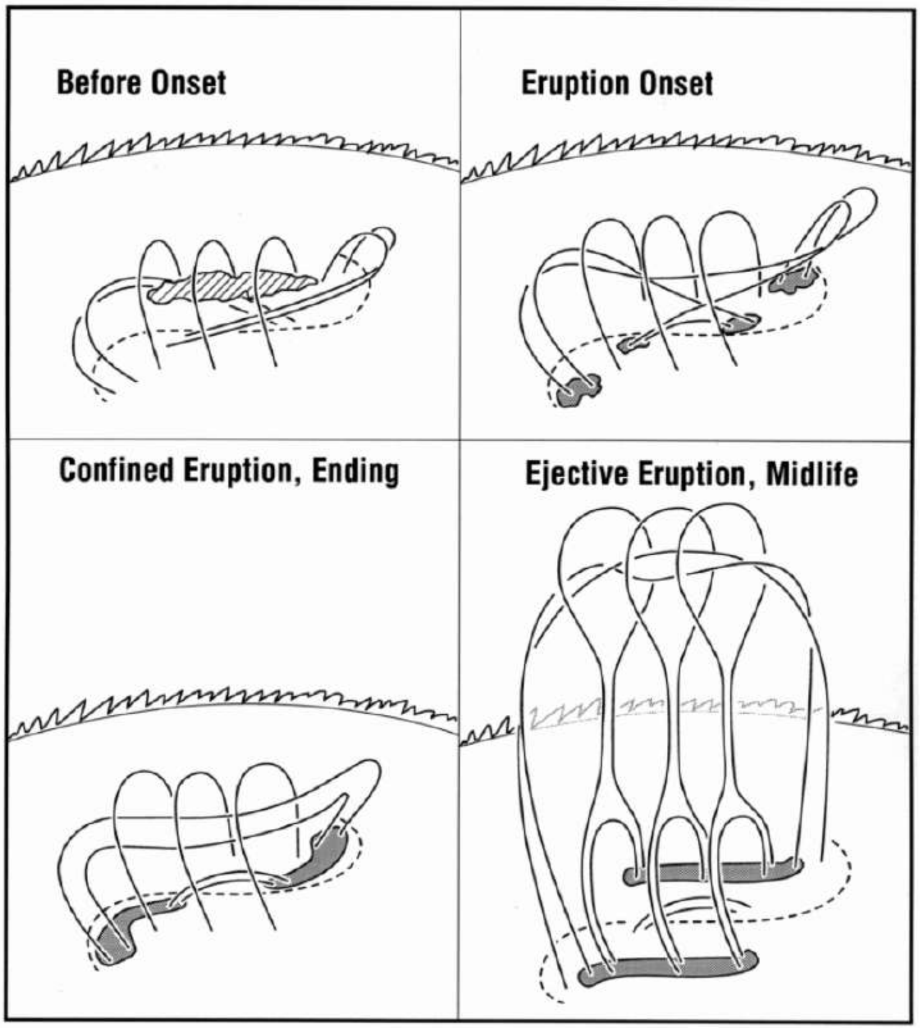

Figure 1.16: the schematic represention of the tether-cutting reconnection model, which depicts the onset of eruption and subsequent activities for both confined and ejective eruptions. Figure taken from Moore *et al.* (2001).

Breakout model

The breakout model (Antiochos *et al.*, 1999; Karpen *et al.*, 2012) fundamentally incorporates a quadrupolar magnetic configuration. The four distinct magnetic flux systems are indicated by blue (central arcade), green (side arcades), and red (overlying field) lines in Figure 1.17. Photospheric shearing motions stretch the inner central arcade parallel to the solar surface. Consequently, the enhanced magnetic pressure associated with the shear causes the central arcade to inflate, which pushes the central arcade toward the overlying fields. As a result, a current sheet (CS) develops between these two flux systems, which is termed as breakout CS. As the system becomes more and more stressed due to continuous shearing motions, the breakout CS becomes sufficiently small and reconnection sets in. The reconnection removes the overlying arcade by transferring its magnetic flux to

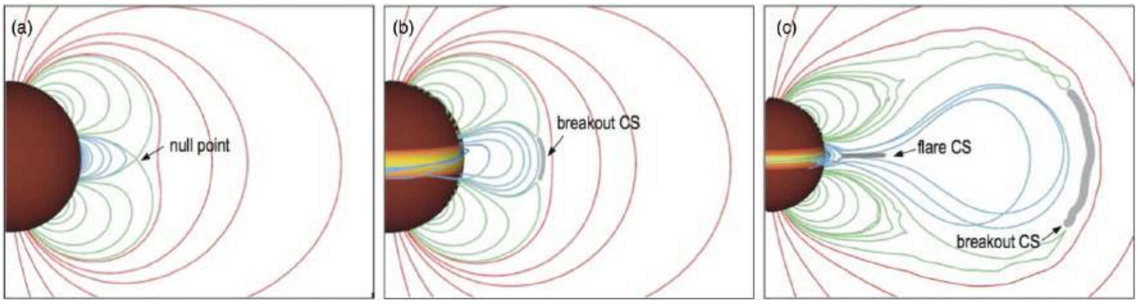

Figure 1.17: selected magnetic field lines at three times during the simulation, illustrating the key structures of the breakout model. The red lines indicate overlying magnetic fields, green lines indicate side lobe fields, whereas the blue lines indicate the core field lines. Gray patches show the locations of the flare and breakout CSs. The red to yellow shadings on the solar surface indicate an increase of azimuthal field strength. Panels (a), (b), and (c) show the magnetic configurations at t = 0, 72,500, and 102,500 s, respectively. Figure is adopted from Karpen *et al.* (2012).

the side aracdes. The resulting decrease in the downward tension of the overlying arcade causes the sheared central arcade to expand faster and thereby creating a feedback process that supports its further eruption. Finally, a flare CS develops (Figure 1.17(c)) between the two field lines stretched by the erupting central arcade. The reconnection at the flare CS mimics the standard flare reconnection scenario which also supports the eruption process.

Recently, through numerical simulations, Wyper *et al.* (2017) showed that the small-scale jets and large-scale CMEs are of physically identical origin and should be interpreted by considering a single energy release mechanism, i.e., magnetic reconnection. In their model, the reconnection is manifested through ‘magnetic breakout’, which is considered to be a universal model for solar eruptions.

1.8 Objectives of the thesis

To explore different important aspects of the solar eruptive phenomena, it is crucial to analyze the multi-wavelength and multi-instrument data together with coronal magnetic field modeling. Considering the flux rope as the primary driver of solar eruptive events, we aim to investigate the trigger, activation, and subsequent evolution of a flux rope in the different atmospheric layers. In this framework, we discuss the scientific objectives of this thesis in the following.

1.8.1 Build-up and early activation of flux ropes

It is now well-understood that the MFR remains at the helm of the solar eruptive events. The tether-cutting reconnection model and associated magnetic flux cancellation processes are believed to be responsible for the build-up of flux ropes in the solar atmosphere prior to the eruption (Savcheva *et al.*, 2012b; Xue *et al.*, 2017). The flux rope can even be formed in the lower atmosphere via a series of magnetic reconnection at the chromospheric level (Kumar *et al.*, 2015; Wang *et al.*, 2015a), and sometimes be heated up to the coronal temperatures to be observed as hot channel (Song *et al.*, 2014; Hernandez-Perez *et al.*, 2019a) in the EUV 94 and 131 Å passbands. The exact process of formation and build-up of MFR is not yet clearly understood. From a theoretical point of view, it was proposed that the flux cancellation along PIL is required to build up enough helicity in a sheared magnetic arcade which can develop into an MFR (Mackay and van Ballegooijen, 2006). The standard flare/CSHKP model considers the pre-existence of an MFR prior to its eruption and explains its role in driving the subsequent flare and associated processes. However, this model does not account for the mechanisms responsible for the activation of flux rope toward eruption. In this thesis, we undertake comprehensive studies to probe the build-up and activation processes of MFRs by analyzing the evolution of magnetic fields of ARs prior to the eruptions along with pre-flare activities.

1.8.2 Magnetic coupling through the solar atmosphere and onset of homologous solar eruptions

The magnetic field plays the most important role in initiating and driving the solar eruptive phenomena. The different atmospheric layers of the Sun are permeated by magnetic field with varying strength, geometry, and topology. Successive flaring activities from the same source AR with similar morphological resemblance in (E)UV observations are known as recurrent/homologous flares. Their study is important to understand the physical processes of peristent storage and release of magnetic energy in the AR corona. Hence, exploration of homologous flares may provide vital clues for understanding the fast variability in space weather. In this thesis, we explore the triggering mechanism of homologous eruptive flares originated from a complex AR. Our works provide insights to understand the coupling between the rapidly evolving photospheric magnetic fields and subsequent changes in the coronal magnetic structures.

1.8.3 Consequences of compact flux rope eruptions and development of broad CMEs

The multipolar complex magnetic regions on the Sun are highly susceptible to produce energetic events in the form of flares, CMEs etc. Observations suggest that the initiation of large-scale solar eruptions is usually linked to small-scale magnetic complexities at the source region. Wang *et al.* (2015b) found evidence of AR clusters which were prone to produce flares/CMEs and their association was identified in the form of inter-connecting loops and channeling filaments. The CME progenitors at the source region often are associated with large-scale pre-eruption structures, viz., transequatorial magnetic loops, interconnecting filaments among ARs, extended bipolar PILs etc. (Zhou *et al.*, 2006; Wang *et al.*, 2007; Su and van Ballegooijen, 2013). It is believed that the early dynamics of a CME necessarily depends on the embedded flux rope system, which acts as a central driver of the CME formation process and its subsequent eruptive acceleration. The combination of data obtained from various space- and ground-based instruments allows us to follow the space-time development of an event from the bottom of the corona to large distances in the interplanetary medium. However, it still remains unclear how the CME develops in the low corona and evolves into a large-scale structure during its subsequent phases. In this PhD thesis, we examine the formation of a sub-category of CMEs in which compact flux rope eruptions resulted into large-scale, broad CMEs.

1.9 Organization of the thesis

This thesis is composed of six chapters. We provide brief description of each chapter in the following.

Chapter 1: Introduction

This chapter provides a detailed description of different aspects of solar eruptive phenomena with a focus on solar flares. The various observational manifestations of MFRs are also described, along with their formation and triggering mechanisms. This chapter eventually defines the scientific objectives of the thesis.

Chapter 2: Observational data and analysis methods

In this chapter, we provide detailed description of observational data taken from various space-borne instruments. The data analysis techniques are also briefly described. The major observational data used in this thesis are obtained from the Solar Dynamics Observatory (SDO), the Reuven Ramaty High Energy Solar Spectroscopic Imager

(RHESSI), the Large Angle and Spectrometric Coronagraph (LASCO). The numerical techniques used for the modeling of coronal magnetic field include Potential Field Source Surface (PFSS) and NLFFF extrapolation techniques.

Chapter 3: Activation of magnetic flux rope and its role in driving long-duration eruptive flare

In this chapter, we present a comprehensive study of the evolutionary phases of a major M6.6 long-duration event with special emphasize on its pre-flare phase. The event occurrs in NOAA 12371 on 2015 June 22. A remarkable aspect of the event is an active pre-flare phase lasting for about an hour during which a hot EUV coronal channel is in the build-up stage and displays co-spatial HXR emission up to energies of 25 keV. This is the first evidence of the HXR coronal channel. The coronal magnetic field configuration based on NLFFF modeling clearly exhibits an MFR oriented along the PIL and co-spatial with the coronal channel. Prior to the flare onset, the MFR undergoes a slow rise phase ($\approx$14 km s^{-1}) for $\approx$12 minutes, which we attribute to the faster build-up and activation of the MFR by tether-cutting reconnection occurring at multiple locations along the MFR itself. The sudden transition in the kinematic evolution of the MFR from the phase of slow to fast rise ($\approx$109 km s^{-1} with acceleration $\approx$110 m s^{-2}) precisely divides the pre-flare and impulsive phase of the flare, which points toward the feedback process between the early dynamics of the eruption and the strength of the flare magnetic reconnection.

Chapter 4: Evolution of magnetic fields and energy release processes during homologous eruptive flares

To explore the origin of homologous flares, we need to understand the intrinsic coupling of magnetic fields passing through different atmospheric layers of the Sun and associated variations in the free magnetic energy in the AR corona. With this motivation, we study the triggering and evolution of three homologous flares of successively increasing intensities. The flares originate from NOAA AR 12017 during 2014 March 28–29 within an interval of $\approx$24 hr. The EUV observations and magnetogram measurements together with coronal magnetic field modeling suggest that the eruptive flares are triggered by the eruption of flux ropes embedded by a densely packed system of bipolar loops within a small part of the AR. In X-rays, the first and second events show similar evolution with single, compact sources, while the third event exhibits multiple emission centroids with a set of strong non-thermal conjugate sources at 50–100 keV during the HXR peak. The photospheric magnetic field over an interval of $\approx$44 hr encompassing the three flares undergoes important phases of emergence and cancellation processes together with significant changes near the PIL within the flaring region. Our observations point toward the tether-cutting mechanism as the plausible triggering process of the eruptions. Between the second and third event, we observe a prominent phase of magnetic flux emergence which temporally correlates with the build-up phase of free magnetic energy in the AR corona. In conclusion, our analysis reveals an efficient coupling between the rapidly evolving photospheric and coronal magnetic fields in the AR that led to a continued phase of the build-up of free magnetic energy, resulting into the three homologous flares of successively increasing intensities.

Chapter 5: Broad coronal mass ejections produced by compact, blowout-eruption solar flares

In this chapter, we investigate the formation mechanism of three homologous broad CMEs originated from a series of solar blowout-eruption flares from NOAA AR 12017 studied in the previous chapter. We obtain a double flux rope system under the densely packed compact bipoles for all the events. The flux ropes erupt sequentially to lead to the homologous flares, each followed by a CME. Each of the three CMEs formed in the wake of the eruptions eventually attains a large angular width, after evolving from the compact eruption-source site. Our observations reveal that these eruptions and CMEs are consistent with the "magnetic-arch-blowout" scenario: each compact-flare blowout eruption is seated in one foot of a far-reaching magnetic arch, explodes up the encasing leg of the arch, and blows out the arch to make a broad CME.

Chapter 6: Conclusions and future prospects

This chapter summarizes the work done, highlights the major findings, and briefly presents the scope for future research.

Chapter 2

Observational Data and Analysis Methods

2.1 Introduction

The solar eruptive phenomena are observed in the outer atmospheric layers (i.e., photosphere, chromosphere, and corona) of the Sun through various ground- and space-based observatories. These eruptive events are accompanied by the generation of radiations encompassing all the segments of the electromagnetic spectrum. Ground-based observatories are useful for the detection of radiation from radio to visible part of the spectrum. However, to detect the radiations ranging from the UV to smaller wavelengths, the space-based observatories are indispensable, beacause of the absorption of these radiations in the Earth's ionosphere. In addition, the outer atmospheric layers of the Sun emit radiations in different wavelength bands depending on their variability in temperature. The photosphere, being the coolest among the other overlying atmospheric layers, emits mostly in the visible wavelength range. The corona, being the hottest layer, emits mostly in the EUV and X-ray wavelength bands. In view of this, it is necessary to conduct multi-wavelength investigations of the solar eruptive events to understand the various physical phenomena that essentially involve different atmospheric layers.

In this thesis, we primarily use the EUV observations of the Sun obtained from the Atmospheric Imaging Assembly (AIA) instrument on board the Solar Dynamics Observatory (SDO) satellite. In addition, we gather data from the Helioseismic and Magnetic Imager (HMI) instrument on board the SDO for the analysis of photospheric magnetic field. These observations are complemented by the X-ray data obtained from the Reuven Ramaty High Energy Solar Spectroscopic Imager (RHESSI) satellite. The observations of CMEs associated with the eruptive flares are carried out using data from the Large Angle

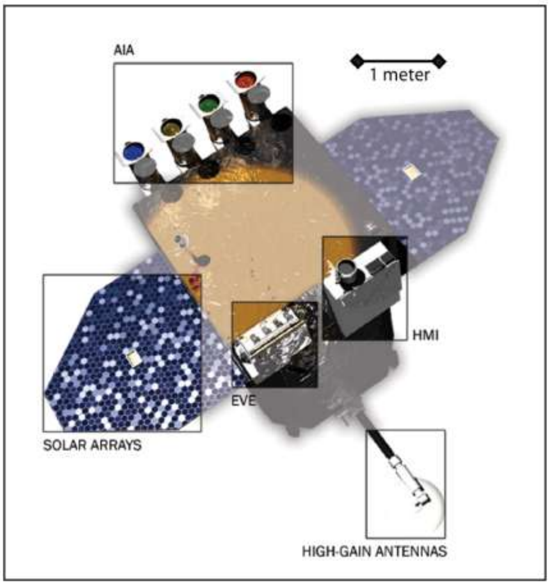

Figure 2.1: the SDO spacecraft with its instruments, high-gain antennas, and associated solar arrays. Figure is adopted from Pesnell *et al.* (2012).

and Spectrometric Coronagraph (LASCO) instrument on board the Solar and Heliospheric Observatory (SOHO) satellite. The detection of flares in the X-ray energy bands is carried out using the data from the Geostationary Operational Environmental Satellite (GOES). Apart from these space-based data, we also use ground-based data of Hα observations for very limited yet specific purpose (see Chapter 3) In the following sections, we present the various aspects of the instruments and satellites, which are used as the data sources for the work presented in this thesis. We also provide brief overview of the data analysis methods and softwares used in our work.

2.2 Solar Dynamics Observatory (SDO)

Solar Dynamics Observatory (SDO; Pesnell *et al.*, 2012) (2010–present) is a National Aeronautics and Space Administration's (NASA) mission under the Living With a Star (LWS) program. The main scientific objectives of SDO mission include the investigation of generation and structuring of solar magnetic field, release of stored magnetic energy into the heliosphere in the form of solar wind, energetic particles, and variations in solar irradiance, etc. The SDO satellite consists of three instruments: Atmospheric Imaging Assembly (AIA), Helioseismic and Magnetic Imager (HMI), and Extreme Ultraviolet Experiment (EVE). In this thesis, we extensively use data from the AIA and HMI instruments.

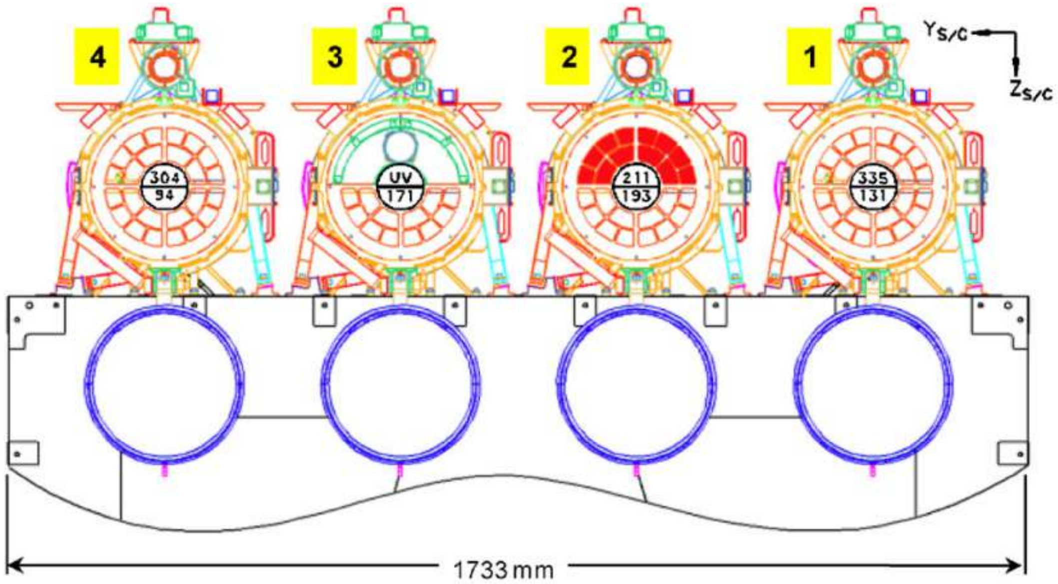

Figure 2.2: the layout of the wavelength channels or band passes in each of the four AIA telescopes. Figure taken from Lemen *et al.* (2012).

2.2.1 Atmospheric Imaging Assembly (AIA)

The Atmospheric Imaging Assembly (AIA; Lemen *et al.*, 2012) is designed to increase our understanding of the mechanisms of solar variability and the release of stored magnetic energy into the heliosphere. It produces simultaneous, high-resolution, low cadence full-disk images of the corona and transition region of the Sun. The resolution of AIA is $1''.5$, while the pixel size of the CCD camera is $0''.6$. The AIA provides full-disk images in seven EUV (94 Å, 131 Å, 171 Å, 193 Å, 211 Å, 304 Å, and 335 Å), two UV (1600 Å and 1700 Å), and in a visible filter (centered at 4500 Å) for co-alignment with images from other telescopes. The time cadence of EUV, UV, and visible filters are 12 s, 24 s, and 1 hr, respectively. The temperature diagnostics corresponding to the AIA observations range from $\approx 6\times10^4$ K to 2×10^7 K.

The AIA consists of four generalized Cassegrain telescopes, optimized to observe in narrow band pass EUV filters. Each telescope has a 20 cm primary mirror and an active secondary mirror. The telescope mirrors have multilayer coatings that are optimized for the selected EUV wavelength of interest. The field-of-view (FOV) of each telescope is $\approx 41'$ circular diameter. The telescope numbers 1, 2, and 4 consist of two different EUV band passes, whereas, the mirror of telescope 3 has a 171 Å band pass on one half and the other half has a broad-band UV coating. The UV channels in the telescope number 3 select the band passes of interest, centered on: 1600 Å, 1700 Å, and a 500 Å FWHM[1]

[1]Full Width at Half Maximum (FWHM) is defined as the width of a line shape for a particular distribution at half of its maximum amplitude.

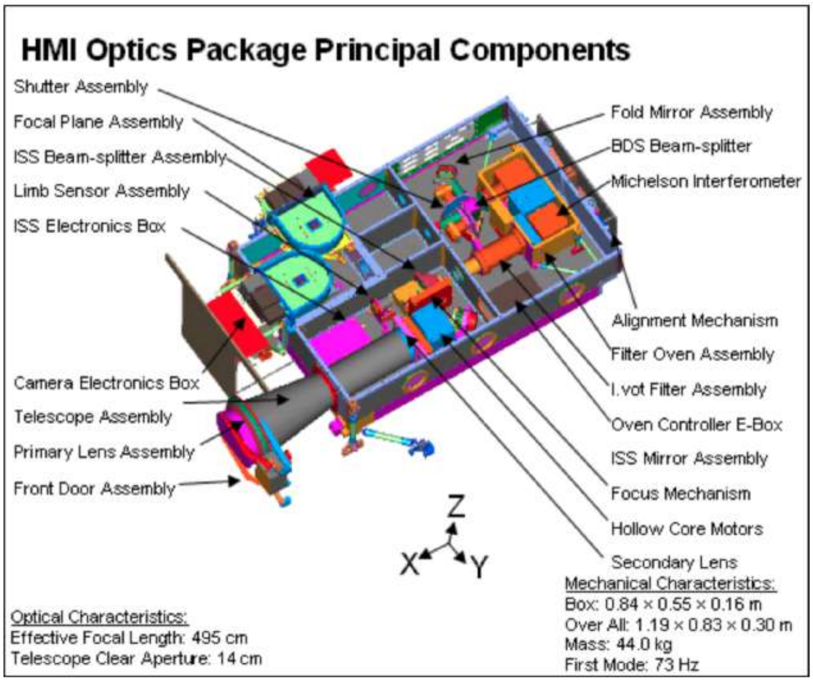

Figure 2.3: the layout of the principal components of HMI optics package. Source: `http://hmi.stanford.edu/Description/hmi-overview/hmi-overview.html`.

band pass filter centered on 4500 Å. At the focal plane of the telescopes, there are back-thinned CCD sensors comprised of 4096×4096 pixels.

2.2.2 Helioseismic and Magnetic Imager (HMI)

Heliosesmic and Magnetic Imager (HMI; Schou *et al.*, 2012) is developed to study the solar interior using helioseismic techniques and for the exploration of the magnetic field near the solar surface. HMI provides stabilized $1''.0$ resolution full-disk Doppler velocity, line-of-sight (LOS) magnetic flux, and continuum (i.e., white light intensity) images in every 45 s. In order to obtain the vector magnetic field measurements, the raw Stokes vectors (I, Q, U, and V) at six wavelength positions are calculated centered at the Fe I 6173 Å spectral line. The vector magnetic field maps are constructed in every 90 or 135 s depending on the image frame sequence selected and are averaged into a 12 minute (720 s) product. The Milne-Eddington inversions are routinely computed from these products (Borrero *et al.*, 2011). To obtain the final vector field, a field direction disambiguation technique is used, since the Stokes vectors cannot distinguish the polarity of the component of the field normal to the LOS component (Metcalf, 1994; Metcalf *et al.*, 2006; Leka *et al.*, 2009). The data products of HMI have pixel size of $0''.5$, obtained through a 4096×4096 pixel CCD camera. The associated optical instruments of HMI consist of a front-window filter, a front illuminated telescope with 140 mm aperture, a set of wave plates for polarimetry, a blocking filter, an image stabilization system, a five stage Lyot filter, two wide-field tunable Michelson Interferometers, etc.

In order to compare the HMI and AIA images, we need to convert the pixel sampling of HMI filtergrams from $0''.5$ pixel^{-1} to $0''.6$ pixel^{-1}. This is achieved by employing the SolarSoftWare (SSW) routine *hmi_prep.pro*.

2.3 Reuven Ramaty High Energy Solar Spectroscopic Imager (RHESSI)

The Reuven Ramaty High Energy Solar Spectroscopic Imager (RHESSI; Lin *et al.*, 2002) (2002–2018) was one of the missions under the NASA's Small Explorer (SMEX) program. It was designed to investigate particle acceleration and energy release processes in solar flares through imaging and spectroscopy of HXR/gamma-ray continua. After more than 16 years of successful functioning, RHESSI was rendered inoperative on 16 August 2018. A summary of the instrumental details of RHESSI is given in Table 2.1.

Table 2.1: RHESSI instrumental characteristics (Lin *et al.*, 2002).

Energy range	3 keV to 17 MeV
Energy resolution (FWHM)	1 keV up to 100 keV 3 keV up to 1 MeV 5 keV up to 17 MeV
Angular resolution	$2''.3$ up to 100 keV $7''$ up to 400 keV $36''$ up to 1 MeV
Temporal resolution	2 s for detailed image, tens of ms for basic image
FOV	Full Sun ($\approx 1°$)
Detectors	9 Germanium detectors cryogenically-cooled to <75 K
Imager	9 pair of grids, with pitches from 34 microns to 2.75 mm, and 1.55 m grid separation

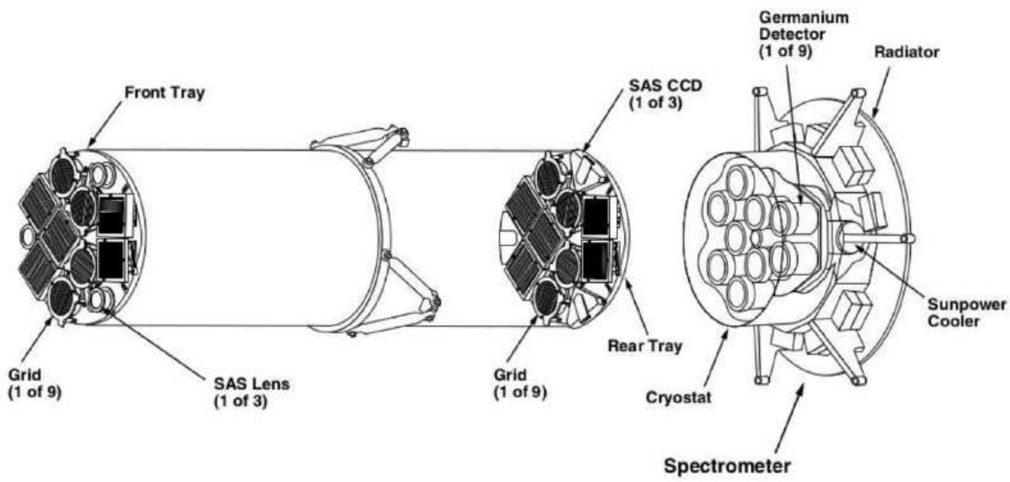

Figure 2.4: the schematic representation of the RHESSI imager. The principal components of RHESSI consist of two identical sets of nine bi-grid RMCs mounted on the front and rear grid trays, respectively. A corresponding set of nine cooled germanium detectors are placed behind the rear grid RMCs. The solar aspect system (SAS) consists of three lenses installed on the front grid tray which focus optical images onto SAS CCDs on the rear grid tray. Figure adopted from Hurford *et al.* (2002).

2.3.1 RHESSI imaging

RHESSI provided first imaging above 100 keV including the imaging of gamma-ray lines. The imaging technique of RHESSI is based upon the Fourier-transform method, which uses a set of 9 bi-grid Rotating Modulation Collimators (RMCs). Each RMC temporally modulates the photon signal from the sources in its FOV as the spacecraft rotates about an axis parallel to the long axis of the RMC (see Figure 2.4).

Each grid of RMC is a planar array of equally-spaced, X-ray-opaque slats separated by transparent slits (see Figure 2.5). The slits of each pair of grids are parallel to each other and their pitches (p) are identical, so that the transmission through the grid pair depends on the direction of the incident X-rays. For slits and slats of equal width, the transmission is modulated from zero to 50% and back to zero for a change in source angle to collimator axis (which is orthogonal to the slits) of p/L, where L is the separation between the grids. The corresponding angular resolution is then defined as p/(2L).

Several image reconstruction algorithms (e.g., BACK PROJECTION, CLEAN, PIXON, etc.) are available in the RHESSI software. These algorithms model the spatial distribution of the photons by employing the observed modulated time profiles, spacecraft roll position, pointing etc. In our work, we examine the X-ray sources in the energy range of 3 keV (SXR) to 100 keV (HXR). For image reconstruction, we primarily use the

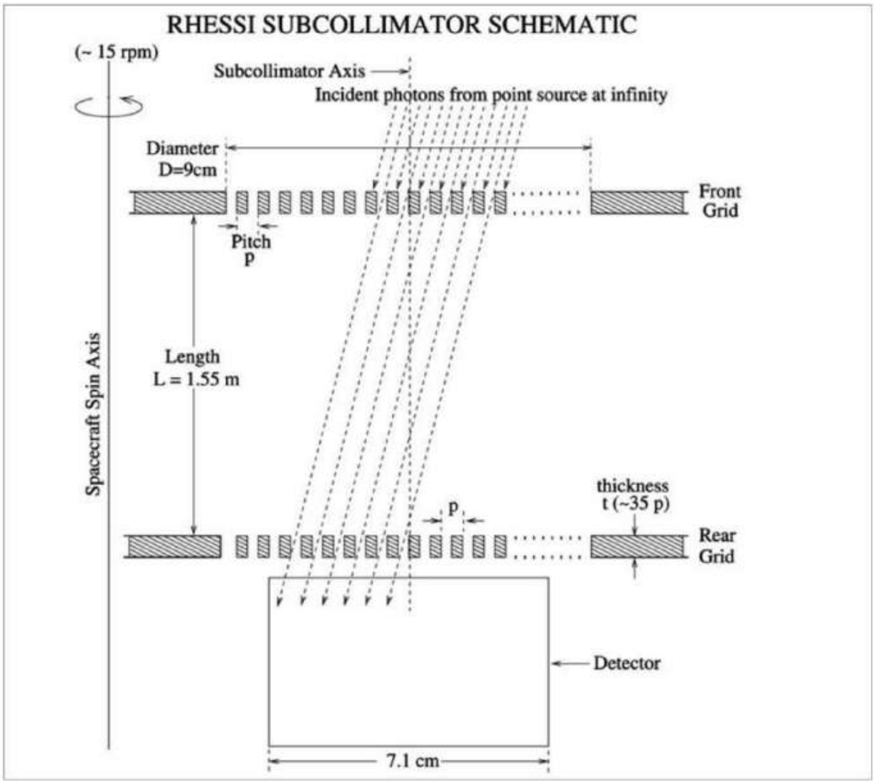

Figure 2.5: schematic view of the RHESSI subcollimators that together define the imaging capability. Figure taken from Lin *et al.* (2002).

CLEAN algorithm, as it provides satisfactory results for extended sources and consumes less computational time. Here, we provide brief descriptions of a few algorithms used by the RHESSI software. The detailed descriptions about them can be found in Hurford *et al.* (2002).

BACK PROJECTION

BACK PROJECTION (Mertz *et al.*, 1986) is the most straightforward and basic method of image reconstruction. The general approach of RHESSI imaging is to use a 'Back Projection' algorithm to generate an initial estimate of the image. This estimate represents a convolution of the source with the instrumental response function. In the 'Back Projection' method, each detected photon is projected back from the detector through the slits of the grid pairs to all possible locations for its origin on the Sun. This creates a probability map made up of parallel ridges aligned with the slit orientation at that time. The spacing between the ridges is equal to twice the FWHM resolution of the sub-collimator. This obtained back projection is repeated for each detected photon and the resulting probability maps are summed to form the 'dirty map'. Although this method is simple and fast, it provides poor quality images with sidelobes. In order to improve the image quality (i.e., to reduce the sidelobes), a variety of other image reconstruction techniques can be used, which are discussed in the following.

CLEAN

CLEAN (Högbom, 1974) is an iterative algorithm based on the assumption that the image can be well represented by a superposition of point sources. According to this algorithm, an image called the 'residual map' is created initially with the Back Projection map (i.e., dirty map). The position of the pixel with the highest flux in the residual map is assigned a point source with a fixed fraction of that flux at that pixel location in a new map of CLEAN components. The normalized Point Spread Function (PSF) at this pixel location is subtracted from the current residual map to yield a new residual map. This process is continued iteratively until a specified number of iterations are reached or the observed modulation profile agrees well with that predicted from the CLEAN components. CLEAN is a relatively fast algorithm to reconstruct X-ray images and provides a reasonable estimation of the X-ray sources. Therefore, this algorithm is highly preferred for image reconstruction.

PIXON

The PIXON (Metcalf *et al.*, 1996) method is another technique which removes the sidelobe pattern of a telescope while mitigating the problems of correlated residuals and spurious sources. The goal of this method is to construct the simplest model for the image that is consistent with the data (i.e., having an acceptable χ^2 fit). Unlike CLEAN, which models the source as a collection of point sources, the PIXON algorithm constructs a superposition of circular sources or pixons of different sizes that best reproduce the measured modulations from the different detectors. Since the model used in PIXON algorithm has minimum complexity, spurious sources are unlikely to arise. Each parameter is determined using a larger fraction of the data and so is supposed to be determined more accurately. As a result, this method is one to two orders of magnitude slower than the other image reconstruction methods. Therefore, the PIXON algorithm is useful only after the faster reconstruction techniques have been used to optimize the time and energy binning.

2.3.2 RHESSI spectroscopy

The RHESSI spectrometer package is composed of nine cryogenically cooled coaxial germanium detectors (GeD) (Smith *et al.*, 2002). The purpose of using ultra-pure germanium in cryogenic temperatures is to prevent natural formation of electron-hole pairs in the conduction band. Due to the interaction of HXR or gamma ray with the crystal, one or more energetic electrons can be released, which ultimately lose energy by creating free pairs. If there is a high electric field ($\approx$1000 V cm^{-1}) across the crystal, the electrons and holes will be pulled to each electrode, creating a current pulse that can be amplified and digitized by suitable electronics. The total charge in the current pulse is proportional to the photon energy.

RHESSI spectroscopy is performed through the Object Spectral Executive (OSPEX; Tolbert and Schwartz, 2020) software package which creates an object-oriented interface for spectral analysis. OSPEX provides an environment where the user reads and displays the input data, selects and subtracts the background, selects time intervals of interest, selects a combination of photon flux model components to describe/fit the data. OSPEX is designed to work with any type of data that can be structured in the form of time-ordered count spectra. Usually a response matrix is needed to relate a model spectrum to the observed response. The entire OSPEX session can be saved in the form of a script and the fit results are stored in the form of a Flexible Image Transport System (FITS) file.

In order to conduct RHESSI X-ray spectroscopic analysis, we generate the spectra with an energy binning of 1/3 keV from 6 to 15 keV, 1 keV from 15 to 100 keV, and 5 keV from 100 keV onward. We only use the front segments of the detectors, excluding detectors 2 and 7, as they have low energy resolution and high threshold energy, respectively (Smith *et al.*, 2002). The spectra are deconvolved with the full detector response matrix. Two models are used to fit the observed X-ray spectra: line emission from an isothermal plasma and thick-target Bremsstrahlung from non-thermal electrons interacting with the chromosphere (Holman *et al.*, 2003). From spectral fits, we derive the temperature (T) and emission measure (EM) of the hot flaring plasma, as well as the non-thermal electron spectral index (δ) for the non-thermal component.

2.4 Solar and Heliospheric Observatory (SOHO)

The Solar and Heliospheric Observatory (SOHO; Domingo *et al.*, 1995) (1995–present) is a joint project between the European Space Agency (ESA) and NASA. This satellite was designed to study both the Sun's interior and its outer atmosphere, the acceleration and propagation of solar wind, and its interaction with the Earth's atmosphere. We use data from SOHO to understand the structure and evolution of CMEs associated with the eruptive flares.

Large Angle and Spectrometric Coronagraph (LASCO)

CME observations are obtained from the Large Angle and Spectrometric Coronagraph (LASCO; Brueckner *et al.*, 1995) on board the SOHO, which images the solar corona by creating an artificial solar eclipse. The LASCO consists of three coronagraphs C1, C2, and C3. The C1 was a spectral imager of the low corona, with a FOV from 1.1 to 3 $R_\odot$ and operated between 1995 to 1998. The C2 and C3 are white light imagers, with FOVs from 1.5 to 6 $R_\odot$ and 3.7 to 30 $R_\odot$, respectively.

2.5 Geostationary Operational Environmental Satellite (GOES)

The GOES is a series of spacecrafts owned and operated by the National Oceanic and Atmospheric Administration (NOAA), while the design, development, and launch of the spacecrafts is managed by the NASA. The GOES satellites circle the Earth in a geosynchronous orbit over the equator at ≈35,800 km above the Earth's surface. The X-ray Sensors (XRS) onboard GOES provide continuous detection of disk-integrated solar X-ray fluxes (Bornmann *et al.*, 1996). There are two sensors on each GOES satellite which provide solar X-ray fluxes corresponding to 0.5–4 and 1–8 Å channels. Both the channels take data simultaneously with time cadence of ≈2 s. The GOES 12 through 15 spacecrafts were modified to further carry a Solar X-ray Imager (SXI) to image the million kelvin solar corona. In our study, we use the GOES XRS measurements in the 1–8 and 0.5–4 Å channels to detect the flaring events, as well as to characterize the temporal evolution of the X-ray fluxes.

2.6 Coronal magnetic field modeling

The different approaches toward the modeling of the coronal magnetic fields rely on the simplifying assumptions regarding their governing equations and the treatment of the lower-boundary data. Among the various available modeling methods, we use the NLFFF model and the PFSS model for our analysis.

2.6.1 Non-Linear Force-Free Field (NLFFF) model

It is well known that the magnetic field dominates the plasma in the inner corona. Gary (2001) constructed a 1D model for the magnetic stratification of the solar atmosphere and argued that about 100 Mm above the chromosphere, the plasma β <<1, i.e., the magnetic field is dominant compared to the plasma pressure and other forces. In this case, the force-free approximation of coronal magnetic field can be applied. So, in magnetically dominated corona, we can write the momentum balance equation as (neglecting the plasma pressure force and gravity force)

$$\mathbf{J} \times \mathbf{B} = 0, \tag{2.1}$$

where, **J** is the current density and **B** is the magnetic field. Equation 2.1 results into the force-free equation

$$\nabla \times \mathbf{B} = \alpha(\mathbf{x})\mathbf{B}, \tag{2.2}$$

where, α is a spatially dependent scalar function. The force-free model is referred to as the Linear Force-Free Field (LFFF) model if α is globally constant, and as the NLFFF model if it varies from field line to field line. In order to find the modelled 3D coronal magnetic field using NLFFF technique, we use numerical code based on 'optimization approach' (Wheatland *et al.*, 2000; Wiegelmann, 2004). The NLFFF extrapolation technique was further refined by Wiegelmann and Inhester (2010); Wiegelmann *et al.* (2012). We use the 'HMI.sharp_cea_720s' series vector magnetograms as the photospheric input boundary condition for the extrapolation. The magnetogram is remapped using a Lambert cylindrical equal-area projection and presented as (B_r, B_θ, B_ϕ) in heliocentric spherical coordinates corresponding to (B_z, -B_y, B_x) in heliographic coordinates (Sun, 2013).

2.6.2 Potential Field Source Surface (PFSS) model

We can represent the magnetic field as $\mathbf{B}=\nabla\phi$, if we neglect the electric current in the coronal volume (i.e., $\nabla \times \mathbf{B} = 0$). In this case, we obtain (considering $\nabla \cdot \mathbf{B} = 0$)

$$\nabla^2\phi = 0, \tag{2.3}$$

where, ϕ is identified as the scalar potential and is obtained from the observational LOS component of the magnetic field on the photosphere (Altschuler and Newkirk, 1969; Schatten *et al.*, 1969). According to Gary (2001), at heights ≈100 Mm above the photosphere, the thermal and dynamical pressures of the expanding solar wind can exceed the coronal magnetic pressure. Under this conjecture, the fields cannot return to the Sun, instead they are dragged out into the heliosphere by the progressing solar wind. In the PFSS model, this effect of the solar wind on the coronal magnetic field is included by setting the scalar potential to a constant value on an outer boundary surface, called the source surface, thus forcing the modelled field to be radially directed there. Utilizing the scalar potential ϕ, the magnetic field distribution on the source surface is calculated for a particular source surface radius (R_S). The magnetic field on the source surface can then be compared with the interplanetary observations to determine R_S. The shape of the field lines and the coronal structure agree best with the $R_S \approx 2.5\ R_\odot$ ($R_\odot$ is the solar radius).

2.7 Resources and tools used for data analysis

Interactive Data Language (IDL)

Interactive Data Language (IDL[2]) is a high-level language for data analysis and visualization. It also includes strong image processing capabilities and extensive mathematical functions. IDL was originally developed during the 1970s at the Laboratory for Atmospheric and Space Physics (LASP) at the University of Colorado, Boulder. The solar observations from multiple space- and ground-based instruments are extensively analyzed using the IDL platform. Apart from solar physics, it is also widely applied in the fields of astronomy, atmospheric physics, and medical science.

SolarSoftWare (SSW)

In our study, we extensively use the SolarSoftWare (SSW[3]; Freeland and Handy, 2012), which is a set of IDL-based integrated software libraries, databases, and system utilities which provide a common environment of data analysis for solar physicists. The SSW system has been built from the software libraries of various missions, viz., Yohkoh, SOHO, TRACE, RHESSI, SDO, etc. It is primarily an IDL based software. However, some instrument teams run executables written in other languages also.

Visualization and Analysis Platform for Ocean, Atmosphere, and Solar Researchers (VAPOR)

The Visualization and Analysis Platform for Ocean, Atmosphere, and Solar Researchers (VAPOR[4]; Clyne *et al.*, 2007) software is an interactive 3D visualization environment that can produce animations and still images. It was originally developed by the National Center for Atmospheric Research (NCAR). VAPOR runs on various UNIX and Windows operating systems, equipped with modern 3D graphics cards. It also provides facility of ad-hoc analysis for the users using an interactive Python interpreter.

[2] https://www.l3harrisgeospatial.com/Software-Technology/IDL
[3] https://www.lmsal.com/solarsoft/
[4] https://www.vapor.ucar.edu/

Chapter 3

Activation of Magnetic Flux Rope and Its Role In Driving Long-duration Eruptive Flare

3.1 Introduction

The source regions of solar eruptions frequently show the presence of interesting observational features, e.g., prominences, filament channels, hot coronal channels, etc., which are accepted as evidences of a fundamental structure called MFR (Cheng *et al.*, 2011; Patsourakos *et al.*, 2013; Joshi *et al.*, 2017a; Mitra *et al.*, 2018; Veronig *et al.*, 2018). MFRs are often defined as a bundle of magnetic field lines that are twisted around each other and wrap around a common axis (Gibson and Fan, 2006; Canou and Amari, 2010; Filippov *et al.*, 2015; Cheng *et al.*, 2017). MFRs not only play a crucial role in triggering the eruption but also constitute a key component of CMEs. Near-Earth in-situ measurements often reveal evidence of MFRs at large-scales in the form of interplanetary magnetic clouds denoting the arrival of Earth-directed CMEs (Burlaga *et al.*, 1981; Klein and Burlaga, 1982; Burlaga *et al.*, 1998; Möstl *et al.*, 2009; Syed Ibrahim *et al.*, 2019). They may subsequently cause geomagnetic disturbances when interacting with Earth's magnetic field (Zhang and Burlaga, 1988; Burlaga *et al.*, 2001; Zurbuchen and Richardson, 2006; Bisoi *et al.*, 2016; Joshi *et al.*, 2018). Here some fundamental questions arise: how do MFRs originate in the solar corona and what are the mechanisms responsible for their eruptions? The multi-wavelength solar observations of the source regions of CMEs and their comparison with coronal magnetic field modeling can yield important insights on these open issues.

The formation of a CME requires the activation and successful eruption of the MFR against solar gravity and the constraining coronal magnetic field. According to the "standard flare/CSHKP model" (Carmichael, 1964; Sturrock, 1966; Hirayama, 1974; Kopp and Pneuman, 1976), the eruptive expansion of the unstable MFR creates strong inflow of plasma and magnetic field lines in the large-scale current sheet that is formed underneath it causing the onset of magnetic reconnection. During magnetic reconnection, the stored magnetic energy is converted to heat energy within a localized region, along with acceleration of plasma and high-energy particles (Priest and Forbes, 2002; Holman *et al.*, 2011). The spatio-temporal characteristics of a flare explored from multi-wavelength and multi-instrument measurements provide useful information about the physical origin of the thermal and non-thermal emissions (Fletcher *et al.*, 2011; Benz, 2017). These observations also put constraints on the standard flare model (Sui *et al.*, 2004; Veronig and Brown, 2004; Joshi *et al.*, 2012).

It is being observed that many flares are associated with prominent pre-flare and precursor activities, which include small-scale brightness enhancements in the flaring region of about a few to tens of minutes prior to its impulsive phase (Veronig *et al.*, 2002; Kundu *et al.*, 2004; Joshi *et al.*, 2011, 2013; Mitra *et al.*, 2020a). While the precursor phase often shows a direct link to the later eruptive phenomenon, the pre-flare activity is viewed as a single or multiple series of small-scale reconnection events within the active region (AR) and may indirectly support the eruption by changing the magnetic and plasma conditions favorably (Fárník *et al.*, 1996; Fárník and Savy, 1998; Chifor *et al.*, 2006; Joshi *et al.*, 2011, 2013; Mitra and Joshi, 2019). Arguably the investigations of pre-flare and precursor activity can provide crucial inputs on the build-up phase of MFR and the triggering mechanism of the subsequent solar eruption.

During 2015 June 15–29, AR NOAA 12371 passed over the visible solar disk and produced several eruptive flares including geoeffective ones. The long-duration event of GOES class M6.6/Hα importance 2B occurred on 2015 June 22 is of particular interest in view of the highly eventful and extended pre-flare phase, its dual peak main phase, and the very distinct observations of the MFR structure and overlying strapping field in the AIA EUV observations. This event has been the subject of several studies in earlier works. Jing *et al.* (2017) reported the large-scale dynamics associated with the flare. They noted propagation of footpoint brightening driven by injection of non-thermal particles and the apparent slippage of loops governed by plasma heating and subsequent cooling. The study by Wang *et al.* (2018) revealed the changes in the photospheric flows and magnetic field structures associated with the flare. Their study revealed the role of back reaction of the coronal fields as caused by the flare energy release. The pre-flare configuration was ana-

Serial	Phases	Duration (UT)	Remarks
1	Pre-flare phase	16:30–17:35	Two distinct peaks (P1 and P2) are observed in GOES SXR light curves at ≈16:45 UT and ≈17:26 UT.
2	M6.6 flare	17:35–18:51	A distinct subpeak at ≈17:44 UT in X-ray light curves (GOES and RHESSI) during the rise phase (17:35 – 18:00 UT); broad maximum phase with dual peak structures (F1 and F2) in GOES light curves at ≈18:00 UT and ≈18:13 UT; eruption of hot channel begins at ≈17:40 UT; CME first detected in LASCO C2 coronagraph at ≈18:36 UT.
3	Post-flare phase	18:51–21:00	Very gradual decline of SXR emission in GOES light curves for ≈2 hr; after which the SXR flux reached to pre-flare background level; emission from large post-flare loops.

Table 3.1: summary of different phases of M6.6 flare (see also Figure 3.2).

lyzed by Awasthi *et al.* (2018). They identified a multiple braided flux rope along the PIL with different degrees of coherency over the pre-flare phase. Liu *et al.* (2018a) analyzed the changes in the photospheric vector magnetic field, which are related to the motion of the flare ribbons. Kang *et al.* (2019) reported the involvement of ideal instabilities, in the forms of double arc and torus instability, along with the tether-cutting mechanism as plausible cause of the eruption of the flux rope and subsequent M6.6 flare.

In this chapter, we analyze the long-duration M-class event of 2015 June 22 (SOL2015-06-22T18:23) with a focus on the pre-flare processes occurring during the extended period prior to the onset of eruption, during which a continuous build-up of the quasi-stable MFR is observed, and how these processes relate to the subsequent impulsive phase when the MFR undergoes spectacular eruption that leads to a fast halo CME. This chapter is arranged as follows. An extensive exploration of the multi-wavelength data in (E)UV, X-ray, and optical bands along with analysis of photosphetic magnetograms are provided in Section 3.2. In Section 3.3, we discuss the results and interpretations. For details of the observational data sources, see Chapter 2.

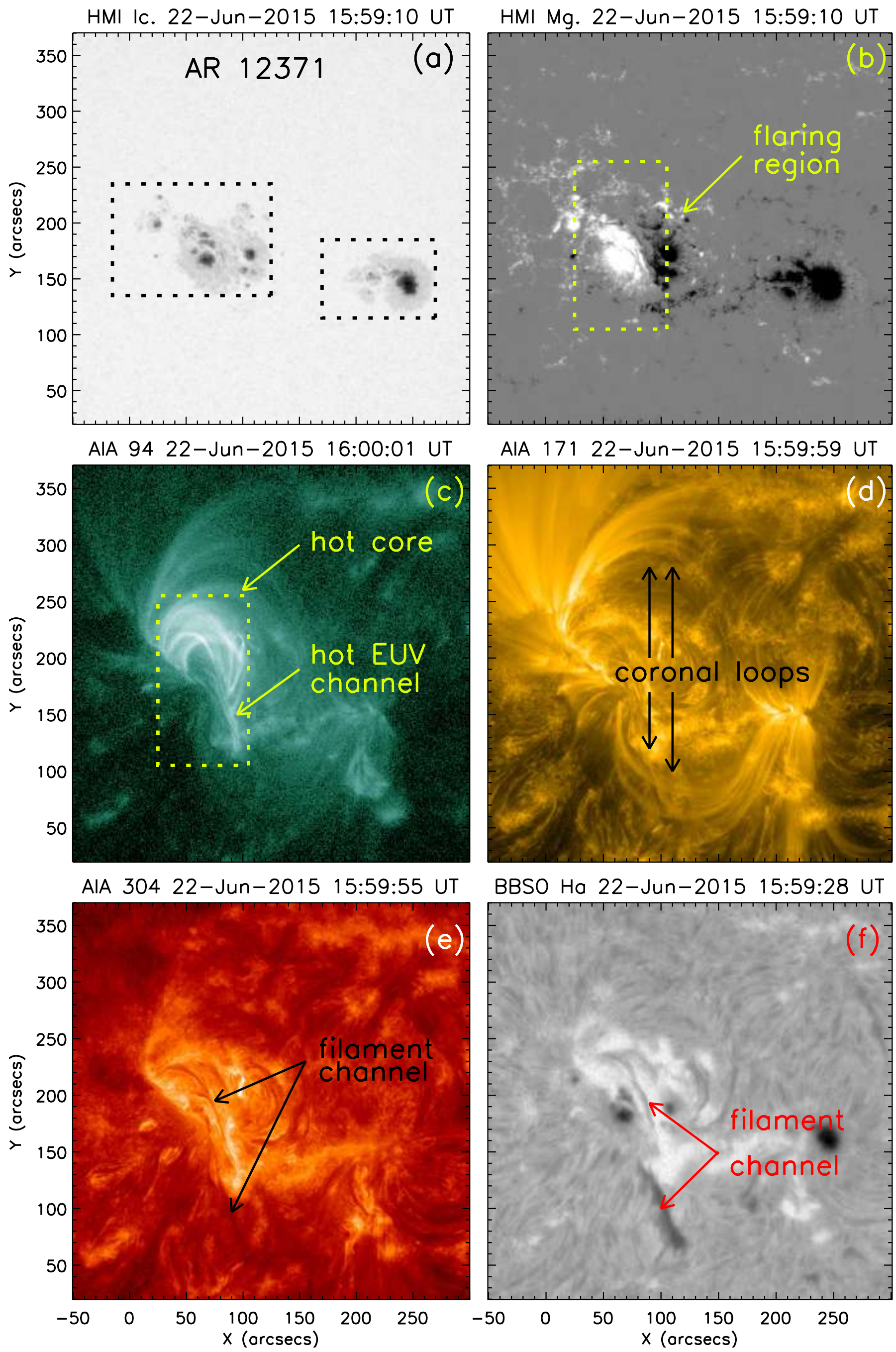

Figure 3.1: multi-wavelength view of AR NOAA 12371 on 2015 June 22. (a) White light image of the AR showing configurations of leading and trailing sunspot groups, which are shown by dotted boxes. (b) HMI LOS magnetogram showing the photospheric magnetic structure of the AR. The flare under investigation primarily originates in the trailing part of the AR. (c) AIA 94 Å image of the pre-flare phase showing the hot core region where the M6.6 class flare occurrs. (d) AIA 171 Å image showing high coronal loops that lie over the sunspot groups. (e) AIA 304 Å image showing faint filament structure in the chromospheric level. (f) BBSO Hα image showing clear filament channel above PIL. Comparison of panels (c), (e), and (f) reveals that, a filament exists in the chromosphere underneath the hot EUV channel.

3.2 Multi-wavelength observations and results

3.2.1 Event overview and light curve analysis

We investigate an M6.6 class flare from AR NOAA 12371 on 2015 June 22 from 16:00 UT to 23:00 UT. The AR was situated at heliographic coordinate ≈N12W08 during the onset of the flare. In Figure 3.1, we present a multi-wavelength view of the AR to compare its morphology at different atmospheric layers of the Sun. The white light image of the AR shows two distinct sunspot groups (shown by dashed boxes in Figure 3.1(a)). A comparison of white light image with LOS magnetogram of the AR suggests that the leading sunspot group is of negative polarity and the trailing sunspot group is comprised of mixed polarity regions making it a $\beta\gamma$ type AR (cf. Figures 3.1(a) and 3.1(b)). The flaring site is located over the trailing sunspot group (shown by yellow dashed box in Figure 3.1(b)). The AIA 94 Å image during the pre-flare phase (Figure 3.1(c)) suggests that, the activity site is associated with intensely emitting closed loops, which we mark by a dotted rectangle and annotate as hot core. Furthermore, we identify a hot channel-like structure at low coronal heights (marked by yellow arrow as hot EUV channel). By examining the images in the AIA 94 Å channel prior to the event over several hours, we find that, the hot channel pre-existed at least ≈5.5 hr before the eruptive flare. A comparison of the AIA 94 Å image with a co-temporal HMI magnetogram suggests that the brightest part of the core region with dense coronal loops essentially lies over the trailing part of the AR showing a complex bipolar magnetic distribution of sunspots. The 171 Å image in Figure 3.1(d) shows high coronal loops connecting the leading and trailing sunspot groups. In Figure 3.1(e), the AIA 304 Å image shows the signature of a filament channel. In Figure 3.1(f), the BBSO Hα image clearly shows the filament channel over PIL (cf. Figures 3.1(b) and (f)). We infer the hot EUV channel to be the coronal counterpart of the chromospheric filament delineating the PIL of the trailing bipolar part of the AR.

The GOES SXR light curves in 1–8 Å and 0.5–4 Å (Figure 3.2(a)), show distinct pre-flare, main, and gradual phases of the long-duration flare event under study. We see two distinct peaks in the pre-flare phase (P1 and P2) at ≈16:45 UT and ≈17:26 UT. A sharp rise in the GOES SXR flux at ≈17:35 UT indicates the start of main phase of the M6.6 flare with dual peak structures (F1 and F2) at ≈18:00 UT and ≈18:13 UT. According to the GOES flare catalog, which is based on the return of the SXR flux to half of its peak value, the flare lasts till 18:51 UT. However, the GOES profiles (Figure 3.2(a)) clearly reveal enhanced SXR emission from the flaring region for several hours (≈up to 21:00 UT), that we mark as prolonged decay phase. In Table 3.1, we summarize the different phases of the flare evolution along with their characteristics, which we discuss in subsequent sections.

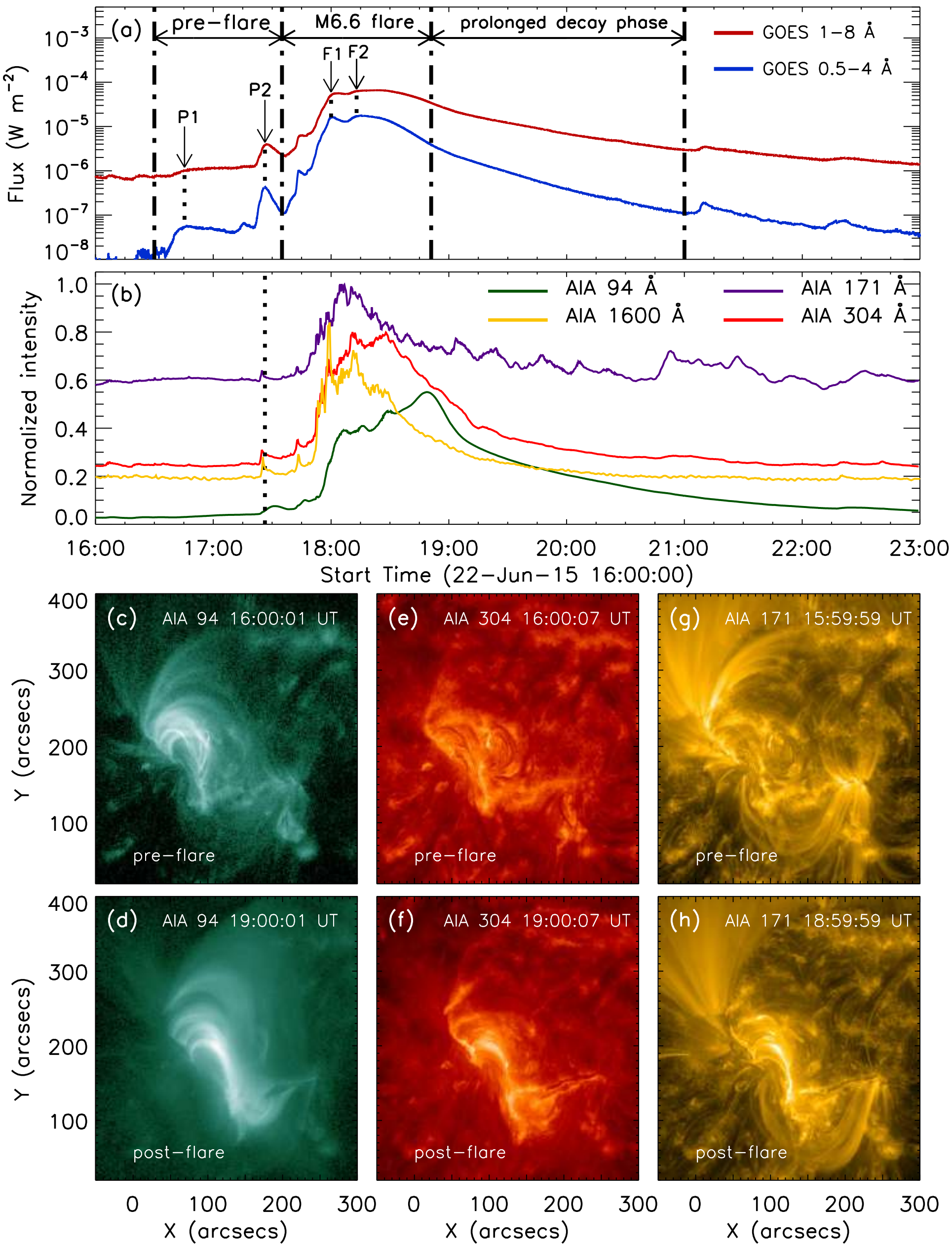

Figure 3.2: panel (a): GOES SXR flux in 1–8 Å and 0.5–4 Å channels from 16:00 UT to 23:00 UT on 2015 June 22. We find two stages in the pre-flare phase that peak at 16:45 UT (marked as P1) and 17:26 UT (marked as P2), respectively. We also observe dual flare-peak structure in the main phase of the M6.6 flare, indicated as F1 and F2 at 18:00 UT and 18:13 UT, respectively. Panel (b): AIA light curves normalized by peak intensity of respective AIA filters. For clear view, light curves are scaled by factors of 0.55 and 0.8 for 94 Å and 304 Å channels, respectively. The peak P2 in GOES SXR light curves in the pre-flare phase corresponds to a peak in AIA light curves, which is shown by dotted line. We readily observe that, the structure of the AR shows significant changes during the course of the flare. As a comparison between pre- and post-flare phases, we plot the AR corona in AIA 94 Å (cf. panels (c) and (d)), 304 Å (cf. panels (e) and (f)), and in 171 Å (cf. panels (g) and (h)).

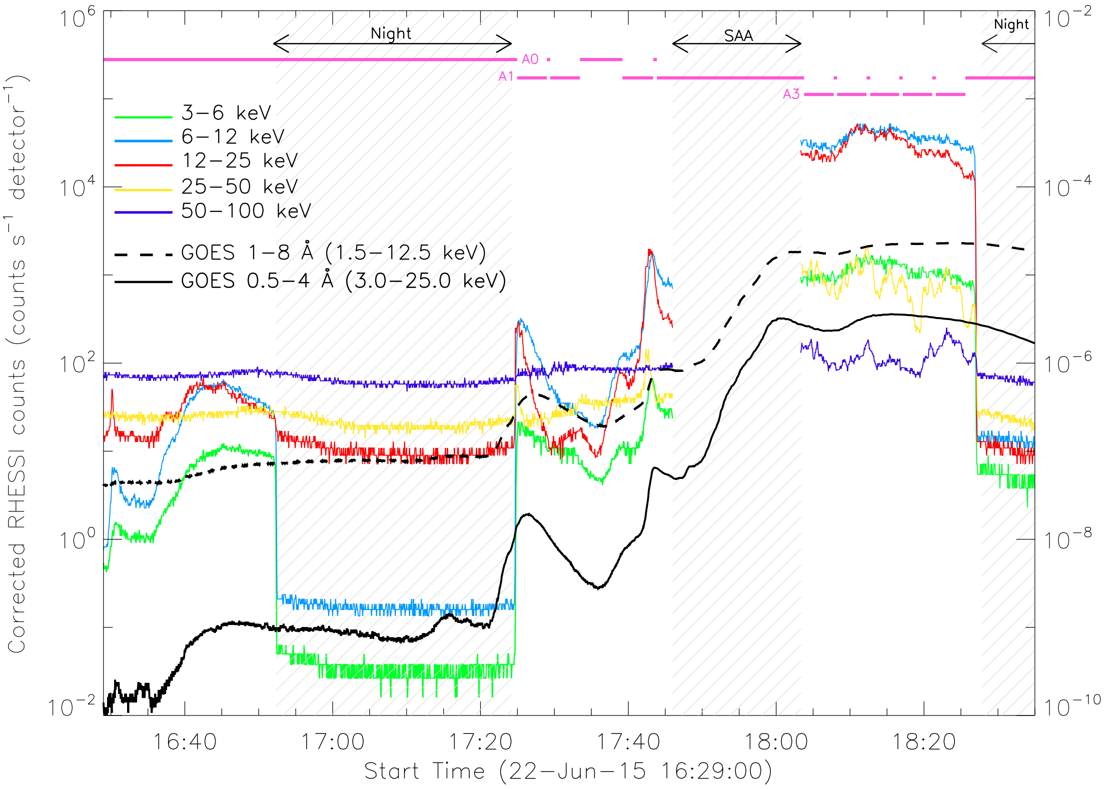

Figure 3.3: temporal evolution of X-ray count rates observed by RHESSI from 16:29 UT to 18:35 UT in energy bands of 3–6, 6–12, 12–25, 25–50, and 50–100 keV with a time cadence of 4 s. GOES SXR light curves in 1–8 Å and 0.5–4 Å channels are also shown by dashed and solid lines, respectively. The hatched regions denote unavailability of solar X-ray data due to RHESSI night (N) and South Atlantic Anomaly (SAA). Different attenuator states (A0, A1, and A3) are shown by horizontal bars at the top.

Normalized intensity light curves of the AIA channels 171 Å, 304 Å, 94 Å, and 1600 Å filters are shown in Figure 3.2(b). In general, these (E)UV light curves show similar trends than the GOES SXR light curves with some time delays in the peak emission among different bands. The first peak P1 of the GOES light curve in 0.5–4 Å channel is not seen in the AIA light curves; while the second peak P2 is clearly visible (shown by dotted lines in Figure 3.2(b)). The 94 Å light curve shows a significant time-shift in the peak compared to other AIA light curves and continued emission for a longer period (up to 21:00 UT). The AIA 171 Å light curve shows significant variability in the decay phase, which is not seen in other AIA light curves. The 1600 Å light curve shows dual peak structure in the main phase of the M6.6 flare similar to GOES light curves.

In Figure 3.2, we provide a comparison of the AR corona during the pre- and post-flare phases of the flare as recorded in different SDO/AIA channels; namely: in 94 Å (cf. Figure 3.2, panels (c) and (d)), in 304 Å (cf. Figure 3.2, panels (e) and (f)), and in 171 Å

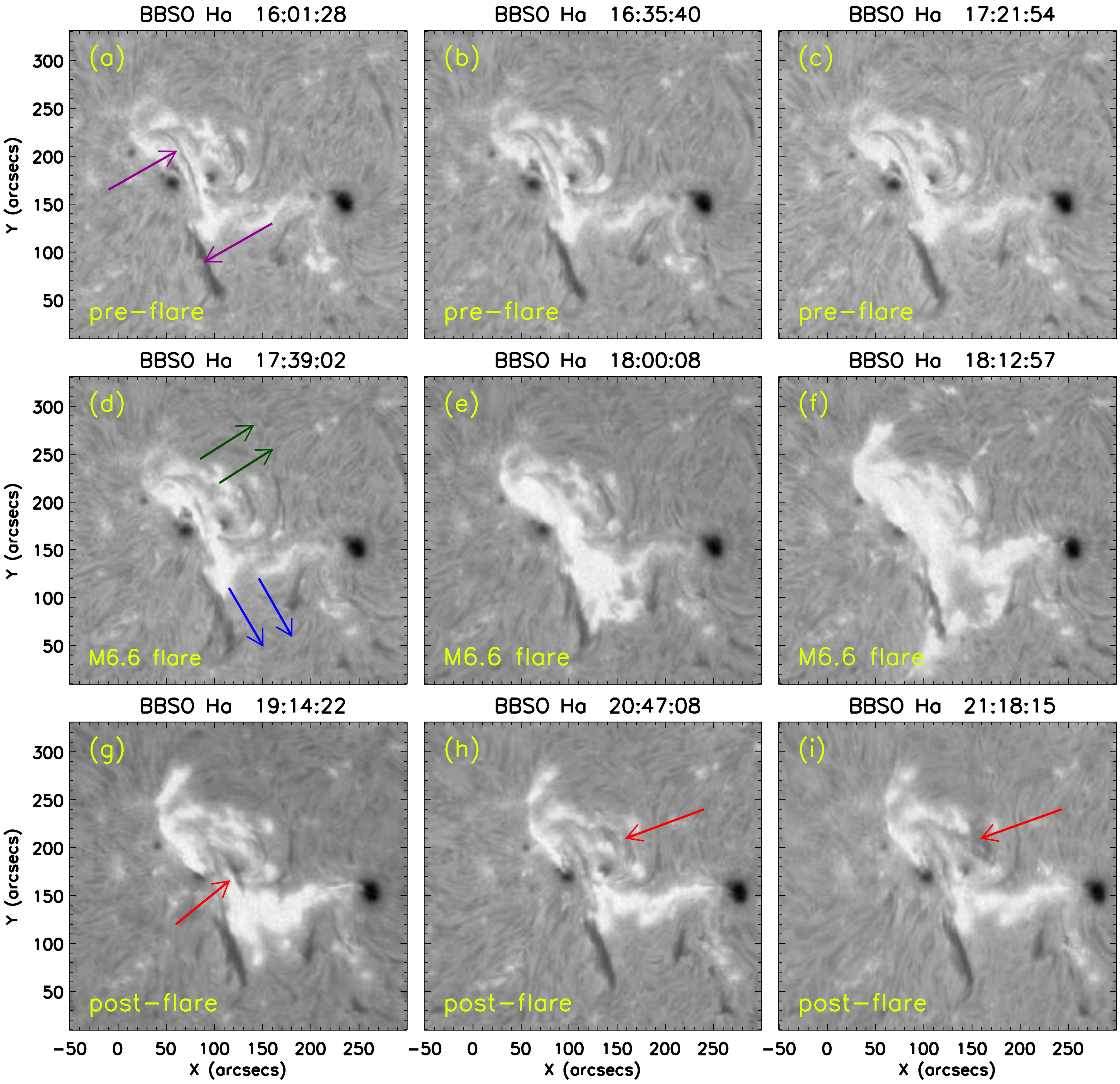

Figure 3.4: BBSO Hα filtergrams showing the temporal evolution of different phases of M6.6 flare, namely, pre-flare phase, main phase, and post-flare phase in panels (a)–(c), (d)–(f), and (g)–(i), respectively. Two distinct parts of the filament (shown by purple arrows in panel (a)), together constitute a filament channel. The onset of M6.6 flare is preceded by activation of the filament channel in two different directions (shown by blue and green arrows in panel (d); For details, see Section 3.2.1). An upward motion of filament material is observed during the post-flare phase, which is shown by red arrows in panels (g)–(i).

(cf. Figure 3.2, panels (g) and (h)). In the pre-flare stage, we observe low lying coronal loops with a faint signature of a hot coronal channel underlying the low coronal loops in the 94 Å image (Figure 3.2(c)). In the post-flare stage, dense and bright post-flare loops are observed to be formed (Figure 3.2(d)). In AIA 304 Å, we observe the signature of filament in pre-flare stage (Figure 3.2(e)), whose eruption gives rise to formation of post-

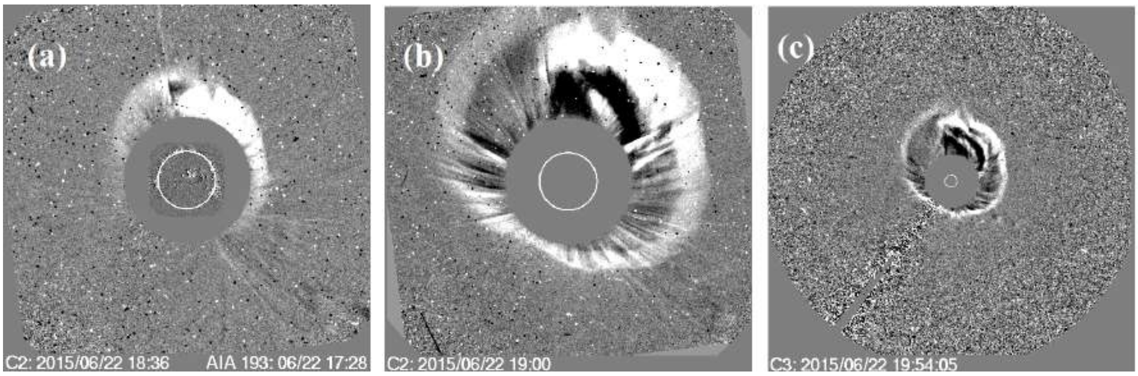

Figure 3.5: running difference images of LASCO C2 (panels (a) and (b)) and C3 (panel (c)) coronagraphs. Panel (a) shows first detection of CME in C2 coronagraph. A full disk image of the Sun in AIA 193 Å is overplotted on the coronagraph occulter. The CME is first detected in C3 coronagraph at ≈18:54 UT.

flare loop arcades (Figure 3.2(f)). In the post-flare stage, AIA 171 Å observations also reveal the formation of dense post-flare loop arcades (Figure 3.2(h)).

In Figure 3.3, we show RHESSI X-ray count rates in different energy bands from 3–100 keV in the interval of 16:30 UT to 18:35 UT. The co-temporal GOES SXR light curves in 1–8 Å and 0.5–4 Å are overplotted on the RHESSI count rates. We observe simultaneous occurrence of peaks in GOES SXR and lower energy RHESSI (<25 keV) light curves in the pre-flare stage (from ≈16:30 UT to ≈17:35 UT). In the main phase of the flare (from ≈17:35 UT onward), the higher energy RHESSI (>25 keV) light curves show distinct small peaks.

To show the overall evolution of the M6.6 flare, we present a few representative Hα images in Figure 3.4. The Hα data are obtained from BBSO (Denker *et al.*, 1999) with a telescope aperture of 10 cm. These Hα observations are taken with a filter of 0.25 Å bandpass centered at the Hα line core and 2048×2048 pixel CCD camera. The images have a temporal cadence of ≈60 s and pixel size ≈1$''$.0 (see page 2 of Sahu *et al.*, 2020). At the pre-flare stage, we observe the presence of a filament channel along the PIL of the AR (shown by purple arrows in Figure 3.4(a)). During the early stage of the main phase of the flare, we observe activation of the filament channel in two different directions: along the length of the channel toward southwest (shown by blue arrows in Figure 3.4(d)) and along northwest direction (shown by green arrows in Figure 3.4(d)). The filament continues to erupt along the northwest direction and produces intense flare brightening (Figure 3.4, panels (e) and (f)). The two-step activation of the filament channel may be associated with the pre-flare activities that lead to the partial eruption of the filament. In the post-flare phase, we identify a filamentary material to be erupted from the core part of the flaring region, which is shown by red arrows in Figures 3.4(g)–(i).

The eruption of the hot channel and the subsequent flare result into a fast halo CME, which is observed by C2 and C3 coronagraphs of LASCO on-board SOHO (Figure 3.5). Various CME parameters are gathered from LASCO CME catalog (Yashiro *et al.*, 2004)[1]. The CME is first detected by C2 at ≈18:36 UT (Figure 3.5(a)) at the height of 4.1 $R_\odot$ and propagates with a projected linear speed of ≈1200 km s^{-1} measured at position angle 357°.

3.2.2 Structure and evolution of the photospheric magnetic field

Coronal magnetic configurations are deeply associated with changes of photospheric magnetic structures. Therefore, to understand the cause of flaring activities and filament eruptions, it is essential to study the changes associated with the photospheric magnetic fields. The magnetic structure of the AR 12371, one day prior to the event under investigation (i.e., 21 June 2015), is shown in Figure 3.6(a). The magnetic structure of the same AR just before the event is shown in Figure 3.6(b). A comparison of panels (a) and (b) reveals that the two sub-regions R_1 and R_2 undergo significant changes. In order to further probe the magnetic changes, a few representative magnetograms of the sub-region R_1 from 2015 June 21 to 2015 June 22 are shown in panels R_1(a)–R_1(e) of Figure 3.6. A light bridge (marked by yellow arrow) is noticeable, which gradually undergoes apparent rotation in clockwise direction. This light bridge separates the negative polarity sunspot and shows an increase in its width. White arrows show motion of a negative polarity region toward southwest (cf. Figures 3.6R_1(a)–R_1(e)). Blue arrows show southward motion of another negative polarity region within sub-region R_1.

In the first two panels of the LOS magnetograms of the R_2 region, the sky blue arrows show an island of negative polarity region, which eventually merges into the major negative polarity region north of it (cf. Figure 3.6, panels R_2(a) and R_2(b)). Notably, the eastern part of R_2 shows a very intriguing dynamical evolution with multiple events of fragmentation and merging of magnetic structures. Eventually the region exhibits significant cancellation of negative magnetic flux (cf. region marked by green arrows in Figures 3.6R_2(a), R_2(c), and R_2(e)).

[1] https://cdaw.gsfc.nasa.gov/CME_list/UNIVERSAL/2015_06/univ2015_06.html

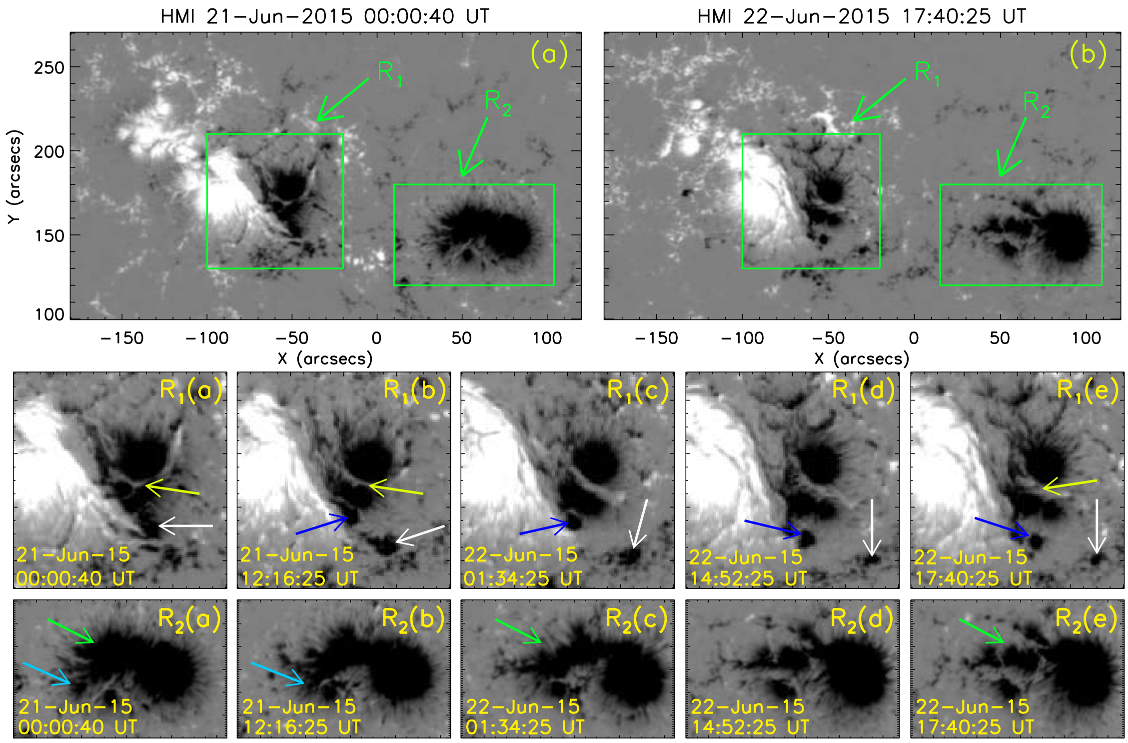

Figure 3.6: panels (a) and (b): HMI LOS magnetograms of the AR NOAA 12371 at 00:00 UT on 2015 June 21 (i.e., one day before the studied event) and 17:40 UT on 2015 June 22 (i.e., in the beginning of the M6.6 flare) are plotted to show the changes in the photospheric magnetic structures. We mark two sub-regions R_1 and R_2 in magnetograms that exhibit significant changes. In panels R_1(a)–R_1(e), we show a few representative snapshots of the sub-region R_1 to highlight important changes. Yellow arrows indicate a light bridge dividing the negative polarity region of the trailing sunspot group, which apparently undergoes rotation in clockwise direction and eventually becomes thicker. White arrows indicate motion of a small negative region toward southwest. Blue arrows indicate southward motion of another negative polarity region. In panels R_2(a)–R_2(e), we show the evolution of the sub-region R_2. The sky blue arrow in panel R_2(a) shows a small negative polarity region, which merges into the bigger negative polarity region (cf. panels R_2(a) and R_2(b)). Green arrows in panels R_2(a), R_2(c), and R_2(e) indicate a region where the magnetic flux rapidly evolves and eventually results in significant cancellation of negative flux.

3.2.3 Build-up and activation of the hot coronal channel

Based on the GOES light curves (Figure 3.2(a)), we define the pre-flare phase from ≈16:30 UT to ≈17:35 UT (see Table 3.1). In Figure 3.7, we show EUV images of the AR during the pre-flare phase by a few representative AIA 94 Å and 304 Å images. Initially,

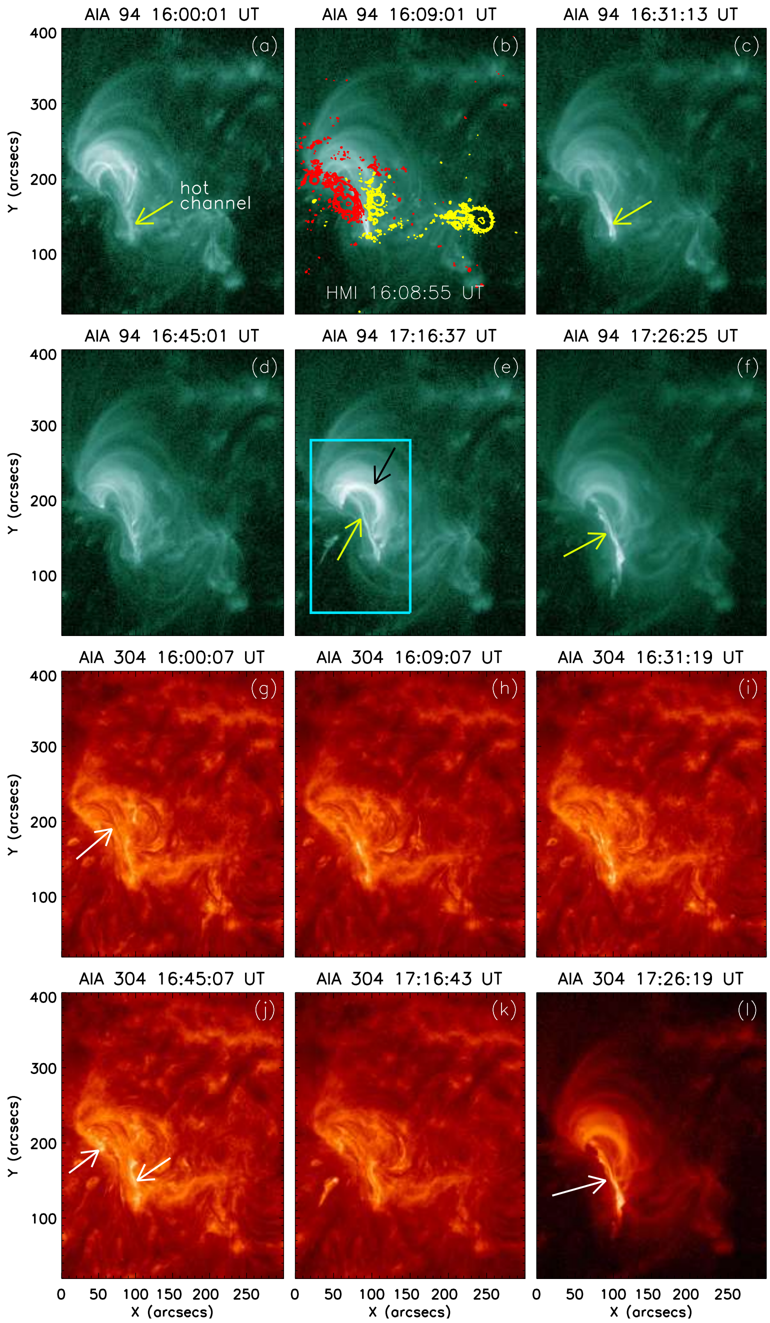

Figure 3.7: pre-flare phase of M6.6 flare shown in AIA 94 Å and 304 Å image sequences. Panels (a)–(f): sequence of AIA 94 Å images showing activation and pre-eruption stages of the hot channel (marked by yellow arrows in panels (a), (c), (e), and (f)) and overlying coronal loops (marked by black arrow in panel (e)). Panel (b) shows overplotted co-temporal HMI LOS magnetogram. The positive and negative polarities are shown by red and yellow contours respectively, with contours levels set as ±[500, 800, 1000, 2000] G. The box in panel (e) indicates the field-of-view of the images plotted in Figure 3.8. Panels (g)–(l): simultaneous imaging in the AIA 304 Å channel. A filament structure is shown by white arrow in panel (g). White arrows in panel (j) show the appearance of two brightenings on the two sides of the filament channel. The white arrow in panel (l) shows enhanced brightening from the filament channel.

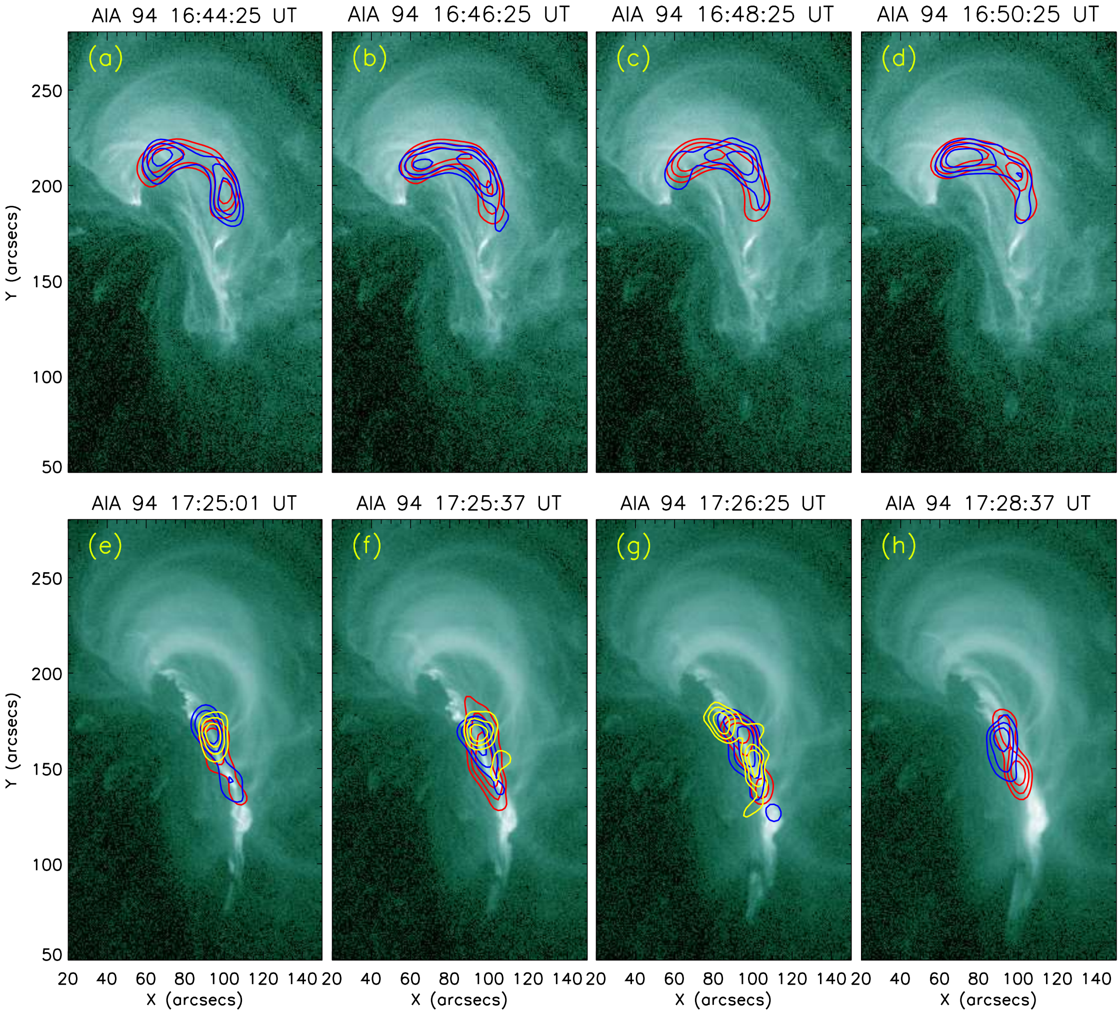

Figure 3.8: sequence of RHESSI X-ray images in 5–10 keV (red contours), 10–15 keV (blue contours), and 15–25 keV (yellow contours) overplotted on co-temporal AIA 94 Å images. Panels (a)–(d): sequence of images for first stage (peaked at P1) of the pre-flare phase, where the X-ray sources are observed to be emitted from the overlying coronal loops. Panels (e)–(h): sequence of images for second stage (peaked at P2) of the pre-flare phase. In this period, X-ray emissions are observed from the low-lying hot EUV channel below the coronal loops. The X-ray images are reconstructed by the CLEAN algorithm with integration time of 40 seconds. The contours drawn are at 70%, 80%, and 90% of the peak flux in each image.

a faint hot channel is identified beneath coronal loops in the 94 Å images (marked by yellow arrow in Figure 3.7(a)). From the HMI LOS magnetogram contours overplotted on the 94 Å image (Figure 3.7(b)), it becomes clear that the hot channel lies over the PIL formed within the trailing sunspot group. Subsequently, the brightening of the hot channel intensifies (marked by yellow arrows in Figures 3.7(c) and 3.7(e)) and it appears distinctly different from the surrounding regions. In view of the spatial association of the

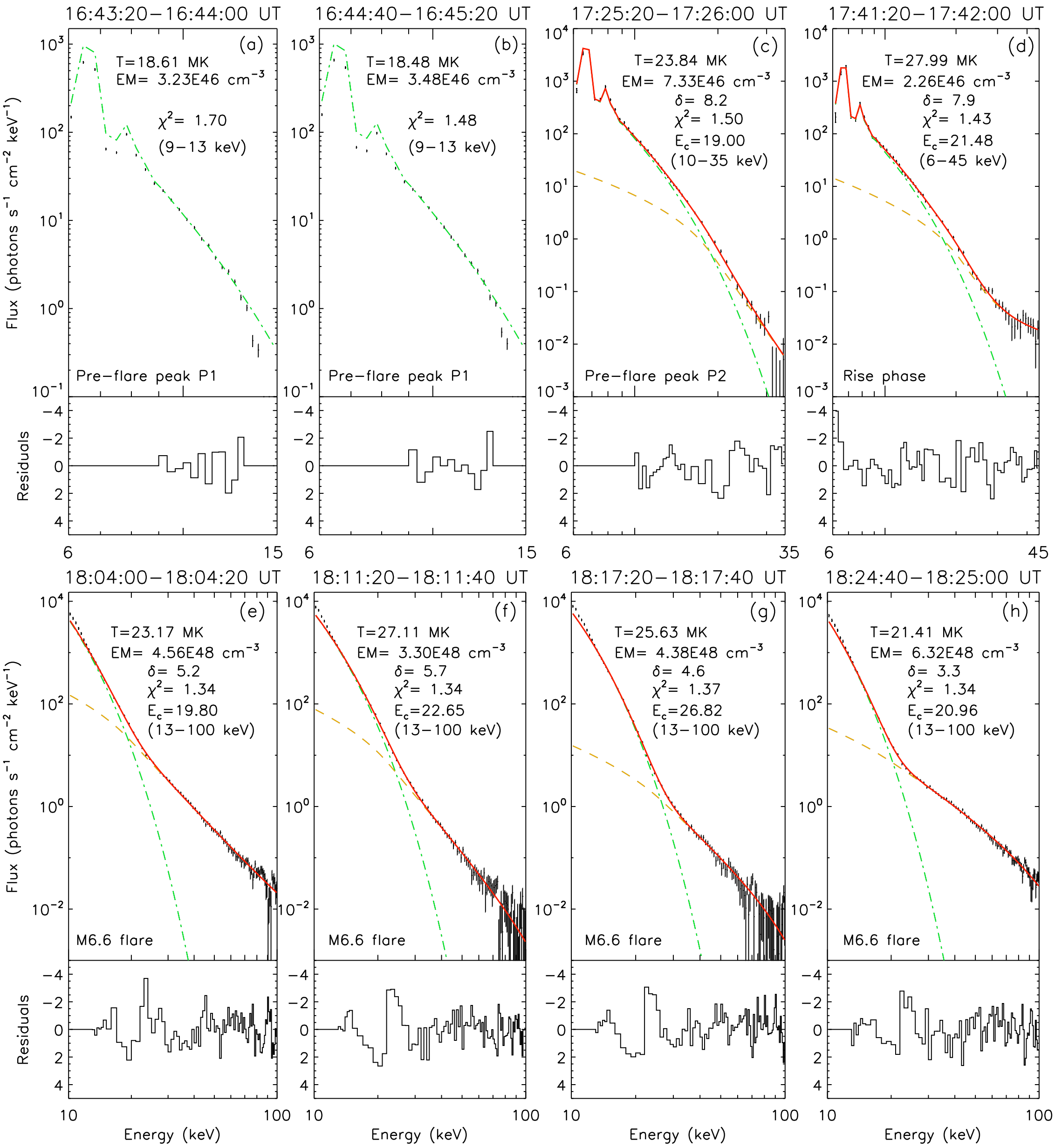

Figure 3.9: X-ray spectral fit of RHESSI data during various phases of the M6.6 flare. Panels (a) and (b) show spectral fit during the peak P1 (≈16:45 UT) and panel (c) shows spectral fit during the peak P2 (≈17:26 UT). We note that, thermal emission is dominant during the peak P1, whereas during the peak P2, we observe appearance of non-thermal component in the spectral fit. Both temperature and emission measure rise during the peak P2 compared to P1. Temporal evolution of spectral fit parameters in the main phase of the M6.6 flare is shown in panels (e)–(h).

hot channel and the overlying low coronal loops showing bright emission during the pre-flare phase, we identify the region shown inside the box in Figure 3.7(e) as the AR core and focus on its evolution in Figure 3.8. The hot channel continues to show enhanced emission till the occurrence of pre-flare peak P2 in GOES light curves (at ≈17:26 UT), which is indicated by yellow arrow in Figure 3.7(f).

In AIA 304 Å images, we observe a filament as the chromospheric counterpart of the hot channel (marked by white arrow in Figure 3.7(g)). Subsequently, we observe two parallel ribbon-like brightenings at ≈16:45 UT (shown by white arrows in Figure 3.7(j)), which are co-temporal with the pre-flare peak P1 (Figure 3.2(a)). Thereafter, the flux rope undergoes enhanced brightening at ≈17:26 UT (Figure 3.7(l)). We note this brightening to be simultaneous with the appearance of pre-flare peak P2 in GOES light curves (Figure 3.2(a)).

In Figure 3.8, we show a sequence of AIA 94 Å images with co-temporal RHESSI X-ray images (as contours) overplotted on each panel. The evolution of the AR core during the first peak (P1) of pre-flare phase is shown in Figures 3.8(a)–(d). During this phase, the X-ray emission up to 15 keV is observed to come from the region of overlying coronal loops. We note that the X-ray emissions have spatially extended structure with multiple centroids, being morphologically directly resembling the coronal loop system of the core region.

During the second peak (P2) of the pre-flare phase, we observe strong X-ray emission from the hot channel (Figures 3.8(e)–(h)) with X-ray emissions up to 25 keV. Evolution of the X-ray sources during this period is very striking. Initially at ≈17:25 UT, we find X-ray emitting sources with distinct centroids in the energy bands up to 15 keV (Figure 3.8(e)). The X-ray emissions in 5–10 keV energy band show nearly double centroid structure throughout the pre-flare peak P2 (Figures 3.8(e)–(h)), whereas, the X-ray centroids in 10–15 keV energy band dissolve (Figure 3.8(e)–(h)). Notably, the X-ray emitting sources in 15–25 keV energy band show appearance of multiple centroids (Figure 3.8(g)), which disappear afterwards (Figure 3.8(h)).

In Figure 3.9, we present spatially integrated, background subtracted RHESSI spectra along with their respective fits and residuals for a few selected intervals. Panels (a)–(c) of Figure 3.9 correspond to the spectra of pre-flare phase intervals. The RHESSI X-ray spectra during the first pre-flare phase (peaked at P1, see Figure 3.2(a)) shows thermal emission only (Figure 3.9, panels (a) and (b)). To estimate the characteristics of hot flaring plasma, namely temperature (T) and emission measure (EM), the best spectral fit results are obtained with fitting in the energy range of 9–13 keV for this interval. At this stage, the plasma temperature is ≈19 MK and emission measure is $\approx 3\times10^{46}$ cm^{-3}. In the second pre-flare phase, which peaks at P2 (Figure 3.2(a)), we find rise in temperature (≈24 MK) as well as emission measure ($\approx 7\times10^{46}$ cm^{-3}; Figure 3.9(c)), which suggests increase of thermal emission along with volume of heated plasma. Notably, during this second phase of the pre-flare activity, the X-ray emission rises to ≈35 keV above the background level. Contrary to the first pre-flare phase, the second pre-flare phase shows distinct yet moderate non-thermal emission above 19 keV, which follows a power-law with a steep electron spectral index (δ) of ≈8.2. The Flux (F) – Energy (E) power-law relationship for photons in the non-thermal component of the spectra using the thick-target Bremsstrahlung model is given by F $\sim$E$^{-\gamma}$, where γ is photon spectral index and is related to electron spectral index (δ) as γ=δ-1. The spectral fit results obtained during the rise and main phase of the flare are presented in Figures 3.9(d)–(f), which are discussed at the end of Section 3.2.4.

3.2.4 Hot channel eruption and further consequences

The main phase of the M6.6 flare is illustrated by a few representative AIA 94 Å images in Figure 3.10. The activated hot channel (indicated by the yellow arrow in Figure 3.10(a)) starts to erupt upward, distending the overlying coronal loop system (indicated by white arrow in Figure 3.10(a)). At this early stage, the X-ray emission is originated at energies $\lessapprox$25 keV and the sources lie in a relatively compact region (Figure 3.10(a)). With the further upward expansion of the hot channel, we observe emission from conjugate HXR sources of 25–50 keV energies (green contours), which appears to be located near the anchored footpoints of the hot channel (Figure 3.10(b)). Importantly, the continuous rise of the GOES flux is superimposed with a distinct peak at ≈17:44 UT, which clearly appears in all the high energy RHESSI X-ray light curves up to 50 keV energies (Figure 3.3). The hot channel rises gradually with clear and intact structure visual in direct AIA 94 Å images. In Figures 3.10(c) and (d), we mark the leading front of the hot channel by white arrows. The GOES light curves further suggest that the flare exhibits an extended maximum phase with dual peak structures at ≈18:00 UT and ≈18:13 UT. The comparison of AIA 94 Å with co-temporal multi-channel RHESSI images clearly reveals two distinct regions of X-ray emission: the high energy HXR sources between 25 and 100 keV appear in pair as conjugate sources while the low energy emission $\lessapprox$25 keV comes from the hotter region occupied with newly formed EUV coronal loops, in the wake of hot channel eruption (Figures 3.10(d)–(g)). We also find an increase in separation of the HXR footpoint sources as the flare progresses. We note that the strength of HXR emission to be higher at the southern footpoint of post-flare loop arcades where the HXR emission upto 50 keV is observed (Figure 3.10(g)), which suggests an asymmetry in the deposition of energy at conjugate footpoint locations. Soon after the second peak, the flaring region starts to show the formation of dense, bright, gradually rising post-flare loop arcades in the northern part (shown by red arrow in Figure 3.10(g)). Gradually the southern part of the flaring region also exhibits the build-up of post-flare loop arcades (indicated by red

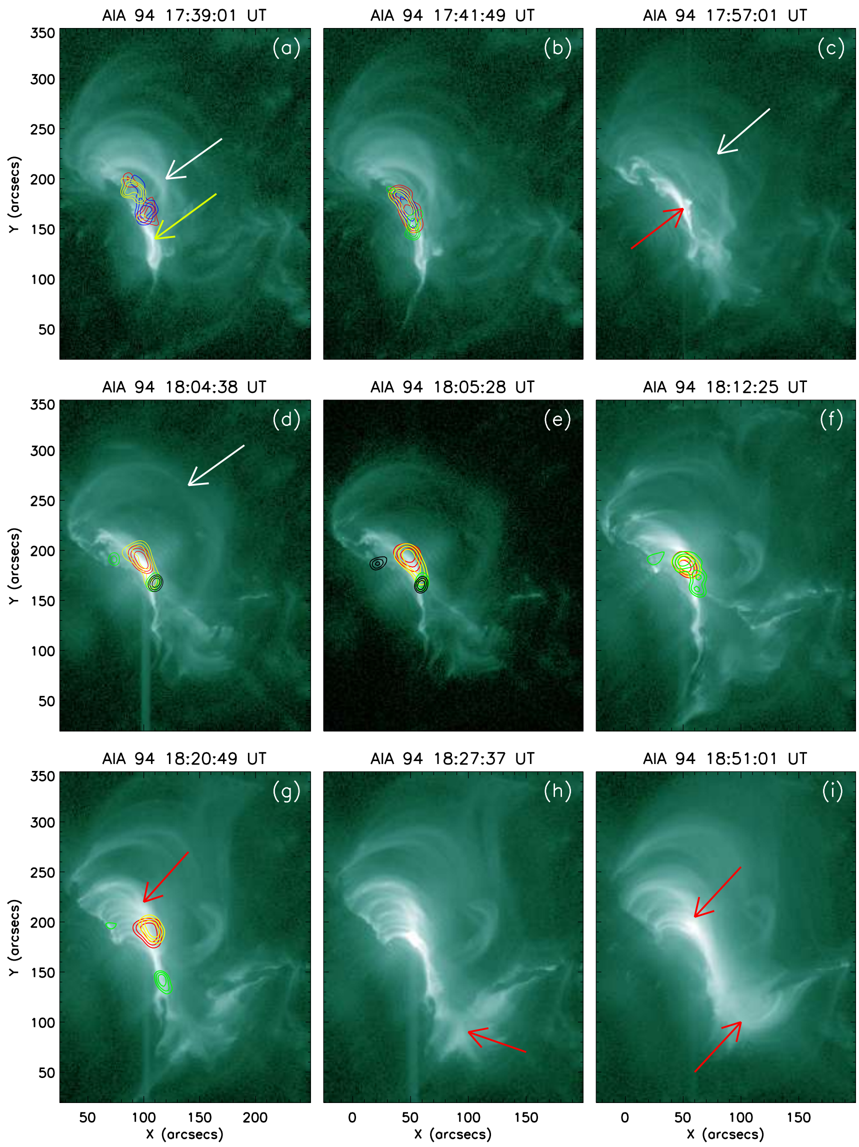

Figure 3.10: sequence of AIA 94 Å images showing evolutionary phases of the eruption of hot channel and associated M6.6 flare. Panel (a) shows hot EUV channel (marked by yellow arrow) and overlying coronal loops (marked by white arrow). The erupting front of the hot channel is shown by white arrows in panels (c) and (d). Red arrow in panel (c) shows start of formation of post-flare loops. RHESSI images in 5–10 keV (red contours), 10–15 keV (blue contours), 15–25 keV (yellow contours), 25–50 keV (green contours), and 50–100 keV (black contours) are reconstructed by CLEAN algorithm with integration time of 32 seconds. The contour levels are set as 70%, 80%, and 90% of the peak flux in each image. Panels (g)–(i) show formation of post-flare loop arcades. The red arrow in panel (g) shows the post-flare loops in the northern part of the flaring region, which ultimately converts into dense post-flare loop arcades. Red arrow in panel (h) shows the start of formation of post-flare loops in the southern part of the flaring region. In panel (i), dense post-flare loop arcades in both northern and southern part of the flaring region are indicated by red arrows.

arrow in Figure 3.10(h)). In Figure 3.10(i), we show well developed, dense post-flare loop arcades in both northern and southern part of the flaring region by red arrows.

The comparison of evolution of HXR sources with respect to the AIA 304 Å images are shown in Figure 3.11. After the activation of the filament, the brightening starts to appear in the form of flare ribbons (shown by green arrows in Figure 3.11(b)), which gradually move apart while exhibiting spatial expansion as well (cf. Figures 3.11(a)–(f)). Also, as expected, the high energy HXR sources of strength ≈25–100 keV show spatial consistency with the flare ribbons. The region marked by white arrow in Figure 3.11(e) undergoes gradual increase in the brightness (cf. Figures 3.11(e)–(i)). In the later stages, we observe distinct yet diffuse emission from post-flare coronal arcades, which is shown by black arrows in Figures 3.11(g)–(i).

As a comparison of phenomena occurring simultaneously in different heights of solar atmosphere, we have shown the flaring region in EUV (AIA 131 Å) and UV (AIA 1600 Å) channels during the first peak of the flare (Figure 3.12). AIA 131 Å image clearly shows the erupting hot channel (i.e., MFR) structure (shown by white arrow in Figure 3.12(a)). We observe simultaneous conjugate and sheared flare ribbon brightenings at the photospheric level in AIA 1600 Å image (marked by red arrows in Figure 3.12(b)).

To understand the activation and eruption of the hot channel, we plot a few AIA 94 Å running difference images (Figure 3.13). In various panels, we mark the expanding hot channel by yellow arrows. As discussed earlier, the eruption results into a fast halo CME (Figure 3.5). In Figure 3.13(g), we plot a time-slice diagram showing evolutionary phases of the hot channel. For the purpose, we specify a narrow slit $\overline{B_1B_2}$, which is indicated in Figure 3.13(a). The time-slice diagram is constructed using the running difference images with a time gap of ≈4 minutes between the successive images. The plot reveals a slow rise (speed ≈14 km s^{-1}) phase of the hot channel between ≈17:37 UT and ≈17:49 UT (shown by red dashed line), which is followed by another phase of its fast eruption. A second order polynomial fit to the height-time measurement taken between ≈17:49 UT and ≈18:00 UT (shown by yellow dashed line) yields the speed of the erupting hot channel as ≈37 km s^{-1} with an acceleration of ≈110 m s^{-2}. The speed of the erupting hot channel reaches to ≈109 km s^{-1} at ≈18:00 UT. Notably, we observe formation of post-flare loops from ≈17:57 UT at a projected height of ≈4 Mm.

In Figures 3.9(d)–(h), we show RHESSI spectral fit results during the rise and main phase of the M6.6 flare. We find a steady rise in temperature as well as spectral hardening during the rise phase (Figure 3.9(d)). In the main phase of the event (Figures 3.9(e)–(h)) the spectra continues to become harder with δ ≈3.3 at ≈18:24 UT. The maximum plasma

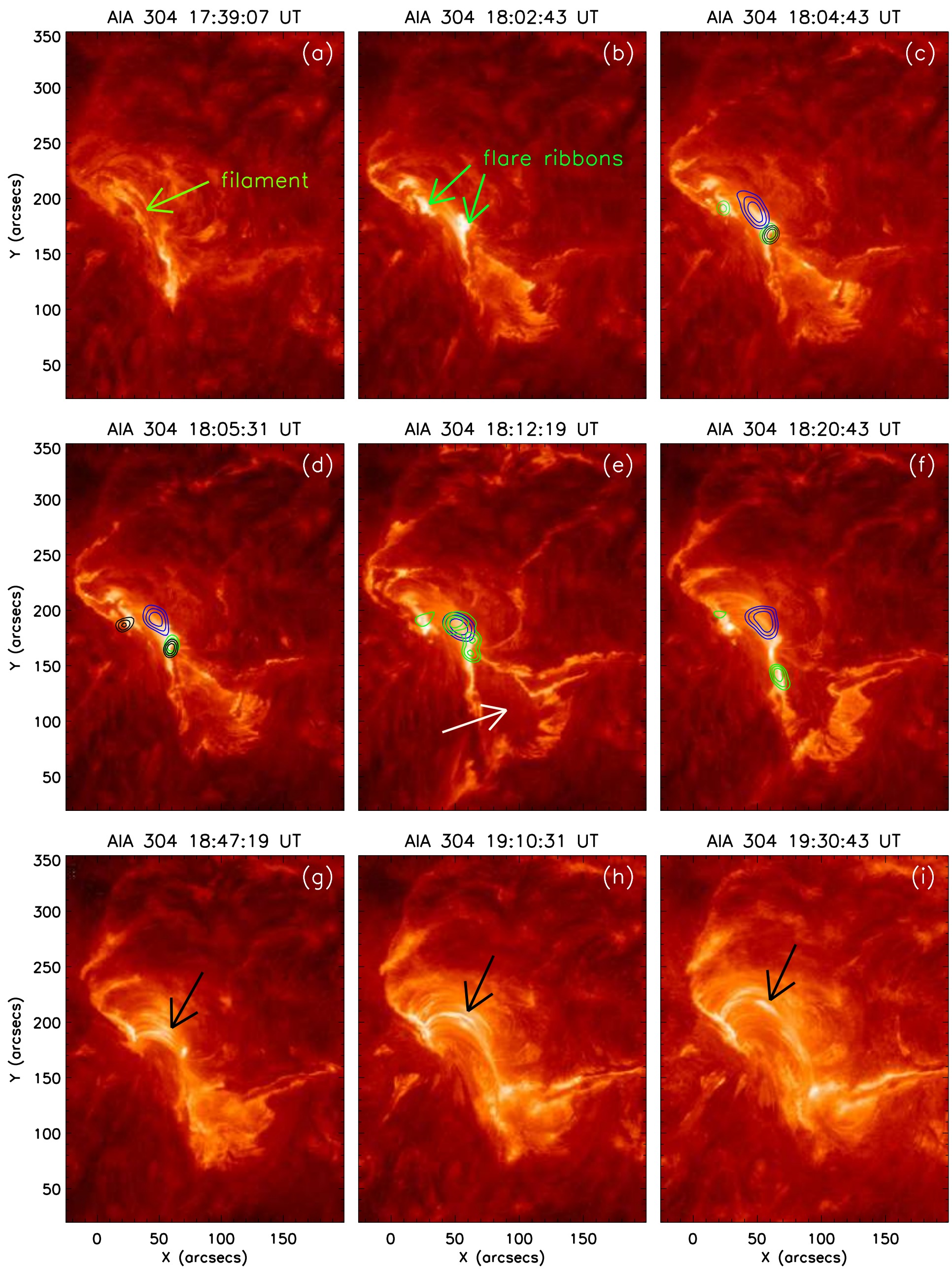

Figure 3.11: sequence of AIA 304 Å images showing eruption of flux rope (i.e., filament) and formation of post-flare loop arcades. The filament is shown by green arrow in panel (a). Subsequently we observe parallel flare ribbons at the footpoints of the erupting filament at ≈18:02 UT (marked by green arrows in panel (b)). RHESSI images in 10–15 keV (blue contours), 25–50 keV (green contours), and 50–100 keV (black contours) are reconstructed by CLEAN algorithm with integration time of 32 seconds. The contours denote 70%, 80%, and 90% of peak flux in each image. White arrow in panel (e) marks a region, which is gradually filled by chromospheric brightening (cf. panels (e)–(i)). We observe diffuse emission from post-flare coronal loops (shown by black arrows in panels (g)–(i)).

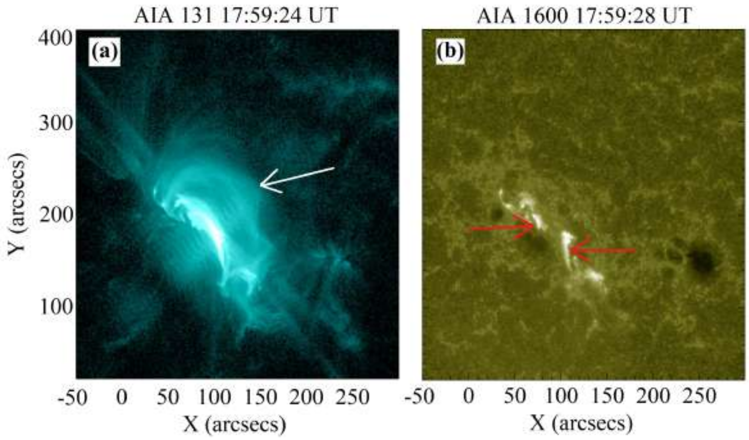

Figure 3.12: panel (a): the erupting hot flux rope structure in the AIA 131 Å image indicated by white arrow. Panel (b): the AIA 1600 Å image co-temporal with the 131 Å image shows conjugate and sheared flare ribbon brightenings, which are indicated by red arrows.

temperature (T ≈27 MK) is observed around the second peak of the M6.6 flare (see Figure 3.9(f)).

3.2.5 Non-Linear Force-Free Field (NLFFF) modeling of active region corona

The coronal magnetic field lines (Figures 3.14(a)–(c)) are extrapolated using the NLFFF model of Wiegelmann (2008) to model the flux rope and associated coronal field lines. The lower boundary of the extrapolation is taken as photospheric LOS magnetogram. The MFR, low lying coronal loops (LLCLs), and high coronal loops (HCLs) are shown by arrows in Figure 3.14(b). Clear MFR is observed to form in between two opposite polarities of the trailing sunspot group (Figure 3.14(c)).

In Figure 3.14, panels (d) and (e), AIA 171 Å and AIA 94 Å images of pre-flare stage (at ≈17:25 UT) distinctly show the hot channel (i.e., MFR), LLCLs, and HCLs. In Figure 3.14(d), we present 171 Å image overplotted with photospheric LOS magnetogram with contour levels as ±[400, 800, 1000, 2000] G. The blue and red contours denote negative and positive polarities, respectively. The rectangular box in Figure 3.14(d) shows a region of hot core, which contains the LLCLs and MFR. The enlarged view of rectangular box is shown in Figure 3.14(e) overplotted with RHESSI contours in 5–10 keV, 10–15 keV, and 15–25 keV. The contours denote 70%, 80%, and 90% of peak flux in each image. Interestingly the X-ray contours are observed to be found along the length of the MFR.

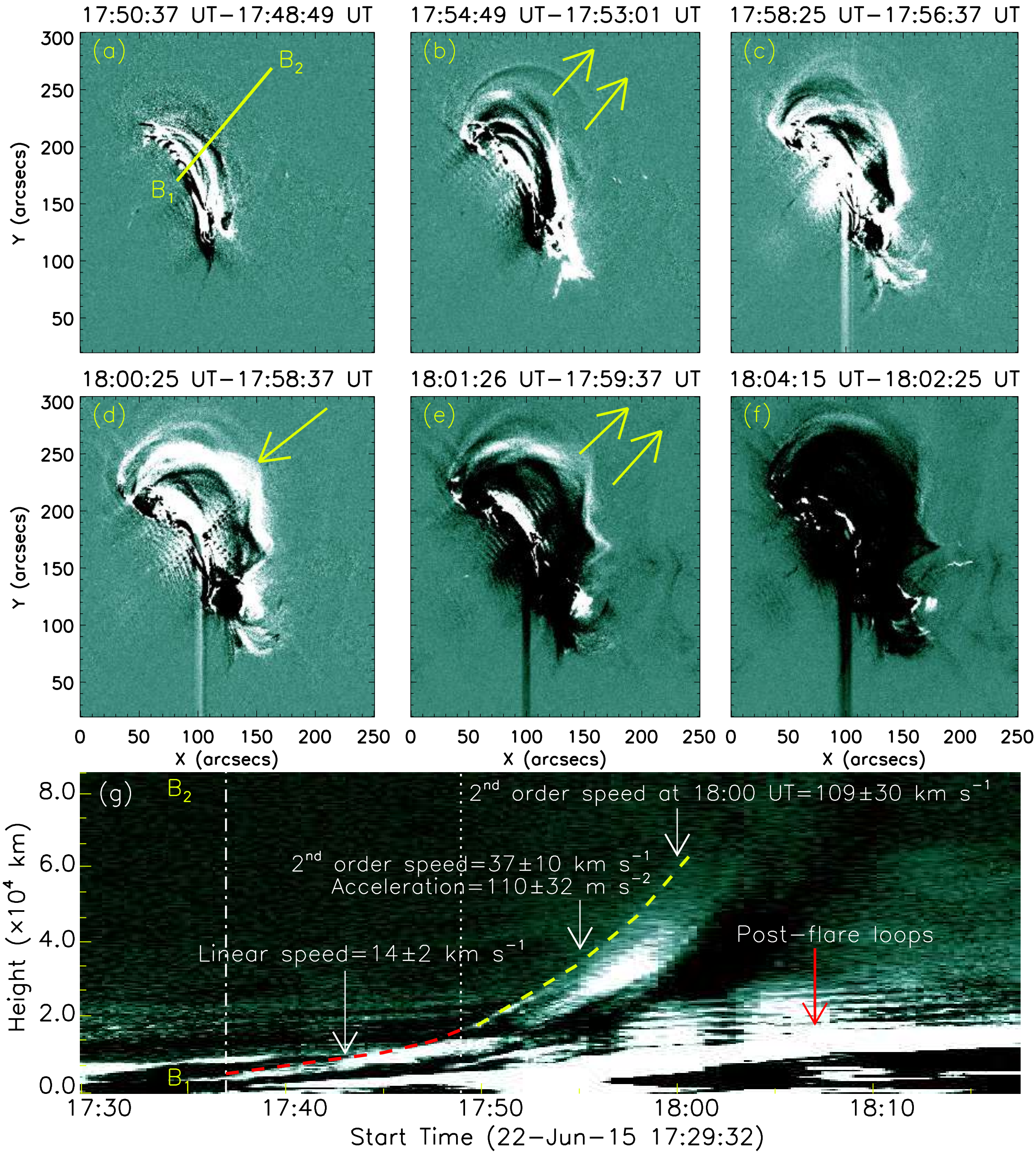

Figure 3.13: sequence of AIA 94 Å running difference images showing the directions of eruption of the hot channel (shown by yellow arrows in panels (b) and (e)). The arrow in panel (d) shows the erupting front. We plot a time-slice diagram of the erupting hot channel in panel (g). The direction, from B_1 to B_2, through which the time-slice plot is drawn, is shown as a yellow slit in panel (a).

3.3 Results and conclusions

In this chapter, we provide a comprehensive multi-wavelength and multi-instrument study of a major eruptive flare of M6.6 GOES flare class, which occurs in AR NOAA 12371

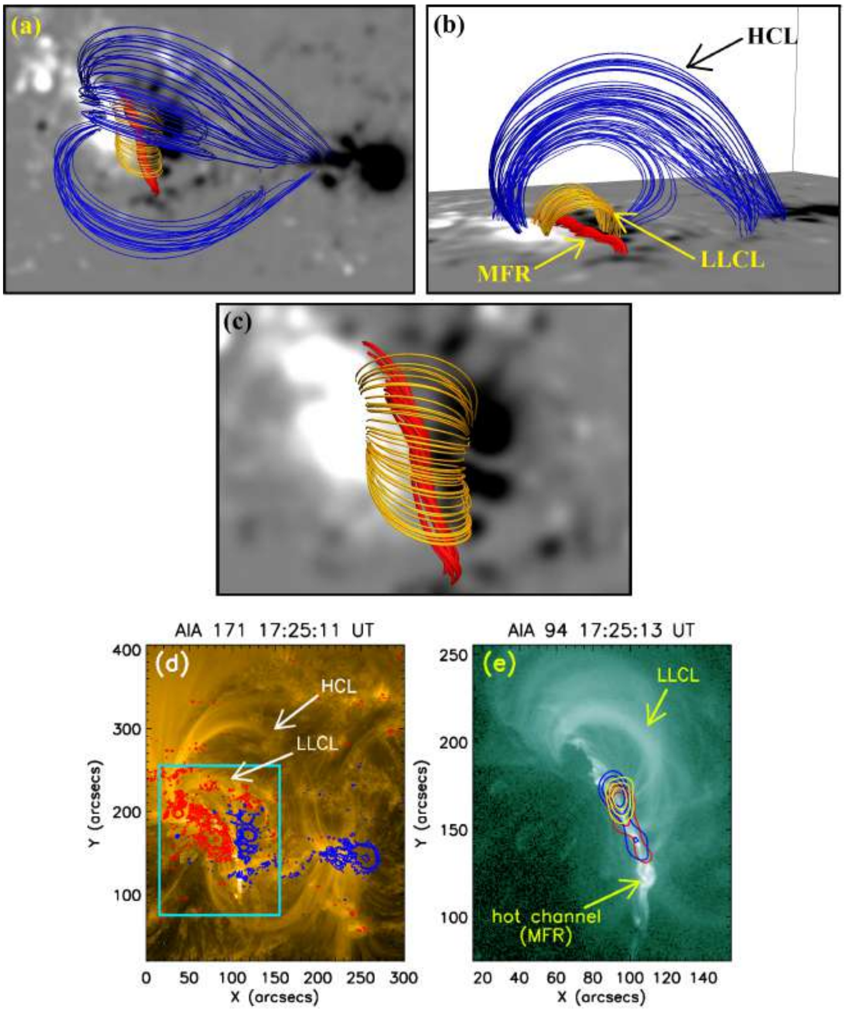

Figure 3.14: coronal magnetic field lines obtained using NLFFF model of extrapolation are shown in panels (a), (b), and (c). The lower boundary of the extrapolation is the photospheric LOS magnetic field. Panels (a) and (b) show the top and side view of the extrapolated field lines, respectively. The MFR, LLCLs, and HCLs are clearly indicated in panel (b). The position of the MFR along the PIL of the AR and the LLCLs are shown in panel (c). AIA 171 Å image of the AR is shown in panel (d) in pre-flare phase (at ≈17:25 UT), overplotted with HMI LOS magnetogram. The positive and negative polarities of magnetogram are shown by red and blue contours respectively with contours levels set as ±[400, 800, 1000, 2000] G. HCL and LLCLs are shown by white arrows in panel (d). The rectangular box indicates a hot core region, whose enlarged view is shown in AIA 94 Å channel in panel (e) overplotted with RHESSI contours in 5–10 keV (red), 10–15 keV (blue), and 15–25 keV (yellow). The X-ray contours are reconstructed by CLEAN algorithm with integration time of 40 seconds. The contours denote 70%, 80%, and 90% of peak flux in each image. LLCLs are also clearly visible above the hot channel/MFR, which is co-spatial with X-ray sources.

on 2015 June 22. The importance of the study lies in investigating the activities right from the early pre-flare phase till the decay of the flare. In particular, we aim to explore the pre-flare processes in detail and the link between the pre-flare and main flare. The important observational results of the study are summarized below:

1. The initiation of the eruption occurrs from a magnetically bipolar region where a hot EUV channel (evidence of MFR) pre-existed (at least ≈5.5 hr before the eruptive M6.6 flare) that exhibits early signatures of activation during the pre-flare phase. The Hα observations reveal the presence of a filament in association with the coronal hot channel. Observations of the pre-flare phase clearly reveal activation of the filament with early eruption signatures, providing further support to our interpretation of pre-flare activities.

2. The hot channel is found to be co-spatial with a MFR detected in NLFFF model extrapolation. A very remarkable finding of the study lies in the detection of elongated as well as localized HXR sources of energies up to 25 keV that lie exactly over the extended central part of the hot channel. To our knowledge, this is the first time when an MFR is being detected in direct HXR observations.

3. An important yet realistic coincidence is the continued presence of X-ray sources during the whole pre-flare phase. In the early pre-flare phase, the X-ray emission comes from the core region, which is comprised of hot, dense bundle of low lying coronal loops, just above the filament channel. On the other hand, during the late pre-flare phase, as explained in item 2 above, the X-ray emission extends up to higher energies and the sources are located in the region where flux rope/hot channel exists. These distinct pre-flare intensity enhancements, therefore, suggest build-up and activation of the MFR by magnetic reconnection involving interaction between the core field region and the slowly evolving MFR.

4. We analyze the evolution of photospheric magnetograms during the extended period (≈42 hr) prior to the pre-flare phase of the eruptive flare. Our observations reveal clockwise rotation of mix polarity sunspot group along with remarkable moving magnetic features.

5. With the onset of the impulsive phase of M6.6 flare, a sudden transition in the kinematic evolution of the MFR is observed in the form of its state of slow rise (≈14 km s^{-1}) to fast acceleration (≈110 m s^{-2} with the speed rises to ≈109 km s^{-1} within AIA field-of-view). This observation points toward a feedback relationship

between source region CME dynamics and the strength of the large-scale magnetic reconnection powering the eruptive flare.

6. The classical signatures of large-scale magnetic reconnection are observed during the impulsive phase in terms of high energy (up to 100 keV) HXR conjugate sources that lie over the (E)UV flare ribbons. The Hα observations show the remaining structures of the filament thus confirming the event to be a partial filament eruption.

The analyses carried out reveal the appearance of EUV hot channels in the corresponding SDO/AIA observations, well before (≈5.5 hr) the eruptive flare. This finding is in agreement with the contemporary understanding that the presence of MFR is a prerequisite for a CME (Fan, 2005; Li and Zhang, 2013; Song *et al.*, 2019). The correspondence between the spatial location of hot channel and MFR in coronal field modeling has been reported in several studies (Liu *et al.*, 2018b; Mitra *et al.*, 2018), which is further confirmed by our analysis. However, the build-up mechanism of the MFR is still an open question, which requires extensive observational and theoretical research. The present study is a step in this direction and suggests that the pre-flare activities play an important role in the process of MFR activation. The pre-flare activity could be related to evolution in the photospheric magnetic structure. However, photospheric magnetic field changes in the ARs occur gradually but eventually lead to the development of complex magnetic field configuration in the corona which can also be seen in the present case. Our observation of rotation of sunspot group (in clock wise direction) over several hours, which encloses the PIL and, in the later phases, overlying developing MFR is probably related to the transfer of twist from sub-photospheric level to the coronal field lines. This long-lasting process would store excess magnetic energy into the coronal flux rope. The brightening up of the core field containing the MFR about 1.25 hr prior to the eruptive flare thus suggests the onset of heating, probably due to the magnetic reconnection, as the flux rope interacts with immediate low-lying arcades. Subsequently, the hot channel undergoes significant intensity enhancement and starts to appear in X-ray images up to 25 keV energies. Coronal pre-flare activity starts with the initiation of intense emission from the MFR and surrounding regions (an observational fact that is traditionally being observed in SXR as enhanced emission; see e.g., Veronig *et al.* 2002; Chifor *et al.* 2007; Hernandez-Perez *et al.* 2019b; Joshi *et al.* 2011, 2013).

Importantly, in our case, the regions of pre-flare activity and main M6.6 flare are co-spatial. The statistical studies carried out with SXR images from Yohkoh, revealed three categories of pre-flare activities in terms of source locations: co-spatial, adjacent, and remote (Fárník and Savy, 1998; Kim *et al.*, 2008). The co-spatial and adjacent cases occurring within few minutes before the main flare are supposed to have direct relevance for the triggering processes related to the main flare (Liu *et al.*, 2009; Joshi *et al.*, 2011; Mitra and Joshi, 2019). Notably, in our study, the EUV and X-ray images clearly show that the pre-flare brightenings are spatially distributed along the hot channel (i.e., MFR) and within the core field region. Further, before the pre-flare activity, the region shows photospheric magnetic field changes along the PIL. These observations present consistency with the tether-cutting model of solar eruption (Moore and Roumeliotis, 1992; Moore *et al.*, 2001), where the build-up of MFR is a consequnce of flux changes along the PIL and, therefore, early reconnection signatures (causing the pre-flare activity) are expected to occur close to PIL and nearby core regions (Yurchyshyn *et al.*, 2006; Chen *et al.*, 2014a; Dhara *et al.*, 2017).

We find direct evidence of pre-flare tether-cutting reconnection in HXR imaging observations at lower energies (up to 25 keV). The HXR emission signifies intense heating of the core region. With the progress of pre-flare activity, the strength of HXR emission increases and a subtle yet clear non-thermal component starts to appear, which we identify as second pre-flare enhancement. The comparison of imaging and spectroscopic observations suggests that both thermal and non-thermal components originate from the EUV hot channel in the late pre-flare phase. Importantly, the HXR source at lower energies presents an elongated morphology and the X-ray sources lie exactly over the EUV hot channel. These observations provide direct support of tether-cutting reconnection. To our knowledge, the observation of extended HXR sources from a developing MFR during the pre-flare phase is a new observational finding. As expected, during this phase the hot channel rises slowly, which is an important feature of CME precursor (Sterling and Moore, 2005; Nagashima *et al.*, 2007; Sterling *et al.*, 2007; Song *et al.*, 2015). The partial eruption of filament begins at this time observed in Hα images, further supporting the physical link between the pre-flare activity and initiation of solar eruption. Importantly, the slowly rising MFR transitions to a phase of fast eruptive expansion with the onset of impulsive phase of the M6.6 flare. Now, the appearance of 'classical' flare signatures, viz., distinct coronal and footpoint HXR sources along with inner flare ribbons formed at both sides of PIL, provide evidence of large-scale magnetic reconnection, which are attributed to the reconnection-opening of overlying field lines (i.e., progression of reconnection in higher coronal fields of the envelope region) stretched by the erupting MFR. The sudden transition in the evolution of MFR from the phase of slow to fast rise precisely divides the pre-flare and impulsive phase of the flare, which we attribute to the feedback relationship between the early dynamics of CME and the associated strength of the large-scale flare magnetic reconnection (Temmer *et al.*, 2008; Vršnak, 2016; Song *et al.*, 2018; Mitra and Joshi, 2019).

Chapter 4

Evolution of Magnetic Fields and Energy Release Processes During Homologous Eruptive Flares

4.1 Introduction

The strongest magnetic field regions of the Sun are known as solar active regions (ARs). The ARs present a diverse nature in their morphology depending upon the distribution and strength of the underlying photospheric magnetic fields (Toriumi and Wang, 2019). Typically, during its growth phase, as an AR expands and evolves, the complexity in the photospheric magnetic field increases. A complex AR may produce several energetic events (viz., flares, CMEs, jets, prominence eruptions, etc.) during its whole lifetime (Joshi *et al.*, 2018; Mitra *et al.*, 2018, 2020b; Sahu *et al.*, 2020; Zuccarello *et al.*, 2021).

Solar eruptions in a repetitive manner may originate from the same location of the AR and sometimes they show morphological resemblance in the multi-wavelength imaging and coronagraphic observations. Such repetitive activities are known as 'homologous eruptions' (Woodgate *et al.*, 1984; Zhang and Wang, 2002). The exploration of homologous eruptions is extremely important to understand the role of photospheric magnetic field variations and associated coronal changes in determining the eruptivity. In this way, by assessing the homology tendency of an AR, we can provide important inputs toward the onset of CMEs and subsequent space weather consequences. In the past, several studies on different features of homologous eruptions were carried out that reveal following aspects to be responsible for the occurrence of homologous activity: flux emergence (Nitta and Hudson, 2001; Chatterjee and Fan, 2013), shearing motion and magnetic flux cancellation (Li *et al.*, 2010; Vemareddy, 2017), persistent photospheric horizontal motion of the magnetic structure along the PIL (Romano *et al.*, 2015, 2018), coronal null point configuration (DeVore and Antiochos, 2008), etc. The homologous solar eruptions form a contemporary research topic in solar physics and the present study aims to provide additional observational inputs in this direction.

In this study, we investigate a detailed evolution of photospheric magnetic fields associated with the three homologous eruptive flares occurred during 2014 March 28–29 in the NOAA AR 12017. Interestingly, the three homologous events are of successively increasing intensities (M2.0, M2.6, X1.0). Flaring activities in AR 12017, especially the X-class event on 2014 March 29, were subjected to various studies pertaining to observational and modeling analyses (Kleint *et al.*, 2015; Li *et al.*, 2015; Liu *et al.*, 2015; Young *et al.*, 2015; Yang *et al.*, 2016; Woods *et al.*, 2017, 2018; Cheung *et al.*, 2019). Liu *et al.* (2015) discussed a scenario of asymmetric filament eruption in the context of nonuniform filament confinement and an MHD instability prior to the X-flare. The study by Yang *et al.* (2016) was comprised of all the flaring activities in the AR during 2014 March 28–29. They concluded that the flares were triggered mainly by the kink instability of the associated filaments. Woods *et al.* (2018) investigated the triggering mechanism of the third event (X1.0 flare) and associated filament eruption. Their study confirmed the existence of two flux ropes within the AR prior to flaring. Interestingly, one of these two flux ropes erupts, which might be due to the tether cutting reconnection (Moore *et al.*, 2001) allowing the flux rope to rise to a torus unstable region.

In this study, our motivation is to conduct a detailed exploration of the temporal, spatial, and spectral characteristics of the three homologous flares. Furthermore, we provide a quantitative estimation of the temporal evolution of free magnetic energy in the AR to understand the complex process of its storage and release during the homologous eruptive events. Section 4.2 gives the details of EUV and X-ray observations of the flares. In Section 4.3, we describe the photospheric magnetic field evolution during the events and associated coronal magnetic configuration. The build-up of photospheric current in relation to the triggering of the eruptions is presented in Section 4.4. The evolutionary stages of the eruptive hot plasma structures are presented in Section 4.5. The details of the storage and release processes of free magnetic energy are described in Section 4.6. We discuss and interpret our results in the final section.

4.2 Multi-wavelength analysis of flare evolution

Our study incorporates three homologous flaring events of successively increasing intensities (M2.0, M2.6, X1.0). The flares occur in the NOAA AR 12017 during 2014 March

Flares	Flare Class	Date	Start	Time (UT) Peak	End
F1	M2.0	2014 Mar 28	19:05	19:18	19:27
F2	M2.6	2014 mar 28	23:44	23:51	23:58
F3	X1.0	2014 Mar 29	17:35	17:48	17:54

Table 4.1: the overview of the flares in NOAA AR 12017 during 2014 March 28–29.

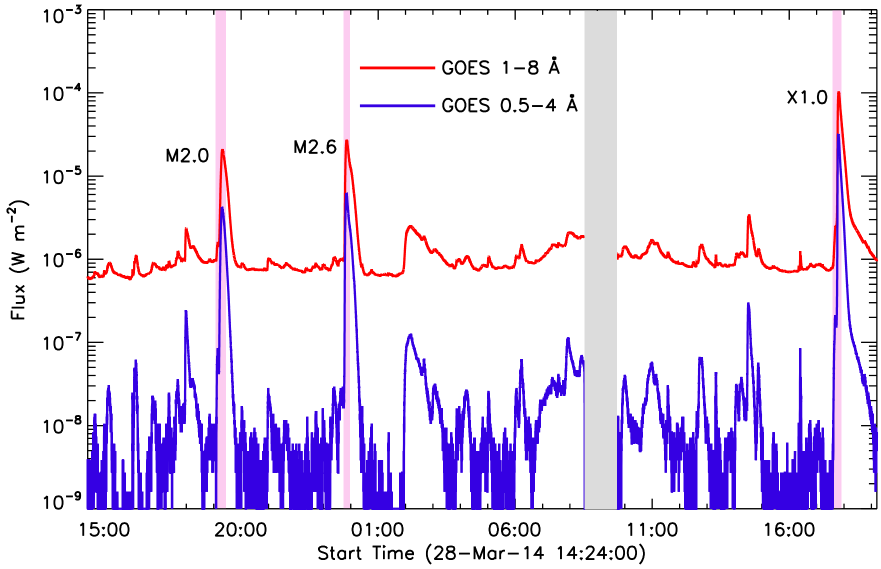

Figure 4.1: GOES light curves in 1–8 and 0.5–4 Å channels showing the three flares (M2.0, M2.6, and X1.0) under analysis. The intervals of the three flares are shown by pink vertical stripes. The gray shaded region indicates an interval when the GOES data were unavailable.

28–29. A summary of the flares is given in Table 4.1, which is based on the GOES flare catalog[1]. The three flares are indicated over the GOES light curves (in 1–8 and 0.5–4 Å channels) in Figure 4.1. The duration of the three flares are marked by vertical pink stripes. The gray shaded region indicates an interval, when the GOES data were unavailable.

4.2.1 Temporal and spatial aspects

The temporal and spatial evolution in EUV 304 Å observations of the M2.0 (F1), M2.6 (F2), and X1.0 (F3) flares are presented in Figures 4.2, 4.4, and 4.5,

[1]https://www.ngdc.noaa.gov/stp/space-weather/solar-data/solar-features/solar-flares/x-rays/goes/xrs/goes-xrs-report_2014.txt

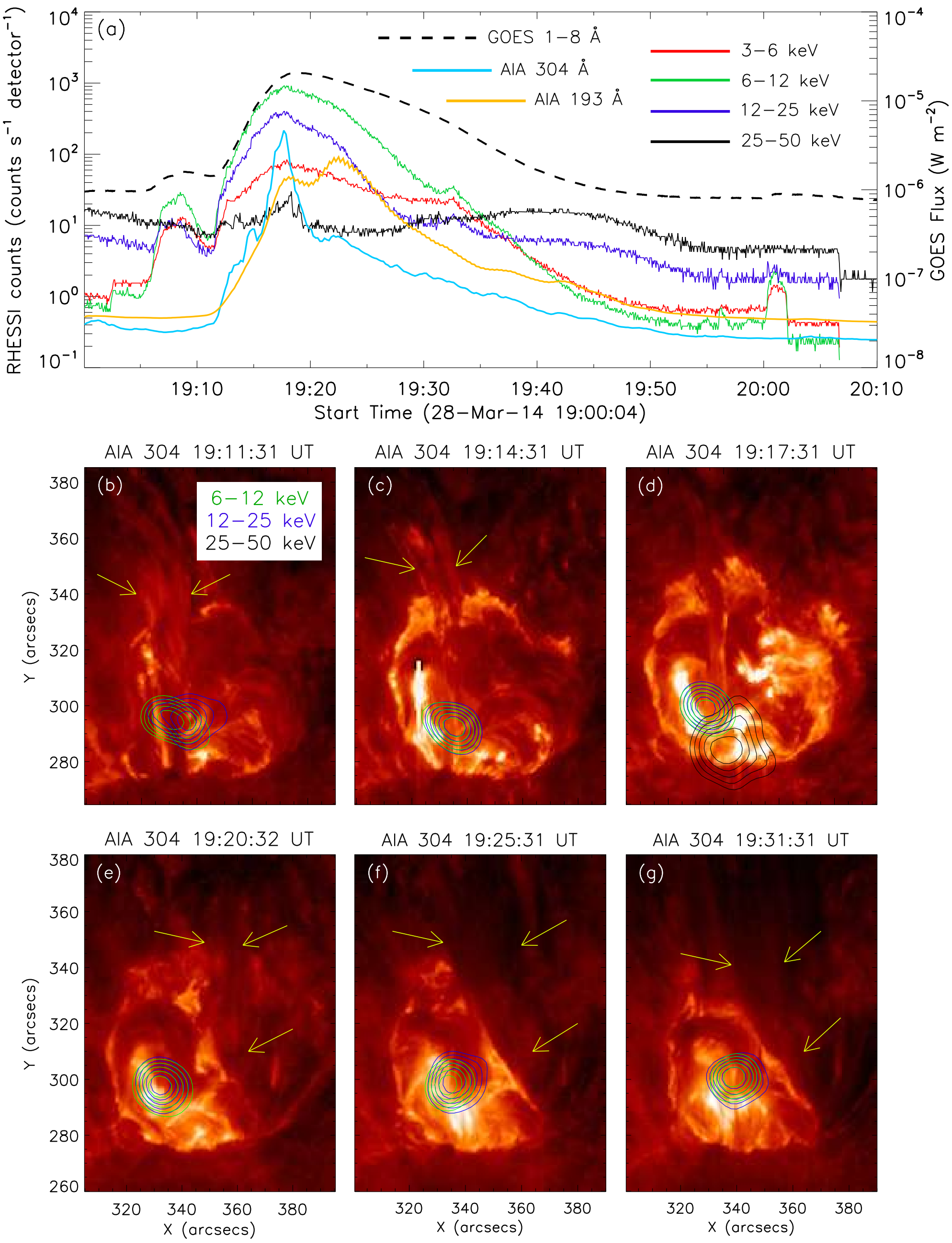

Figure 4.2: panel (a): RHESSI X-ray count rates in different energy bands between 3 and 50 keV energies are represented during the M2.0 event. The GOES flux profile in the 1–8 Å channel, AIA 193, and 304 Å light curves of the flaring region are also overplotted. Panels (b)–(g): evolution of the flare shown in AIA 304 Å images. The X-ray contours in 6–12, 12–25, and 25–50 keV are overplotted on EUV images. The X-ray images are reconstructed by the CLEAN algorithm with integration time of 20 s. The contours drawn are at 50%, 60%, 70%, 80%, and 90% of the peak flux in each image. The yellow arrows (except in panel (d)) indicate the plasma eruptions originating from the core region.

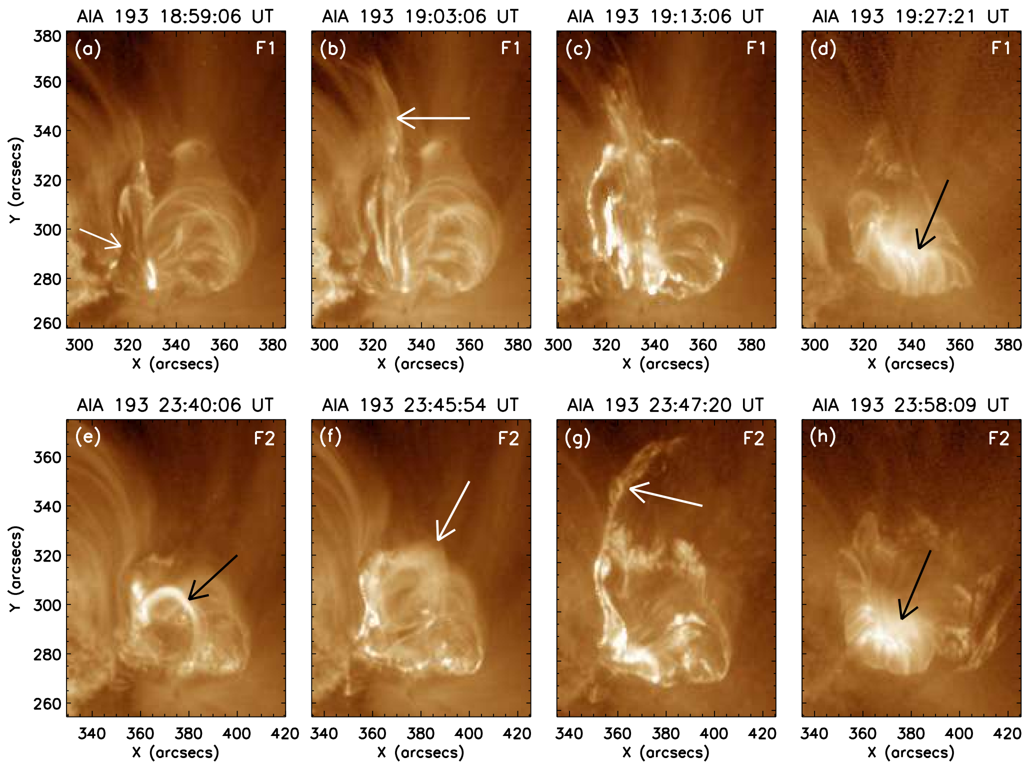

Figure 4.3: panels (a)–(d): evolution of the M2.0 flare (F1) in the AIA 193 Å images. In panel (a), we indicate an activated filament by an arrow with clear brightening at its base. Panel (b) shows the subsequent jet-like eruption of the filament. Panel (c) denotes the extended brightening within the flaring region, which marks the start of the impulsive phase of the flare. In panel (d), we indicate the compact post-flare loop system by an arrow. Panels (e)–(h): evolution of the M2.6 flare (F2) in the AIA 193 Å images. In panel (e), we mark a bright loop system in the core region observed prior to the flare. This loop system erupts subsequently in a coherent manner, which we indicate by an arrow in panel (f). Thereafter, the erupting structure evolves non-coherently. We mark the bright eastern part of the erupting structure by an arrow in panel (g). We indicate the compact, bright post-flare loop arcades in panel (h) by an arrow.

respectively. The panel (a) in these figures presents light curves of the flares, while panels (b)–(g) show their spatial evolution. The temporal evolution of the flares is studied with GOES 1–8 Å, AIA 304 Å, and RHESSI X-ray light curves. We reconstruct RHESSI X-ray light curves in various energy bands, viz., 3–6, 6–12, 12–25, 25–50, and 50–100 keV. For F1, we do not show the 50–100 keV light curve, because of the lack of significant X-ray flux above 50 keV energy. To explore the spatial structures in the flaring region and their evolution at the upper chromospheric level, we plot a few representative AIA 304 Å images overplotted by the RHESSI X-ray sources at various energy bands. We note that X-ray emission sources at 6–12 keV are exactly co-spatial with the lower energy sources at 3–6 keV, hence not shown in these figures. To understand the evolution of the spatial structures at the flaring corona, we show the EUV 193 Å images in Figures 4.3(a)–(d), (e)–(h), and 4.6 for F1, F2, and F3, respectively.

M2.0 flare

Before the beginning of the rise phase of F1, we observe a pre-flare enhancement in the X-ray light curves at ≈19:08 UT. We note that this pre-flare hump is absent in the AIA 304 Å light curve, which represents emission from the flaring region exclusively. This observation suggests that this pre-flare emission is not associated with the flaring event under analysis. We observe plasma eruption from the eastern part of the flaring region in the form of collimated stream (indicated by arrows in Figure 4.2, panels (b) and (c)) at the outset of F1. At the base of the collimated structure, we note X-ray emission upto 25 keV, shown by contours of different energy bands. During the peak of the flare (≈19:18 UT), the HXR source of 25–50 keV appears at the flaring core (shown by black contours in Figure 4.2(d)). After the flare peak, we observe eruption of cool (i.e., dark) plasma from the western part of the core region (shown by arrows in Figures 4.2(e)–(g)). During this interval, the X-ray sources upto 25 keV energies are observed as a single source, suggesting X-ray production from a compact and dense system of coronal loops. The X-ray sources in the decay phase (Figure 4.2, panels (f) and (g)) further confirm this scenario as the X-ray emission is observed to originate above the closely-packed post-flare loop system.

The evolutionary stages of F1 in the EUV 193 Å images are shown in Figures 4.3(a)–(d). Prior to the flare, we detect an activated filament (indicated by arrow in Figure 4.3(a)) with clear signature of activity in the form of brightening at its base. Subsequently, the filament erupts in a jet-like manner (marked by arrow in Figure 4.3(b)) with morphological similarity with the collimated stream observed in EUV 304 Å images (see Figure 4.2, panels (b) and (c)). The start of the impulsive rise phase of the flare can be discerned in the form of extended brightening over the flaring region (Figure 4.3(c); see also Figure 4.2(a)). Afterwards, we observe the formation of compact post-flare loop arcades in the core region (shown by arrow in Figure 4.3(d)).

M2.6 flare

The evolutionary stages of F2 are shown in Figure 4.4 through the EUV 304 Å image sequences. Like F1, in this case also, we observe a single X-ray source throughout the flare evolution. Furthermore, the X-ray sources from lower to higher energies (e.g., 6–12, 12–25, 25–50, and 50–100 keV) are observed to be co-spatial. During the peak of the

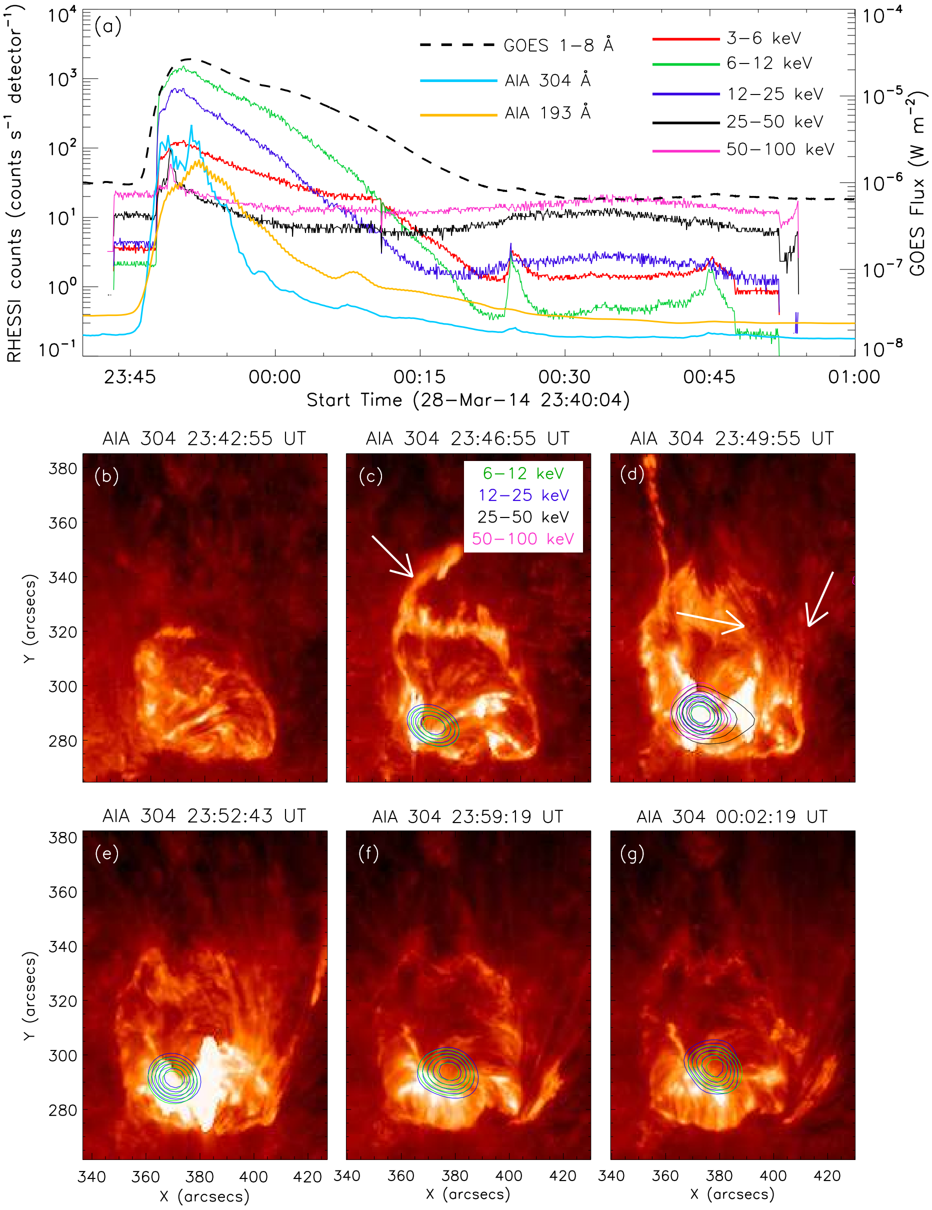

Figure 4.4: panel (a): RHESSI X-ray count rates in different energy bands between 3 and 100 keV are illustrated during the M2.6 event. The GOES flux profile in the 1–8 Å channel, AIA 193, and 304 Å light curves of the flaring region are also overplotted for comparison with the X-ray light curves. Panel (b): the pre-flare configuration of the flaring region observed in AIA 304 Å, devoid of significant X-ray emissions. Panels (c)–(g): evolution of the flare in AIA 304 Å observations along with the RHESSI X-ray sources overplotted on the EUV images. In panels (c) and (d), we indicate the plasma structures to be erupted from the eastern and western parts of the flaring region, respectively. The X-ray contours in 6–12, 12–25, 25–50, and 50–100 keV are overplotted on the EUV images. The X-ray images are reconstructed by the CLEAN algorithm with integration time of 20 s. The contours drawn are at 50%, 60%, 70%, 80%, and 90% of the peak flux in each image.

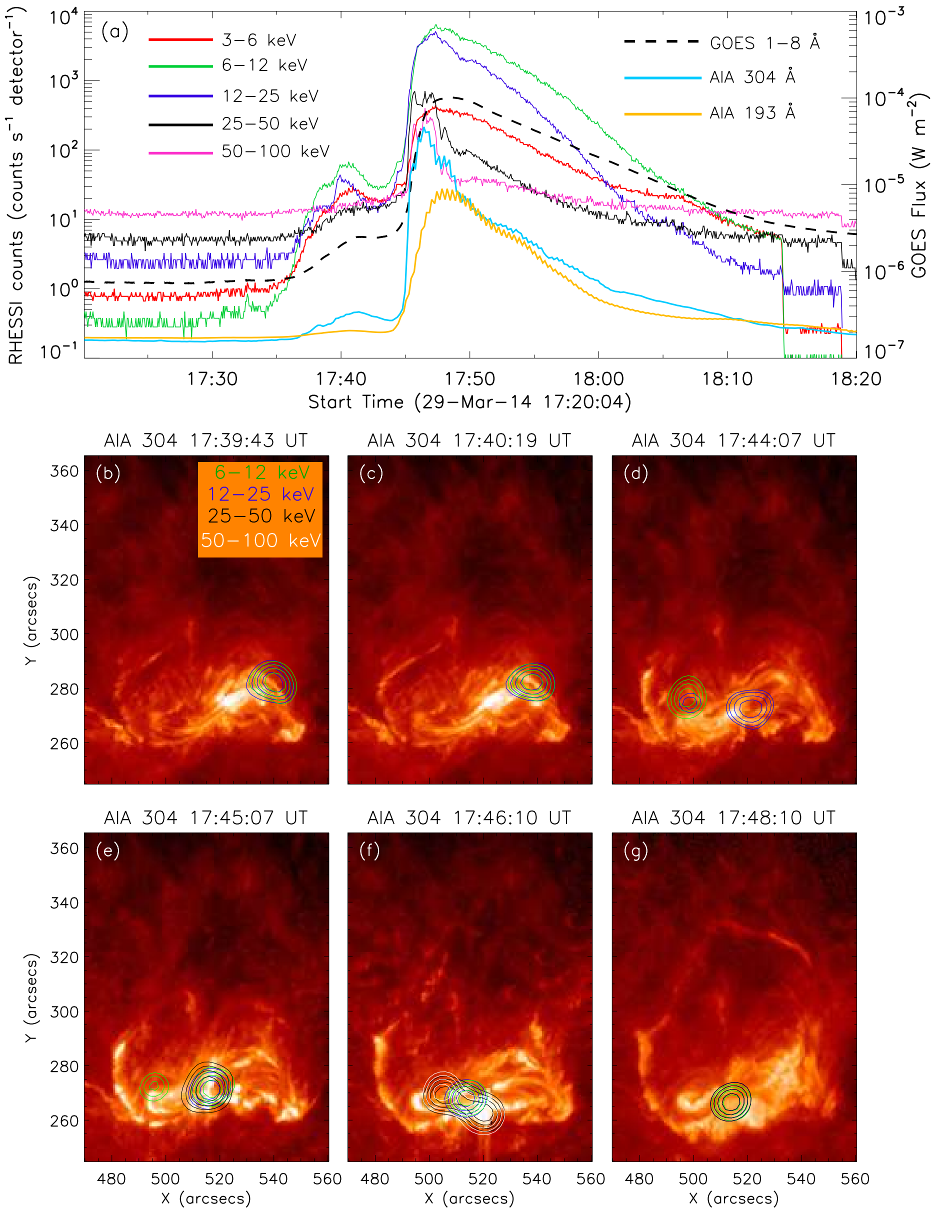

Figure 4.5: panel (a): RHESSI X-ray count rates in different energy bands between 3 and 100 keV are represented during the X1.0 event. GOES flux profile in the 1–8 Å chanel, AIA 193, and 304 Å light curves of the flaring region are overplotted. Panels (b)–(g): AIA 304 Å observations showing the evolution of the flare. X-ray contours in 6–12, 12–25, 25–50, and 50–100 keV are overplotted on the EUV images. The X-ray images are reconstructed by the CLEAN algorithm with integration time of 20 s. The contours drawn are at 60%, 70%, 80%, and 90% of the peak flux in each image.

flare (≈23:50 UT), the X-ray sources in the energy band of 50–100 keV are observed to appear in the core region (Figure 4.4(d)). Thereafter, the 50–100 keV source disappears, while the X-ray emission in the lower energy bands persists (Figures 4.4(e)–(g)). We note a double peak structure in the AIA 304 Å light curve during the peak time of the flare (see Figure 4.4(a)). This double peak structure suggests two successive episodes of intense brightening that accompanies eruptions from the eastern and western parts of the flaring region, respectively (indicated by arrows in Figure 4.4, panels (c) and (d)), which ultimately result into the flaring intensity of M2.6 class. Notably, the eruptions in this case are not jet-like ejections as in the case of F1.

In Figures 4.3(e)–(h), we show the EUV 193 Å images presenting the evolutionary stages of F2. Prior to the flare, we observe a bright, activated loop system in the core region (indicated by arrow in Figure 4.3(e)). This loop structure erupts subsequently (marked by arrow in Figure 4.3(f)) in a nearly coherent manner, which also marks the beginning of the impulsive phase of the flare (see Figure 4.4(a)). Thereafter, the erupting loop system loses its coherency and we mark its bright eastern part by an arrow in Figure 4.3(g). Later on, the dense and compact post-flare loop arcades are observed to form in the core region (indicated by arrow in Figure 4.3(h)).

X1.0 flare

The evolution of the X1.0 flare (F3) is shown by a few representative AIA 304 Å images in Figures 4.5(b)–(g). Prior to the impulsive phase of the event, starting at ≈17:44 UT, we observe clear signature of pre-flare activity persisting for ≈8 min (≈17:36–17:44 UT). This pre-flare phase is discernible in all the X-ray and EUV light curves (Figure 4.5(a)). This pre-flare activity is observed in the AIA images as enhanced brightening from the western part of the core region, which also emits X-ray sources upto 25 keV (Figure 4.5, panels (b) and (c)). Thereafter, the X-ray sources evolve at two separate locations and we observe emission upto 25 keV from both the eastern and western parts of the flaring core region (Figure 4.5(d)). The X-ray emission in the 6–12 keV energy range persists in the eastern part of the core, whereas, the strong emission in the energy range of 25–50 keV is observed to appear in the western part of the flaring core (Figure 4.5(e)). During the peak of HXR light curves, we observe clear X-ray sources in the 50–100 keV energy band. Importantly, this high energy source presents elongated structure with two distinct centroids (Figure 4.5(f)). Subsequently, the X-ray emission upto 50 keV persists, observed as a single source structure in multiple energy bands (Figure 4.5(g)).

The evolution of F3 in the EUV 193 Å images is presented in Figure 4.6. Similar to the EUV 304 Å observations, in these images also, we observe clear signature of enhanced brightening from the western part of the core revealing the pre-flare activity (indicated by arrows in Figure 4.6, panels (a) and (b)). Subsequently, this pre-flare enhancement spreads over the whole core region (Figure 4.6, panels (c) and (d)). During the main phase of the flare, intense and widespread flare emissions are observed from the core (Figure 4.6,

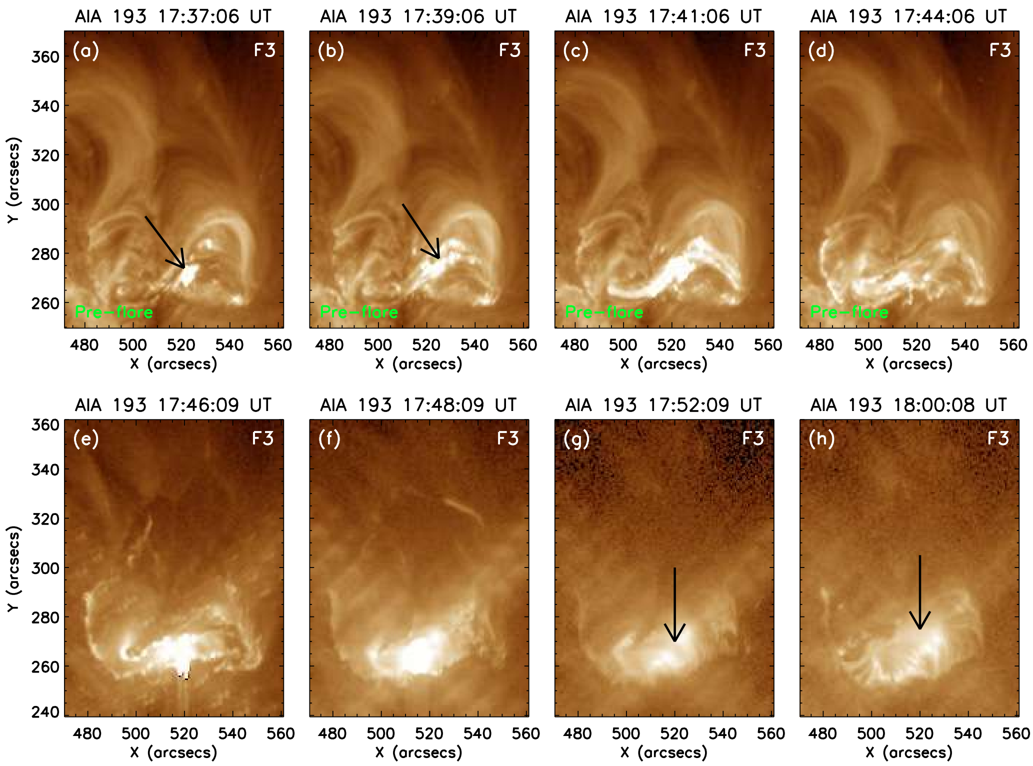

Figure 4.6: evolution of the X1.0 flare (F3) in the AIA 193 Å images. Panels (a)–(d) denote the morphological changes during the pre-flare phase of the flare, while the panels (e)–(h) correspond to the main phase of the flare. We note a pre-flare activity in the form of intense brightening from the western part of the core, which we indicate by arrows in panels (a) and (b). Subsequently, this pre-flare intensity enhancement spreads over a large area within the core region (panels (c) and (d)). During the main phase of the flare, enhanced intensity is observed from an extended part of the core region (panels (e) and (f)). Afterwards, the dense post-flare loop arcades are observed to form, which gradually gets elongated over a broad area of the core, indicated by an arrows in panels (g) and (h).

panels (e) and (f)). Thereafter, the post-flare loop arcades are observed to form (shown by arrow in Figure 4.6(g)), which gradually gets denser, brighter, and are observed to extend over a large area of the core (marked by arrow in Figure 4.6(h)).

4.2.2 RHESSI X-ray spectroscopy

The results obtained from the spectral fit of X-ray emission from the flaring region are presented in Figures 4.7(a), (b), and (c) for F1, F2, and F3, respectively. For F1, the GOES flare peak (≈19:18 UT on 2014 March 28) coincides with the HXR (25–50 keV) peak. A high value of electron spectral index (i.e., δ=8.7) indicates mild non-thermal component of flaring X-ray emission. During the peak of F2, the electron spectral index

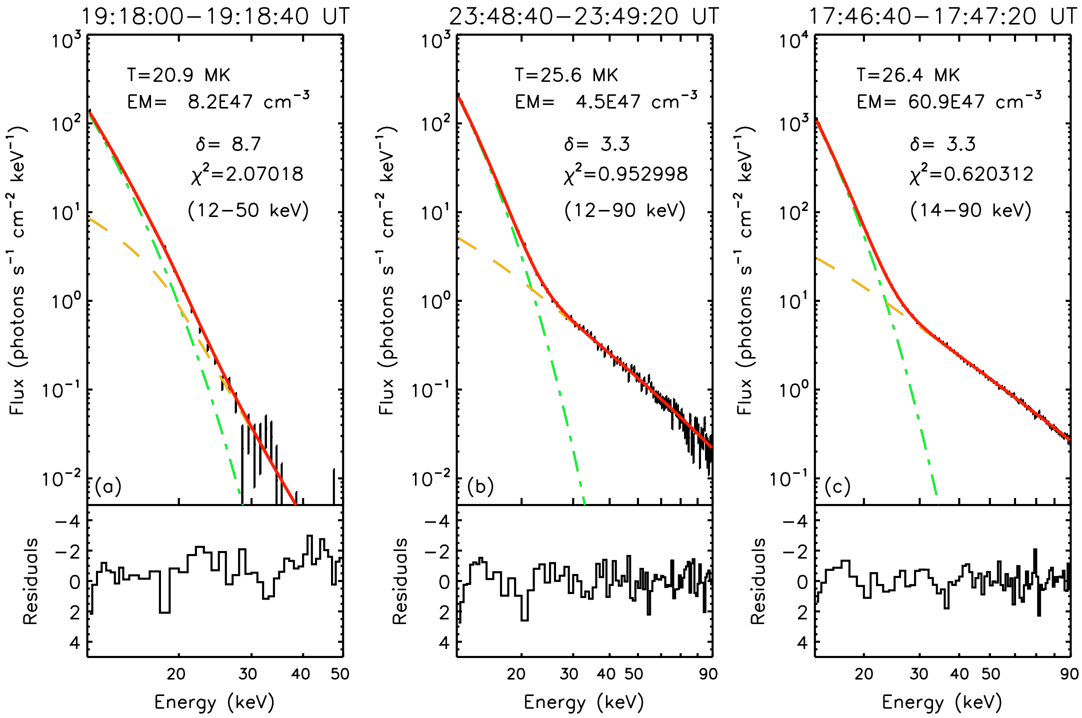

Figure 4.7: results of RHESSI X-ray spectral fit, along with their residuals, are shown for all the events under analysis. We use an isothermal model (shown by green dash-dotted line) for thermal fit and thick-target Bremsstrahlung model (shown by yellow dashed line) for non-thermal fit of the observed spectra. The red solid line indicates the sum of the two components. Each spectrum is accumulated with an integration time of 40 s using the front segments of the detectors 1–9 (except 2 and 7). The energy ranges selected for the spectral fit are annotated in the respective panels. In panels (a), (b), and (c), we show the spectra at the peak of the HXR emissions during the M2.0, M2.6, and X1.0 flares, respectively.

decreases to 3.3, indicating a much harder non-thermal spectrum compared to F1. From the thermal spectral fit, we obtain temperature of the flaring region as ≈25.6 MK, which is higher than the temperature (≈20.9 MK) during the peak of F1. During F3, the hardness of the spectrum remains almost the same as that of F2. However, the emission measure (≈61×10^{47} cm^{-3}) increases by an order of magnitude during F3 compared to the previous two events (see Figures 4.7(a)–(c)). This indicates a significant enhancement in the electron density of hot (T ≈26 MK) plasma within the flaring volume.

4.3 Structure and evolution of magnetic fields

We show the HMI continuum and LOS magnetogram images of the AR 12017 prior to F1 in Figures 4.8(a) and (b), respectively. The leading part of the AR consists of prominent

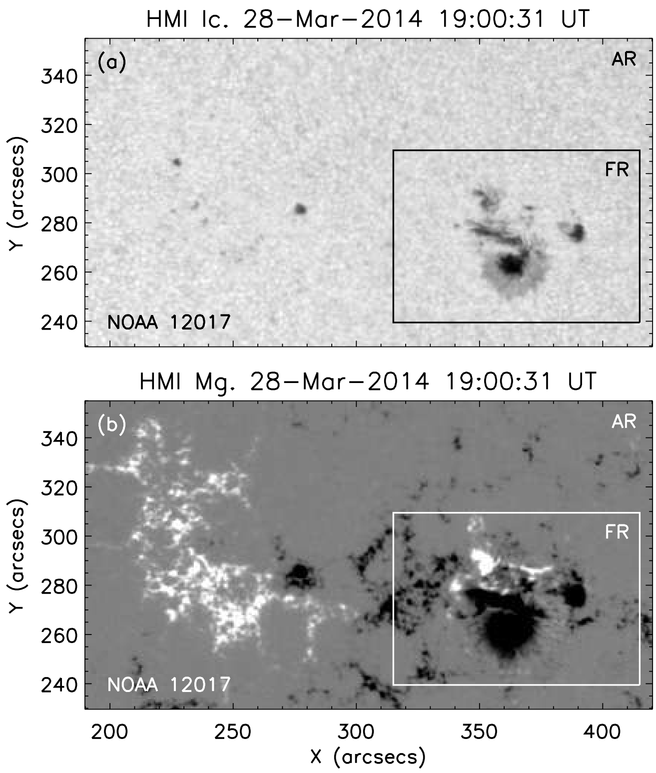

Figure 4.8: panel (a): HMI continuum intensity image of the NOAA AR 12017. We observe a large sunspot area in the leading part of the AR, which we mark by a black box. The flares of our study occur within this marked area of the AR. Hence, we term it as 'Flaring Region' (FR). We observe dispersed small sunpots in the trailing part of the AR. Panel (b): the HMI LOS magnetogram image co-temporal with the intensity image in the upper panel. Within the FR (marked by a white box), we observe a strong negative polarity region, accompanied by weak, intermixed positive polaities, located north of it.

sunspot groups of predominantly negative polarity (marked by black and white boxes in Figure 4.8, panels (a) and (b), respectively), which is the source of the eruptive flares under analysis. Hence, we term it as the 'Flaring Region' (FR). On the trailing part of the AR, we observe sparsely located small sunspots (Figure 4.8(a)) with dispersed flux of predominantly positive polarity (Figure 4.8(b)).

4.3.1 Photospheric magnetic fields

We analyze the structural and temporal evolution of photospheric magnetic field of the flaring region in Figure 4.9. To examine the magnetic flux changes quantitatively, we plot the spatial variations of positive and negative magnetic flux of the region of interest (shown in Figures 4.9(b)–(m)). In Figure 4.9(a), we provide the time profiles of the integrated magnetic fluxes through the selected area (see Figures 4.9(b)–(m)) together with

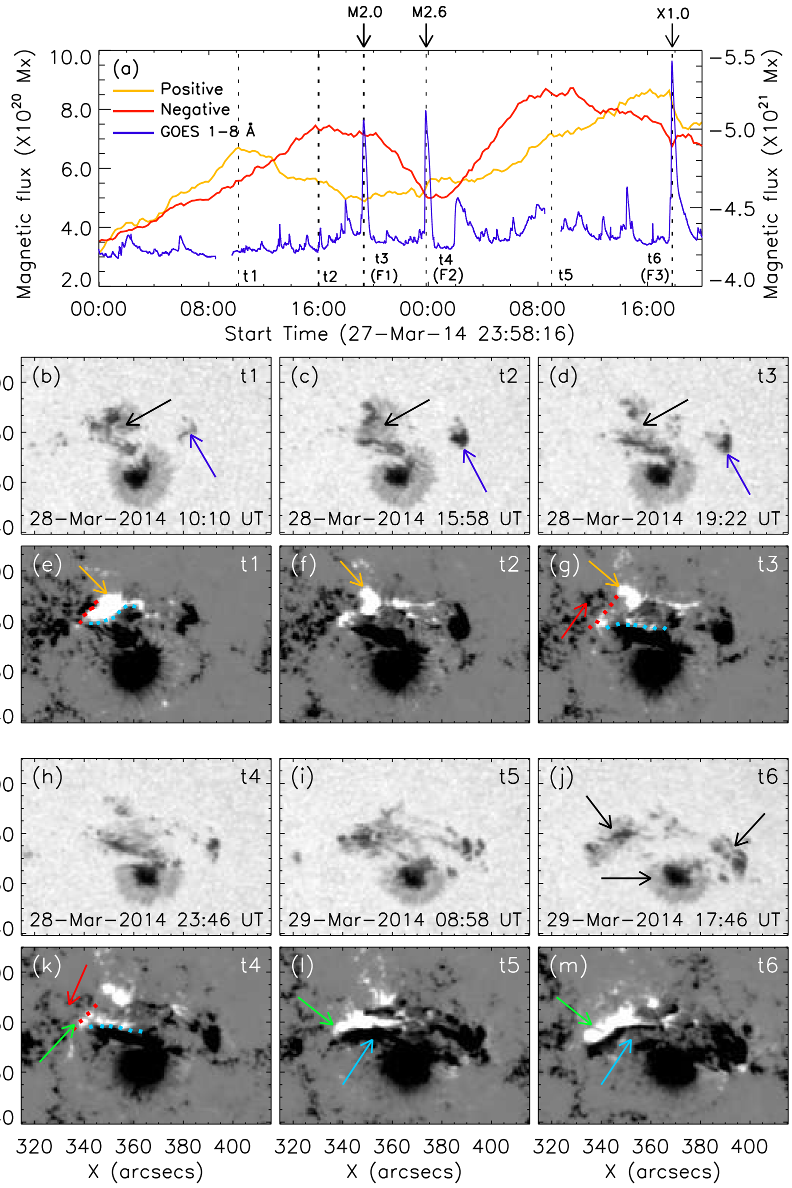

Figure 4.9: panel (a): the temporal evolution of magnetic flux obtained from the flaring region along with the GOES SXR light curve in 1–8 Å channel. Panels (b)–(d): intensity images of the flaring region at three instances t1, t2, and t3 as marked in panel (a). The black arrows denote small-scale changes in the northern sunspot group, while the blue arrows indicate growth of a compact sunspot group. Panels (e)–(g): LOS magnetogram images co-temporal with continuum observations (shown in the previous row) at times t1, t2, and t3. The yellow and red arrows are used to indicate the changes in postive and negative fluxes, respectively. Panels (h)–(j): intensity images of the flaring region at t4, t5, and t6 as marked in panel (a). The arrows in panel (j) indicate three distinct sunspot groups. Panels (k)–(m): LOS magnetogram images for t4, t5, and t6 co-temporal with corresponding continuum observations (shown in the previous row). The green and sky blue arrows are used to indicate the changes in postive and negative fluxes, respectively. The red and sky-blue dotted lines in panels (e), (g), and (k) denote the PILs in the eastern and western parts of the flaring region, respectively.

the GOES 1–8 Å SXR light curve. The time profiles of magnetic fluxes start from 00:00 UT on 2014 March 28 to 20:00 UT on 2014 March 29 (≈44 hr) covering all the flare events under analysis. Also, the chosen interval includes a time span of ≈19 hr before F1 to examine the build-up of pre-flare photospheric flux in detail.

In Figure 4.9(a), we select six different epochs (t1, t2, t3, t4, t5, and t6) to explore the spatial changes in the photospheric magnetic field distribution. Among these epochs t3, t4, and t6 are selected at the peak time of the flares under analysis. The continuum and LOS magnetogram images during the epochs (t1–t6) are presented in Figures 4.9(b)–(m). We observe substantial structural changes in the photospheric magnetic field of the flaring region over the selected interval of ≈44 hr (see Figures 4.9(b)–(m)).

In Figures 4.9(b)–(g), we show the evolution of flaring region with co-temporal continuum and magnetogram observations for three epochs t1, t2, and t3, which present magnetic field changes prior to F1. The inspection of these images reveals an increase followed by decrease of sunspot area in the northern sunspot group (shown by black arrows in Figures 4.9(b)–(d)). We also observe growth of compact sunspot groups on the western side of the main sunspot group (indicated by dark-blue arrows in Figures 4.9(b)–(d)). Figures 4.9(e)–(g) show the co-temporal LOS magnetogram observations corresponding to continuum images in Figures 4.9(b)–(d). In Figures 4.9(e) and (g), we focus on the eastern and western PILs marked by red and sky-blue dotted lines, respectively. The yellow arrows indicate a gradual decrease of positive flux near the eastern PIL (Figures 4.9(e)–(g)), whereas the red arrows indicate subsequent decrease of negative flux (see Figures 4.9(g) and (k)). We further note that the orientation of the western PIL changes from t1 to t3 (see the sky-blue dotted lines in Figures 4.9(e) and (g)).

In Figures 4.9(h)–(m), we present the continuum and LOS magnetogram observations showing the evolution of the flaring region during the epochs t4, t5, and t6, which are used to explore the changes in the photospheric magnetic field structures associated with F2 and F3. Notably, after F2, the photospheric configuration of sunspot groups and associated magnetic fields at the northern region exhibit striking changes (see Figures 4.9(h)–(j)). We observe that, during the interval between F2 and F3, the northern sunspot group with relatively compact configuration undergoes rapid expansion, which results in its fragmentation into three distinct parts (indicated by arrows in Figure 4.9(j)). The magnetogram images co-temporal with the continuum observations are shown in Figures 4.9(k)–(m). The eastern and western PILs are indicated by red and sky-blue dotted lines, respectively in Figure 4.9(k). We observe clear features of flux cancellation and emergence. The sky-blue arrows indicate a substantial cancellation of negative flux near the western PIL, whereas the green arrows indicate a gradual increase of postive flux near the

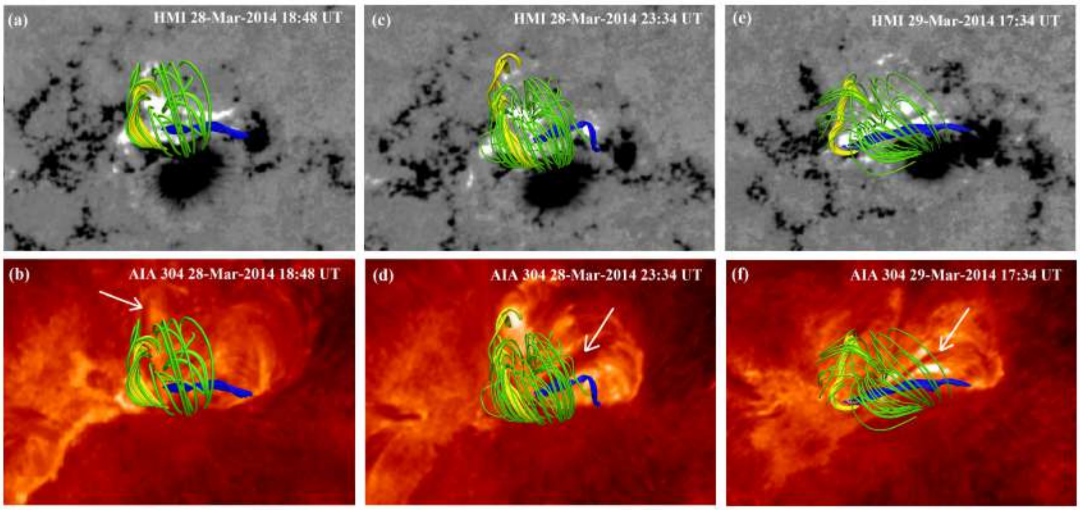

Figure 4.10: the pre-flare coronal magnetic structures obtained through NLFFF modeling, presented over the photospheric radial magntic fields (top panels) and the AIA 304 Å observations (bottom panels) in and around the flaring region for all the events. The panels (a) and (b), (c) and (d), (e) and (f) denote the epochs corresponding to F1, F2, F3, respectively. We note the existence of two flux ropes, shown by yellow and blue field lines, to reside over the eastern and western PILs of the flaring region (top panels; see Figure 4.9), respectively. The flux ropes are enveloped by the low-lying bipolar green field lines. In the bottom panels, we mark the filaments by arrows, observed through EUV imaging.

same PIL. These observations showing flux emergence and cancellation are in agreement with the qualitative estimation shown in Figure 4.9(a).

4.3.2 Magnetic configuration of flaring corona

In Figure 4.10, we represent the pre-flare coronal magnetic structures in and around the flaring region obtained through NLFFF extrapolation. The first, second, and third columns denote the epochs corresponding to F1, F2, and F3, respectively. In the top panels, we show the extrapolated coronal field lines taking the HMI SHARP CEA radial magnetic fields as the background, whereas, in the bottom panels, we show the AIA 304 Å images in the background using the visualization software VAPOR (Li *et al.*, 2019). In all the cases, we find existence of two flux ropes lying over the compact eastern and western PILs of the flaring region (see Figure 4.9), shown by yellow and blue field lines, respectively. The flux ropes are encompassed by the low-lying bipolar field lines (shown in green). The sequential eruptions of the flux ropes and neighboring core field gave rise to the eruptive flares under analysis. We observe filaments in the AIA 304 Å images,

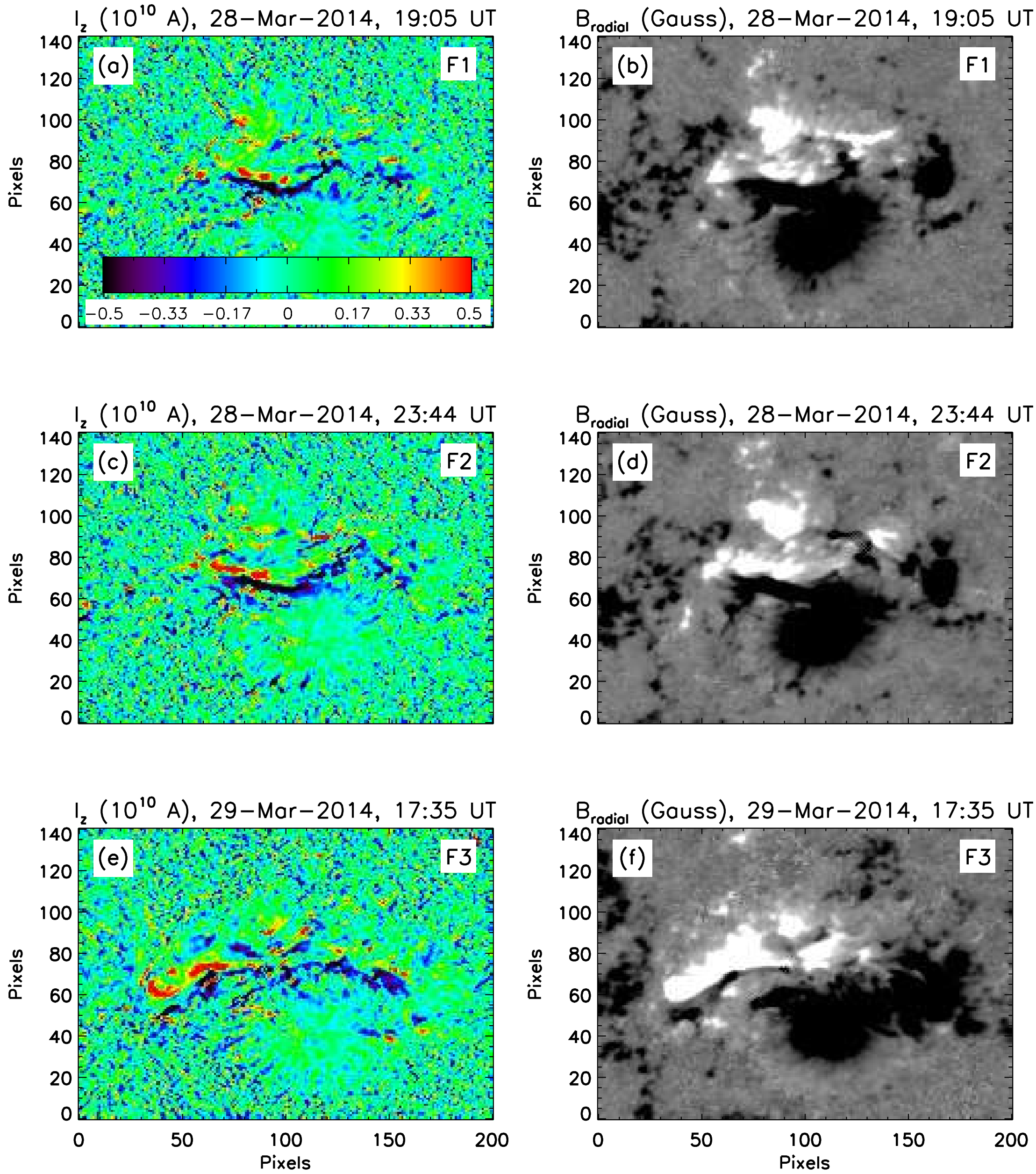

Figure 4.11: the comparison of photospheric longitudinal current (I_z; first column) and the radial component of the magntic field (B_{radial}; second column) before the onset of the flares. The panels (a) and (b), (c) and (d), (e) and (f) correspond to F1, F2, F3, respectively. In panel (a), we denote the colorbar corresponding to the distribution of I_z in panels (a), (c), and (e). We saturate the I_z and B_{radial} values to $\pm 0.5\times10^{10}$A and $\pm$500G, respectively in all the panels. We note that the current distribution is strong near the western PIL of the flaring region (see Figure 4.9) and it gets elongated along the PIL before F3. The morphological changes in the longitudinal current distribution are similar to the structural changes in the distribution of the radial magnetic field component (see panels (e) and (f)).

which are indicated by arrows in the bottom panels. The detailed investigation on the modeling of coronal magnetic fields during the three events is in progress and will be presented in a subsequent study.

4.4 Morphology and evolution of photospheric longitudinal currents

We show the morphological changes associated with the photospheric longitudinal current in response to the magnetic field changes in Figure 4.11. On the photosphere, the vertical component of the electric current density (i.e., J_z) can be obtained from the horizontal magnetic field components (i.e., B_x and B_y) using the Ampere's law (Kontogiannis *et al.*, 2017; Fleishman and Pevtsov, 2018; Fursyak *et al.*, 2020):

$$J_z = \frac{1}{\mu_0}\Big(\frac{dB_y}{dB_x} - \frac{dB_x}{dB_y}\Big). \tag{4.1}$$

The magnetic field components (B_z, -B_y, B_x) in Heliographic Cartesian Coordinate can be approximately obtained from the corresponding field components (B_r, B_θ, B_ϕ) in the Heliocentric Spherical Coordinate (Gary and Hagyard, 1990). In order to calculate the longitudinal current (I_z) from longitudinal current density (J_z), we need to multiply J_z with the area of one pixel, i.e., 13.14×10^{10} m^2. In Figure 4.11, we present the distribution of current (i.e., I_z) along with the structure of the radial component of magnetic field (i.e., B_r) within the flaring region before the start of the flares. The top, middle, and bottom panels of Figure 4.11 correspond to F1, F2, and F3, respectively. For better visualization, we saturate the current values at ±0.5×10^{10} A in all the panels. The color code for all the I_z-maps (Figures 4.11(a), (c), and (e)) is shown by a colorbar in Figure 4.11(a). We observe significant amount of current concentration along the western PIL (see the sky-blue dotted lines in Figures 4.9(e), (g), and (k)) of the flaring region for all events. Notably, the negative current largely dominates the positive current in all the cases. Between F2 and F3, the western PIL undergoes elongation (Figure 4.11(f); see also Figures 4.9(k)–(m)). In a similar way, the region of strong photospheric currents that predominantly exists at the flaring core region, is observed to show an extended morphological structure prior to F3 (see Figures 4.11(a), (c), and (e)).

4.5 Onset of eruption

For a quantitative understanding of the eruption from the flaring core, we present the time-slice diagrams in Figure 4.12. The Figure 4.12, panels (a) and (b), (c) and (d),

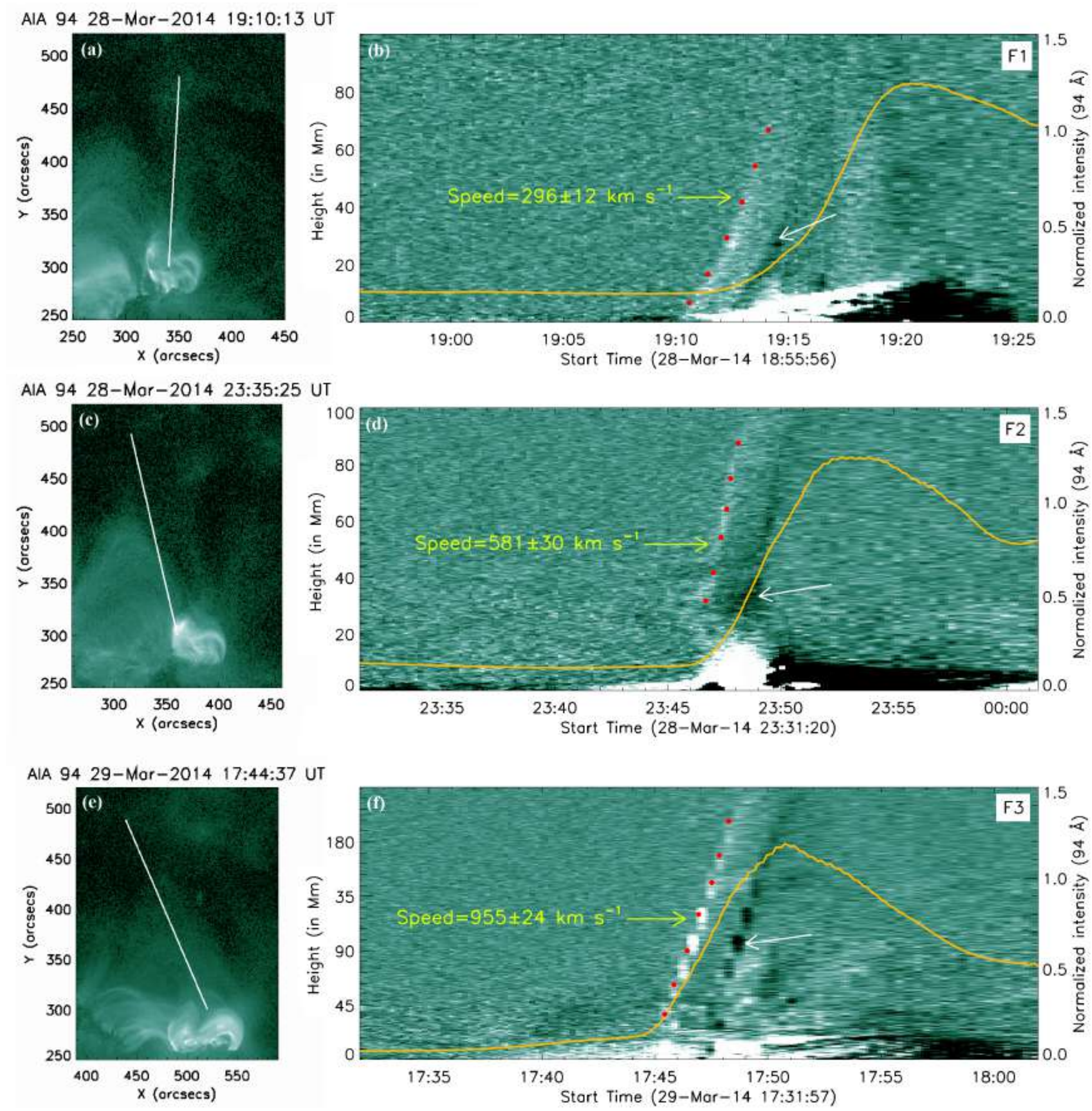

Figure 4.12: the evolutionary stages of the eruption of hot plasma structures from the core flaring region. The panels (a) and (b), (c) and (d), (e) and (f) correspond to F1, F2, F3, respectively. The left column shows the direction of the slits over AIA 94 Å direct images, along which we calculate the height-time profiles of the eruptions. In the right column, we show the time-slice diagrams obtained from the AIA 94 Å running difference images by tracking the intensity variation along the slits. The erupting hot plasma structures are indicated by red dots in panels (b), (d), and (f). The speeds of the erupting structures are annotated in these panels with the corresponding uncertainty in the measurements. We note that the speeds are gradually increasing from F1 to F3. Following the hot plasma eruption, we observe the eruption of a dark (i.e, cool) structure, which we mark by white arrows in these panels. The flare intensity profiles in the AIA 94 Å channel are also overplotted by orange curves.

(e) and (f) correspond to F1, F2, F3, respectively. In the left column of this figure, we show the direction of the slits, along which we observe significant eruptive features. In the right column, we show the corresponding time-slice diagrams in AIA 94 Å running difference images, constructed by tracking the eruptive signatures along the slits. We mark the erupting hot plasma structures by red dots in Figures 4.12(b), (d), and (f). We note that the speeds of the hot plasma ejections show an increasing trend from F1 to F3 (i.e., ≈296, 581, and 955 km s^{-1}). Following the hot plasma eruption, an eruption of dark (i.e., cool) material ensues, which we indicate by white arrows. To compare the eruption of the plasma structure with the temporal evolution of the flare, we overplot the AIA 94 Å flare light curves in all the panels. We note that the rise of the 94 Å intensity is near simultaneous with the onset of the hot plasma eruption from the flaring core. Subsequently, the eruptions from the source region result into CMEs. According to LASCO CME catalog[2], the linear speed of CMEs within LASCO FOV associated with F1, F2, and F3 are 420, 503, and 528 km s^{-1}, respectively.

4.6 Evolution of free magnetic energy

Our analysis is comprised of holomologous eruptive flares, which show gradully increasing SXR intensities (M2.0, M2.6, and X1.0). To investigate this scenario in the framework of storage and release process of free magnetic energy associated with the complex magnetic configuration of the AR, we calculate the temporal evolution of free energy during an interval of ≈30 hr, which is demonstrated in Figure 4.13. The free magnetic energy (E_F) is defined as the difference between the non-potential (E_{NP}) and potential (E_P) magnetic energies. i.e.,

$$E_F = E_{NP} - E_P, \tag{4.2}$$

where E_{NP} is calculated from the magnetic fields obtained through the NLFFF extrapolation. The different forms of energies can be calculated from the magnetic field information using the following relation

$$E = \int_V \frac{B^2}{8\pi} dV. \tag{4.3}$$

We observe that there is prominent decrease of free magnetic energy due to the occurrence of the flaring events. We calculate the decrease to be 17%, 9.5%, and 38% for the events M2.0, M2.6, and X1.0, respectively. There is a data gap in GOES light curve (in the 1–8 Å channel) from 08:30 UT to 09:40 UT on 2014 March 29, which is indicated by a hatched region. To confirm if the GOES SXR flux enhancement is associated with the

[2] https://cdaw.gsfc.nasa.gov/CME_list/UNIVERSAL/2014_03/univ2014_03.html

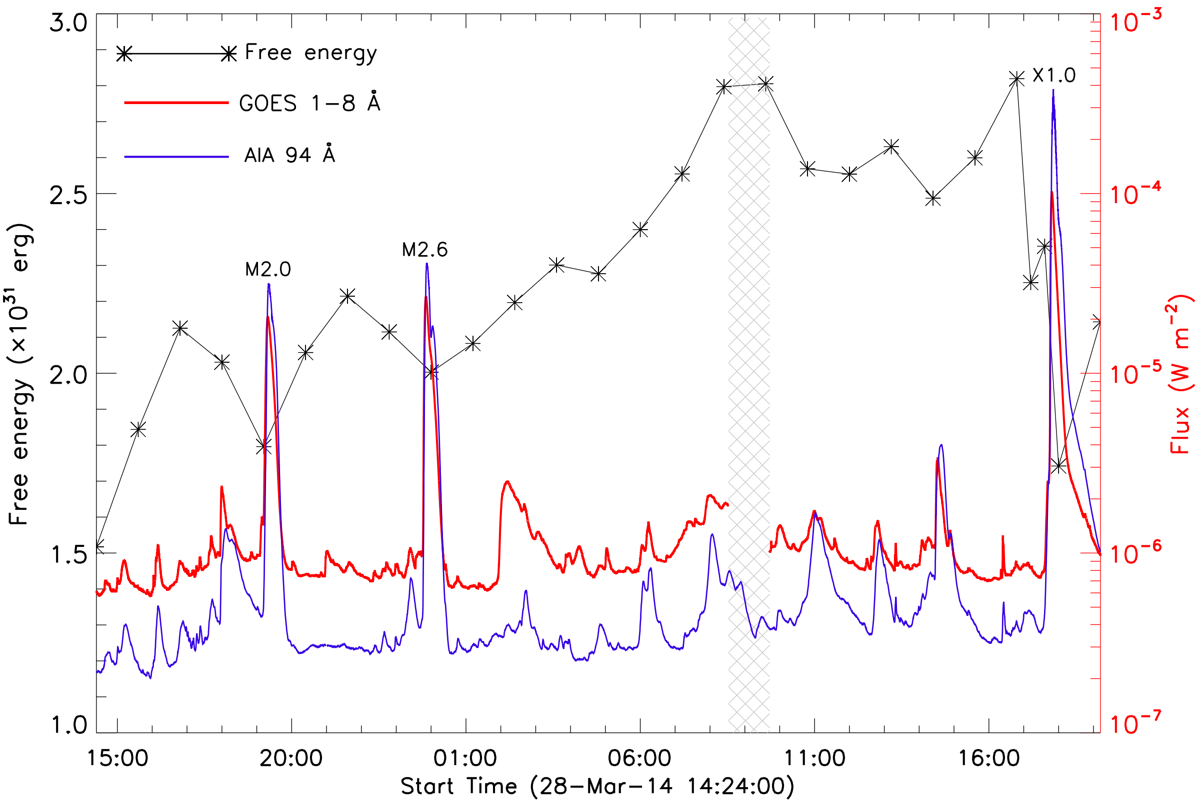

Figure 4.13: the evolution of free magnetic energy during an interval of ≈30 hr encompassing all the flares under study. The free energy is calculated in the coronal volume encompassing the AR, taking the HMI SHARP CEA cutout as the photospheric boundary. We also plot full disk GOES light curve in the 1–8 Å channel. The hatched region shows an interval during which GOES data were unavailable. To complement the data gap, we plot EUV 94 Å intensity curve obtained from the AIA recorded from the AR.

flaring activity in the AR 12017 of our interest, we show the AIA 94 Å light curve deduced exclusively from the AR. It is observed, that in general, the EUV light curve matches well with the GOES light curve and the prominent SXR peaks represent activity in the AR.

4.7 Discussion

In this study, we explore the multi-wavelength evolution of three homologous flaring events of successively increasing intensities and associated energy release processes. The events occur during 2014 March 28–29 in NOAA AR 12017 within an interval of ≈24 hr. The flares are triggered by the eruptions of flux ropes from the core of the AR. The importance of this study lies in the investigation of the intrinsic coupling of magnetic fields and associated processes from the photosphere to the corona that resulted into the repetitive build-up of compact MFRs and their subsequent eruptions, observed in the form of homologous eruptive flares of successively increasing intensities. The important observational aspects of this study are summarized as follows.

1. According to the GOES observations, the durations of the flares of our analysis are 22, 14, and 19 minutes for M2.0 (F1), M2.6 (F2), and X1.0 (F3) flares, respectively (see Table 4.1). A statistical analysis of almost 50,000 GOES SXR flares during the period 1976–2000 is presented in Veronig *et al.* (2002). Their analysis reveals that the average values of the duration for M and X class flares are 24 and 30 minutes, respectively. In view of this, the duration of F1 is close to the value as revealed in the study of Veronig *et al.* (2002), while F2 and F3 are of shorter duration. Notably, although F1 and F2 are of comparable intensity and homologous in nature, the duration of F2 is significantly smaller than that of F1. On the other hand, F3, despite being a large X-class flare, exhibits shorter duration compared to F1.

2. Inspection of the RHESSI X-ray images in multiple energy bands within the energy range of 3–100 keV during the evolution of F1 and F2 reveals a single X-ray source persisting throughout the flaring intervals. In both the events, the X-ray emissions are observed to come from the dense and closely-packed coronal loop system. The X-ray observations during the third event reveal emissions from different spatial locations within the flaring region (see Figure 4.5). During the onset of the impulsive phase of the third flare, we observe X-ray emissions from both the eastern and western parts of the flaring region (Figure 4.5, panels (d) and (e)). Notably, conjugate X-ray sources with two distinct centroids in the 50–100 keV energy range are observed within the core region during the peak of the X1.0 flare (Figure 4.5(f)). The origin of these conjugate X-ray sources is likely to be caused by the deposition of energy by the energetic electrons at the footpoints of the post-reconnected loop system, as depicted in the standard flare model (see e.g., Joshi *et al.*, 2009).

3. We observe significant cancellation of magnetic fluxes (both postive and negative) near the PILs within the flaring region (see Figure 4.9 and Section 4.3.1). A detailed comparison of HMI magnetograms and EUV images (see Figures 4.2–4.6 and Figure 4.9) of the flaring region reveals that the source region of eruptions are spatially linked to compact PILs within the core where flux ropes lie (see Figure 4.10). In particular, we observe significant magnetic flux changes near the eastern PIL before F1 and F2, whereas, the change of flux is maximum near the western PIL before F3 (see Figure 4.9). The EUV observational results reveal that the eruptions initiate from the eastern PIL during F1 and F2, whereas during F3, the significant portion of the eruption gets triggered from the western PIL. Thus, our observations

imply a precise link between the location of flare onset and the region of prominent flux variations. The coupling between photospheric and coronal magnetic activity as a driver for flux rope eruption is consistent with the scenario proposed in the 'tether-cutting' model (Moore and Roumeliotis, 1992; Moore *et al.*, 2001) for solar eruptions.

4. The sequential eruptions of the flux ropes from the flaring core give rise to corresponding CMEs. The inspection of the series of AIA 94 Å running difference images reveals eruptions of hot coherent plasma structures (i.e., heated flux ropes) from the core region (Figure 4.12). We note that the speed of the flux rope eruptions in the source region, significantly increases from F1 to F3. The comparison of the speeds of eruptive flux ropes at the source region with the corresponding CMEs in LASCO FOV (see Section 4.5) reveals that the first flux rope undergoes acceleration (296 vs 420 km s^{-1}), the second one moves with approximately constant speed (581 vs 503 km s^{-1}), while the last eruption exhibits deceleration (955 vs 528 km s^{-1}).

5. The build-up of electric current on the photosphere is directly associated with the emergence of current-carrying flux (Tan *et al.*, 2006; Török *et al.*, 2014); their study is important to understand the build-up of non-potentiality in the AR corona (Schrijver *et al.*, 2005; Dalmasse *et al.*, 2015). Our study reveals that a strong current accumulation occurs near the western PIL of the flaring region (Figure 4.11), where one of the two flux ropes lies (Figure 4.10). Furthermore, before F3, the magnetic flux near the western PIL is observed to undergo expansion showing an extended morphology (Figure 4.11(f)). In response to this, the longitudinal current distribution gets elongated along the same PIL before F3 (Figure 4.11(e)). In general, the role of photospheric currents have important consequences in triggering solar eruptive events. Mitra *et al.* (2020a) studies the role of precursor flare activity in triggering a dual-peak M-class flare. Their study reveals the presence of strong, localized regions of photospheric currents of opposite polarities at the precursor location, making the region susceptible to small-scale magnetic reconnection.

6. The photospheric flux emergence and shearing motion introduce strong electric currents and inject energy into the AR corona. The coronal fields get reconfigured in this process and result into the accumulation of free magnetic energy in the coronal volume (Régnier, 2012; Vekstein, 2016). This stored free energy is regarded as a prime factor responsible for the explosive phenomena. The successively increasing intensities of the homologous flares of our analysis point toward a complex

‘storage and release’ process of magnetic energies in the AR. For a quantitative understanding of the energy storage and release process, we study the evolution of free magnetic energy for a time span covering the three homologous events (Figure 4.13). We find that the maximum release of free magnetic energy (i.e., 38%) is observed during the strongest event (i.e., F3/X1.0 flare). It is also remarkable to notice that the third event got a prolonged period for the storage of free magnetic energy (i.e., a period of $\approx$17 hr between F2 and F3), during which no major flare above class C occurs in the AR. Interestingly, this ‘storage phase’ largely overlaps with a peristent phase of flux emergence (see Figure 4.9(a); the interval between t4 and t5). In conclusion, our analysis reveals that the dominant variation in magnetic flux (both at large-scale involving the full flaring region as well as small-scales close to the compact PIL) and build-up of free magnetic energy in and around the flaring region is the root cause for the homologous eruptive flares of successively increasing intensities.

In summary, our analysis provides a detailed investigation of multi-wavelength evolution of three homologous eruptive flares by combining HXR, EUV, white light, and magnetogram observations. We provide a quantitative estimation of the evolution of free magnetic energy in the corona associated with the AR, and explore its link with the ongoing photospheric and coronal processes. Thus, our study brings out the link between the photospheric developments resulting into the rapid build-up and subsequent eruption of coronal magnetic structures.

Chapter 5

Broad Coronal Mass Ejections Produced by Compact, Blowout-eruption Homologous Flares

5.1 Introduction

Traditionally, solar flares were identified through the observation of parallel brightenings (i.e., flare ribbons) on the both sides of a magnetic PIL in an active region (AR) of the Sun. Historically, the flare ribbons were extensively observed in the Hα observations of the Sun. In the case of an eruptive flare, typically a rising filament/flux rope stretches the overlying field lines creating a current sheet underneath. Magnetic reconnection gets initiated at this current sheet and the field lines successively reconnect to form apparently expanding post-flare loops and separating Hα ribbons at their footpoints, as the reconnection site approaches to successively greater heights in the corona (e.g., Shibata, 1999). The CSHKP model (see Section 1.3.3) incorporates a 2D configuration of solar flares with a translational symmetry along the reconnecting X-line (the third dimension) (Jing *et al.*, 2008), hence it is also known as the "standard 2D model" of solar flares. In the recent past, there has been significant improvement in our understanding of solar flares owing to the data from the advanced space-borne satellites and associated numerical developments, which resulted in the formulation of a 3D model of solar flares (e.g., Aulanier *et al.*, 2012) by combining a number of wide observational evidences. Importantly, this 3D model not only considers the third dimension, but it also includes the 'strong-to-weak' transition of shear from pre-flare magnetic configuration to post-flare loops. The interpretation of solar flares in the 3D regime is based upon several complex observational characteristics: coronal sigmoids (Sterling and Hudson, 1997; Moore *et al.*, 2001;

Aulanier *et al.*, 2010; Green *et al.*, 2011; Joshi *et al.*, 2017a, 2018; Mitra *et al.*, 2018), systematic HXR footpoint motions along flare ribbons (Fletcher and Hudson, 2002; Joshi *et al.*, 2009), sheared flare loops (Asai *et al.*, 2003; Warren *et al.*, 2011), etc. In addition to these complex magnetic features, some new aspects of the flare ribbons in the 3D domain have been identified, such as photospheric current ribbons (Janvier *et al.*, 2014), three flare ribbons (Wang *et al.*, 2014), circular flare ribbons (Masson *et al.*, 2009; Devi *et al.*, 2020; Joshi *et al.*, 2021; Mitra and Joshi, 2021), J-shaped ribbons (Chandra *et al.*, 2009; Schrijver *et al.*, 2011; Savcheva *et al.*, 2015; Joshi *et al.*, 2017c), etc. Since the nature of solar flares is intrinsically 3D, the energy release processes via magnetic reconnection are supposed to be 3D in nature. In view of this idea, there have been several intriguing concepts regarding 3D magnetic reconnection: slipping and slip-running reconnection (Aulanier *et al.*, 2006a), null point reconnection (Priest and Pontin, 2009; Wang and Liu, 2012; Prasad *et al.*, 2020), interchange reconnection (Fisk, 2005; Rappazzo *et al.*, 2012; Owens *et al.*, 2020), interchange slip-running reconnection (Masson *et al.*, 2012), etc. All these reconnection processes essentially involve the large-scale restructuring of coronal magnetic fields. Coronal field lines are rooted at the photosphere and are continuously shuffled by the steady convective motions at the interior layers. This shuffling process interlaces the field lines to generate complex magnetic field topologies, such as magnetic null points and their associated separatrix surfaces, separator lines, quasi-separatrix layers, etc. (Demoulin *et al.*, 1997; Aulanier *et al.*, 2005; Pontin *et al.*, 2007; Jiang *et al.*, 2021). These intriguing coronal structures act as preferential sites for current accumulation and subsequent magnetic reconnection. In view of this, in our analysis, we synthesize the multi-wavelength measurements of solar atmospheric layers vis-à-vis the topological rearrangement in the coronal magnetic structures.

Right from the start of the era of direct SXR imaging of the Sun, there has been consensus about the two-element classification of solar flares, viz., eruptive and confined (Pallavicini *et al.*, 1977; Svestka and Cliver, 1992; Moore *et al.*, 2001). An eruptive flare is the one which is accompanied by a CME, whereas a confined flare occurs without CME. In general, an eruptive flare is characterized by the appearance of two ribbons on both sides of the PIL that spread apart with time as observed in Hα images and at other wavelengths. They are followed by large-scale hot post-flare loops observed in SXR and are of long-duration (e.g., tens of minutes to a few hours), whereas a confined flare occurs in a relatively compact region and lasts for a short period (e.g., less than an hour) (Kushwaha *et al.*, 2014; Cai *et al.*, 2021). Even some large X-class flares have been found to belong to the confined category (Green *et al.*, 2002; Wang and Zhang, 2007), though their occurrence is rare. It is worth mentioning that, though the relationship between flares and CMEs is strongly coupled, it is not a cause-and-effect one (Zhang *et al.*, 2001; Temmer *et al.*, 2010; Kharayat *et al.*, 2021).

CMEs are identified as "homologous" when they originate from the same location of an AR with a similar morphological appearance in coronagraphic observations (Liu *et al.*, 2017). The cause of occurrence of these homologous CMEs was explored by several studies; Zhang and Wang (2002) stated that repeated flare-CME activities are triggered by the continuous emergence of moving magnetic features in the vicinity of the main polarity of the AR. The study of a series of eruptions by Chertok *et al.* (2004) revealed that the homology tendency appears due to repeated transient perturbations of the global coronal structure, partial eruption, and relatively fast restoration of the same large-scale structures involved in the repeating CME events. In a magnetohydrodynamic simulation of the development of homologous CMEs by Chatterjee and Fan (2013), the repeated CME activities originated from the repeated formations and partial eruptions of kink-unstable flux ropes as a result of the continued flux rope emergence under a pre-existing coronal potential arcade.

Morphologically, CMEs are complex structures that exhibit a range of shapes and sizes (Schwenn, 2006; Webb and Howard, 2012). Recently, it has been proposed that there is a broad class of CMEs, called "over-and-out" CMEs, which come from flare-producing magnetic explosions of various sizes and are laterally far offset from the flaring location. A subclass of CMEs of this particular variety was originally identified by Bemporad *et al.* (2005), where the authors reported observations of a series of narrow ejections that occurred at the solar limb. These ejections originated from homologous compact flares, whose source was an island of included polarity located inside the base of a coronal streamer. These ejections resulted in narrow CMEs that moved out along the streamer. It was concluded that each CME was produced by means of the transient inflation or blowing open of an outer loop of the streamer arcade by ejecta, hence they were termed as "streamer puff" CMEs. Later, Moore and Sterling (2007) presented new evidence that strengthened the conclusion of Bemporad *et al.* (2005) and it was inferred that the "streamer puff" CMEs are essentially a subgroup of "over-and-out" CMEs. For an "over-and-out" CME, there would be a spatially far-offset ejective flare explosion or filament eruption and no discernible flare arcade directly under the CME. Together with the work of Bemporad *et al.* (2005), Moore and Sterling (2007) put forward the concept of "Magnetic-Arch-Blowout" (MAB) to provide a plausible explanation for the production of "over-and-out" CMEs. First, a compact magnetic explosion located in a streamer arcade produces a compact ejective flare. This generates an escaping plasmoid, which becomes the core of the ensuing CME. Second, the source of the explosion, being compact relative to the streamer arcade, should blow out only a short section of the arcade. Observationally, the erupting plasmoid would be laterally deflected by the guiding leg of the streamer arcade and would overpower the arcade near its top, where the arcade field is weaker than its legs. Third, the blowing out of an outer loop of the streamer arcade could result in coronal dimming at the feet of the loop. The lateral extent of the dimming would demarcate the extent of the opened section of the arcade, which participated in the eruption process. Later, Sterling *et al.* (2011) presented another observational evidence of the MAB scenario, applicable for CMEs that are not produced from streamer regions (see Figure 6 of Sterling *et al.*, 2011). They investigated two precursor eruptions leading to an X-class flare, where the first precursor was a MAB event. In this case, an initial standard-model eruption of the AR's core field blew out an east-lobe loop of the core region, leading to a CME displaced toward the east of the flaring region. We note that in all the above cases, the basic physical process of the eruption remains the same, whereas, they differ only in terms of different coronal magnetic environments hosting the compact blowout-eruption flares.

In this study, we analyze three compact homologous eruptive flares, associated with CMEs of large angular width that resemble the "over-and-out" CMEs discussed above. The eruptions originate from NOAA AR 12017 within a span of ≈24 hr during 2014 March 28–29 (see Chapter 4). Each successive eruption is of increasing intensity (M2.0, M2.6, and X1.0, respectively) and results from the sequential eruption of compact coronal flux ropes lying over the same location of the AR, as discussed in Chapter 4 (see Section 4.1). The third event presented in our analysis (i.e., X1.0 flare) was well observed by various ground- and space-based observatories (Kleint *et al.*, 2015; Li *et al.*, 2015; Liu *et al.*, 2015; Young *et al.*, 2015; Woods *et al.*, 2018). The study by Kleint *et al.* (2015) revealed that a filament eruption was observed above a region of previous flux emergence, which possibly led to a change in magnetic field configuration, causing the X-flare. Liu *et al.* (2015) discussed a scenario of asymmetric filament eruption due to nonuniform filament confinement and a MHD instability. This disturbed the fan-spine-like field encompassing the filament leading to breakout-type reconnection at the coronal quasi-null region. Subsequently, the filament eruption triggered intense reconnection at the quasi-null, producing a circular flare ribbon. These studies mainly concentrated on the single X-lass flare, which is the strongest among the three major flares. The scope of our study is much broader in that we study the evolution of all three successive major eruptions, all of which originate at the same location of mixed polarity under dense compact arcades. Importantly, all the compact magnetic explosions produce an initial perturbation in the system that ultimately results in the formation of a broad CME. Furthermore, in all three

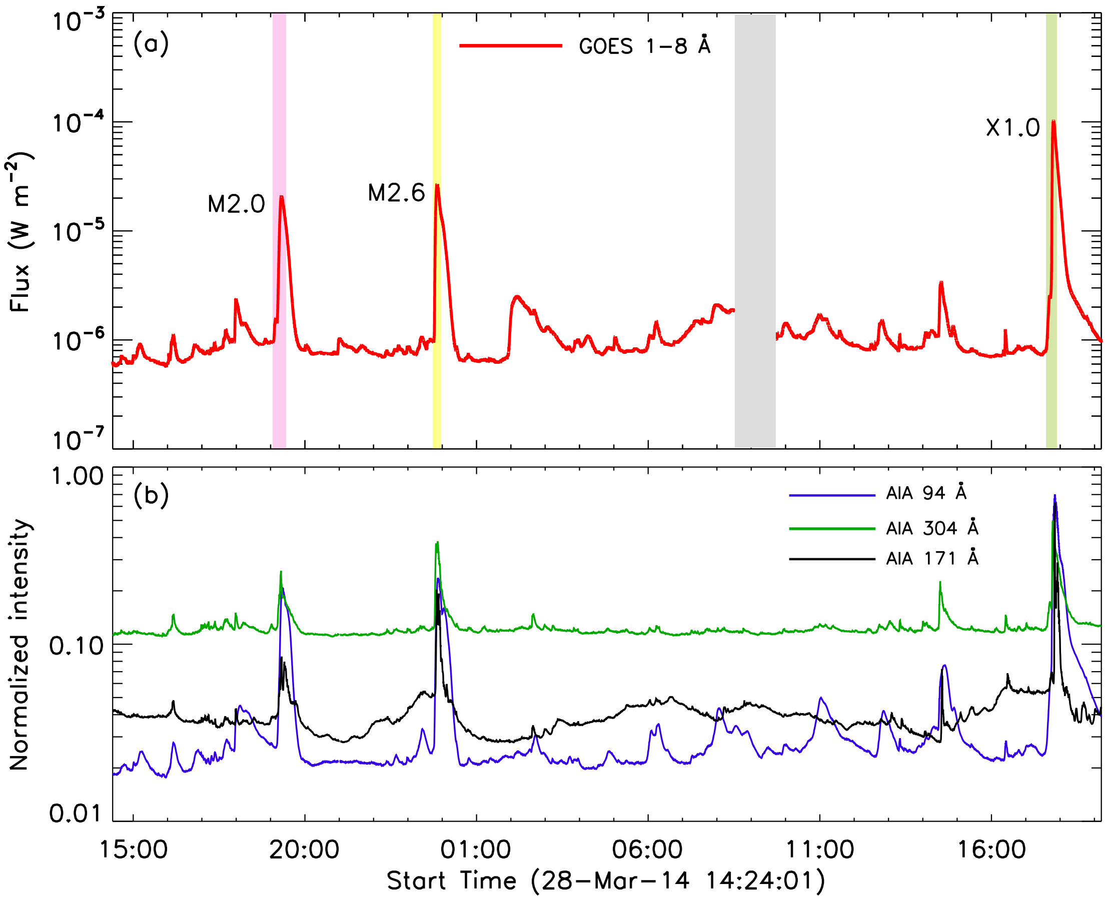

Figure 5.1: panel (a): GOES SXR flux in 1–8 Å channel indicating the three flare events of intensities M2.0, M2.6, and X1.0. The shaded regions in purple, yellow, and olive green represent the flare durations according to the GOES flare catalog. The gray shaded region indicates a period over which GOES data were unavailable. Panel (b): normalized intensity light curves of AIA passbands 94 Å [log(T) = 6.8], 304 Å [log(T) = 4.7], and 171 Å [log(T) = 5.7] multiplied by factors of 0.7, 0.5, and 1.2, respectively, for clear visualization. The light curves denote the variation of intensity over the AR under analysis.

cases, the source region of the CMEs, marked by coronal dimming, exhibits lateral offset from the flaring location–a typical characteristic of "over-and-out" CMEs. Although the eruptions of compact flux ropes are progenitors of the CMEs, the actual large-scale structure of the CMEs is linked to the configuration and topological changes in the large-scale magnetic field connecting to magnetic flux far from the flare site. The analyses and results are described in Section 5.2. The interpretations and conclusions are provided in Section 5.3.

Event Number	Flare Class	Date	Time (UT) Start	Peak	End	Heliographic Coordinate
1	M2.0	2014 Mar 28	19:04	19:18	19:27	N11W21
2	M2.6	2014 mar 28	23:44	23:51	23:58	N11W23
3	X1.0	2014 Mar 29	17:35	17:48	17:54	N11W32

Table 5.1: summary of the flares in NOAA AR 12017 during 2014 March 28–29.

5.2 Analysis and results

5.2.1 Relationship between Coronal Mass Ejections and their Source Region

We provide the GOES light curve in the 1–8 Å channel from ≈14:30 UT on 2014 March 28 to ≈19:00 UT on 2014 March 29 in Figure 5.1(a). The light curve clearly indicates the occurrence of three large flares of class M2.0, M2.6, and X1.0 (the flare intervals are marked by vertical shaded regions in different colors). All these flares are of the eruptive category and produce spectacular, large-scale structures of CMEs observed in the white light coronagraphic images from LASCO[1]. We find that the eruptive flares show successively increasing intensities (viz., M2.0, M2.6, and X1.0). We also note that there are no significant flaring activities (of class >M) at least one day before and after the events under analysis. These events occur in NOAA AR 12017, which presents a $\beta\gamma$ type photospheric magnetic configuration during the reported activities. This AR is typical in the sense that it exhibits multiple flaring episodes within a short span of ≈2 days during 2014 March 28–29, and it has been the subject of several studies. Yang *et al.* (2016) investigate the magnetic field of the AR during the aforementioned period and find the presence of a MFR in a NLFFF extrapolation, which is prone to kink instability. Furthermore, the closed quasi-separatrix layer structure surrounding the MFR becomes smaller as a consequence of the eruption. Chintzoglou *et al.* (2019) reveal that NOAA AR 12017 hosts a "collisional PIL", which develops owing to the collision between two emerging flux tubes nested within the AR. Also, during the entire evolution over the visible solar disk, the AR shows significant cancellation (up to 40%) of the unsigned magnetic flux of the smallest emerging bipolar magnetic region.

In Figure 5.1(b), we plot the EUV light curves based on AIA imaging observations in 94, 171, and 304 Å channels. The AIA light curves are obtained from intensity variation

[1] https://cdaw.gsfc.nasa.gov/CME_list/UNIVERSAL/2014_03/univ2014_03.html

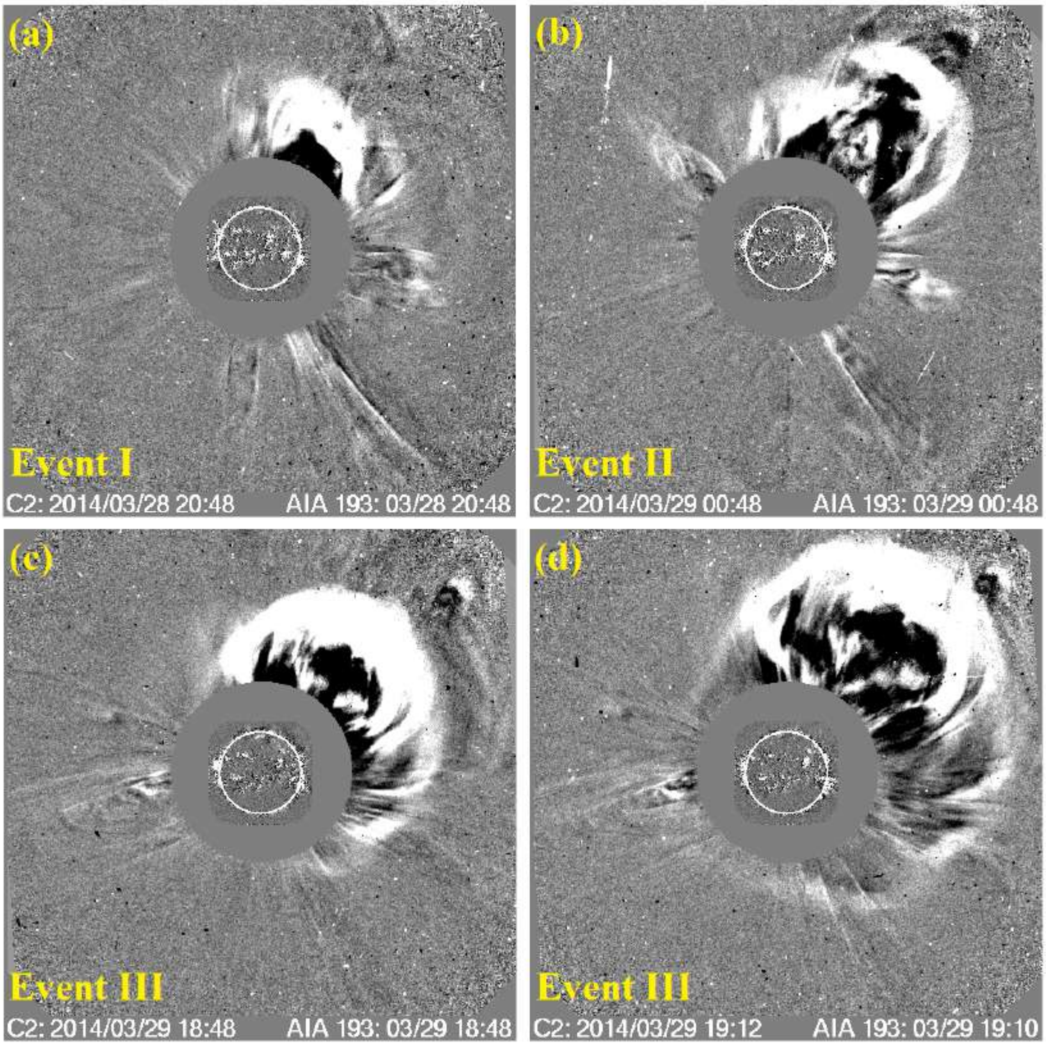

Figure 5.2: depiction of the wide CMEs formed due to the large-scale eruptions associated with the events under analysis. Panels (a) and (b) show the CMEs associated with events I and II and the CME produced in the aftermath of event III is shown in panels (c) and (d). In all panels, the CME images are from the LASCO C2 coronagraph and the coronagraph occulter is overplotted by an AIA 193 Å image.

over the whole NOAA AR 12017 (marked by a red rectangle in Figure 5.3(b)). We note that the EUV 94 Å light curve resembles the GOES 1–8 Å light curve fairly well. A summary of the flaring events is given in Table 5.1, which is based on the GOES flare catalog[2].

In Figure 5.2, we provide LASCO C2 images of three CMEs (marked as Event I, II, and III). The CMEs associated with events I and II are non-halo (with angular sizes of 103° and 111°, respectively), whereas the CME associated with event III is a halo CME.

[2] https://www.ngdc.noaa.gov/stp/space-weather/solar-data/solar-features/solar-flares/x-rays/goes/xrs/goes-xrs-report_2014.txt

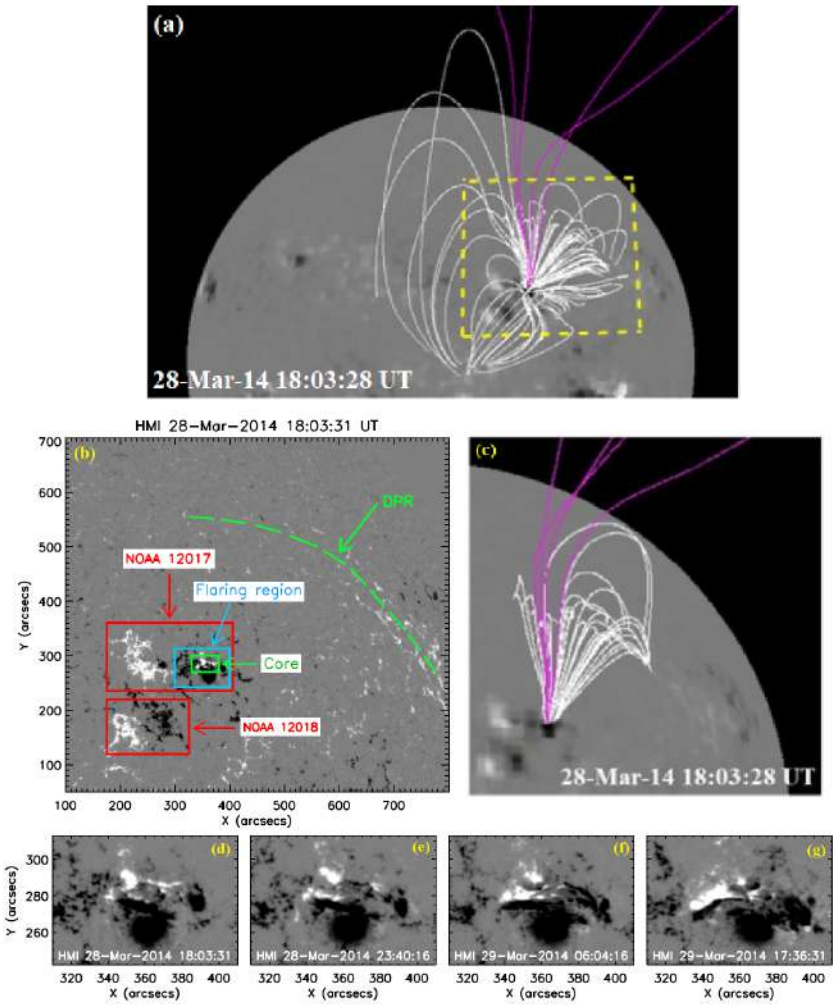

Figure 5.3: panel (a): the large-scale field surrounding the AR from which the eruptions occur. The white and pink lines denote closed and open field lines, respectively, overlaid onto the LOS magnetogram. The yellow dashed box is enlarged in panels (b) and (c). In panel (b), we show the photospheric LOS magnetogram. NOAA AR 12017 and 12018 are indicated by the red rectangles. We note that NOAA AR 12017, the AR of our interest, displays an approximate spatial extension of 230″×125″. We mark the flaring region within this AR with a sky-blue box. Inside this, we mark the "core" location of the mixed-polarity magnetic field with a green box. The spatial extension of the core is ≈50″×30″, and it is the source of all the compact blowout-eruption flares. Notably, the core region is much smaller (≈19 times) than the size of the AR. We show the distant positive-polarity region (DPR) as a green dashed line. In panel (c), we show the large-scale connectivity between the negative polarity of the flaring region and the DPR as white lines (see panels (b) and (c)) before the time of event I. The pink lines are open field lines originating from the flaring region. In panels (d)–(g), we show the evolution of the flaring region. In panels (d) and (e), we show the morphology of this region before events I and II, respectively, whereas, the magnetic configuration before event III is shown in panels (f) and (g).

Table 5.2: some parameters of the CMEs produced by the events under investigation.

CME	Speed (km s^{-1}) V_L	V_S	Angular width (degree)	Mass ($\times 10^{15}$ gm)	Kinetic energy ($\times 10^{30}$ erg)
CME 1	420	464	103	2.6	2.3
CME 2	503	327	111	2.3	2.9
CME 3	528	505	360	5.0	7.0

Note: CME 1, CME 2, and CME 3 are made by events I, II, and III, respectively. V_L and V_S are linear speed and second-order speed at 20 solar radii, respectively.

We note that the linear speed of the CMEs increases gradually from event I to event III, with values of 420, 503, and 528 km s^{-1}, respectively. Several parameters of these CMEs are listed in Table 5.2.

The large-scale coronal connectivities are thought to play a major role in the development of broad CME structures. In order to visualize large-scale coronal magnetic field lines, we carry out PFSS extrapolation for a few representative instances (see Figures 5.3(a), (c), and 5.4, panels (b) and (c)). In Figure 5.3(a), we show the extrapolated field lines in and around the AR before event I. To show the detailed magnetic structure on the photosphere, the region marked within the yellow dashed box in Figure 5.3(a) is shown in Figure 5.3, panels (b) and (c). In Figure 5.3(b), NOAA AR 12017 and 12018 are marked by red rectangles. NOAA AR 12017 is the AR of our interest. The flaring region lies in the leading part of the AR, which is marked by a sky-blue box. In all three cases, the eruption begins with a compact blowout-eruption of a flux rope from a small region of mixed polarity within the flaring region. We term this small region as the "core", and mark it with a green box (see also Figure 5.8). Notably, the size (i.e., area under the green box) of the core region is significantly smaller (≈19 times) than the extent of the AR (i.e., the area under the red rectangle denoting NOAA AR 12017). A careful examination of the magnetogram reveals the presence of extended and dispersed magnetic flux of positive polarity, located toward the northwest of the flaring site, substantially away from the AR boundaries. This distant positive-polarity region (DPR) extends like an arc, which we manually mark by a green dashed line in Figure 5.3(b). Importantly, we note clear magnetic connectivities between the negative polarity of the flaring region and the DPR, which we denote as white field lines in Figure 5.3(c), adjacent to open field lines (shown in pink), originating from the flaring region. The DPR acts as a proxy for the remote footpoints of large-scale coronal field lines (i.e., a magnetic arch; MA), which are involved in the formation of large-scale CMEs. To explore the fine details of the flaring region, we show zoomed images of this region in Figures 5.3(d)–(g). Panels (d) and (e) represent the magnetic configuration before events I and II, whereas panels (f) and (g) represent the magnetic structure of the flaring region before event III. Comparison of panels (d)–(g) of Figure 5.3 clearly reveals substantial small-scale changes (i.e., various epochs of emergence and cancellation) in the photospheric magnetic field of the flaring region over the time period spanning the three events.

Each of the eruptive flares is followed by collimated surges of cool material from the flaring region. In Figure 5.4(a), we show a representative image of the surge from the flaring region observed after event II. We choose this particular observation because of its clear visibility. In Figure 5.4, panels (b) and (c), we show the large-scale coronal field lines (shown as white lines), demonstrated by PFSS extrapolation, connecting the flaring region with the DPR. The epochs in these panels denote instances a few hours after event II and a few hours before event III, respectively. The pink lines represent open field lines emanating from the flaring region. We note that the large-scale coronal magnetic field configuration remains unchanged during the course of the events (see Figures 5.3(c) and 5.4, panels (b) and (c)). Interestingly, the surge nearly follows the open field lines (see Figures 5.4(a)–(c)).

5.2.2 Trio of Blowout-eruption Flares and Associated Magnetic Environment

The temporal and morphological analyses of the eruptive flares are presented in Figures 5.5–5.7. Panel (a) in these figures show the GOES light curves of the events in the 1–8 and 0.5–4 Å channels, along with the AIA light curves in 94 and 171 Å, while panels (b)–(i) provide a few representative AIA images. For imaging analysis, we examine AIA observations taken in the 94 and 171 Å channels. The AIA 94 Å [log (T) = 6.8] channel is apt for imaging the flaring coronal structures while AIA 171 Å [log(T) = 5.7] channel is useful to infer the low-temperature structures formed in the corona and transition region. The selected FOV of the AIA images encompasses the flaring region (see Figures 5.3(d)–(g)) and surrounding regions into which the eruption evolves.

Figure 5.5 reveals several temporal and spatial aspects of the first (M2.0 flare) event. A comparison of LOS photospheric magnetic flux with the EUV images (see panels (b) and (f)) during the pre-flare stage reveals small-scale connectivities (marked by white arrows in panel (f)) between opposite magnetic polarities within the core region. In the 171 Å image in panel (f), we note several structures that extend outward (marked by a green arrow), suggestive of either large-scale or quasi-open field lines. The presence of

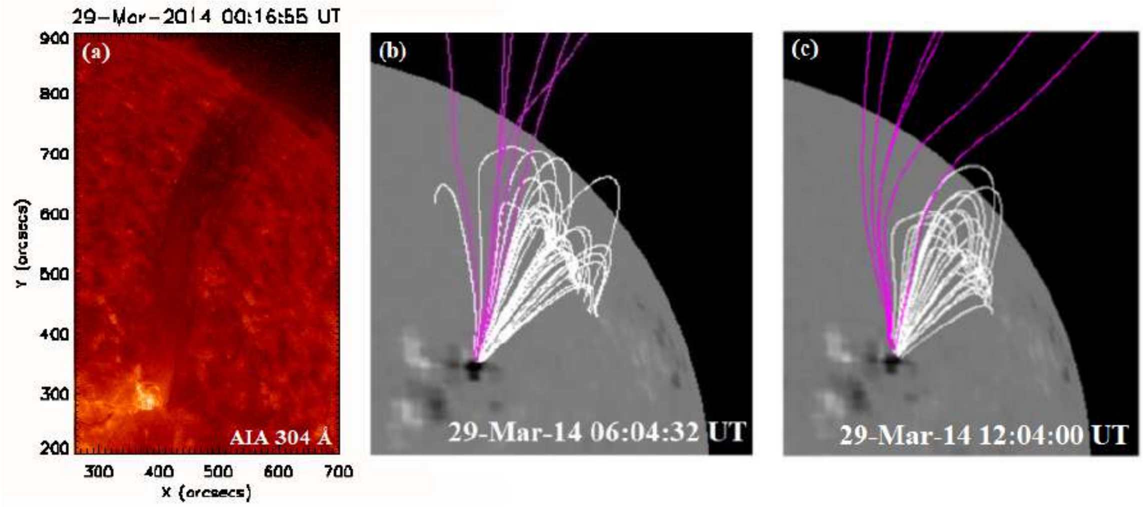

Figure 5.4: in panel (a), we show a surge consisting of cool material expelled from the flaring region, observed to occur after event II. Panels (b) and (c) show the large-scale connectivity, revealed by PFSS model extrapolation, between the flaring region and the DPR at instances shortly after event II and shortly before event III, respectively. The surge nearly follows the open pink lines (see panels (a)–(c)). The large-scale connectivity between the flaring region and the DPR remains unchanged before event I, after event II, and before event III (see panels (b) and (c) with Figure 5.3(c)).

open field lines is well supported by the global PFSS extrapolation presented in Figures 5.3 and 5.4 (see also Section 5.2.1). The sequence of AIA images reveals two stages of eruptions, which we term as ejecta I and II. Ejecta I originates from the eastern part of the core at ≈19:03 UT (marked as "ejecta I" in panels (c) and (g)). Ejecta II starts at ≈19:18 UT from the western part of the core (marked as "ejecta II" in panels (d) and (h)). The onset times of the two ejecta are indicated in the GOES light curves in panel (a). We observe that ejecta I precedes the flare while ejecta II occurs during the impulsive phase, shortly before the peak. In panels (d) and (h), we mark a wide circular ribbon structure by sky-blue arrows, situated north of the mixed-polarity core region. The compact post-flare loops, formed as a result of standard flare reconnection between the legs of the field lines stretched by the erupting flux rope, are indicated by a red arrow (panel (d)). We explain the formation of the circular ribbon and the compact post-flare loops with the help of a schematic diagram (Figure 5.11) in Section 5.3. After the peak, we observe a gradual decline in the light curves, indicating the decay phase, which is marked by the growth of dense post-flare loop arcades (shown in panels (e) and (i)). Multiple eruptions in close succession like this were observed before, and it is plausible that the first eruption leads to

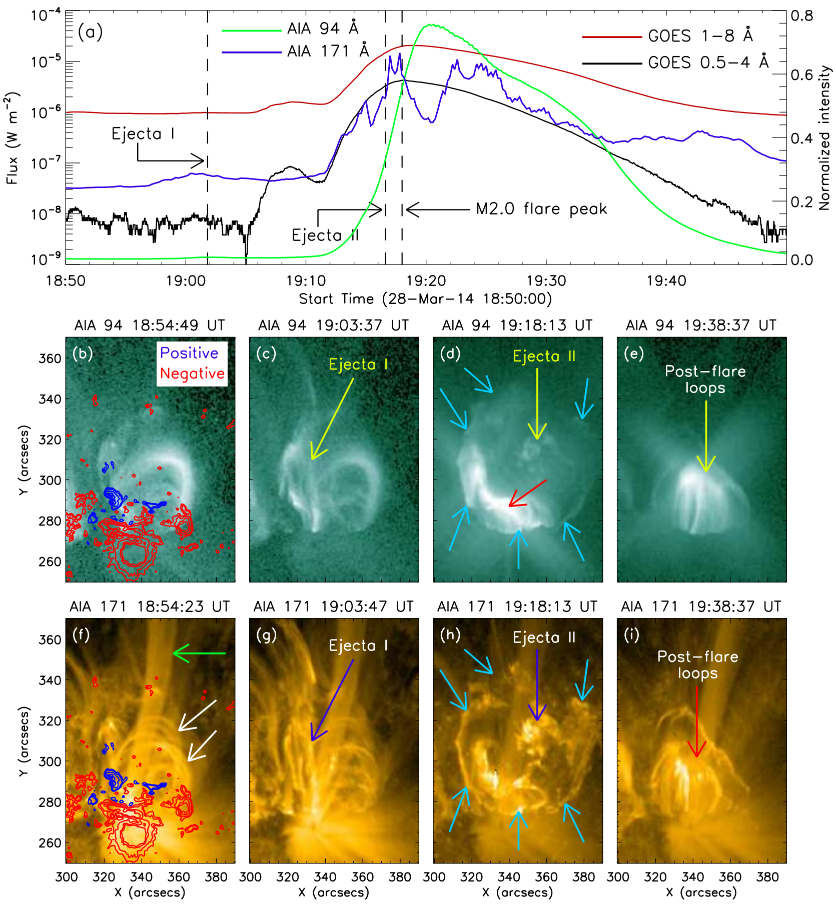

Figure 5.5: panel (a): the GOES light curves in 1–8 and 0.5–4 Å channels and the intensity curves for event I, obtained from the flaring region recorded in AIA 94 and 171 Å channels. The light curves span from 18:50 UT to 19:50 UT on 2014 March 28 showing the epochs of the first event, which had the M2.0 flare and two associated ejecta. Panels (b)–(e): evolution of the eruption in the AIA 94 Å channel. In panel (b), we overlay the LOS magnetic contours with red and blue, representing negative and positive magnetic polarities, respectively. Panels (c) and (d) indicate ejecta I and II, respectively. In panels (d) and (h), we demarcate a wide circular ribbon structure north of the core region by sky-blue arrows. The compact post-flare loops result from the standard flare reconnection between the legs of the field lines stretched by the erupting flux rope are indicated by a red arrow in panel (d). In panel (e), we show the growing post-flare loop arcades. Panels (f)–(i) show the flare evolution in the AIA 171 Å channel. The same magnetic contours as in panel (b) are also shown in panel (f). The magnetic contour levels are set at ±[200, 400, 800, 1000, 2000] G. In panel (f), the two white arrows indicate small-scale connectivities within the flaring region, whereas the green arrow shows several structures that extend outward. Ejecta I, ejecta II, and the post-flare arcades are indicated in panels (g), (h), and (i), respectively. The peak of the flare occurs just after the eruption of ejecta II (see panel (a))

a destabilization of nearby fields in the same region leading to the second eruption (e.g., Török *et al.*, 2011; Sterling *et al.*, 2014; Joshi *et al.*, 2020).

In Figure 5.6(a), we show the temporal variation of the second (M2.6 flare) event. In the following panels, we demonstrate the structural changes associated with the eruption's evolution in EUV 94 and 171 Å images. During the pre-flare stage, the coronal configuration of the flaring region shows similarity to that of event I in the form of small-scale connectivities and the existence of quasi-open-type field lines (see panels (b) and (f)). Similar to event I, here also we observe two discrete eruptions in association with the flaring activities. The first eruption starts in the eastern part of the core region just after the beginning of the impulsive phase at ≈23:46 UT. We mark this eruption as "ejecta I" (panels (c) and (g)). The second eruption originates from the western part of the core just after the ejecta I at ≈23:48 UT, which we term as "ejecta II" (shown in panels (d) and (h)). These successive eruptions show similar morphological behavior to that of event I with respect to their origin and the subsequent path followed by them. The flare reaches its peak at ≈23:51 UT (see panel (a)). Thereafter, the post-flare loops are observed to form (shown in panels (e) and (i)).

The temporal and spatial evolutionary phases of the third (X1.0 flare) event are depicted in Figure 5.7. During the pre-eruptive stage of the eruption, we note the existence of a nullpoint-like structure connecting the opposite magnetic polarities of the flaring region, which is evident in the 171 Å image in panel (g). Unlike the two previous events, both of which consist of two ejective episodes, in this case there is only a single eruption from the core region, which starts at ≈17:45 UT, as marked in panel (a). The eruption apparently destroys the null-point-like structure during the build-up to the maximum phase of the X1.0 flare. The flare peaks at ≈17:48 UT (indicated in panel (a)). After that, the dense post-flare arcades are formed (shown in panels (e) and (i)).

Notably, we observe circular ribbon structures during the peak of all the events (see panels (d) and (h) of Figures 5.5–5.7).

To understand the magnetic complexities of the core region on the size scale of the AR, we employ coronal magnetic field modeling using the NLFFF extrapolation technique. We demonstrate the results of the extrapolation carried out during the pre-flare stages of the events in Figure 5.8. The extrapolation results clearly demonstrate the existence of two adjacent flux rope systems for each of the three events. We note that the compact flux ropes lie over the compact region of strong mixed polarity within the core region (marked by a green box in Figure 5.3(b)). The flux ropes lying on the eastern and western parts of the core are shown as red and yellow field lines, respectively. We note a system of low-lying closed field lines (shown in green) connecting the negative and pos-

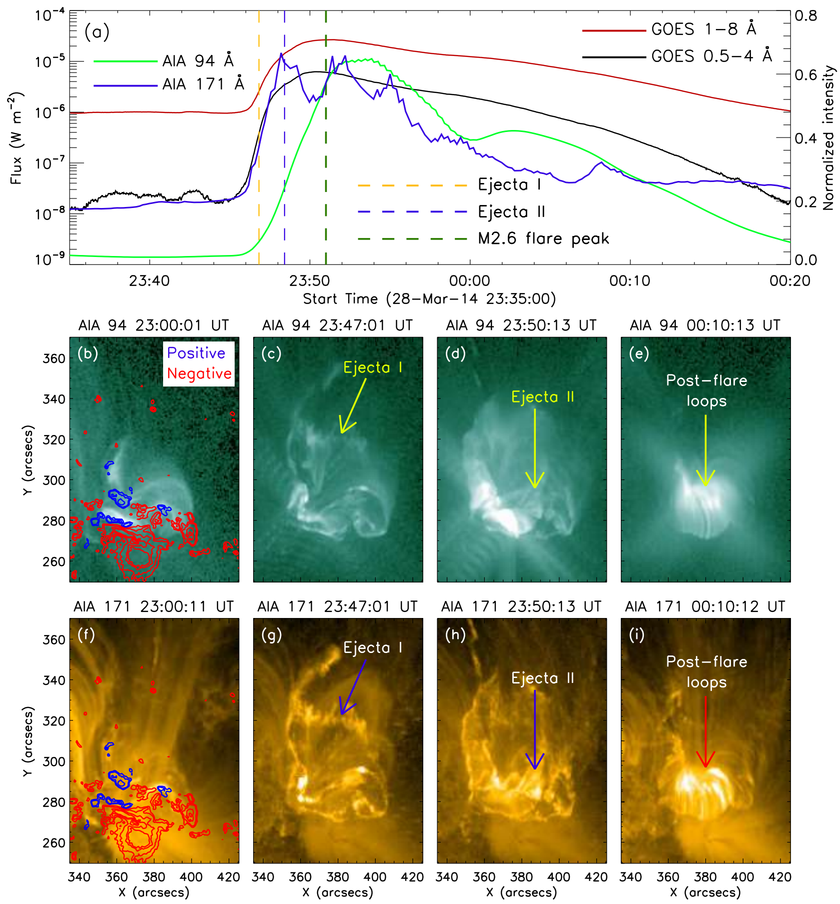

Figure 5.6: panel (a): the GOES light curves in 1–8 and 0.5–4 Å channels along with the intensity curves obtained from the flaring region in AIA 94 and 171 Å channels for event II. The time range of the light curves spans between 23:35 UT on 2014 March 28 and 00:20 UT on March 29. The flare peak and the two ejecta are indicated by dashed lines in different colors. Panels (b)–(e): evolution of the flare shown in the AIA 94 Å channel. The LOS magnetogram is overplotted as contours on the 94 Å image in panel (a), with colors as denoted in this panel. Ejecta I and II are shown in panels (c) and (d), respectively. The post-flare loops are shown in panel (e). In panels (f)–(i), we show the flare evolution in AIA 171 Å observations. The LOS magnetogram is overplotted on the 171 Å image in panel (f). The magnetic contour levels are ±[200, 400, 800, 1000, 2000] G in all the panels. Panels (g) and (h) show ejecta I and II, respectively. The formation of bright post-flare loops is shown in panel (i).

itive polarities of the core that constrain the two flux ropes. A comparison of modelled coronal field structure (Figure 5.8) with the corresponding imaging observations (Figures 5.5–5.7) suggests sequential eruptions of the eastern and western flux ropes during events I and II, whereas, only a single flux rope erupts for the case of event III. For event III, ob-

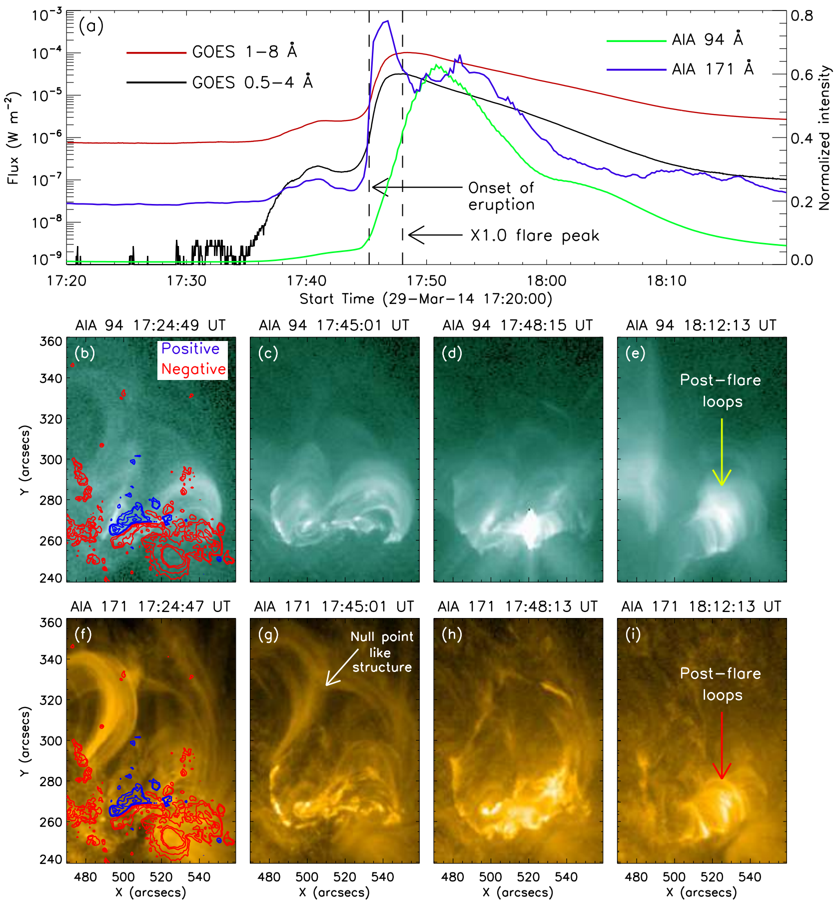

Figure 5.7: in panel (a), we plot the GOES light curves in 1–8 and 0.5–4 Å channels for the case of event III, along with the intensity curves from the AIA 94 and 171 Å channels recorded from the flaring region. The time interval chosen for this panel runs from 17:20 UT to 18:20 UT on 2014 March 29. We indicate the onset of eruption and the flare peak by dashed lines. In this case, we observe a single eruption from the core region, unlike events I and II, where we observe two successive eruptions denoted as ejecta I and II in Figures 5.5 and 5.6. Panels (b)–(e) show the evolution of the flare in AIA 94 Å images. In panel (b), we overplot the magnetic contours onto the 94 Å image. In panel (e), we show the post-flare loop arcades. In panels (f)–(i), we show the flare evolution in the AIA 171 Å channel. The magnetic contours drawn in panel (f) are the same as in panel (b). The contour levels are set at ±[200, 400, 800, 1000, 2000] G. We observe an inverted Y-shaped null-pointlike structure in the pre-eruptive stage, indicated in panel (g). The formation of post-flare loop arcades is shown in panel (i).

servational results suggest the eruption of western flux rope (shown as yellow field lines in Figure 5.8(c)) from the core region.

Even though the third eruption does not have two “ejecta” as in the first two events, there is nonetheless enhanced activity in this third event prior to the main eruption. It

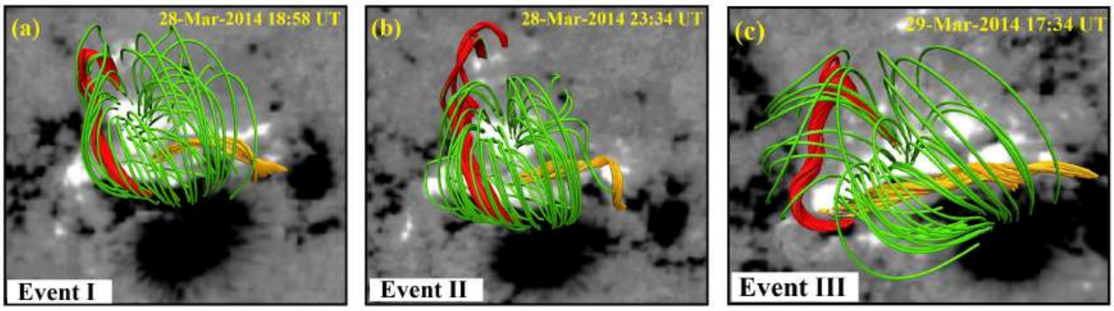

Figure 5.8: pre-eruptive configurations of the core region in zoomed view, obtained from the NLFFF extrapolations using HMI vector magnetograms. The core consists of closed bipolar field lines (shown in green) constraining the underlying flux ropes. The flux ropes form over the strong mixed-polarity region within the core. We show the flux ropes lying over the eastern and western parts of the core region as red and yellow field lines, respectively.

is visible in the GOES plot of Figure 5.7(a) peaking shortly after 17:40 UT, and it corresponds to an initial movement of the filament prior to eruption, with accompanying brightenings (visible in 94, 304, and 171 Å images). The difference for this third event from those first two is that in this case the pre-flare motions and brightenings are along the same main magnetic neutral line (or along the same portion of that neutral line) from which the main eruption occurs, rather than manifesting as an earlier "ejecta" event at a different location in the AR. This is similar to the stop-and-start "slowrise" evolution seen in other filament eruption events (e.g., Sterling and Moore, 2005). For each of these three cases, the erupting flux ropes act as a "seed" toward the formation of large-scale CME structures.

5.2.3 Magnetic-Arch-Blowout and Coronal Dimming

All the events analyzed in this study are eruptive in nature, and each of the three eruptions lead to the formation of broad CMEs. Although the CMEs possess large-scale structures with wide angular width (>100° to halo; Figure 5.2), the corresponding source ARs of flare blowout-eruptions were much compact (see the spatial comparison shown in Figure 5.3(b)). This phenomenon of the CME being much wider than the source region is being recognized for some time (e.g., Harrison, 1995; Dere *et al.*, 1997; Gopalswamy and Thompson, 2000). Moore *et al.* (2007) argue that such a widening between the source region and the CME is a consequence of the magnetic pressure of the exploding field coming into pressure balance with the interplanetary field in the solar wind, which is far weaker than the AR coronal field surrounding the source region, meaning that the CME

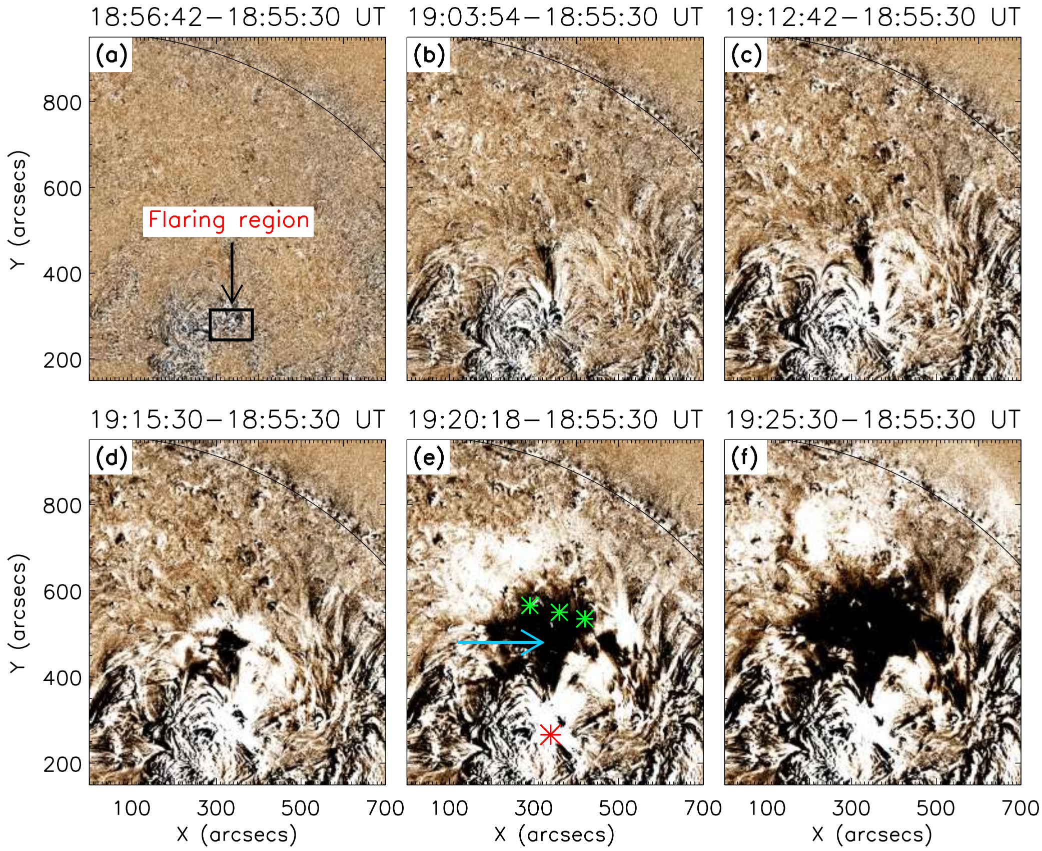

Figure 5.9: panels (a)–(f): a sequence of AIA 193 Å fixed-difference images showing the coronal dimming accompanying the large-scale eruptions for the case of event I. An image before the start of the flare (at 18:55:30 UT) is subtracted from all the subsequent images. In panel (a), we mark the flaring region by a box. Panel (c) approximately denotes the start of the flare (see Figure 5.5(a)). In panel (d), we observe the appearance of slight dimming adjacent to the flaring region. Panel (e) shows the subsequent growth of the dimming, which is marked by an arrow. We indicate the center of the flaring region with a red star and a part of the DPR with green stars. These marked locations denote the footpoints of the large-scale field lines (i.e., MA) involved in the formation of broad CMEs (see Figure 5.3, panels (b) and (c)). Panel (f) shows a later image, in which the dimming expands.

field has to expand substantially for that new pressure balance to ensue. We show with AIA 193 Å fixed-difference images the large-scale coronal changes accompanying the early evolution and subsequent development of the broad CMEs during our three events. Some snapshots of these observations during the course of event I are represented in Figure 5.9. Note that the FOV chosen in Figures 5.9(a)–(f) represents a much larger area compared to the FOV shown in Figures 5.5–5.7. For comparison, in Figure 5.9(a), we indicate the flaring region (see the sky-blue box in Figure 5.3(b)). The saturated pixels in and around the flaring region in panel (c) approximately mark the start of the flare.

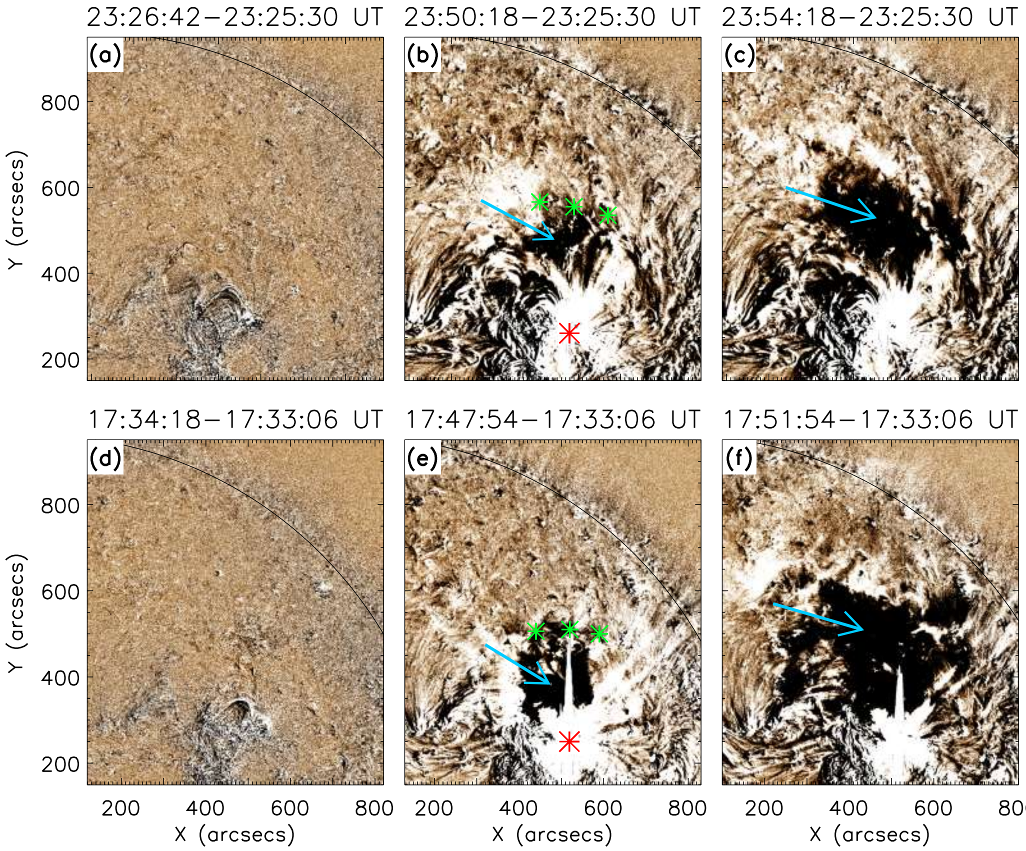

Figure 5.10: panels (a)–(c): the eruptions from the core region and subsequent appearance of coronal dimming for event II, observed in 193 Å fixed-difference images. The dimmings are indicated in panels (b) and (c) by arrows. Panels (d)–(f): the post-eruption coronal features are depicted in 193 Å fixed-difference images for event III. The dimmings are indicated in panels (e) and (f) by arrows. In panels (b) and (e), we mark the center of the flaring region with red stars and a part of the DPR with green stars. These marked locations are essentially the footpoints of the large-scale field lines (i.e., MA), whose blowout-eruption results in the formation of broad CMEs.

The eruption of flux ropes from the core region is followed by EUV dimming. The onset of the dimming can be realized in the form of a slight dark region adjacent to the flaring region which is manifested as a result of sudden plasma depletion (see Figure 5.9(d)). The dimming region expands gradually, indicated by an arrow in Figure 5.9(e). We further observe spreading out of an "EIT Wave" (or "EUV Wave") (e.g., Thompson and Myers, 2009; Gallagher and Long, 2011; Long *et al.*, 2014) from the source region of eruptions. EIT waves are now generally accepted to be the signature of fast-mode waves or shocks in the corona that are launched by erupting flux ropes (e.g., the reviews by Warmuth, 2015; Long *et al.*, 2017). In the following panel (f), we show a widespread dimming formed northward of the AR.

The morphological features observed during the course of the eruptions for events II and III are shown in the upper and lower panels of Figure 5.10, respectively. Following the flux rope eruptions, the EUV coronal dimming is observed subsequently to grow to cover a large area (marked by sky-blue arrows in Figure 5.10, panels (b) and (c)).

Event III presents much more pronounced large-scale structures compared to events I and II. However, it shows morphological similarities with the previous events in terms of the development of coronal dimming and the resulting broad CME, which actually becomes a halo CME for event III. The dimmings are indicated by sky-blue arrows in Figure 5.10, panels (e) and (f). In Figures 5.9(e), 5.10(b), and (e), we mark the location of the flaring region and a part of the DPR with red and green stars, respectively. These locations actually denote the footpoints of the large-scale field lines (i.e., MA), whose blowout-eruption results in the formation of the broad CMEs and accompanying EUV dimming.

5.3 Discussion

In this analysis, we investigate the formation mechanism of three homologous, broad CMEs resulting from eruptive flares in the compact bipolar region of NOAA AR 12017 during 2014 March 28–29. All the events are comprised of flux rope eruptions, formed over the same PIL of the AR. Our work presents a clear example of a large-scale coronal magnetic configuration that is successively blown out by compact flux rope eruptions leading to a series of broad CMEs.

The observation of NOAA AR 12017 through EUV imaging clearly reveals filaments at the core of the AR near the PILs. The magnetic field enveloping the filaments along the PIL erupts successively three times within a time span of ≈24 hr. Our NLFFF extrapolation results reveal the existence of twisted magnetic structures that would envelop the filament plasma material and are capable of storing the free magnetic energy (e.g., Fan and Gibson, 2007; Zhang *et al.*, 2012; Toriumi and Wang, 2019; Mitra *et al.*, 2020a; Sahu *et al.*, 2020) required for the subsequent multiple eruptions. For events I and II, the flux rope containing the filament near the eastern part of the core erupts first (obtained in modeling as the red flux rope structure in Figure 5.8, panels (a) and (b)) followed by the eruption of flux rope containing the filament from the western part (indicated by yellow flux rope structure in Figure 5.8, panels (a) and (b)). For event III, we observe a single filament/flux rope eruption from the western part of the core region; the extrapolation results indicate that this is likely triggered by the eruption of the yellow flux rope shown in Figure 5.8(c). The sequential eruption of filaments leads to homologous flares followed by CMEs. The eruptions occur from a very compact site (i.e., core) within the flaring region (see Figure 5.3(b)), while the resulting CMEs are of wide angular width (>100° to halo) (see Figure 5.2). Woods *et al.* (2018) explore the triggering mechanism of the filament eruption that occurs with the event III of our study. The authors confirm the existence of two flux ropes present within the AR prior to flaring. Interestingly, only one of these two flux ropes erupts during the flare. Woods *et al.* (2018) interpret that tether-cutting reconnection allows one of the flux ropes to rise to a torus-unstable region prior to flaring, resulting in its successful eruption.

To explore the large-scale coronal magnetic field changes producing broad CMEs, we conduct PFSS extrapolation to visualize global potential coronal loops in and around the AR (shown in Figures 5.3(a), (c), and 5.4, panels (b) and (c)). We observe large-scale field lines connecting the DPR with the flaring region. In view of the formation of broad CMEs, we propose a scenario in which the erupting MFRs disrupt these large-scale coronal loops to develop into broad CMEs. We note that the open field lines (shown in pink) originating from the flaring region can act as a "runway" for the successful successive eruption of the flux ropes. The influence of large-scale open field lines in the kinematic and dynamic evolution of CMEs has also been investigated in some previous recent studies (e.g., Chen, 2013; Georgoulis *et al.*, 2019; Gou *et al.*, 2019).

We analyze the AIA 193 Å fixed-difference images during the course of the events over an extended neighborhood of the flaring region. We observe that the eruptions are followed by substantial coronal dimming (Sterling and Hudson, 1997; Reinard and Biesecker, 2008; Mason *et al.*, 2014) which gradually expands (see Figures 5.9 and 5.10). Previous studies show that coronal dimming corresponds to the temporary regions of strongly reduced coronal emission in EUV and SXRs that form in the wake of CMEs. In general, their formation is interpreted as density depletion due to the expansion and expulsion of plasma during the early evolution of CME. The presence of large-scale open field lines, as demonstrated in the present study, would further support the growth of dimming regions as open field lines act as conduits for outward plasma flow.

The blowout-eruptions of compact flux ropes from the core region and their sequential interactions with the overlying large-scale coronal fields result in broad CMEs. The present observations exhibit excellent conformity with the MAB scenario originally proposed by Moore and Sterling (2007). Essentially, the erupting compact flux ropes explode up the large-scale field lines connecting the flaring region of the AR and the DPR (see Figure 5.3, panels (b) and (c)). In a feedback process controlled by reconnection, the activated flux rope blows out the large-scale field lines which in turn strengthens the magnetic field of the erupting CME-flux rope.

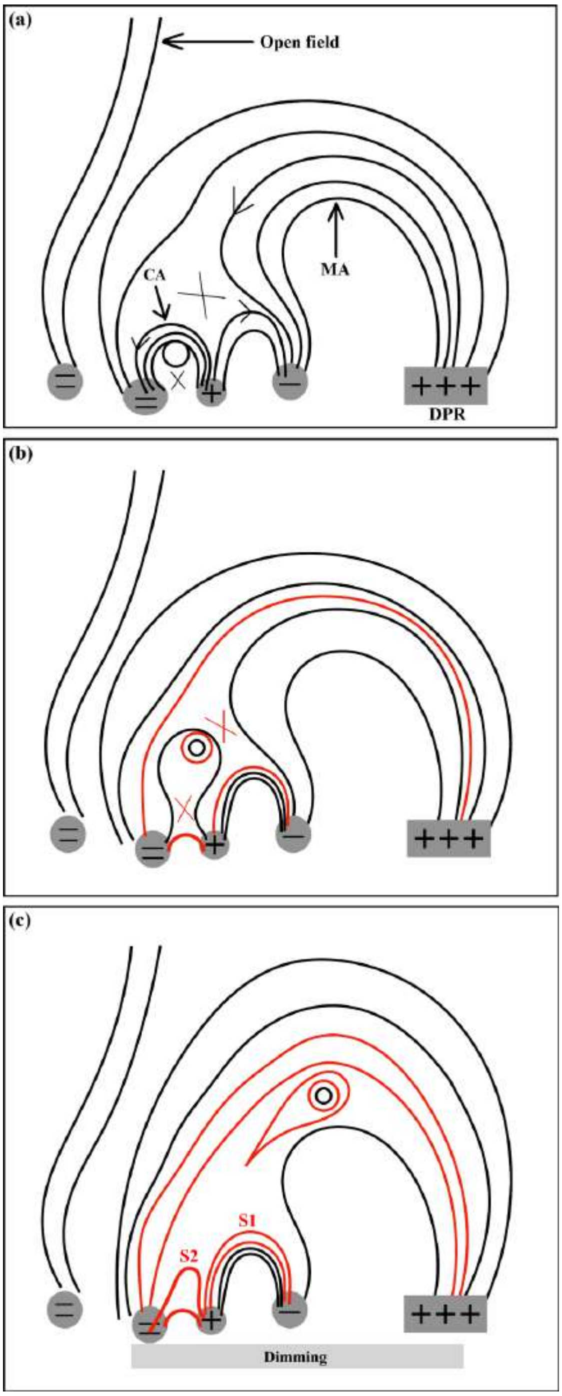

Figure 5.11: schematic representation of the MAB scenario for the production of broad CMEs resulting from homologous compact major blowout-eruptions, viewed from solar west. Panel (a): the large MA connects the DPR and the negative flux region of the AR. The large negative sunspot of the AR is denoted by circles with double negative signs, from where the open field lines also originate. On the right of the large sunspot, we show a compact bipolar region hosting the compact arcade (CA), enveloping the flux rope. On the right of CA, we show another set of field lines, which connect the compact region and a larger negative flux region, situated north of the compact region (see panels (b) and (f) of Figures 5.5–5.7). The plausible reconnection sites are marked by cross signs. Panel (b): the reconnection between CA and MA, weakens the MA field lines and creates a pathway for the eruption of the flux rope. Panel (c): the external reconnection between CA and MA produces the set of field lines labeled S1, and the internal reconnection between the legs of the field lines stretched by the erupting flux rope creates the set of field lines labeled S2. The brightening in the outer footpoints of the S1 field lines is observationally confirmed by the wide circular ribbon structure, whereas the S2 field lines exhibit themselves as compact post-flare loop arcades (see panels (d) and (h) of Figures 5.5–5.7). The extent of the dimming resulting from the blowout-eruption of MA is also indicated in panel (c).

We show a schematic representation (viewed from solar west) of the MAB scenario in Figure 5.11, which explains the production of the broad CMEs resulting from our three homologous compact major blowout-eruption solar flares. In Figure 5.11(a), we show the large-scale fields (see white field lines in Figures 5.3(c) and 5.4, panels (b) and (c)), which has one end rooted in the DPR, while the other end terminating at a part of the large leading negative sunspot of the AR and at a negative flux region situated north of the compact mixed-polarity region (labeled as "core" in Figure 5.3(b)). The large leading negative sunspot of the AR is denoted by circles with double negative signs. The large field lines connecting the DPR and the AR essentially form an MA. The open field lines (see pink field lines in Figures 5.3(a), (c), and 5.4, panels (b) and (c)) originate from the large negative sunspot in the adjacent neighborhood of the MA. In Figure 5.11(a), on the right of the large negative sunspot, we show the positive polarity of the compact region, which hosts the compact arcade (CA; see green field lines in Figure 5.8) enveloping the flux rope. On the right of the CA we show another set of field lines; these connect to a distant dispersed negative polarity region, situated north of the compact mixed-polarity region (see panels (b) and (f) of Figures 5.5–5.7). The eruption of the flux rope induces reconnection (i.e., external reconnection) between the CA and MA field lines. Another reconnection, which is standard flare reconnection (i.e., internal reconnection) will set in between the legs of the field lines stretched by the erupting flux rope. The plausible reconnection sites are marked by cross signs (Figure 5.11, panels (a) and (b)) and the post-reconnection loops are drawn in red in Figure 5.11, panels (b) and (c). The reconnection weakens the MA field lines gradually and creates a "pathway" for the subsequent eruption of the flux rope. The eruption of the flux rope continues along the curve of the large MA loops. As this process continues, the flux rope eventually blows out the large MA loops, making the strong dimming region (indicated in Figure 5.11(c)) extending from the AR up to the DPR (observed to form northward of the AR; see Figures 5.9 and 5.10). The extent of the dimming region demarcates the lateral section of the MA that gets blown out and results in the broad CME structure. In Figure 5.11(c), we indicate two sets (S1 and S2) of post-reconnection field lines, where the observations indicate that S1 is larger in size than S2, since the negative footpoint of S1 connects to a relatively distant region compared to S2 (see panels (b) and (f) of Figures 5.5–5.7). The brightness along the outer footpoints of the S1 field lines is observationally confirmed by a wide circular ribbon structure, that is clearly visible during the peak of the flares (see panels (d) and (h) of Figures 5.5–5.7). The S2 field lines exhibit themselves as relatively compact post-flare loop arcades (indicated by the red arrow in Figure 5.5(d); see also Figure 5.5(h), and panels (d) and (h) of Figures 5.6, 5.7)), appearing within the circular ribbon periphery. The flux rope is channeled long the curve of the MA structure, as its eruption continues. Thus, the flux rope experiences substantial deviation from its original path, as the eruption proceeds. This kind of lateral deflection during the eruption was also observed in previous studies related to the "over-and-out" type CMEs (Jiang *et al.*, 2009; Yang *et al.*, 2011, 2012b,a). We observe large surges from the flaring region during the post-eruptive stages of all the events. The surges, consisting of cool plasma expelled from the flaring region, nearly follow the open field lines shown in Figures 5.3(c), 5.4, and 5.11. Notably, a significant portion of the surge erupts from the eastern part of the flaring region for event I and from the western part for the following events, which is likely due to the changes in the magnetic configurations of the flaring region.

Between our study and the study of Moore and Sterling (2007), there are some similarities as well as dissimilarities in terms of the pre-eruptive configuration of different observational features detected, but in both cases the central idea involving the physics of eruption remains the same. Unlike the eruption in Moore and Sterling (2007), the eruptions in our analysis do not occur in the foot of one leg of a large MA in the base of a large streamer; another difference is that our CMEs have greater angular widths than did the Moore and Sterling (2007) CME. On the other hand, our case and the Moore and Sterling (2007) paper have important similarities: e.g., both studies have compact ejective flares seated at one foot of a large MA, and in both cases the origin of the CMEs occurs laterally far offset from the flaring location. In view of the above, we note that our analysis presents important observational evidence of the MAB scenario for CME formation resulting from homologous compact major blowout-eruption solar flares. Our work essentially generalizes the MAB mechanism formulated in Moore and Sterling (2007) to more general cases, including cases with homologous flares.

In summary, our study incorporates a comprehensive analysis of three homologous ejective eruptive events triggered by a sequence of three compact flux rope eruptions and subsequent blowout of three broad CMEs. The eruptions produce flares of successively increasing intensities (M2.0, M2.6, X1.0), and generate large-scale EUV dimmings. The occurrence of homologous and broad CMEs has important consequences for space weather conditions. A comprehensive understanding of such events and their generation mechanism is vital as the space era progresses.

Chapter 6

Conclusions and Future Prospects

The combination of multi-wavelength and multi-instrument observational data, complemented by the coronal magnetic field modeling techniques helps us to explore some of the important and debatable aspects related to the solar eruptive phenomena. This chapter highlights the work presented in my thesis and discuss future research plans.

6.1 Summary and conclusions

The prime objective of this thesis is to explore the initiation and evolution of MFRs during solar eruptive phenomena along with associated energy release processes that cause intense flaring emission. In Chapter 1, we introduce the subject in detail and formulate the scientific objectives of the thesis. Detailed description of the observational data sources and analysis methods are provided in Chapter 2.

In Chapter 3, we explore the initial activation and subsequent eruption of an MFR leading to a major eruptive flare. We observe hot coronal channels in the high temprature sensitive EUV passbands (e.g., 94 Å and 131 Å), which we identify as MFRs in the pre-eruption phase. Coronal magnetic field modeling results obtained from the NLFFF extrapolation technique reveal the existence of an MFR oriented along the PIL of the flaring region, co-spatial to the hot channel. A remarkable aspect of this study is an active pre-flare phase lasting for about an hour during which the hot channel is in the build-up stage and displays co-spatial HXR emission up to energies of 25 keV. To our knowledge, this is the first evidence of the HXR coronal hot channel. Prior to the flares's impulsive phase, the MFR undergoes slow rise ($\approx$14 km s^{-1}) for $\approx$12 minutes, which we attribute to the faster build-up and activation of the MFR by tether-cutting reconnection at multiple locations along the MFR itself. Thereafter, a sudden transition in the kinematic evolution of the MFR is observed from the phase of slow to fast rise ($\approx$109 km s^{-1} with acceleration

$\approx$110 m s^{-2}), which precisely divides the pre-flare and impulsive phase of the flare. This 'slow-to-fast' transition of the erupting MFR points toward the feedback process between the early dynamics of the eruption and the strength of the flare magnetic reconnection, provided by the outflowing magnetized plasma material from the reconnection site.

The origin of various forms of solar activity is inherently guided by the complexity of the solar magnetic field. The strong and concentrated magnetic flux emerges from the solar interior and appears on the photosphere in the form of active regions (ARs). The large and complex ARs usually produce multiple, strong flaring events with powerful CMEs. In complex ARs, the production of homologous flares is not uncommon which occur from the same location of an AR with morphological resemblance. In Chapter 4, we focus on the occurrence of homologous eruptive flares together with the intrinsic association between the photospheric and coronal magnetic fields that results into the repetitive flaring process. For this purpose, we select three homologus eruptive flares with successively increasing intensities (i.e., M2.0, M2.6, and X1.0) from a complex NOAA AR 12017. The coronal magnetic field modeling results suggest that the flares are triggered by the eruption of compact MFRs embedded by a densely packed system of bipolar loops within a small part of the AR. The photospheric magnetic field over an interval of $\approx$44 hr encompassing the three events undergoes important phases of emergence and cancellation processes together with significant changes near the PILs within the flaring region. Notably, between the second and third event, we observe a prominent phase of magnetic flux emergence which temporally correlates with the build-up phase of free magnetic energy in the AR corona. Our observational results suggest an efficient coupling between the rapidly evolving photospheric and coronal magnetic fields in the AR that lead to a continued phase of the build-up of free magnetic energy in response to persistent photospheric flux emergence, resulting into the three homologous flares of successively increasing intensities.

The homologous eruptive flares studied in Chapter 4 originate from the eruptions of compact flux ropes located over a short PIL in a strong, mixed magnetic polarity region. However, the CMEs resulting from these compact eruptions show large-scale structures in the coronagraphic images. This important aspect, i.e., production of broad CMEs from compact blowout-eruption solar flares, is explored in Chapter 5. We carry out PFSS extrapolation in and around a larger area about the eruption-source site. We find a set of large-scale coronal magnetic field lines (magnetic-arch) connect the core (i.e., source of eruptions) of the flaring region to a distant, dispersed polarity region. Our observational results point toward the MAB scenario to be responsible for the production of broad CMEs. According to the MAB scenario: each compact-flare blowout-eruption is seated in one foot of a far-reaching magnetic arch, explodes up the encasing leg of the arch, and blows out the arch to make a broad CME. The explanation of the MAB scenario was initially given by Moore and Sterling (2007) in case of eruptions within narrow coronal streamers. In our case, we generalize the MAB scanario for the production of broad CMEs resulting from compact homologous eruptions involving interaction between the compact eruptions and large-scale coronal magnetic structures. Our explanation on the formation mechanism of broad CMEs is observationally substantiated by the appearance of large EUV dimmings surrounding a large area of the core region. The spatial extent of the dimming demarcates the extent of the opened section of the magnetic arch, which participates in the eruption process.

In essence, my PhD thesis provides detailed multi-wavelength investigations of the origin and development of solar eruptions. In our studies, we emphasize on the build-up, activation, and subsequent evolution of MFRs that ultimately evolve into the CMEs. The detection of HXR emission from activated MFR and development of generalized MAB mechanism for the production of broad CMEs are among the novel findings presented in this thesis.

6.2 Future prospects

In future, my plan is to carry out research works in line of the topics addressed in this thesis. The future works will be aimed at strengthening the ideas and reults presented in this thesis. Some of the studies which may be pursued in future are briefly listed below.

- We plan to study the formation of broad CMEs in the context of generalized MAB scenario discussed in Chapter 5. For this purpose, we will manually examine the source regions of broad CMEs occurred during the maximum phase of cycle 24 and identify cases where CMEs are linked with compact blowout-eruption solar flares. The study will shed light on the development of large-scale CME structure in the lower corona.

- Our current analyses comprise of the eruptive flares resulting into CMEs. In future, we plan to carry out investigation of the failed/confined eruptions that do not result into the formation of CMEs. In this work, we will undertake extensive exploration of coronal magnetic field configurations in 3D.

- We plan to explore small-scale energetic processes in solar corona, such as, A and sub-A class flares, compact jets, etc. To identify the small-scale transients and their temporal behavior, we will utilize the unprecedented data from the Solar X-Ray Monitor on board the Chandrayaan-2 Orbiter (XSM; Mithun *et al.*, 2020).

References

Altschuler, M. D., and Newkirk, G., 1969 Sep., "Magnetic Fields and the Structure of the Solar Corona. I: Methods of Calculating Coronal Fields," *Solar Phys.* **9**, 131–149.

Amari, T., Aly, J. J., Mikic, Z., and Linker, J., 2010 Jul., "Coronal Mass Ejection Initiation: On the Nature of the Flux Cancellation Model," *Astrophys. J. Lett.* **717**, L26–L30.

Amari, T., Luciani, J. F., Aly, J. J., Mikic, Z., and Linker, J., 2003 Mar., "Coronal Mass Ejection: Initiation, Magnetic Helicity, and Flux Ropes. I. Boundary Motion-driven Evolution," *Astrophys. J.* **585**, 1073–1086.

Amari, T., Luciani, J. F., Mikic, Z., and Linker, J., 1999 Jun., "Three-dimensional Solutions of Magnetohydrodynamic Equationsfor Prominence Magnetic Support: Twisted Magnetic Flux Rope," *Astrophys. J. Lett.* **518**, L57–L60.

Antiochos, S. K., Dahlburg, R. B., and Klimchuk, J. A., 1994 Jan., "The Magnetic Field of Solar Prominences," *Astrophys. J. Lett.* **420**, L41.

Antiochos, S. K., DeVore, C. R., and Klimchuk, J. A., 1999 Jan., "A Model for Solar Coronal Mass Ejections," *Astrophys. J.* **510**, 485–493.

Asai, A., Ishii, T. T., Kurokawa, H., Yokoyama, T., and Shimojo, M., 2003 Mar., "Evolution of Conjugate Footpoints inside Flare Ribbons during a Great Two-Ribbon Flare on 2001 April 10," *Astrophys. J.* **586**, 624–629.

Aulanier, G., Démoulin, P., Mein, N., van Driel-Gesztelyi, L., Mein, P., and Schmieder, B., 1999 Feb., "3-D magnetic configurations supporting prominences. III. Evolution of fine structures observed in a filament channel," *Astron. Astrophys.* **342**, 867–880.

Aulanier, G., Janvier, M., and Schmieder, B., 2012 Jul., "The standard flare model in three dimensions. I. Strong-to-weak shear transition in post-flare loops," *Astron. Astrophys.* **543**, A110

Aulanier, G., Pariat, E., and Démoulin, P., 2005 Dec., “Current sheet formation in quasi-separatrix layers and hyperbolic flux tubes,” *Astron. Astrophys.* **444**, 961–976.

Aulanier, G., Pariat, E., Démoulin, P., and DeVore, C. R., 2006 Nov.a, “Slip-Running Reconnection in Quasi-Separatrix Layers,” *Solar Phys.* **238**, 347–376.

Aulanier, G., and Schmieder, B., 2002 May, “The magnetic nature of wide EUV filament channels and their role in the mass loading of CMEs,” *Astron. Astrophys.* **386**, 1106–1122.

Aulanier, G., Török, T., Démoulin, P., and DeLuca, E. E., 2010 Jan., “Formation of Torus-Unstable Flux Ropes and Electric Currents in Erupting Sigmoids,” *Astrophys. J.* **708**, 314–333.

Aulanier, G., DeVore, C. R., and Antiochos, S. K., 2006 Aug.b, “Solar Prominence Merging,” *Astrophys. J.* **646**, 1349–1357.

Awasthi, A. K., Liu, R., Wang, H., Wang, Y., and Shen, C., 2018 Apr, “Pre-eruptive Magnetic Reconnection within a Multi-flux-rope System in the Solar Corona,” *Astrophys. J.* **857**, 124

Baker, D., Balstad, R., Bodeau, M., Cameron, E., Fennell, J., Fisher, G., Forbes, K., Kintner, P., Leffler, L., Lewis, W., Reagan, J., Small, A., Stansell, T., and Strachan, L., 2008 12, *Severe Space Weather Events - Understanding Societal and Economic Impacts: A Workshop Report.*, ISBN 978-0-309-12769

Bemporad, A., Sterling, A. C., Moore, R. L., and Poletto, G., 2005 Dec., “A New Variety of Coronal Mass Ejection: Streamer Puffs from Compact Ejective Flares,” *Astrophys. J. Lett.* **635**, L189–L192.

Benz, A. O., 2017 Dec, “Flare Observations,” *Living Reviews in Solar Physics* **14**, 2

Bernasconi, P. N., Rust, D. M., Georgoulis, M. K., and Labonte, B. J., 2002 Sep., “Moving Dipolar Features in an Emerging Flux Region,” *Solar Phys.* **209**, 119–139.

Bisoi, S. K., Chakrabarty, D., Janardhan, P., Rastogi, R. G., Yoshikawa, A., Fujiki, K., Tokumaru, M., and Yan, Y., 2016 May, “The prolonged southward IMF-B_z event of 2-4 May 1998: Solar, interplanetary causes and geomagnetic consequences,” *Journal of Geophysical Research (Space Physics)* **121**, 3882–3904.

Bornmann, P. L., Speich, D., Hirman, J., Matheson, L., Grubb, R., Garcia, H., and Viereck, R., 1996 Oct., “GOES x-ray sensor and its use in predicting solar-terrestrial disturbances," in *GOES-8 and Beyond*, Society of Photo-Optical Instrumentation Engineers (SPIE) Conference Series, Vol. 2812, edited by Washwell, E. R., pp. 291–298.

Borrero, J. M., Tomczyk, S., Kubo, M., Socas-Navarro, H., Schou, J., Couvidat, S., and Bogart, R., 2011 Oct., "VFISV: Very Fast Inversion of the Stokes Vector for the Helioseismic and Magnetic Imager," *Solar Phys.* **273**, 267–293.

Boursier, Y., Lamy, P., Llebaria, A., Goudail, F., and Robelus, S., 2009 Jun., "The ARTEMIS Catalog of LASCO Coronal Mass Ejections. Automatic Recognition of Transient Events and Marseille Inventory from Synoptic maps," *Solar Phys.* **257**, 125–147.

Brown, J. C., 1971 Jul., "The Deduction of Energy Spectra of Non-Thermal Electrons in Flares from the Observed Dynamic Spectra of Hard X-Ray Bursts," *Solar Phys.* **18**, 489–502.

Brueckner, G. E., Howard, R. A., Koomen, M. J., Korendyke, C. M., Michels, D. J., Moses, J. D., Socker, D. G., Dere, K. P., Lamy, P. L., Llebaria, A., Bout, M. V., Schwenn, R., Simnett, G. M., Bedford, D. K., and Eyles, C. J., 1995 Dec., "The Large Angle Spectroscopic Coronagraph (LASCO)," *Solar Phys.* **162**, 357–402.

Burlaga, L., Fitzenreiter, R., Lepping, R., Ogilvie, K., Szabo, A., Lazarus, A., Steinberg, J., Gloeckler, G., Howard, R., Michels, D., Farrugia, C., Lin, R. P., and Larson, D. E., 1998 Jan, "A magnetic cloud containing prominence material: January 1997," *J. Geophys. Res.* **103**, 277–286.

Burlaga, L., Sittler, E., Mariani, F., and Schwenn, R., 1981 Aug, "Magnetic loop behind an interplanetary shock: Voyager, Helios, and IMP 8 observations," *J. Geophys. Res.* **86**, 6673–6684.

Burlaga, L. F., Skoug, R. M., Smith, C. W., Webb, D. F., Zurbuchen, T. H., and Reinard, A., 2001 Oct, "Fast ejecta during the ascending phase of solar cycle 23: ACE observations, 1998-1999," *J. Geophys. Res.* **106**, 20957–20978.

Cai, Z. M., Zhang, Q. M., Ning, Z. J., Su, Y. N., and Ji, H. S., 2021 Apr., "Energy Partition in Four Confined Circular-Ribbon Flares," *Solar Phys.* **296**, 61

Cairns, I. H., Knock, S. A., Robinson, P. A., and Kuncic, Z., 2003 Apr., "Type II Solar Radio Bursts: Theory and Space Weather Implications," *Space Sci. Rev.* **107**, 27–34.

Canou, A., and Amari, T., 2010 Jun, "A Twisted Flux Rope as the Magnetic Structure of a Filament in Active Region 10953 Observed by Hinode," *Astrophys. J.* **715**, 1566–1574.

Carmichael, H., 1964, "A Process for Flares," in *NASA Special Publication*, Vol. 50, p. 451.

Chandra, R., Schmieder, B., Aulanier, G., and Malherbe, J. M., 2009 Aug., "Evidence of Magnetic Helicity in Emerging Flux and Associated Flare," *Solar Phys.* **258**, 53–67.

Chatterjee, P., and Fan, Y., 2013 Nov., "Simulation of Homologous and Cannibalistic Coronal Mass Ejections produced by the Emergence of a Twisted Flux Rope into the Solar Corona," *Astrophys. J. Lett.* **778**, L8

Chen, H., Zhang, J., Cheng, X., Ma, S., Yang, S., and Li, T., 2014 Deca, "Direct Observations of Tether-cutting Reconnection during a Major Solar Event from 2014 February 24 to 25," *Astrophys. J. Lett.* **797**, L15

Chen, P. F., 2011 Apr., "Coronal Mass Ejections: Models and Their Observational Basis," *Living Reviews in Solar Physics* **8**, 1

Chen, P. F., Harra, L. K., and Fang, C., 2014 Mar.b, "Imaging and Spectroscopic Observations of a Filament Channel and the Implications for the Nature of Counter-streamings," *Astrophys. J.* **784**, 50

Chen, Y., 2013 05, "A review of recent studies on coronal dynamics: Streamers, coronal mass ejections, and their interactions," *Chinese Science Bulletin* **58**, doi: \bibinfo{doi}{10.1007/s11434-013-5669-6}

Cheng, X., Ding, M. D., Guo, Y., Zhang, J., Vourlidas, A., Liu, Y. D., Olmedo, O., Sun, J. Q., and Li, C., 2014 Jan.a, "Tracking the Evolution of a Coherent Magnetic Flux Rope Continuously from the Inner to the Outer Corona," *Astrophys. J.* **780**, 28

Cheng, X., Ding, M. D., Zhang, J., Srivastava, A. K., Guo, Y., Chen, P. F., and Sun, J. Q., 2014 Jul.b, "On the Relationship Between a Hot-channel-like Solar Magnetic Flux Rope and its Embedded Prominence," *Astrophys. J. Lett.* **789**, L35

Cheng, X., Zhang, J., Ding, M. D., Olmedo, O., Sun, X. D., Guo, Y., and Liu, Y., 2013 Jun., "Investigating Two Successive Flux Rope Eruptions in a Solar Active Region," *Astrophys. J. Lett.* **769**, L25

Cheng, X., Zhang, J., Liu, Y., and Ding, M. D., 2011 May, "Observing Flux Rope Formation During the Impulsive Phase of a Solar Eruption," *Astrophys. J. Lett.* **732**, L25

Cheng, X., Zhang, J., Saar, S. H., and Ding, M. D., 2012 Dec., "Differential Emission Measure Analysis of Multiple Structural Components of Coronal Mass Ejections in the Inner Corona," *Astrophys. J.* **761**, 62

Cheng, X., Guo, Y., and Ding, M., 2017 Aug, "Origin and Structures of Solar Eruptions I: Magnetic Flux Rope," *Science in China Earth Sciences* **60**, 1383–1407.

Chertok, I. M., Grechnev, V. V., Hudson, H. S., and Nitta, N. V., 2004 Feb., "Homologous large-scale activity in solar eruptive events of 24-26 November 2000," *Journal of Geophysical Research (Space Physics)* **109**, A02112

Cheung, M. C. M., Rempel, M., Chintzoglou, G., Chen, F., Testa, P., Martínez-Sykora, J., Sainz Dalda, A., DeRosa, M. L., Malanushenko, A., Hansteen, V., De Pontieu, B., Carlsson, M., Gudiksen, B., and McIntosh, S. W., 2019 Nov., "A comprehensive three-dimensional radiative magnetohydrodynamic simulation of a solar flare," *Nature Astronomy* **3**, 160–166.

Cheung, M. C. M., and Isobe, H., 2014 Jul., "Flux Emergence (Theory)," *Living Reviews in Solar Physics* **11**, 3

Chifor, C., Mason, H. E., Tripathi, D., Isobe, H., and Asai, A., 2006 Nov, "The early phases of a solar prominence eruption and associated flare: a multi-wavelength analysis," *Astron. Astrophys.* **458**, 965–973.

Chifor, C., Tripathi, D., Mason, H. E., and Dennis, B. R., 2007 Sep, "X-ray precursors to flares and filament eruptions," *Astron. Astrophys.* **472**, 967–979.

Chintzoglou, G., Patsourakos, S., and Vourlidas, A., 2015 Aug., "Formation of Magnetic Flux Ropes during a Confined Flaring Well before the Onset of a Pair of Major Coronal Mass Ejections," *Astrophys. J.* **809**, 34

Chintzoglou, G., Zhang, J., Cheung, M. C. M., and Kazachenko, M., 2019 Jan., "The Origin of Major Solar Activity: Collisional Shearing between Nonconjugated Polarities of Multiple Bipoles Emerging within Active Regions," *Astrophys. J.* **871**, 67

Clyne, J., Mininni, P., Norton, A., and Rast, M., 2007 Aug., "Interactive desktop analysis of high resolution simulations: application to turbulent plume dynamics and current sheet formation," *New Journal of Physics* **9**, 301.

Dalmasse, K., Aulanier, G., Démoulin, P., Kliem, B., Török, T., and Pariat, E., 2015 Sep., "The Origin of Net Electric Currents in Solar Active Regions," *Astrophys. J.* **810**, 17

Demastus, H. L., Wagner, W. J., and Robinson, R. D., 1973 Aug., “Coronal Disturbances. I: Fast Transient Events Observed in the Green Coronal Emission Line During the Last Solar Cycle,” *Solar Phys.* **31**, 449–459.

Demoulin, P., Bagala, L. G., Mandrini, C. H., Henoux, J. C., and Rovira, M. G., 1997 Sep., “Quasi-separatrix layers in solar flares. II. Observed magnetic configurations..” *Astron. Astrophys.* **325**, 305–317.

Denker, C., Johannesson, A., Marquette, W., Goode, P. R., Wang, H., and Zirin, H., 1999 Jan., “Synoptic Hα Full-Disk Observations of the Sun from BigBear Solar Observatory - I. Instrumentation, Image Processing, Data Products, and First Results,” *Solar Phys.* **184**, 87–102.

Dennis, B. R., 1988 Mar., “Solar Flare Hard X-Ray Observations,” *Solar Phys.* **118**, 49–94.

Dere, K. P., Brueckner, G. E., Howard, R. A., Koomen, M. J., Korendyke, C. M., Kreplin, R. W., Michels, D. J., Moses, J. D., Moulton, N. E., Socker, D. G., St. Cyr, O. C., Delaboudinière, J. P., Artzner, G. E., Brunaud, J., Gabriel, A. H., Hochedez, J. F., Millier, F., Song, X. Y., Chauvineau, J. P., Marioge, J. P., Defise, J. M., Jamar, C., Rochus, P., Catura, R. C., Lemen, J. R., Gurman, J. B., Neupert, W., Clette, F., Cugnon, P., van Dessel, E. L., Lamy, P. L., Llebaria, A., Schwenn, R., and Simnett, G. M., 1997 Oct., “EIT and LASCO Observations of the Initiation of a Coronal Mass Ejection,” *Solar Phys.* **175**, 601–612.

Devi, P., Joshi, B., Chandra, R., Mitra, P. K., Veronig, A. M., and Joshi, R., 2020 Jun., “Development of a Confined Circular-Cum-Parallel Ribbon Flare and Associated Pre-Flare Activity,” *Solar Phys.* **295**, 75

DeVore, C. R., and Antiochos, S. K., 2008 Jun., “Homologous Confined Filament Eruptions via Magnetic Breakout,” *Astrophys. J.* **680**, 740–756.

Dhara, S. K., Belur, R., Kumar, P., Banyal, R. K., Mathew, S. K., and Joshi, B., 2017 Oct, “Trigger of Successive Filament Eruptions Observed by SDO and STEREO,” *Solar Phys.* **292**, 145

Domingo, V., Fleck, B., and Poland, A. I., 1995 Apr., “SOHO: The Solar and Heliospheric Observatory,” *Space Sci. Rev.* **72**, 81–84.

Dryer, M., 1994 Sep., “Interplanetary Studies: Propagation of Disturbances Between the Sun and the Magnetosphere,” *Space Sci. Rev.* **67**, 363–419.

Duan, A., Jiang, C., Hu, Q., Zhang, H., Gary, G. A., Wu, S. T., and Cao, J., 2017 Jun., "Comparison of Two Coronal Magnetic Field Models to Reconstruct a Sigmoidal Solar Active Region with Coronal Loops," *Astrophys. J.* **842**, 119

Fan, Y., 2001 Jun., "The Emergence of a Twisted Ω-Tube into the Solar Atmosphere," *Astrophys. J. Lett.* **554**, L111–L114.

Fan, Y., 2005 Sep, "Coronal Mass Ejections as Loss of Confinement of Kinked Magnetic Flux Ropes," *Astrophys. J.* **630**, 543–551.

Fan, Y., and Gibson, S. E., 2007 Oct., "Onset of Coronal Mass Ejections Due to Loss of Confinement of Coronal Flux Ropes," *Astrophys. J.* **668**, 1232–1245.

Fan, Y., 2009 Dec., "Magnetic Fields in the Solar Convection Zone," *Living Reviews in Solar Physics* **6**, 4

Fárník, F., Hudson, H. S., Karlický, M., and Kosugi, T., 2003 Mar., "X-ray and radio observations of the activation stages of an X-class solar flare," *Astron. Astrophys.* **399**, 1159–1166.

Fárník, F., and Savy, S. K., 1998 Dec, "Soft X-Ray Pre-Flare Emission Studied in Yohkoh-SXT Images," *Solar Phys.* **183**, 339–357.

Fárník, F., Hudson, H., and Watanabe, T., 1996 Apr, "Spatial Relations between Preflares and Flares," *Solar Phys.* **165**, 169–179.

Filippov, B., Martsenyuk, O., Srivastava, A. K., and Uddin, W., 2015 Mar, "Solar Magnetic Flux Ropes," *Journal of Astrophysics and Astronomy* **36**, 157–184.

Fisher, R. R., Lee, R. H., MacQueen, R. M., and Poland, A. I., 1981 Mar., "New Mauna Loa coronagraph systems," *Appl.* **20**, 1094–1101.

Fisk, L. A., 2005 Jun., "The Open Magnetic Flux of the Sun. I. Transport by Reconnections with Coronal Loops," *Astrophys. J.* **626**, 563–573.

Fleishman, G. D., and Pevtsov, A. A., 2018 Mar., "Electric Currents in the Solar Atmosphere," in *Electric Currents in Geospace and Beyond*, Vol. 235, edited by Keiling, A., Marghitu, O., and Wheatland, M., pp. 43–65.

Fletcher, L., Dennis, B. R., Hudson, H. S., Krucker, S., Phillips, K., Veronig, A., Battaglia, M., Bone, L., Caspi, A., Chen, Q., Gallagher, P., Grigis, P. T., Ji, H., Liu, W., Milligan, R. O., and Temmer, M., 2011 Sep, "An Observational Overview of Solar Flares," *Space Sci. Rev.* **159**, 19–106.

Fletcher, L., and Hudson, H. S., 2002 Nov., "Spectral and Spatial Variations of Flare Hard X-ray Footpoints," *Solar Phys.* **210**, 307–321.

Forbes, T. G., 2000 Oct., "A review on the genesis of coronal mass ejections," *J. Geophys. Res.* **105**, 23153–23166.

Forbes, T. G., Malherbe, J. M., and Priest, E. R., 1989 Sep., "The Formation of Flare Loops by Magnetic Reconnection and Chromospheric Ablation," *Solar Phys.* **120**, 285–307.

Freeland, S. L., and Handy, B. N., 2012 Aug., "SolarSoft: Programming and data analysis environment for solar physics,"

Fursyak, Y. A., Kutsenko, A. S., and Abramenko, V. I., 2020 Feb., "Distributed Electric Currents in Solar Active Regions," *Solar Phys.* **295**, 19

Gallagher, P. T., and Long, D. M., 2011 Jul., "Large-scale Bright Fronts in the Solar Corona: A Review of "EIT waves"," *Space Sci. Rev.* **158**, 365–396.

Gary, G. A., 2001 Oct., "Plasma Beta above a Solar Active Region: Rethinking the Paradigm," *Solar Phys.* **203**, 71–86.

Gary, G. A., and Hagyard, M. J., 1990 Mar., "Transformation of vector magnetograms and the problems associated with the effects of perspective and the azimuthal ambiguity," *Solar Phys.* **126**, 21–36.

Georgoulis, M. K., Nindos, A., and Zhang, H., 2019 Jul., "The source and engine of coronal mass ejections," *Philosophical Transactions of the Royal Society of London Series A* **377**, 20180094.

Gibson, S. E., and Fan, Y., 2006 Dec, "Coronal prominence structure and dynamics: A magnetic flux rope interpretation," *Journal of Geophysical Research (Space Physics)* **111**, A12103

Gibson, S. E., Fan, Y., Török, T., and Kliem, B., 2006 Jun.a, "The Evolving Sigmoid: Evidence for Magnetic Flux Ropes in the Corona Before, During, and After CMES," *Space Sci. Rev.* **124**, 131–144.

Gibson, S. E., Fletcher, L., Del Zanna, G., Pike, C. D., Mason, H. E., Mandrini, C. H., Démoulin, P., Gilbert, H., Burkepile, J., Holzer, T., Alexander, D., Liu, Y., Nitta, N., Qiu, J., Schmieder, B., and Thompson, B. J., 2002 Aug., "The Structure and Evolution of a Sigmoidal Active Region," *Astrophys. J.* **574**, 1021–1038.

Gibson, S. E., Foster, D., Burkepile, J., de Toma, G., and Stanger, A., 2006 Apr.b, "The Calm before the Storm: The Link between Quiescent Cavities and Coronal Mass Ejections," *Astrophys. J.* **641**, 590–605.

Gibson, S., 2015 Jan., "Coronal Cavities: Observations and Implications for the Magnetic Environment of Prominences," in *Solar Prominences*, Astrophysics and Space Science Library, Vol. 415, edited by Vial, J.-C. and Engvold, O., p. 323.

Gibson, S. E., 2018 Oct., "Solar prominences: theory and models. Fleshing out the magnetic skeleton," *Living Reviews in Solar Physics* **15**, 7

Gopalswamy, N., 2010 Dec., "Corona Mass Ejections: a Summary of Recent Results," in *20th National Solar Physics Meeting*, Vol. 20, edited by Dorotovic, I., pp. 108–130.

Gopalswamy, N., 2016 Dec., "History and development of coronal mass ejections as a key player in solar terrestrial relationship," *Geoscience Letters* **3**, 8

Gopalswamy, N., and Thompson, B. J., 2000 Nov., "Early life of coronal mass ejections," *Journal of Atmospheric and Solar-Terrestrial Physics* **62**, 1457–1469.

Gopalswamy, N., 2006 Sep., "Coronal Mass Ejections of Solar Cycle 23," *Journal of Astrophysics and Astronomy* **27**, 243–254.

Gosling, J. T., Hildner, E., MacQueen, R. M., Munro, R. H., Poland, A. I., and Ross, C. L., 1974 Nov., "Mass ejections from the Sun: A view from Skylab," *J. Geophys. Res.* **79**, 4581.

Gou, T., Liu, R., Kliem, B., Wang, Y., and Veronig, A. M., 2019 Mar., "The Birth of A Coronal Mass Ejection," *Science Advances* **5**, 7004.

Green, L. M., and Kliem, B., 2009 Aug., "Flux Rope Formation Preceding Coronal Mass Ejection Onset," *Astrophys. J. Lett.* **700**, L83–L87.

Green, L. M., Kliem, B., Török, T., van Driel-Gesztelyi, L., and Attrill, G. D. R., 2007 Dec., "Transient Coronal Sigmoids and Rotating Erupting Flux Ropes," *Solar Phys.* **246**, 365–391.

Green, L. M., Kliem, B., and Wallace, A. J., 2011 Feb., "Photospheric flux cancellation and associated flux rope formation and eruption," *Astron. Astrophys.* **526**, A2

Green, L. M., Matthews, S. A., van Driel-Gesztelyi, L., Harra, L. K., and Culhane, J. L., 2002 Feb., "Multi-wavelength observations of an X-class flare without a coronal mass ejection.." *Solar Phys.* **205**, 325–339.

Harra, L. K., Williams, D. R., Wallace, A. J., Magara, T., Hara, H., Tsuneta, S., Sterling, A. C., and Doschek, G. A., 2009 Feb., "Coronal Nonthermal Velocity Following Helicity Injection Before an X-Class Flare," *Astrophys. J. Lett.* **691**, L99–L102.

Harrison, R. A., 1995 Dec., "The nature of solar flares associated with coronal mass ejection.." *Astron. Astrophys.* **304**, 585.

Hernandez-Perez, A., Su, Y., Veronig, A. M., Thalmann, J., Gömöry, P., and Joshi, B., 2019 Apr.a, "Pre-eruption Processes: Heating, Particle Acceleration, and the Formation of a Hot Channel before the 2012 October 20 M9.0 Limb Flare," *Astrophys. J.* **874**, 122

Hernandez-Perez, A., Su, Y., Veronig, A. M., Thalmann, J., Gömöry, P., and Joshi, B., 2019 Aprb, "Pre-eruption Processes: Heating, Particle Acceleration, and the Formation of a Hot Channel before the 2012 October 20 M9.0 Limb Flare," *Astrophys. J.* **874**, 122

Hirayama, T., 1974 Feb, "Theoretical Model of Flares and Prominences. I: Evaporating Flare Model," *Solar Phys.* **34**, 323–338.

Hirayama, T., 1985 Oct., "Modern Observations of Solar Prominences," *Solar Phys.* **100**, 415.

Hirayama, T., and Nakagomi, Y., 1974 Jan., "Observations of Prominences in He II with a New 25 CM Coronagraph," *Publ. Astron. Soc. Jpn.* **26**, 53.

Högbom, J. A., 1974 Jun., "Aperture Synthesis with a Non-Regular Distribution of Interferometer Baselines," *Astron. Astrophys. Suppl.* **15**, 417.

Holman, G. D., Aschwanden, M. J., Aurass, H., Battaglia, M., Grigis, P. C., Kontar, E. P., Liu, W., Saint-Hilaire, P., and Zharkova, V. V., 2011 Sep, "Implications of X-ray Observations for Electron Acceleration and Propagation in Solar Flares," *Space Sci. Rev.* **159**, 107–166.

Holman, G. D., Sui, L., Schwartz, R. A., and Emslie, A. G., 2003 Oct, "Electron Bremsstrahlung Hard X-Ray Spectra, Electron Distributions, and Energetics in the 2002 July 23 Solar Flare," *Astrophys. J. Lett.* **595**, L97–L101.

House, L. L., Wagner, W. J., Hildner, E., Sawyer, C., and Schmidt, H. U., 1981 Mar., "Studies of the corona with the Solar Maximum Mission coronagraph/polarimeter," *Astrophys. J. Lett.* **244**, L117–L121.

Howard, R. A., Moses, J. D., Vourlidas, A., Newmark, J. S., Socker, D. G., Plunkett, S. P., Korendyke, C. M., Cook, J. W., Hurley, A., Davila, J. M., Thompson, W. T., St Cyr, O. C., Mentzell, E., Mehalick, K., Lemen, J. R., Wuelser, J. P., Duncan, D. W., Tarbell, T. D., Wolfson, C. J., Moore, A., Harrison, R. A., Waltham, N. R., Lang, J., Davis, C. J., Eyles, C. J., Mapson-Menard, H., Simnett, G. M., Halain, J. P., Defise, J. M., Mazy, E., Rochus, P., Mercier, R., Ravet, M. F., Delmotte, F., Auchere, F., Delaboudiniere, J. P., Bothmer, V., Deutsch, W., Wang, D., Rich, N., Cooper, S., Stephens, V., Maahs, G., Baugh, R., McMullin, D., and Carter, T., 2008 Apr., "Sun Earth Connection Coronal and Heliospheric Investigation (SECCHI)," *Space Sci. Rev.* **136**, 67–115.

Hudson, H. S., Lemen, J. R., St. Cyr, O. C., Sterling, A. C., and Webb, D. F., 1998 Jan., "X-ray coronal changes during Halo CMEs," *Geophys. Res. Lett.* **25**, 2481–2484.

Hughes, D. W., and Cattaneo, F., 1987 Jan., "A new look at the instability of a stratified horizontal magnetic field," *Geophysical and Astrophysical Fluid Dynamics* **39**, 65–81.

Hundhausen, A. J., Sawyer, C. B., House, L., Illing, R. M. E., and Wagner, W. J., 1984 May, "Coronal mass ejections observed during the solar maximum mission: Latitude distribution and rate of occurrence," *J. Geophys. Res.* **89**, 2639–2646.

Hurford, G. J., Schmahl, E. J., Schwartz, R. A., Conway, A. J., Aschwanden, M. J., Csillaghy, A., Dennis, B. R., Johns-Krull, C., Krucker, S., and Lin, R. P., 2002 Nov, "The RHESSI Imaging Concept," *Solar Phys.* **210**, 61–86.

Janvier, M., Aulanier, G., Bommier, V., Schmieder, B., Démoulin, P., and Pariat, E., 2014 Jun., "Electric Currents in Flare Ribbons: Observations and Three-dimensional Standard Model," *Astrophys. J.* **788**, 60

Jiang, C., Feng, X., Liu, R., Yan, X., Hu, Q., Moore, R. L., Duan, A., Cui, J., Zuo, P., Wang, Y., and Wei, F., 2021 Jul., "A fundamental mechanism of solar eruption initiation," *Nature Astronomy* doi:\bibinfo{doi}{10.1038/s41550-021-01414-z}

Jiang, C., Feng, X., Wu, S. T., and Hu, Q., 2013 Jul., "Magnetohydrodynamic Simulation of a Sigmoid Eruption of Active Region 11283," *Astrophys. J. Lett.* **771**, L30

Jiang, Y., Yang, J., Zheng, R., Bi, Y., and Yang, X., 2009 Mar., "A Narrow Streamer-Puff Coronal Mass Ejection from the Nonradial Eruption of an Active-Region Filament," *Astrophys. J.* **693**, 1851–1858.

Jing, J., Chae, J., and Wang, H., 2008 Jan., "Spatial Distribution of Magnetic Reconnection in the 2006 December 13 Solar Flare as Observed by Hinode," *Astrophys. J. Lett.* **672**, L73.

Jing, J., Liu, R., Cheung, M. C. M., Lee, J., Xu, Y., Liu, C., Zhu, C., and Wang, H., 2017 Jun, "Witnessing a Large-scale Slipping Magnetic Reconnection along a Dimming Channel during a Solar Flare," *Astrophys. J. Lett.* **842**, L18

Joshi, B., Ibrahim, M. S., Shanmugaraju, A., and Chakrabarty, D., 2018 Jul., "A Major Geoeffective CME from NOAA 12371: Initiation, CME-CME Interactions, and Interplanetary Consequences," *Solar Phys.* **293**, 107

Joshi, B., Kushwaha, U., Cho, K. S., and Veronig, A. M., 2013 Jul, "RHESSI and TRACE Observations of Multiple Flare Activity in AR 10656 and Associated Filament Eruption," *Astrophys. J.* **771**, 1

Joshi, B., Kushwaha, U., Veronig, A. M., Dhara, S. K., Shanmugaraju, A., and Moon, Y.-J., 2017 Jan.a, "Formation and Eruption of a Flux Rope from the Sigmoid Active Region NOAA 11719 and Associated M6.5 Flare: A Multi-wavelength Study," *Astrophys. J.* **834**, 42

Joshi, B., Thalmann, J. K., Mitra, P. K., Chandra, R., and Veronig, A. M., 2017 Dec.b, "Observational and Model Analysis of a Two-ribbon Flare Possibly Induced by a Neighboring Blowout Jet," *Astrophys. J.* **851**, 29

Joshi, B., Veronig, A., Cho, K. S., Bong, S. C., Somov, B. V., Moon, Y. J., Lee, J., Manoharan, P. K., and Kim, Y. H., 2009 Dec., "Magnetic Reconnection During the Two-phase Evolution of a Solar Eruptive Flare," *Astrophys. J.* **706**, 1438–1450.

Joshi, B., Veronig, A., Manoharan, P. K., and Somov, B. V., 2012 Jan, "Signatures of Magnetic Reconnection in Solar Eruptive Flares: A Multi-wavelength Perspective," *Astrophysics and Space Science Proceedings* **33**, 29.

Joshi, B., Veronig, A. M., Lee, J., Bong, S.-C., Tiwari, S. K., and Cho, K.-S., 2011 Dec, "Pre-flare Activity and Magnetic Reconnection during the Evolutionary Stages of Energy Release in a Solar Eruptive Flare," *Astrophys. J.* **743**, 195

Joshi, N. C., Joshi, B., and Mitra, P. K., 2021 Mar., "Evolutionary stages and triggering process of a complex eruptive flare with circular and parallel ribbons," *Mon. Not. Roy. Astron. Soc.* **501**, 4703–4721.

Joshi, N. C., Liu, C., Sun, X., Wang, H., Magara, T., and Moon, Y. J., 2015 Oct., "The Role of Erupting Sigmoid in Triggering a Flare with Parallel and Large-scale Quasi-circular Ribbons," *Astrophys. J.* **812**, 50

Joshi, N. C., Sterling, A. C., Moore, R. L., and Joshi, B., 2020 Sep., "Sequential Lid Removal in a Triple-decker Chain of CME-producing Solar Eruptions," *Astrophys. J.* **901**, 38

Joshi, N. C., Sterling, A. C., Moore, R. L., Magara, T., and Moon, Y.-J., 2017 Aug.c, "Onset of a Large Ejective Solar Eruption from a Typical Coronal-jet-base Field Configuration," *Astrophys. J.* **845**, 26

Kahler, S. W., 1992 Jan., "Solar flares and coronal mass ejections.." *Annu.* **30**, 113–141.

Kang, J., Inoue, S., Kusano, K., Park, S.-H., and Moon, Y.-J., 2019 Dec, "Onset Mechanism of M6.5 Solar Flare Observed in Active Region 12371," *Astrophys. J.* **887**, 263

Karpen, J. T., Antiochos, S. K., and DeVore, C. R., 2012 Nov., "The Mechanisms for the Onset and Explosive Eruption of Coronal Mass Ejections and Eruptive Flares," *Astrophys. J.* **760**, 81

Kawabata, Y., Iida, Y., Doi, T., Akiyama, S., Yashiro, S., and Shimizu, T., 2018 Dec., "Statistical Relation between Solar Flares and Coronal Mass Ejections with Respect to Sigmoidal Structures in Active Regions," *Astrophys. J.* **869**, 99

Kharayat, H., Joshi, B., Mitra, P. K., Manoharan, P. K., and Monstein, C., 2021 Jun., "A Transient Coronal Sigmoid in Active Region NOAA 11909: Build-up Phase, M-class Eruptive Flare, and Associated Fast Coronal Mass Ejection," *Solar Phys.* **296**, 99

Kim, S., Moon, Y. J., Kim, Y. H., Park, Y. D., Kim, K. S., Choe, G. S., and Kim, K. H., 2008 Aug, "Preflare Eruption Triggered by a Tether-cutting Process," *Astrophys. J.* **683**, 510–515.

Klein, L. W., and Burlaga, L. F., 1982 Feb, "Interplanetary magnetic clouds at 1 AU," *J. Geophys. Res.* **87**, 613–624.

Kleint, L., Battaglia, M., Reardon, K., Sainz Dalda, A., Young, P. R., and Krucker, S., 2015 Jun., "The Fast Filament Eruption Leading to the X-flare on 2014 March 29," *Astrophys. J.* **806**, 9

Kliem, B., Titov, V. S., and Török, T., 2004 Jan., "Formation of current sheets and sigmoidal structure by the kink instability of a magnetic loop," *Astron. Astrophys.* **413**, L23–L26.

Kontogiannis, I., Georgoulis, M. K., Park, S.-H., and Guerra, J. A., 2017 Nov., "Non-neutralized Electric Currents in Solar Active Regions and Flare Productivity," *Solar Phys.* **292**, 159

Koomen, M., Howard, R., Hansen, R., and Hansen, S., 1974 Feb., "The Coronal Transient of 16 June 1972," *Solar Phys.* **34**, 447–452.

Kopp, R. A., and Pneuman, G. W., 1976 Oct, "Magnetic reconnection in the corona and the loop prominence phenomenon.." *Solar Phys.* **50**, 85–98.

Krucker, S., Battaglia, M., Cargill, P. J., Fletcher, L., Hudson, H. S., MacKinnon, A. L., Masuda, S., Sui, L., Tomczak, M., Veronig, A. L., Vlahos, L., and White, S. M., 2008 Oct., "Hard X-ray emission from the solar corona," *Astron. Astrophys. Rev.* **16**, 155–208.

Kumar, P., Yurchyshyn, V., Wang, H., and Cho, K.-S., 2015 Aug., "Formation and Eruption of a Small Flux Rope in the Chromosphere Observed by NST, IRIS, and SDO," *Astrophys. J.* **809**, 83

Kundu, M. R., Garaimov, V. I., White, S. M., and Krucker, S., 2004 Jan, "Nobeyama Radioheliograph and RHESSI Observations of the X1.5 Flare of 2002 April 21," *Astrophys. J.* **600**, 1052–1060.

Kushwaha, U., Joshi, B., Cho, K.-S., Veronig, A., Tiwari, S. K., and Mathew, S. K., 2014 Aug., "Impulsive Energy Release and Non-thermal Emission in a Confined M4.0 Flare Triggered by Rapidly Evolving Magnetic Structures," *Astrophys. J.* **791**, 23

Labrosse, N., Heinzel, P., Vial, J. C., Kucera, T., Parenti, S., Gunár, S., Schmieder, B., and Kilper, G., 2010 Apr., "Physics of Solar Prominences: I—Spectral Diagnostics and Non-LTE Modelling," *Space Sci. Rev.* **151**, 243–332.

Leake, J. E., Linton, M. G., and Török, T., 2013 Dec., "Simulations of Emerging Magnetic Flux. I. The Formation of Stable Coronal Flux Ropes," *Astrophys. J.* **778**, 99

Leka, K. D., Barnes, G., Crouch, A. D., Metcalf, T. R., Gary, G. A., Jing, J., and Liu, Y., 2009 Nov., "Resolving the 180° Ambiguity in Solar Vector Magnetic Field Data: Evaluating the Effects of Noise, Spatial Resolution, and Method Assumptions," *Solar Phys.* **260**, 83–108.

Lemen, J. R., Title, A. M., Akin, D. J., Boerner, P. F., Chou, C., Drake, J. F., Duncan, D. W., Edwards, C. G., Friedlaender, F. M., Heyman, G. F., Hurlburt, N. E., Katz, N. L., Kushner, G. D., Levay, M., Lindgren, R. W., Mathur, D. P., McFeaters, E. L., Mitchell, S., Rehse, R. A., Schrijver, C. J., Springer, L. A., Stern, R. A., Tarbell, T. D., Wuelser, J.-P., Wolfson, C. J., Yanari, C., Bookbinder, J. A., Cheimets, P. N., Caldwell, D., Deluca, E. E., Gates, R., Golub, L., Park, S., Podgorski, W. A., Bush, R. I., Scherrer, P. H., Gummin, M. A., Smith, P., Auker, G., Jerram, P., Pool, P., Soufli, R., Windt, D. L., Beardsley, S., Clapp, M., Lang, J., and Waltham, N., 2012 Jan., "The Atmospheric Imaging Assembly (AIA) on the Solar Dynamics Observatory (SDO)," *Solar Phys.* **275**, 17–40.

Li, L. P., and Zhang, J., 2013 Apr, "Eruptions of two flux ropes observed by SDO and STEREO," *Astron. Astrophys.* **552**, L11

Li, S., Jaroszynski, S., Pearse, S., Orf, L., and Clyne, J., 2019 Aug., "VAPOR: A Visualization Package Tailored to Analyze Simulation Data in Earth System Science," *Atmosphere* **10**, 488.

Li, Y., Ding, M. D., Qiu, J., and Cheng, J. X., 2015 Sep., "Chromospheric Evaporation in an X1.0 Flare on 2014 March 29 Observed with IRIS and EIS," *Astrophys. J.* **811**, 7

Li, Y., Lynch, B. J., Welsch, B. T., Stenborg, G. A., Luhmann, J. G., Fisher, G. H., Liu, Y., and Nightingale, R. W., 2010 Jun., "Sequential Coronal Mass Ejections from AR8038 in May 1997," *Solar Phys.* **264**, 149–164.

Lin, R. P., Dennis, B. R., Hurford, G. J., Smith, D. M., Zehnder, A., Harvey, P. R., Curtis, D. W., Pankow, D., Turin, P., Bester, M., Csillaghy, A., Lewis, M., Madden, N., van Beek, H. F., Appleby, M., Raudorf, T., McTiernan, J., Ramaty, R., Schmahl, E., Schwartz, R., Krucker, S., Abiad, R., Quinn, T., Berg, P., Hashii, M., Sterling, R., Jackson, R., Pratt, R., Campbell, R. D., Malone, D., Landis, D., Barrington-Leigh, C. P., Slassi-Sennou, S., Cork, C., Clark, D., Amato, D., Orwig, L., Boyle, R., Banks, I. S., Shirey, K., Tolbert, A. K., Zarro, D., Snow, F., Thomsen, K., Henneck, R., McHedlishvili, A., Ming, P., Fivian, M., Jordan, J., Wanner, R., Crubb, J., Preble, J., Matranga, M., Benz, A., Hudson, H., Canfield, R. C., Holman, G. D., Crannell, C., Kosugi, T., Emslie, A. G., Vilmer, N., Brown, J. C., Johns-Krull, C., Aschwanden, M., Metcalf, T., and Conway, A., 2002 Nov., "The Reuven Ramaty High-Energy Solar Spectroscopic Imager (RHESSI)," *Solar Phys.* **210**, 3–32.

Lin, R. P., and Hudson, H. S., 1976 Oct., "Non-thermal processes in large solar flares.." *Solar Phys.* **50**, 153–178.

Lites, B. W., 2005 Apr., "Magnetic Flux Ropes in the Solar Photosphere: The Vector Magnetic Field under Active Region Filaments," *Astrophys. J.* **622**, 1275–1291.

Liu, C., Cao, W., Chae, J., Ahn, K., Prasad Choudhary, D., Lee, J., Liu, R., Deng, N., Wang, J., and Wang, H., 2018 Deca, "Evolution of Photospheric Vector Magnetic Field Associated with Moving Flare Ribbons as Seen by GST," *Astrophys. J.* **869**, 21

Liu, C., Deng, N., Liu, R., Lee, J., Pariat, É., Wiegelmann, T., Liu, Y., Kleint, L., and Wang, H., 2015 Oct., "A Circular-ribbon Solar Flare Following an Asymmetric Filament Eruption," *Astrophys. J. Lett.* **812**, L19

Liu, L., Wang, Y., Liu, R., Zhou, Z., Temmer, M., Thalmann, J. K., Liu, J., Liu, K., Shen, C., Zhang, Q., and Veronig, A. M., 2017 Aug., "The Causes of Quasi-homologous CMEs," *Astrophys. J.* **844**, 141

Liu, R., Liu, C., Wang, S., Deng, N., and Wang, H., 2010 Dec., "Sigmoid-to-flux-rope Transition Leading to a Loop-like Coronal Mass Ejection," *Astrophys. J. Lett.* **725**, L84–L90.

Liu, T., Su, Y., Cheng, X., van Ballegooijen, A., and Ji, H., 2018 Novb, "Magnetic Field Modeling of Hot Channels in Four Flare/Coronal Mass Ejection Events," *Astrophys. J.* **868**, 59

Liu, W., Wang, T.-J., Dennis, B. R., and Holman, G. D., 2009 Jun, "Episodic X-Ray Emission Accompanying the Activation of an Eruptive Prominence: Evidence of Episodic Magnetic Reconnection," *Astrophys. J.* **698**, 632–640.

Long, D. M., Bloomfield, D. S., Chen, P. F., Downs, C., Gallagher, P. T., Kwon, R. Y., Vanninathan, K., Veronig, A. M., Vourlidas, A., Vršnak, B., Warmuth, A., and Žic, T., 2017 Jan., "Understanding the Physical Nature of Coronal "EIT Waves"," *Solar Phys.* **292**, 7

Long, D. M., Bloomfield, D. S., Gallagher, P. T., and Pérez-Suárez, D., 2014 Sep., "CorPITA: An Automated Algorithm for the Identification and Analysis of Coronal "EIT Waves"," *Solar Phys.* **289**, 3279–3295.

Low, B. C., 1996 Aug., "Solar Activity and the Corona," *Solar Phys.* **167**, 217–265.

Low, B. C., 2001 Nov., "Coronal mass ejections, magnetic flux ropes, and solar magnetism," *J. Geophys. Res.* **106**, 25141–25164.

Low, B. C., and Hundhausen, J. R., 1995 Apr., "Magnetostatic Structures of the Solar Corona. II. The Magnetic Topology of Quiescent Prominences," *Astrophys. J.* **443**, 818.

MacCombie, W. J., and Rust, D. M., 1979 Feb., "Physical parameters in long-decay coronal enhancements.." *Solar Phys.* **61**, 69–88.

Mackay, D. H., Karpen, J. T., Ballester, J. L., Schmieder, B., and Aulanier, G., 2010 Apr., "Physics of Solar Prominences: II—Magnetic Structure and Dynamics," *Space Sci. Rev.* **151**, 333–399.

Mackay, D. H., and van Ballegooijen, A. A., 2006 Apr., "Models of the Large-Scale Corona. I. Formation, Evolution, and Liftoff of Magnetic Flux Ropes," *Astrophys. J.* **641**, 577–589.

Manchester, I., W., Gombosi, T., DeZeeuw, D., and Fan, Y., 2004 Jul., "Eruption of a Buoyantly Emerging Magnetic Flux Rope," *Astrophys. J.* **610**, 588–596.

Manoharan, P. K., van Driel-Gesztelyi, L., Pick, M., and Demoulin, P., 1996 Sep., "Evidence for Large-Scale Solar Magnetic Reconnection from Radio and X-Ray Measurements," *Astrophys. J. Lett.* **468**, L73.

Martin, S. F., 1998 Sep., "Conditions for the Formation and Maintenance of Filaments (Invited Review)," *Solar Phys.* **182**, 107–137.

Mason, J. P., Woods, T. N., Caspi, A., Thompson, B. J., and Hock, R. A., 2014 Jul., "Mechanisms and Observations of Coronal Dimming for the 2010 August 7 Event," *Astrophys. J.* **789**, 61

Masson, S., Aulanier, G., Pariat, E., and Klein, K. L., 2012 Feb., "Interchange Slip-Running Reconnection and Sweeping SEP Beams," *Solar Phys.* **276**, 199–217.

Masson, S., Pariat, E., Aulanier, G., and Schrijver, C. J., 2009 Jul., "The Nature of Flare Ribbons in Coronal Null-Point Topology," *Astrophys. J.* **700**, 559–578.

McKenzie, D. E., and Canfield, R. C., 2008 Apr., "Hinode XRT observations of a long-lasting coronal sigmoid," *Astron. Astrophys.* **481**, L65–L68.

Mertz, L. N., Nakano, G. H., and Kilner, J. R., 1986 Dec., "Rotational aperture synthesis for X rays.." *Journal of the Optical Society of America A* **3**, 2167–2170.

Metcalf, T. R., 1994 Dec., "Resolving the 180-degree ambiguity in vector magnetic field measurements: The 'minimum' energy solution," *Solar Phys.* **155**, 235–242.

Metcalf, T. R., Hudson, H. S., Kosugi, T., Puetter, R. C., and Pina, R. K., 1996 Jul., "Pixon-based Multiresolution Image Reconstruction for Yohkoh's Hard X-Ray Telescope," *Astrophys. J.* **466**, 585.

Metcalf, T. R., Leka, K. D., Barnes, G., Lites, B. W., Georgoulis, M. K., Pevtsov, A. A., Balasubramaniam, K. S., Gary, G. A., Jing, J., Li, J., Liu, Y., Wang, H. N., Abramenko, V., Yurchyshyn, V., and Moon, Y. J., 2006 Sep., "An Overview of Existing Algorithms for Resolving the 180 Ambiguity in Vector Magnetic Fields: Quantitative Tests with Synthetic Data," *Solar Phys.* **237**, 267–296.

Mithun, N. P. S., Vadawale, S. V., Sarkar, A., Shanmugam, M., Patel, A. R., Mondal, B., Joshi, B., Janardhan, P., Adalja, H. L., Goyal, S. K., Ladiya, T., Tiwari, N. K., Singh, N., Kumar, S., Tiwari, M. K., Modi, M. H., and Bhardwaj, A., 2020 Oct., "Solar X-Ray Monitor on Board the Chandrayaan-2 Orbiter: In-Flight Performance and Science Prospects," *Solar Phys.* **295**, 139

Mitra, P. K., and Joshi, B., 2019 Oct, "Preflare Processes, Flux Rope Activation, Large-scale Eruption, and Associated X-class Flare from the Active Region NOAA 11875," *Astrophys. J.* **884**, 46

Mitra, P. K., and Joshi, B., 2021 May, "Successive occurrences of quasi-circular ribbon flares in a fan-spine-like configuration involving hyperbolic flux tube," *Mon. Not. Roy. Astron. Soc.* **503**, 1017–1035.

Mitra, P. K., Joshi, B., and Prasad, A., 2020 Feb.a, "Identification of Pre-flare Processes and Their Possible Role in Driving a Large-scale Flux Rope Eruption with Complex M-class Flare in the Active Region NOAA 12371," *Solar Phys.* **295**, 29

Mitra, P. K., Joshi, B., Prasad, A., Veronig, A. M., and Bhattacharyya, R., 2018 Dec, "Successive Flux Rope Eruptions from δ-sunspots Region of NOAA 12673 and Associated X-class Eruptive Flares on 2017 September 6," *Astrophys. J.* **869**, 69

Mitra, P. K., Joshi, B., Veronig, A. M., Chandra, R., Dissauer, K., and Wiegelmann, T., 2020 Sep.b, "Eruptive-Impulsive Homologous M-class Flares Associated with Double-decker Flux Rope Configuration in Minisigmoid of NOAA 12673," *Astrophys. J.* **900**, 23

Moore, R. L., Falconer, D. A., Porter, J. G., and Suess, S. T., 1999 Nov., "On Heating the Sun's Corona by Magnetic Explosions: Feasibility in Active Regions and Prospects for Quiet Regions and Coronal Holes," *Astrophys. J.* **526**, 505–522.

Moore, R. L., and Roumeliotis, G., 1992, "Triggering of Eruptive Flares - Destabilization of the Preflare Magnetic Field Configuration," in *IAU Colloq. 133: Eruptive Solar Flares*, Vol. 399, edited by Svestka, Z., Jackson, B. V., and Machado, M. E., p. 69.

Moore, R. L., Schmieder, B., Hathaway, D. H., and Tarbell, T. D., 1997 Nov., "3-D Magnetic Field Configuration Late in a Large Two-Ribbon Flare," *Solar Phys.* **176**, 153–169.

Moore, R. L., and Sterling, A. C., 2007 May, "The Coronal-dimming Footprint of a Streamer-Puff Coronal Mass Ejection: Confirmation of the Magnetic-Arch-Blowout Scenario," *Astrophys. J.* **661**, 543–550.

Moore, R. L., Sterling, A. C., Hudson, H. S., and Lemen, J. R., 2001 May, "Onset of the Magnetic Explosion in Solar Flares and Coronal Mass Ejections," *Astrophys. J.* **552**, 833–848.

Moore, R. L., Sterling, A. C., and Suess, S. T., 2007 Oct., "The Width of a Solar Coronal Mass Ejection and the Source of the Driving Magnetic Explosion: A Test of the Standard Scenario for CME Production," *Astrophys. J.* **668**, 1221–1231.

Moreno-Insertis, F., 2007 Oct., "Three-dimensional numerical experiments of flux emergence into the corona," in *New Solar Physics with Solar-B Mission*, Astronomical Society of the Pacific Conference Series, Vol. 369, edited by Shibata, K., Nagata, S., and Sakurai, T., p. 335.

Möstl, C., Farrugia, C. J., Miklenic, C., Temmer, M., Galvin, A. B., Luhmann, J. G., Kilpua, E. K. J., Leitner, M., Nieves-Chinchilla, T., Veronig, A., and Biernat, H. K., 2009 Apr, "Multispacecraft recovery of a magnetic cloud and its origin from magnetic reconnection on the Sun," *Journal of Geophysical Research (Space Physics)* **114**, A04102

Nagashima, K., Isobe, H., Yokoyama, T., Ishii, T. T., Okamoto, T. J., and Shibata, K., 2007 Oct, "Triggering Mechanism for the Filament Eruption on 2005 September 13 in NOAA Active Region 10808," *Astrophys. J.* **668**, 533–545.

Newcomb, W. A., 1961 Apr., "Convective Instability Induced by Gravity in a Plasma with a Frozen-In Magnetic Field," *Physics of Fluids* **4**, 391–396.

Nindos, A., Patsourakos, S., Vourlidas, A., and Tagikas, C., 2015 Aug., "How Common Are Hot Magnetic Flux Ropes in the Low Solar Corona? A Statistical Study of EUV Observations," *Astrophys. J.* **808**, 117

Nitta, N. V., and Hudson, H. S., 2001 Jan., "Recurrent flare/CME events from an emerging flux region," *Geophys. Res. Lett.* **28**, 3801–3804.

Okamoto, T. J., Tsuneta, S., Lites, B. W., Kubo, M., Yokoyama, T., Berger, T. E., Ichimoto, K., Katsukawa, Y., Nagata, S., Shibata, K., Shimizu, T., Shine, R. A., Suematsu, Y., Tarbell, T. D., and Title, A. M., 2009 May, "Prominence Formation Associated with an Emerging Helical Flux Rope," *Astrophys. J.* **697**, 913–922.

Olmedo, O., Zhang, J., Wechsler, H., Poland, A., and Borne, K., 2008 Apr., "Automatic Detection and Tracking of Coronal Mass Ejections in Coronagraph Time Series," *Solar Phys.* **248**, 485–499.

Owens, M., Lockwood, M., Macneil, A., and Stansby, D., 2020 Mar., "Signatures of Coronal Loop Opening via Interchange Reconnection in the Slow Solar Wind at 1 AU," *Solar Phys.* **295**, 37

Pallavicini, R., Serio, S., and Vaiana, G. S., 1977 Aug., "A survey of soft X-ray limb flare images: the relation between their structure in the corona and other physical parameters.." *Astrophys. J.* **216**, 108–122.

Parenti, S., 2014 Mar., "Solar Prominences: Observations," *Living Reviews in Solar Physics* **11**, 1

Pariat, E., Aulanier, G., Schmieder, B., Georgoulis, M. K., Rust, D. M., and Bernasconi, P. N., 2004 Oct., "Resistive Emergence of Undulatory Flux Tubes," *Astrophys. J.* **614**, 1099–1112.

Patsourakos, S., Vourlidas, A., and Stenborg, G., 2013 Feb, "Direct Evidence for a Fast Coronal Mass Ejection Driven by the Prior Formation and Subsequent Destabilization of a Magnetic Flux Rope," *Astrophys. J.* **764**, 125

Pécseli, H., and Engvold, O., 2000 May, "Modeling of prominence threads in magnetic fields: Levitation by incompressible MHD waves," *Solar Phys.* **194**, 73–86.

Pesnell, W. D., Thompson, B. J., and Chamberlin, P. C., 2012 Jan., "The Solar Dynamics Observatory (SDO)," *Solar Phys.* **275**, 3–15.

Pevtsov, A. A., 2002 May, "Active-Region Filaments and X-ray Sigmoids," *Solar Phys.* **207**, 111–123.

Pontin, D. I., Bhattacharjee, A., and Galsgaard, K., 2007 May, "Current sheet formation and nonideal behavior at three-dimensional magnetic null points," *Physics of Plasmas* **14**, 052106–052106.

Prasad, A., Dissauer, K., Hu, Q., Bhattacharyya, R., Veronig, A. M., Kumar, S., and Joshi, B., 2020 Nov., "Magnetohydrodynamic Simulation of Magnetic Null-point Reconnections and Coronal Dimmings during the X2.1 Flare in NOAA AR 11283," *Astrophys. J.* **903**, 129

Priest, E. R., and Forbes, T. G., 2002 Jan, "The magnetic nature of solar flares," *Astron. Astrophys. Rev.* **10**, 313–377.

Priest, E. R., and Pontin, D. I., 2009 Dec., "Three-dimensional null point reconnection regimes," *Physics of Plasmas* **16**, 122101–122101.

Rappazzo, A. F., Matthaeus, W. H., Ruffolo, D., Servidio, S., and Velli, M., 2012 Oct., "Interchange Reconnection in a Turbulent Corona," *Astrophys. J. Lett.* **758**, L14

Régnier, S., 2012 Mar., "Magnetic Energy Storage and Current Density Distributions for Different Force-Free Models," *Solar Phys.* **277**, 131–151.

Reid, H. A. S., and Ratcliffe, H., 2014 Jul., "A review of solar type III radio bursts," *Research in Astronomy and Astrophysics* **14**, 773–804.

Reinard, A. A., and Biesecker, D. A., 2008 Feb., "Coronal Mass Ejection-Associated Coronal Dimmings," *Astrophys. J.* **674**, 576–585.

Riley, P., Lionello, R., Mikić, Z., and Linker, J., 2008 Jan., "Using Global Simulations to Relate the Three-Part Structure of Coronal Mass Ejections to In Situ Signatures," *Astrophys. J.* **672**, 1221–1227.

Robbrecht, E., Berghmans, D., and Van der Linden, R. A. M., 2009 Feb., "Automated LASCO CME Catalog for Solar Cycle 23: Are CMEs Scale Invariant?," *Astrophys. J.* **691**, 1222–1234.

Romano, P., Elmhamdi, A., Falco, M., Costa, P., Kordi, A. S., Al-Trabulsy, H. A., and Al-Shammari, R. M., 2018 Jan., "Homologous White Light Solar Flares Driven by Photospheric Shear Motions," *Astrophys. J. Lett.* **852**, L10

Romano, P., Zuccarello, F., Guglielmino, S. L., Berrilli, F., Bruno, R., Carbone, V., Consolini, G., de Lauretis, M., Del Moro, D., Elmhamdi, A., Ermolli, I., Fineschi, S., Francia, P., Kordi, A. S., Landi Degl'Innocenti, E., Laurenza, M., Lepreti, F., Marcucci, M. F., Pallocchia, G., Pietropaolo, E., Romoli, M., Vecchio, A., Vellante, M., and Villante, U., 2015 Oct., "Recurrent flares in active region NOAA 11283," *Astron. Astrophys.* **582**, A55

Rust, D. M., and Kumar, A., 1996 Jun., "Evidence for Helically Kinked Magnetic Flux Ropes in Solar Eruptions," *Astrophys. J. Lett.* **464**, L199.

Sahu, S., Joshi, B., Mitra, P. K., Veronig, A. M., and Yurchyshyn, V., 2020 Jul., "Hard X-Ray Emission from an Activated Flux Rope and Subsequent Evolution of an Eruptive Long-duration Solar Flare," *Astrophys. J.* **897**, 157

Savcheva, A., Pariat, E., McKillop, S., McCauley, P., Hanson, E., Su, Y., Werner, E., and DeLuca, E. E., 2015 Sep., "The Relation between Solar Eruption Topologies and Observed Flare Features. I. Flare Ribbons," *Astrophys. J.* **810**, 96

Savcheva, A., Pariat, E., van Ballegooijen, A., Aulanier, G., and DeLuca, E., 2012 Maya, "Sigmoidal Active Region on the Sun: Comparison of a Magnetohydrodynamical Simulation and a Nonlinear Force-free Field Model," *Astrophys. J.* **750**, 15

Savcheva, A. S., Green, L. M., van Ballegooijen, A. A., and DeLuca, E. E., 2012 Nov.b, "Photospheric Flux Cancellation and the Build-up of Sigmoidal Flux Ropes on the Sun," *Astrophys. J.* **759**, 105

Savcheva, A., and van Ballegooijen, A., 2009 Oct., "Nonlinear Force-free Modeling of a Long-lasting Coronal Sigmoid," *Astrophys. J.* **703**, 1766–1777.

Schatten, K. H., Wilcox, J. M., and Ness, N. F., 1969 Mar., "A model of interplanetary and coronal magnetic fields," *Solar Phys.* **6**, 442–455.

Schmieder, B., Archontis, V., and Pariat, E., 2014 Dec., "Magnetic Flux Emergence Along the Solar Cycle," *Space Sci. Rev.* **186**, 227–250.

Schmieder, B., Heinzel, P., Wiik, J. E., Lemen, J., Anwar, B., Kotrc, P., and Hiei, E., 1995 Feb., "Relation between Cool and Hot Post-Flare Loops of 26 June 1992 Derived from Optical and X-Ray (SXT-YOHKOH) Observations," *Solar Phys.* **156**, 337–361.

Schou, J., Scherrer, P. H., Bush, R. I., Wachter, R., Couvidat, S., Rabello-Soares, M. C., Bogart, R. S., Hoeksema, J. T., Liu, Y., Duvall, T. L., Akin, D. J., Allard, B. A., Miles, J. W., Rairden, R., Shine, R. A., Tarbell, T. D., Title, A. M., Wolfson, C. J., Elmore, D. F., Norton, A. A., and Tomczyk, S., 2012 Jan., "Design and Ground Calibration of the Helioseismic and Magnetic Imager (HMI) Instrument on the Solar Dynamics Observatory (SDO)," *Solar Phys.* **275**, 229–259.

Schrijver, C. J., Aulanier, G., Title, A. M., Pariat, E., and Delannée, C., 2011 Sep., "The 2011 February 15 X2 Flare, Ribbons, Coronal Front, and Mass Ejection: Interpreting the Three-dimensional Views from the Solar Dynamics Observatory and STEREO Guided by Magnetohydrodynamic Flux-rope Modeling," *Astrophys. J.* **738**, 167

Schrijver, C. J., De Rosa, M. L., Title, A. M., and Metcalf, T. R., 2005 Jul., "The Nonpotentiality of Active-Region Coronae and the Dynamics of the Photospheric Magnetic Field," *Astrophys. J.* **628**, 501–513.

Schwenn, R., 1996 Mar., "An Essay on Terminology, Myths and Known Facts: Solar Transient - Flare - CME - Driver Gas - Piston - BDE - Magnetic Cloud - Shock Wave - Geomagnetic Storm," *Astrophys. Space Sci.* **243**, 187.

Schwenn, R., 2006 Aug., "Space Weather: The Solar Perspective," *Living Reviews in Solar Physics* **3**, 2

Sheeley, J., N. R., Michels, D. J., Howard, R. A., and Koomen, M. J., 1980 May, "Initial observations with the SOLWIND coronagraph," *Astrophys. J. Lett.* **237**, L99–L101.

Shibata, K., 1999 Dec., "Reconnection Models of Flares," in *Proceedings of the Nobeyama Symposium*, edited by Bastian, T. S., Gopalswamy, N., and Shibasaki, K., pp. 381–389.

Smith, D. M., Lin, R. P., Turin, P., Curtis, D. W., Primbsch, J. H., Campbell, R. D., Abiad, R., Schroeder, P., Cork, C. P., Hull, E. L., Land is, D. A., Madden, N. W., Malone, D., Pehl, R. H., Raudorf, T., Sangsingkeow, P., Boyle, R., Banks, I. S., Shirey, K., and Schwartz, R., 2002 Nov, "The RHESSI Spectrometer," *Solar Phys.* **210**, 33–60.

Song, H. Q., Chen, Y., Qiu, J., Chen, C. X., Zhang, J., Cheng, X., Shen, Y. D., and Zheng, R. S., 2018 Apr, "The Acceleration Process of a Solar Quiescent Filament in the Inner Corona," *Astrophys. J. Lett.* **857**, L21

Song, H. Q., Chen, Y., Zhang, J., Cheng, X., Fu, H., and LI, G., 2015 May, "Acceleration Phases of a Solar Filament During Its Eruption," *Astrophys. J. Lett.* **804**, L38

Song, H. Q., Zhang, J., Chen, Y., and Cheng, X., 2014 Sep., "Direct Observations of Magnetic Flux Rope Formation during a Solar Coronal Mass Ejection," *Astrophys. J. Lett.* **792**, L40

Song, H. Q., Zhang, J., Cheng, X., Li, L. P., Tang, Y. Z., Wang, B., Zheng, R. S., and Chen, Y., 2019 Sep, "On the Nature of the Bright Core of Solar Coronal Mass Ejections," *Astrophys. J.* **883**, 43

Sterling, A. C., Harra, L. K., and Moore, R. L., 2007 Nov, "New Evidence for the Role of Emerging Flux in a Solar Filament's Slow Rise Preceding Its CME-producing Fast Eruption," *Astrophys. J.* **669**, 1359–1371.

Sterling, A. C., and Hudson, H. S., 1997 Dec., "Yohkoh SXT Observations of X-Ray "Dimming" Associated with a Halo Coronal Mass Ejection," *Astrophys. J. Lett.* **491**, L55–L58.

Sterling, A. C., and Moore, R. L., 2005 Sep, "Slow-Rise and Fast-Rise Phases of an Erupting Solar Filament, and Flare Emission Onset," *Astrophys. J.* **630**, 1148–1159.

Sterling, A. C., Moore, R. L., Falconer, D. A., and Knox, J. M., 2014 Jun., "New Aspects of a Lid-removal Mechanism in the Onset of an Eruption Sequence that Produced a Large Solar Energetic Particle (SEP) Event," *Astrophys. J. Lett.* **788**, L20

Sterling, A. C., Moore, R. L., and Harra, L. K., 2011 Dec., "Lateral Offset of the Coronal Mass Ejections from the X-flare of 2006 December 13 and Its Two Precursor Eruptions," *Astrophys. J.* **743**, 63

Sturrock, P. A., 1966 Aug, "Model of the High-Energy Phase of Solar Flares," *Nature* **211**, 695–697.

Su, Y., and van Ballegooijen, A., 2013 Feb., "Rotating Motions and Modeling of the Erupting Solar Polar-crown Prominence on 2010 December 6," *Astrophys. J.* **764**, 91

Sui, L., Holman, G. D., and Dennis, B. R., 2004 Sep, "Evidence for Magnetic Reconnection in Three Homologous Solar Flares Observed by RHESSI," *Astrophys. J.* **612**, 546–556.

Sun, X., 2013 Sep, "On the Coordinate System of Space-Weather HMI Active Region Patches (SHARPs): A Technical Note," *arXiv e-prints*, arXiv:1309.2392

Svestka, Z., and Cliver, E. W., 1992, "History and Basic Characteristics of Eruptive Flares," in *IAU Colloq. 133: Eruptive Solar Flares*, Vol. 399, edited by Svestka, Z., Jackson, B. V., and Machado, M. E., p. 1.

Syed Ibrahim, M., Joshi, B., Cho, K. S., Kim, R. S., and Moon, Y. J., 2019 May, "Interplanetary Coronal Mass Ejections During Solar Cycles 23 and 24: Sun-Earth Propagation Characteristics and Consequences at the Near-Earth Region," *Solar Phys.* **294**, 54

Tan, B., Ji, H., Huang, G., Zhou, T., Song, Q., and Huang, Y., 2006 Dec., "Evolution of Electric Currents Associated with Two M-Class Flares," *Solar Phys.* **239**, 137–148.

Tandberg-Hanssen, E., 1995, *The nature of solar prominences*, Vol. 199

Temmer, M., Veronig, A. M., Kontar, E. P., Krucker, S., and Vršnak, B., 2010 Apr., "Combined STEREO/RHESSI Study of Coronal Mass Ejection Acceleration and Particle Acceleration in Solar Flares," *Astrophys. J.* **712**, 1410–1420.

Temmer, M., Veronig, A. M., Vršnak, B., and Miklenic, C., 2007 Jan., "Energy Release Rates along Hα Flare Ribbons and the Location of Hard X-Ray Sources," *Astrophys. J.* **654**, 665–674.

Temmer, M., Veronig, A. M., Vršnak, B., Rybák, J., Gömöry, P., Stoiser, S., and Maričić, D., 2008 Jan, "Acceleration in Fast Halo CMEs and Synchronized Flare HXR Bursts," *Astrophys. J. Lett.* **673**, L95.

Tenerani, A., Velli, M., Rappazzo, A. F., and Pucci, F., 2015 Nov., "Magnetic Reconnection: Recursive Current Sheet Collapse Triggered by "Ideal" Tearing," *Astrophys. J. Lett.* **813**, L32

Thompson, B. J., and Myers, D. C., 2009 Aug., "A Catalog of Coronal "EIT Wave" Transients," *Astrophys. J. Suppl.* **183**, 225–243.

Tolbert, K., and Schwartz, R., 2020 Jul., "OSPEX: Object Spectral Executive," Astrophysics Source Code Library, record ascl:2007.018

Toriumi, S., and Wang, H., 2019 May, "Flare-productive active regions," *Living Reviews in Solar Physics* **16**, 3

Török, T., Leake, J. E., Titov, V. S., Archontis, V., Mikić, Z., Linton, M. G., Dalmasse, K., Aulanier, G., and Kliem, B., 2014 Feb., "Distribution of Electric Currents in Solar Active Regions," *Astrophys. J. Lett.* **782**, L10

Török, T., Panasenco, O., Titov, V. S., Mikić, Z., Reeves, K. K., Velli, M., Linker, J. A., and De Toma, G., 2011 Oct., "A Model for Magnetically Coupled Sympathetic Eruptions," *Astrophys. J. Lett.* **739**, L63

Tousey, R., 1973 Jan., "The solar corona.." in *Space Research Conference*, Vol. 2, pp. 713–730.

van Ballegooijen, A. A., and Martens, P. C. H., 1989 Aug., "Formation and Eruption of Solar Prominences," *Astrophys. J.* **343**, 971.

Vekstein, G., 2016 Aug., "Storing free magnetic energy in the solar corona," *Journal of Plasma Physics* **82**, 925820401

Vemareddy, P., 2017 Aug., "Successive Homologous Coronal Mass Ejections Driven by Shearing and Converging Motions in Solar Active Region NOAA 12371," *Astrophys. J.* **845**, 59

Veronig, A., Vršnak, B., Temmer, M., and Hanslmeier, A., 2002 Aug, "Relative timing of solar flares observed at different wavelengths," *Solar Phys.* **208**, 297–315.

Veronig, A. M., and Brown, J. C., 2004 Mar, "A Coronal Thick-Target Interpretation of Two Hard X-Ray Loop Events," *Astrophys. J. Lett.* **603**, L117–L120.

Veronig, A. M., Podladchikova, T., Dissauer, K., Temmer, M., Seaton, D. B., Long, D., Guo, J., Vršnak, B., Harra, L., and Kliem, B., 2018 Dec, "Genesis and Impulsive Evolution of the 2017 September 10 Coronal Mass Ejection," *Astrophys. J.* **868**, 107

Vršnak, B., 2016 Nov, "Solar eruptions: The CME-flare relationship," *Astronomische Nachrichten* **337**, 1002.

Wang, H., Cao, W., Liu, C., Xu, Y., Liu, R., Zeng, Z., Chae, J., and Ji, H., 2015 Apr.a, "Witnessing magnetic twist with high-resolution observation from the 1.6-m New Solar Telescope," *Nature Communications* **6**, 7008

Wang, H., and Liu, C., 2012 Dec., "Circular Ribbon Flares and Homologous Jets," *Astrophys. J.* **760**, 101

Wang, H., Liu, C., Deng, N., Zeng, Z., Xu, Y., Jing, J., and Cao, W., 2014 Jan., "Study of Two Successive Three-ribbon Solar Flares on 2012 July 6," *Astrophys. J. Lett.* **781**, L23

Wang, J., Liu, C., Deng, N., and Wang, H., 2018 Feb, "Evolution of Photospheric Flow and Magnetic Fields Associated with the 2015 June 22 M6.5 Flare," *Astrophys. J.* **853**, 143

Wang, J., Zhang, Y., He, H., Chen, A., Jin, C., and Zhou, G., 2015 Sep.b, "Cluster of solar active regions and onset of coronal mass ejections," *Science China Physics, Mechanics, and Astronomy* **58**, 5682

Wang, J., Zhang, Y., Zhou, G., Harra, L. K., Williams, D. R., and Jiang, Y., 2007 Aug., "Solar Trans-equatorial Activity," *Solar Phys.* **244**, 75–94.

Wang, Y., and Zhang, J., 2007 Aug., "A Comparative Study between Eruptive X-Class Flares Associated with Coronal Mass Ejections and Confined X-Class Flares," *Astrophys. J.* **665**, 1428–1438.

Warmuth, A., 2015 Sep., "Large-scale Globally Propagating Coronal Waves," *Living Reviews in Solar Physics* **12**, 3

Warren, H. P., O'Brien, C. M., and Sheeley, J., Neil R., 2011 Dec., "Observations of Reconnecting Flare Loops with the Atmospheric Imaging Assembly," *Astrophys. J.* **742**, 92

Warren, H. P., and Warshall, A. D., 2001 Oct., "Ultraviolet Flare Ribbon Brightenings and the Onset of Hard X-Ray Emission," *Astrophys. J. Lett.* **560**, L87–L90.

Webb, D. F., and Howard, T. A., 2012 Jun., "Coronal Mass Ejections: Observations," *Living Reviews in Solar Physics* **9**, 3

Wheatland, M. S., Sturrock, P. A., and Roumeliotis, G., 2000 Sep., "An Optimization Approach to Reconstructing Force-free Fields," *Astrophys. J.* **540**, 1150–1155.

Wiegelmann, T., 2004 Jan., "Optimization code with weighting function for the reconstruction of coronal magnetic fields," *Solar Phys.* **219**, 87–108.

Wiegelmann, T., 2008 Mar, "Nonlinear force-free modeling of the solar coronal magnetic field," *Journal of Geophysical Research (Space Physics)* **113**, A03S02

Wiegelmann, T., and Inhester, B., 2010 Jun., "How to deal with measurement errors and lacking data in nonlinear force-free coronal magnetic field modelling?." *Astron. Astrophys.* **516**, A107

Wiegelmann, T., Thalmann, J. K., Inhester, B., Tadesse, T., Sun, X., and Hoeksema, J. T., 2012 Nov., "How Should One Optimize Nonlinear Force-Free Coronal Magnetic Field Extrapolations from SDO/HMI Vector Magnetograms?." *Solar Phys.* **281**, 37–51.

Woodgate, B. E., Martres, M. J., Smith, J., J. B., Strong, K. T., McCabe, M. K., Machado, M. E., Gaizauskas, V., Stewart, R. T., and Sturrock, P. A., 1984 Jan., "Progress in the study of homologous flares on the sun - Part II," *Advances in Space Research* **4**, 11–17.

Woods, M. M., Harra, L. K., Matthews, S. A., Mackay, D. H., Dacie, S., and Long, D. M., 2017 Feb., "Observations and Modelling of the Pre-flare Period of the 29 March 2014 X1 Flare," *Solar Phys.* **292**, 38

Woods, M. M., Inoue, S., Harra, L. K., Matthews, S. A., Kusano, K., and Kalmoni, N. M. E., 2018 Jun., "The Triggering of the 2014 March 29 Filament Eruption," *Astrophys. J.* **860**, 163

Wyper, P. F., Antiochos, S. K., and DeVore, C. R., 2017 Apr., "A universal model for solar eruptions," *Nature* **544**, 452–455.

Xue, Z., Yan, X., Yang, L., Wang, J., and Zhao, L., 2017 May, "Observing Formation of Flux Rope by Tether-cutting Reconnection in the Sun," *Astrophys. J. Lett.* **840**, L23

Yang, J., Jiang, Y., Zheng, R., Hong, J., Bi, Y., and Yang, L., 2011 Jun., "Quadrupolar Dimmings During a Partial Halo Coronal Mass Ejection Event," *Solar Phys.* **270**, 551–559.

Yang, J., Jiang, Y., Bi, Y., Li, H., Hong, J., Yang, D., Zheng, R., and Yang, B., 2012 Apr.a, "An Over-and-out Halo Coronal Mass Ejection Driven by the Full Eruption of a Kinked Filament," *Astrophys. J.* **749**, 12

Yang, J., Jiang, Y., Zheng, R., Bi, Y., Hong, J., and Yang, B., 2012 Jan.b, "Sympathetic Filament Eruptions from a Bipolar Helmet Streamer in the Sun," *Astrophys. J.* **745**, 9

Yang, K., Guo, Y., and Ding, M. D., 2016 Jun., "Quantifying the Topology and Evolution of a Magnetic Flux Rope Associated with Multi-flare Activities," *Astrophys. J.* **824**, 148

Yashiro, S., Akiyama, S., Gopalswamy, N., and Howard, R. A., 2006 Oct., "Different Power-Law Indices in the Frequency Distributions of Flares with and without Coronal Mass Ejections," *Astrophys. J. Lett.* **650**, L143–L146.

Yashiro, S., Gopalswamy, N., Michalek, G., St. Cyr, O. C., Plunkett, S. P., Rich, N. B., and Howard, R. A., 2004 Jul, "A catalog of white light coronal mass ejections observed by the SOHO spacecraft," *Journal of Geophysical Research (Space Physics)* **109**, A07105

Young, P. R., Tian, H., and Jaeggli, S., 2015 Feb., "The 2014 March 29 X-flare: Subarcsecond Resolution Observations of Fe XXI λ1354.1," *Astrophys. J.* **799**, 218

Yurchyshyn, V., Karlický, M., Hu, Q., and Wang, H., 2006 May, "Evidence for Tether-Cutting Reconnection in a Quadrupole Magnetic Configuration in the April 9, 2001, M7.9 Flare," *Solar Phys.* **235**, 147–160.

Zhang, G., and Burlaga, L. F., 1988 Apr, "Magnetic clouds, geomagnetic disturbances, and cosmic ray decreases," *J. Geophys. Res.* **93**, 2511–2518.

Zhang, J., Dere, K. P., Howard, R. A., Kundu, M. R., and White, S. M., 2001 Sep., "On the Temporal Relationship between Coronal Mass Ejections and Flares," *Astrophys. J.* **559**, 452–462.

Zhang, J., Cheng, X., and Ding, M.-D., 2012 Mar., "Observation of an evolving magnetic flux rope before and during a solar eruption," *Nature Communications* **3**, 747

Zhang, J., and Wang, J., 2002 Feb., "Are Homologous Flare-Coronal Mass Ejection Events Triggered by Moving Magnetic Features?." *Astrophys. J. Lett.* **566**, L117–L120.

Zhao, X. P., and Webb, D. F., 2003 Jun., "Source regions and storm effectiveness of frontside full halo coronal mass ejections," *Journal of Geophysical Research (Space Physics)* **108**, 1234

Zhou, G. P., Wang, J. X., and Zhang, J., 2006 Jan., "Large-scale source regions of earth-directed coronal mass ejections," *Astron. Astrophys.* **445**, 1133–1141.

Zhou, G. P., Zhang, J., and Wang, J. X., 2016 May, "Observations of Magnetic Flux-rope Oscillation during the Precursor Phase of a Solar Eruption," *Astrophys. J. Lett.* **823**, L19

Zirker, J. B., 1989 Sep., "Quiescent Prominences," *Solar Phys.* **119**, 341–356.

Zuccarello, F., Ermolli, I., Korsós, M. B., Giorgi, F., Guglielmino, S. L., Erdélyi, R., and Romano, P., 2021 Dec., "Comparative case study of two methods to assess the eruptive potential of selected active regions," *Research in Astronomy and Astrophysics* **21**, 313

Zurbuchen, T. H., and Richardson, I. G., 2006 Mar, "In-Situ Solar Wind and Magnetic Field Signatures of Interplanetary Coronal Mass Ejections," *Space Sci. Rev.* **123**, 31–43.

Zwaan, C., 1987 Jan., "Elements and patterns in the solar magnetic field.." *Annu.* **25**, 83–111.

The Astrophysical Journal, 897:157 (19pp), 2020 July 10 https://doi.org/10.3847/1538-4357/ab962b

Hard X-Ray Emission from an Activated Flux Rope and Subsequent Evolution of an Eruptive Long-duration Solar Flare

Suraj Sahu[1,2], Bhuwan joshi[1], Prabir K. Mitra[1], Astrid M. Veronig[3,4], and V. Yurchyshyn[5]
[1] Udaipur Solar Observatory, Physical Research Laboratory, Udaipur 313001, India; suraj@prl.res.in
[2] Indian Institute of Technology Gandhinagar, Gujarat 382355, India
[3] Institute of Physics, University of Graz, A-8010 Graz, Austria
[4] Kanzelhöhe Observatory for Solar and Environmental Research, University of Graz, A-9521 Treffen, Austria
[5] Big Bear Solar Observatory, New Jersey Institute of Technology, Big Bear City, CA 92314, USA
Received 2020 March 15; revised 2020 May 11; accepted 2020 May 11; published 2020 July 14

Abstract

In this paper, we present a comprehensive study of the evolutionary phases of a major M6.6 long duration event with special emphasize on its pre-flare phase. The event occurred in NOAA 12371 on 2015 June 22. A remarkable aspect of the event was an active pre-flare phase lasting for about an hour during which a hot EUV coronal channel was in the build-up stage and displayed cospatial hard X-ray (HXR) emission up to energies of 25 keV. This is the first evidence of the HXR coronal channel. The coronal magnetic field configuration based on nonlinear-force-free-field modeling clearly exhibited a magnetic flux rope (MFR) oriented along the polarity inversion line (PIL) and cospatial with the coronal channel. We observed significant changes in the AR's photospheric magnetic field during an extended period of ≈42 hr in the form of rotation of sunspots, moving magnetic features, and flux cancellation along the PIL. Prior to the flare onset, the MFR underwent a slow rise phase (≈14 km s^{-1}) for ≈12 minutes, which we attribute to the faster build-up and activation of the MFR by tether-cutting reconnection occurring at multiple locations along the MFR itself. The sudden transition in the kinematic evolution of the MFR from the phase of slow to fast rise (≈109 km s^{-1} with acceleration ≈110 m s^{-2}) precisely divides the pre-flare and impulsive phase of the flare, which points toward the feedback process between the early dynamics of the eruption and the strength of the flare magnetic reconnection.

Unified Astronomy Thesaurus concepts: Solar active regions (1974); Solar active region filaments (1977); Solar flares (1496); Solar magnetic reconnection (1504); Solar x-ray emission (1536)

Supporting material: animations

1. Introduction

Solar eruptions are complex phenomena with multiple facets right from their genesis in the solar atmosphere to subsequent consequences in the near-Sun, interplanetary, and near-Earth regions (Gopalswamy et al. 2001; Webb & Howard 2012; Archontis & Vlahos 2019). Decades of observational and theoretical research has elucidated different aspects of it, namely, solar flares, eruptive prominences, coronal mass ejections (CMEs), coronal jets, etc., which are observationally defined as disjoint terms but occur as a result of physically coupled processes (e.g., see reviews by Priest & Forbes 2002; Fletcher et al. 2011). Exploration of solar eruptive phenomena using multiwavelength, multi-instrument, and multipoint observations is key toward better understanding of the origin and prediction of space weather events (Koskinen et al. 2017; Green et al. 2018).

The source regions of solar eruptions frequently show the presence of interesting observational features, e.g., prominences, filament channels, hot coronal channels, etc., which have been accepted as evidence of a fundamental structure called the magnetic flux rope (MFR; Cheng et al. 2011; Patsourakos et al. 2013; Joshi et al. 2017; Mitra et al. 2018; Veronig et al. 2018). MFRs are often defined as a bundle of magnetic field lines that are twisted around each other and wrap around a common axis (Gibson & Fan 2006; Canou & Amari 2010; Filippov et al. 2015; Cheng et al. 2017). MFRs not only play a crucial role in triggering the eruption but also constitute a key component of CMEs. Near-Earth in situ measurements often reveal evidence of MFRs at large scales in the form of interplanetary magnetic clouds signifying the arrival of Earth-directed CMEs (Burlaga et al. 1981, 1998; Klein & Burlaga 1982; Möstl et al. 2009; Syed Ibrahim et al. 2019), that may subsequently cause geomagnetic disturbances when interacting with Earth's magnetic field (Zhang & Burlaga 1988; Burlaga et al. 2001; Zurbuchen & Richardson 2006; Bisoi et al. 2016; Joshi et al. 2018). Here some basic questions arise: how do MFRs originate in the solar corona and what are the mechanisms responsible for their eruptions? The analysis of multiwavelength solar observations of the source regions of CMEs and their comparison with coronal magnetic field modeling yield important insights on these open issues.

The formation of a CME requires the activation and successful eruption of the MFR against solar gravity and the overlying coronal magnetic field. According to the standard flare model also known as the CSHKP model (Carmichael 1964; Sturrock 1966; Hirayama 1974; Kopp & Pneuman 1976), the eruptive expansion of the unstable MFR creates strong inflow of plasma and magnetic field lines in the large-scale current sheet that is formed underneath it causing the onset of magnetic reconnection. During magnetic reconnection, the stored magnetic energy is released in the form of intense heating within a localized region as well as acceleration of plasma and high energy particles (Priest & Forbes 2002; Holman et al. 2011). The spatio-temporal characteristics of a solar flare explored from multiwavelength and multiband measurements provide useful information about the origin of the nonthermal and thermal emissions (Fletcher et al. 2011;

Benz 2017). These observations also pose constraints on the standard flare model (Sui et al. 2004; Veronig & Brown 2004; Joshi et al. 2012).

It has been observed that many flares are associated with pre-flare and precursor activities, which include small-scale brightness enhancements in the flaring region of about a few to tens of minutes prior to its impulsive phase (Veronig et al. 2002; Kundu et al. 2004; Joshi et al. 2011, 2013; Mitra et al. 2020). While the precursor phase often shows a direct link to the later eruptive phenomenon, the pre-flare activity is viewed as a single or multiple series of small-scale reconnection events within the active region and may indirectly support the eruption by changing the magnetic and plasma conditions favorably (Fárník et al. 1996; Fárník & Savy 1998; Chifor et al. 2006; Joshi et al. 2011, 2013; Mitra & Joshi 2019). Arguably the observations of pre-flare or precursor activity have the potential to provide insight on the build-up phase of MFR and the triggering mechanism of the subsequent solar eruption.

During 2015 June 15–29, AR NOAA 12371 passed over the solar visible disk and produced several eruptive flares including geoeffective ones. The long duration event of GOES class M6.6/Hα importance 2B occurred on 2015 June 22 is of particular interest in view of the highly eventful and extended pre-flare phase, its dual peak main phase, as well as the very distinct observations of the MFR structure and overlying strapping field in the Atmospheric Imaging Assembly (AIA) EUV filtergrams. This event has been the subject of several studies. Jing et al. (2017) reported on the large-scale dynamics associated with the flare. They noted propagation of footpoint brightening driven by injection of nonthermal particles and the apparent slippage of loops governed by plasma heating and subsequent cooling. Wang et al. (2018) studied the changes in photospheric flows and magnetic field structures associated with the flare. Their study reveals the role of back reaction of the coronal fields as caused by the flare energy release. Awasthi et al. (2018) analyzed the pre-flare configuration and identified a multiple braided flux rope along the polarity inversion line (PIL) with different degrees of coherency over the pre-flare phase. Liu et al. (2018a) analyzed the changes in the photospheric vector magnetic field, which are related to the motion of the flare ribbons. Kang et al. (2019) reported the involvement of ideal instabilities (double arc instability and torus instability) and the tether-cutting mechanism as plausible causes of the eruption of the flux rope and subsequent M6.6 flare.

In this study, we revisit SOL2015-06-22T18:23 to investigate the processes occurring during the extended period prior to the onset of eruption, the pre-flare activity while the quasi-stable MFR continued to build up, and how these processes relate to the subsequent impulsive phase when the MFR underwent spectacular eruption that led to a fast halo CME. The paper is organized as follows. In Section 2, we provide a brief discussion about observational data and techniques. Section 3 provides an extensive exploration of the multi-wavelength data in (E)UV, X-ray, and optical bands along with analysis of photosphetic magnetograms. The results are discussed in Section 4.

2. Observational Data and Techniques

This study is primarily based on data from the AIA (Lemen et al. 2012) and the Heliosesmic and Magnetic Imager (HMI; Schou et al. 2012) on board the Solar Dynamics Observatory (SDO; Pesnell et al. 2012). AIA records full disk images of the corona and transition region up to 0.5 $R_\odot$ above the photosphere in EUV and UV filters. It produces narrowband images centered on specific lines corresponding to seven EUV passbands: they are 94 Å (Fe XVIII), 131 Å (Fe VIII, XXI), 171 Å (Fe IX), 193 Å (Fe XII, XXIV), 211 Å (Fe XIV), 304 Å (He II), and 335 Å (Fe XVI). UV observations are made at 1600 Å (C IV) and 1700 Å (nearby continuum). AIA produces 4096 × 4096 pixel images at a pixel resolution of $0\farcs6$ pixel^{-1} with a temporal cadence of 12 s for the EUV filters and 24 s for the UV filters. In this study, we have extensively analyzed the observations taken in the 94 Å (log $T = 6.8$) and the 304 Å (log $T = 4.7$) channels besides examining images at other AIA channels.

HMI provides full disk measurements of the intensity, Doppler shift, line-of-sight (LOS) magnetic field, and vector magnetic field at the solar photosphere using the 6173 Å Fe I absorption line. Images are produced with 4096 × 4096 pixel at a pixel resolution of $0\farcs5$ pixel^{-1} and a temporal cadence of 45 s for velocity, intensity, and LOS magnetic field. For the vector magnetic field, the temporal cadence is 720 s. In order to compare the images from HMI with AIA, we use the SSW routine *hmi_prep.pro*, which converts the resolution of the HMI images from $0\farcs5$ pixel^{-1} to $0\farcs6$ pixel^{-1}, which is the pixel resolution of AIA.

The Hα images studied are full disk observations from Big Bear Solar Observatory (BBSO; Denker et al. 1999) with a telescope aperture of 10 cm. These Hα observations are taken with a filter of 0.25 Å bandpass centered at the Hα line core and 2048 × 2048 pixel CCD camera. The images have a temporal cadence of ≈60 s and pixel resolution $\approx 1\farcs0$.

The temporal, spatial, and spectral evolution of the hard X-ray (HXR) emission from the flaring region is analyzed using data from the Reuven Ramaty High Energy Solar Spectroscopic Imager (RHESSI; Lin et al. 2002). RHESSI observed the full Sun with an unprecedented combination of spatial resolution (as fine as $\sim 2\farcs3$) and energy resolution (1–10 keV) in the energy range 3 keV–17 MeV. To reconstruct RHESSI HXR images at different energy bands, we have used the CLEAN algorithm (Hurford et al. 2002). For HXR spectroscopy, we generated RHESSI spectra with an energy binning of 1/3 keV from 6 to 15 keV, 1 keV from 15 to 100 keV, and 5 keV from 100 keV onward. We only used front segments of the detectors, and excluded detectors 2 and 7 (which have lower energy resolution and high threshold energies, respectively; Smith et al. 2002). The spectra were deconvolved with the full detector response matrix. Two fitting models have been used: line emission from an isothermal plasma and thick-target bremsstrahlung from nonthermal electrons interacting with the chromosphere (Holman et al. 2003). From spectral fits, we derived the temperature (T) and emission measure (EM) of the hot flaring plasma, as well as the nonthermal electron spectral index (δ) for the nonthermal component.

The CME associated with the M6.6 flare under study was observed by the C2 and C3 instruments of the Large Angle and Spectrometric Coronagraph (LASCO; Brueckner et al. 1995) on board the Solar and Heliospheric Observatory (SOHO; Domingo et al. 1995). C2 and C3 are white light coronagraphs that image the solar corona with a field of view of 1.5–6 $R_{\odot}$ and 3.7–30 $R_{\odot}$, respectively.

To model the coronal magnetic field distribution, we used the hmi.sharp_cea_720s series vector magnetogram of SDO/HMI as the input boundary condition. The magnetogram is remapped using a Lambert cylindrical equal-area projection and presented as (B_r, B_θ, B_ϕ) in heliocentric spherical coordinates corresponding to (B_z, B_y, B_x) in heliographic coordinates (Sun 2013). The magnetogram represents an area of 474 × 226 pixel^2 of the AR, which corresponds to an area of 343 × 163 Mm^2 on the surface of the Sun. The extrapolation was done up to a height of 163 Mm above the photosphere. To visualize the extrapolated field lines, we used Visualization and Analysis Platform for Ocean, Atmosphere, and Solar Researchers[6] (Clyne et al. 2010) software.

3. Multiwavelength Observations and Results

3.1. Event Overview and Light-curve Analysis

We investigate an M6.6 class flare from AR NOAA 12371 on 2015 June 22 from 16:00 UT to 23:00 UT. The active region was situated at heliographic coordinate ≈N12W08 during the onset of the flare. In Figure 1, we present a multiwavelength view of the active region to compare its morphology at different atmospheric layers of the Sun. The white light image of the active region shows two distinct sunspot groups (shown by dashed boxes in Figure 1(a)). A comparison of white light image with LOS magnetogram of the active region suggests that the leading sunspot group is of negative polarity and the trailing sunspot group is comprised of mixed polarity regions making it a $\beta\gamma$ type active region (see Figures 1(a) and (b)). The flaring site is located over the trailing sunspot group (shown by the yellow dashed box in Figure 1(b)). The AIA 94 Å image during the pre-flare phase (Figure 1(c)) suggests that, the activity site was associated with intensely emitting closed loops, which we mark by a dotted rectangle and annotate as hot core. Furthermore, we identify a hot channel-like structure at low coronal heights (marked by a yellow arrow as the hot EUV channel). By examining the images in the AIA 94 Å channel prior to the event over several hours, we find that, the hot channel pre-existed at least ≈5.5 hr before the eruptive flare. A comparison of the AIA 94 Å image with a cotemporal HMI magnetogram suggests that the brightest part of the core region with dense coronal loops essentially lie over the trailing part of the active region showing a complex bipolar magnetic distribution of sunspots. The 171 Å image in Figure 1(d) shows high coronal loops (HCLs) connecting the leading and trailing sunspot groups. In Figure 1(e), the AIA 304 Å image shows the signature of a filament channel. In Figure 1(f), the BBSO Hα image clearly shows the filament channel over PIL (see Figures 1(b) and (f)). We infer the hot EUV channel to be the coronal counterpart of the chromospheric filament delineating the PIL of the trailing bipolar part of the active region.

The GOES soft X-ray (SXR) light curves in 1–8 and 0.5–4 Å (Figure 2(a)), show distinct pre-flare, main, and gradual phases of the long duration flare event under study. We see two distinct peaks in the pre-flare phase (P1 and P2) at ≈16:45 UT and ≈17:26 UT. A sharp rise in the GOES SXR flux at ≈17:35 UT indicates the start of the main phase of the M6.6 flare with dual peak structures (F1 and F2) at ≈18:00 UT and ≈18:13 UT. According to the GOES flare catalog, which is based on the return of the SXR flux to half of its peak value, the flare lasted until 18:51 UT. However, the GOES profiles (Figure 2(a)) clearly reveal enhanced SXR emission from the flaring region for several hours (≈up to 21:00 UT), that we mark as prolonged decay phase. In Table 1, we summarize the different phases of the flare evolution along with their characteristics, which we discuss in subsequent sections.

Normalized intensity light curves of the AIA channel 171, 304, 94, and 1600 Å filters are shown in Figure 2(b). In general, these (E)UV light curves show similar trends than the GOES SXR light curves with some time delays in the peak emission among different bands. The first peak P1 of the GOES light curve in 0.5–4 Å channel is not seen in the AIA light curves; while the second peak P2 is clearly visible (shown by dotted lines in Figure 2(b)). The 94 Å light curve shows a significant time-shift in the peak compared to other AIA light curves and continued emission for a longer period (up to 21:00 UT). The AIA 171 Å light curve shows significant variability in the decay phase, which is not seen in other AIA light curves. The 1600 Å light curve shows dual peak structure in the main phase of the M6.6 flare similar to GOES light curves.

In Figure 2, we provide a comparison of the active region corona during the pre- and post-flare phases of the flare as recorded in different SDO/AIA channels, namely, in 94 Å (see Figures 2(c)–(d)), in 304 Å (see Figures 2(e)–(f)), and in 171 Å (see Figures 2(g)–(h)). In the pre-flare stage, we observe low-lying coronal loops (LLCLs) with a faint signature of a hot coronal channel underlying the low coronal loops in the 94 Å image (Figure 2(c)). In the post-flare stage, dense and bright post-flare loops are observed to be formed (Figure 2(d)). In AIA 304 Å, we observe the signature of the filament in the pre-flare stage (Figure 2(e)), whose eruption gives rise to formation of post-flare loop arcades (Figure 2(f)). In the post-flare stage, AIA 171 Å observations also reveal the formation of dense post-flare loop arcades (Figure 2(h)).

In Figure 3, we show RHESSI X-ray count rates in different energy bands from 3 to 100 keV in the interval of 16:30 UT to 18:35 UT. The cotemporal GOES SXR light curves in 1–8 and 0.5–4 Å are overplotted on the RHESSI count rates. We observe the simultaneous occurrence of peaks in GOES SXR and lower energy RHESSI (<25 keV) light curves in the pre-flare stage (from ≈16:30 UT to ≈17:35 UT). In the main phase of the flare (from ≈17:35 UT onward), the higher energy RHESSI (>25 keV) light curves show distinct small peaks.

To show the overall evolution of the M6.6 flare, we present a few representative Hα images in Figure 4, which are obtained from BBSO. At the pre-flare stage, we observe the presence of a filament channel along the PIL of the active region (shown by purple arrows in Figure 4(a)). During the early stage of the main phase of the flare, we observe activation of the filament channel in two different directions: along the length of the channel toward the southwest (shown by blue arrows in Figure 4(d)) and along the northwest direction (shown by green arrows in Figure 4(d)). The filament continued to erupt along the northwest direction and produced intense flare brightening (Figures 4(e)–(f)). The two-step activation of the filament channel may be associated with the pre-flare activities that led to the partial eruption of the filament. In the post-flare phase, we identify a filamentary material to be erupted from the core part of the flaring region, which is shown by red arrows in Figures 4(g)–(i).

[6] https://www.vapor.ucar.edu/

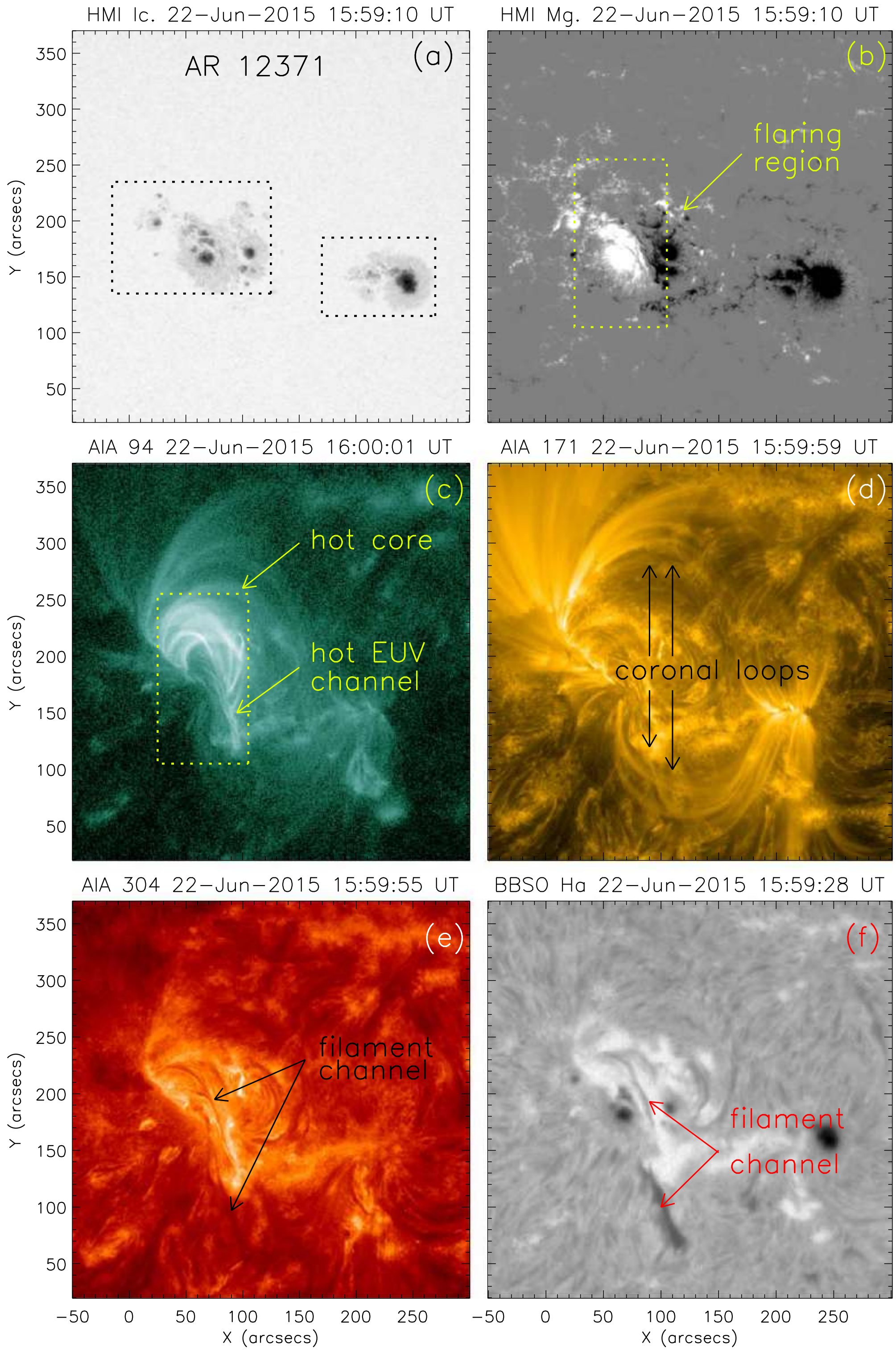

Figure 1. Multiwavelength view of active region NOAA 12371 on 2015 June 22. (a) White light image of the active region showing configurations of leading and trailing sunspot groups, which are shown by dotted boxes. (b) HMI LOS magnetogram showing the photospheric magnetic structure of the active region. The flare under investigation primarily originated in the trailing part of the active region. (c) AIA 94 Å image of the pre-flare phase showing the hot core region where the M6.6 class flare occurred. (d) AIA 171 Å image showing HCLs that lie over the sunspot groups. (e) AIA 304 Å image showing faint filament structure in the chromospheric level. (f) BBSO Hα image showing clear filament channel above PIL. Comparison of panels (c), (e), and (f) reveals that, a filament exists in the chromosphere underneath the hot EUV channel.

The eruption of the hot channel and the subsequent flare resulted into a fast halo CME, which was observed by C2 and C3 coronagraphs of LASCO on board SOHO (Figure 5). Various CME parameters have been gathered from the LASCO CME catalog (Yashiro et al. 2004).[7] The CME was first detected by C2 at ≈18:36 UT (Figure 5(a)) at the height of

[7] https://cdaw.gsfc.nasa.gov/CME_list/UNIVERSAL/2015_06/univ2015_06.html

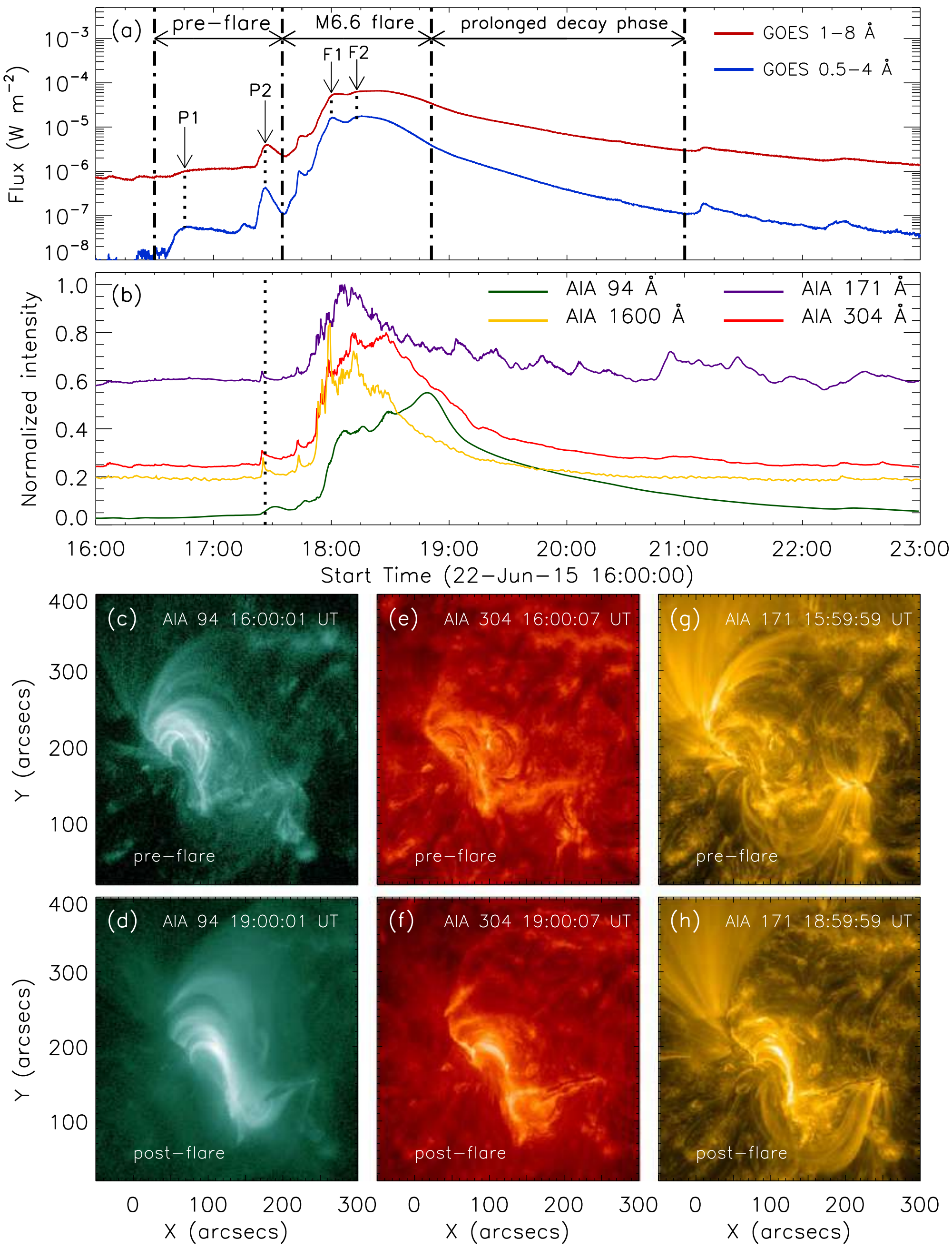

Figure 2. Panel (a): GOES SXR flux in 1–8 and 0.5–4 Å channel from 16:00 UT to 23:00 UT on 2015 June 22. We find two stages in the pre-flare phase that peak at 16:45 UT (marked as P1) and 17:26 UT (marked as P2), respectively. We also observe dual flare-peak structure in the main phase of the M6.6 flare, indicated as F1 and F2 at 18:00 UT and 18:13 UT, respectively. Panel (b): AIA light curves normalized by peak intensity of respective AIA filters. For a clear view, light curves have been scaled by factors of 0.55 and 0.8 for 94 Å and 304 Å channels, respectively. The peak P2 in GOES SXR light curves in the pre-flare phase corresponds to a peak in AIA light curves, which is shown by the dotted line. We readily observe that the structure of the active region shows significant changes during the course of the flare. As a comparison between pre- and post-flare phases, we plot the active region corona in AIA 94 Å (see panels (c) and (d)), 304 Å (see panels (e) and (f)), and in 171 Å (see panels (g) and (h)). An animation of this figure showing the temporal evolution of the flare is available. The animation includes the GOES SXR flux light curve (top) and the corresponding AIA 94, 304, and 171 Å images (bottom) running from 16:00 UT to 23:00 UT on 2015 June 22.

(An animation of this figure is available.)

$4.1\,R_\odot$ and propagated with a projected linear speed of $\approx$1200 km s^{-1} measured at position angle 357°.

3.2. Structure and Evolution of the Photospheric Magnetic Field

Coronal magnetic configurations are deeply associated with changes of photospheric magnetic structures. Therefore, to understand the cause of flaring activities and filament eruptions, it is essential to study the changes associated with the photospheric magnetic fields. The magnetic structure of the AR 12371, one day prior to the event under investigation (i.e., 2015 June 21), is shown in Figure 6(a). The magnetic structure of the same AR just before the event is shown in Figure 6(b). A comparison of panels (a) and (b) reveals that the two subregions R_1 and R_2 underwent significant changes (see the animation associated with Figure 6). In order to

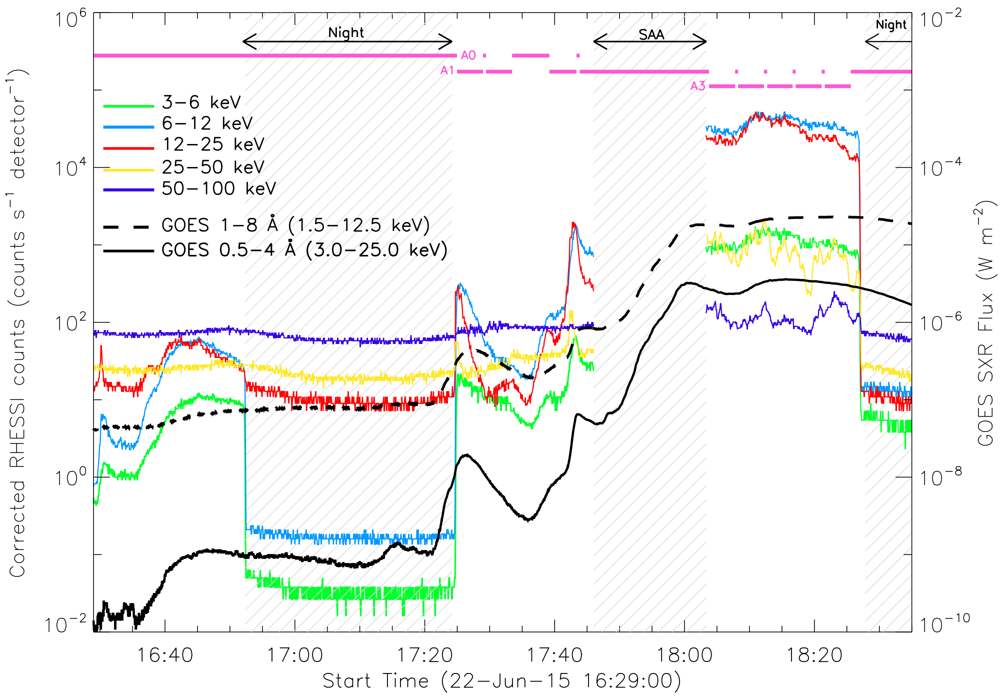

Figure 3. Temporal evolution of X-ray count rates observed by RHESSI from 16:29 UT to 18:35 UT in energy bands of 3–6, 6–12, 12–25, 25–50, and 50–100 keV with a time cadence of 4 s. GOES SXR light curves in 1–8 Å and 0.5–4 Å channels are also shown by dashed and solid lines, respectively. The hatched regions denote unavailability of solar X-ray data due to RHESSI night (N) and South Atlantic Anomaly. Different attenuator states (A0, A1, and A3) are shown by horizontal bars at the top.

Table 1
Summary of Different Phases of M6.6 Flare

Serial No.	Phases	Duration (UT)	Remarks
1	Pre-flare phase	16:30–17:35	Two distinct peaks (P1 and P2) are observed in GOES SXR light curves at ≈16:45 UT and ≈17:26 UT.
2	M6.6 flare	17:35–18:51	A distinct subpeak at ≈17:44 UT in X-ray light curves (GOES and RHESSI) during the rise phase (17:35–18:00 UT); broad maximum phase with dual peak structures (F1 and F2) in GOES light curves at ≈18:00 UT and ≈18:13 UT; eruption of hot channel begins at ≈17:40 UT; CME first detected in LASCO C2 coronagraph at ≈18:36 UT.
3	Post-flare phase	18:51–21:00	Very gradual decline of SXR emission in GOES light curves for ≈2 hr; after which the SXR flux reached to pre-flare background level; emission from large post-flare loops.

further probe the magnetic changes, a few representative magnetograms of the subregion R_1 from 2015 June 21 to 2015 June 22 are shown in panels R_1(a)–R_1(e) of Figure 6. A light bridge (marked by a yellow arrow) is noticeable, which gradually underwent apparent rotation in the clockwise direction. This light bridge separated the negative polarity sunspot and showed an increase in its width. White arrows show motion of a negative polarity region toward the southwest (see Figures 6R_1(a)–R_1(e)). Blue arrows show southward motion of another negative polarity region within subregion R_1.

In the first two panels of the LOS magnetograms of the R_2 region the sky blue arrows show an island of negative polarity region, which eventually merged into the major negative polarity region north of it (see Figures 6 R_2(a)–R_2(b)). Notably, the eastern part of R_2 showed a very intriguing dynamical evolution with multiple events of fragmentation and merging of magnetic structures. Eventually the region exhibited significant cancellation of negative magnetic flux (see the region marked by green arrows in Figures 6R_2(a), R_2(c), and R_2(e)).

3.3. Build-up and Activation of the Hot Coronal Channel

Based on the GOES light curves (Figure 2(a)), we have defined the pre-flare phase from ≈16:30 UT to ≈17:35 UT (see Table 1). In Figure 7, we show EUV images of the active region during the pre-flare phase by a few representative AIA 94 and 304 Å images. Initially, a faint hot channel is identified beneath coronal loops in the 94 Å images (marked by yellow arrow in Figure 7(a)). From the HMI LOS magnetogram contours overplotted on the 94 Å image (Figure 7(b)), it becomes clear that the hot channel lies over the PIL formed within the trailing sunspot group. Subsequently, the brightening of the hot channel intensifies (marked by yellow arrows in Figures 7(c) and (e)) and it appears distinctly different from the surrounding regions. In view of the spatial association of the hot channel and the overlying low coronal loops showing bright emission during the pre-flare phase, we identify the region shown inside the box in Figure 7(e) as the active region core and focus on its evolution in Figure 8. The hot channel continues to show enhanced emission until the occurrence of pre-flare peak P2 in GOES light curves (at ≈17:26 UT), which is indicated by the yellow arrow in Figure 7(f).

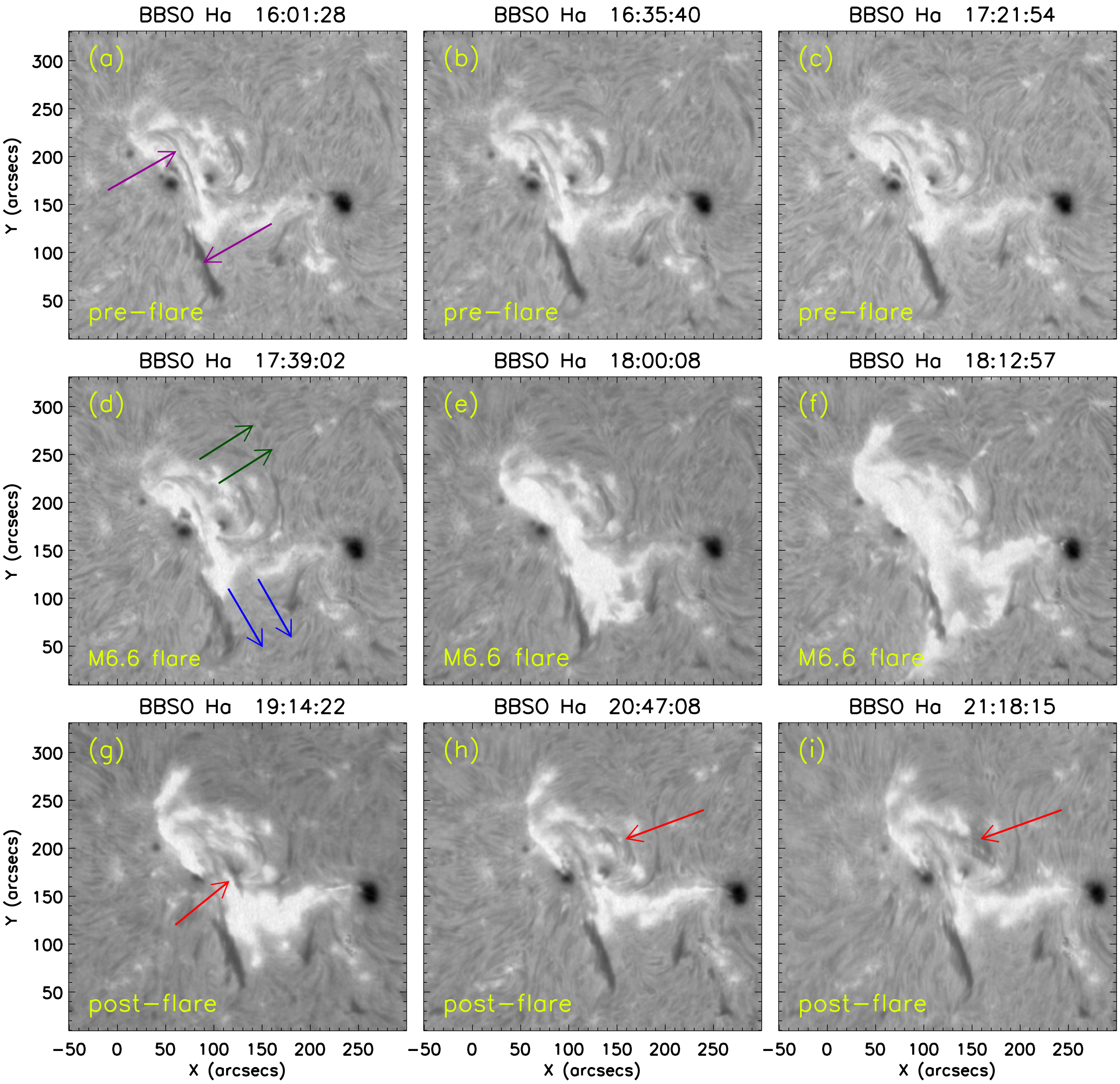

Figure 4. BBSO Hα filtergrams showing the temporal evolution of different phases of M6.6 flare, namely, pre-flare phase, main phase, and post-flare phase in panels (a)–(c), (d)–(f), and (g)–(i), respectively. Two distinct parts of the filament (shown by purple arrows in panel (a)), together constitute a filament channel. The onset of the M6.6 flare is preceded by activation of the filament channel in two different directions (shown by blue and green arrows in panel (d); for details, see Section 3.1). An upward motion of filament material is observed during the post-flare phase, which is shown by red arrows in panels (g)–(i).

In AIA 304 Å images, we observe a filament as the chromospheric counterpart of the hot channel (marked by the white arrow in Figure 7(g)). Subsequently, we observe two parallel ribbon-like brightenings at ≈16:45 UT (shown by white arrows in Figure 7(j)), which are cotemporal with the pre-flare peak P1 (Figure 2(a)). Thereafter, the flux rope undergoes enhanced brightening at ≈17:26 UT (Figure 7(l)). We note this brightening to be simultaneous with the appearance of pre-flare peak P2 in GOES light curves (Figure 2(a)).

In Figure 8, we show a sequence of AIA 94 Å images with cotemporal RHESSI X-ray images (as contours) overplotted on each panel. The evolution of the active region core during the first peak (P1) of pre-flare phase is shown in Figures 8(a)–(d). During this phase, the X-ray emission up to 15 keV is observed to come from the region of overlying coronal loops. We note that the X-ray emissions have spatially extended structure with multiple centroids, morphologically directly resembling the coronal loop system of the core region.

During the second peak (P2) of the pre-flare phase, we observe strong X-ray emission from the hot channel (Figures 8(e)–(h)) with X-ray emission up to 25 keV. Evolution of the X-ray sources during this period is very striking. Initially at ≈17:25 UT, we find X-ray emitting sources with distinct centroids in the energy bands up to 15 keV (Figure 8(e)). The X-ray emissions in 5–10 keV energy band show nearly double centroid structure throughout the pre-flare peak P2 (Figures 8(e)–(h)), whereas, the X-ray centroids in the 10–15 keV energy band dissolve (Figures 8(e)–(h)). Notably,

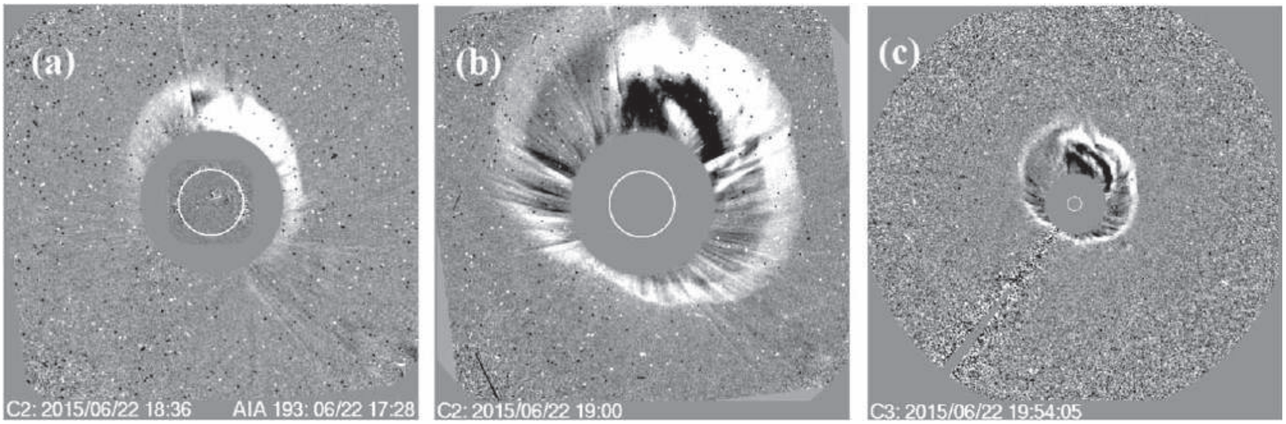

Figure 5. Running difference images of LASCO C2 (panels (a) and (b)) and C3 (panel (c)) coronagraph. Panel (a) shows first detection of CME in the C2 coronagraph. A full disk image of the Sun in AIA 193 Å is overplotted on the coronagraph occulter. The CME was first detected in the C3 coronagraph at ≈18:54 UT.(https://cdaw.gsfc.nasa.gov/movie/make_javamovie.php?stime=20150622_1708&etime=20150622_2105&img1=lasc2rdf&title=20150622.183605.p358g;V=1209km/s)

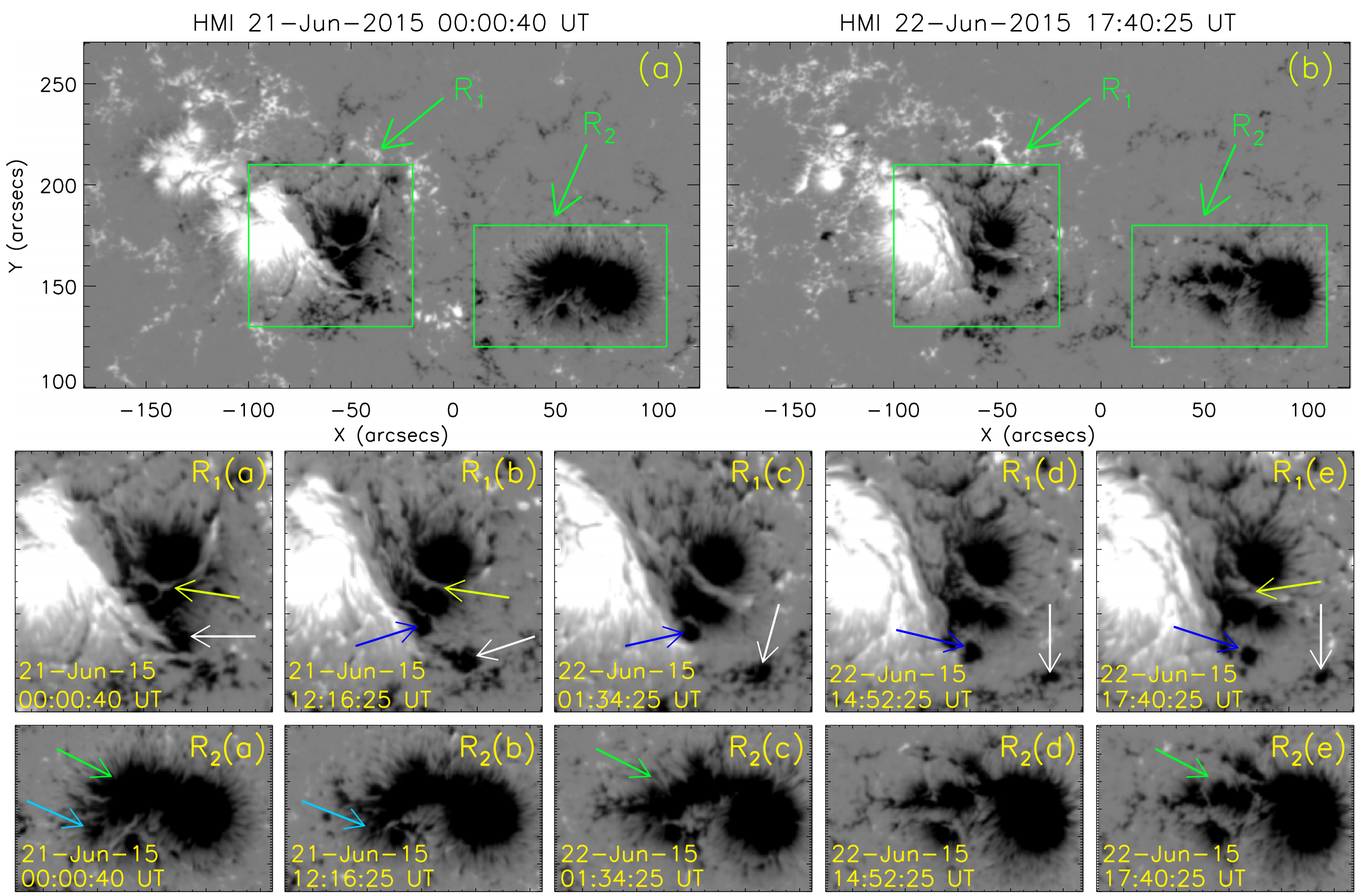

Figure 6. Panels (a)–(b): HMI LOS magnetograms of the active region NOAA 12371 at 00:00 UT on 2015 June 21 (i.e., one day before the studied event) and 17:40 UT on 2015 June 22 (i.e., in the beginning of the M6.6 flare) are plotted to show the changes in the photospheric magnetic structures. We mark two subregions R_1 and R_2 in magnetograms that exhibited significant changes. In panels R_1(a)–R_1(e), we show a few representative snapshots of the subregion R_1 to highlight important changes. Yellow arrows indicate a light bridge dividing the negative polarity region of the trailing sunspot group, which apparently underwent rotation in the clockwise direction and eventually became thicker. White arrows indicate motion of a small negative region toward the southwest. Blue arrows indicate southward motion of another negative polarity region. In panels R_2(a)–R_2(e), we show the evolution of the subregion R_2. The sky blue arrow in panel R_2(a) shows a small negative polarity region, which merged into the bigger negative polarity region (see panels R_2(a) and R_2(b)). Green arrows in panels R_2(a), R_2(c), and R_2(e) indicate a region where the magnetic flux rapidly evolved and eventually resulted in significant cancellation of negative flux. An unannotated animation of the HMI LOS magnetograms is available. The animated magnetograms run from 00:00 UT on June 21 to 18:10 UT on June 22.

(An animation of this figure is available.)

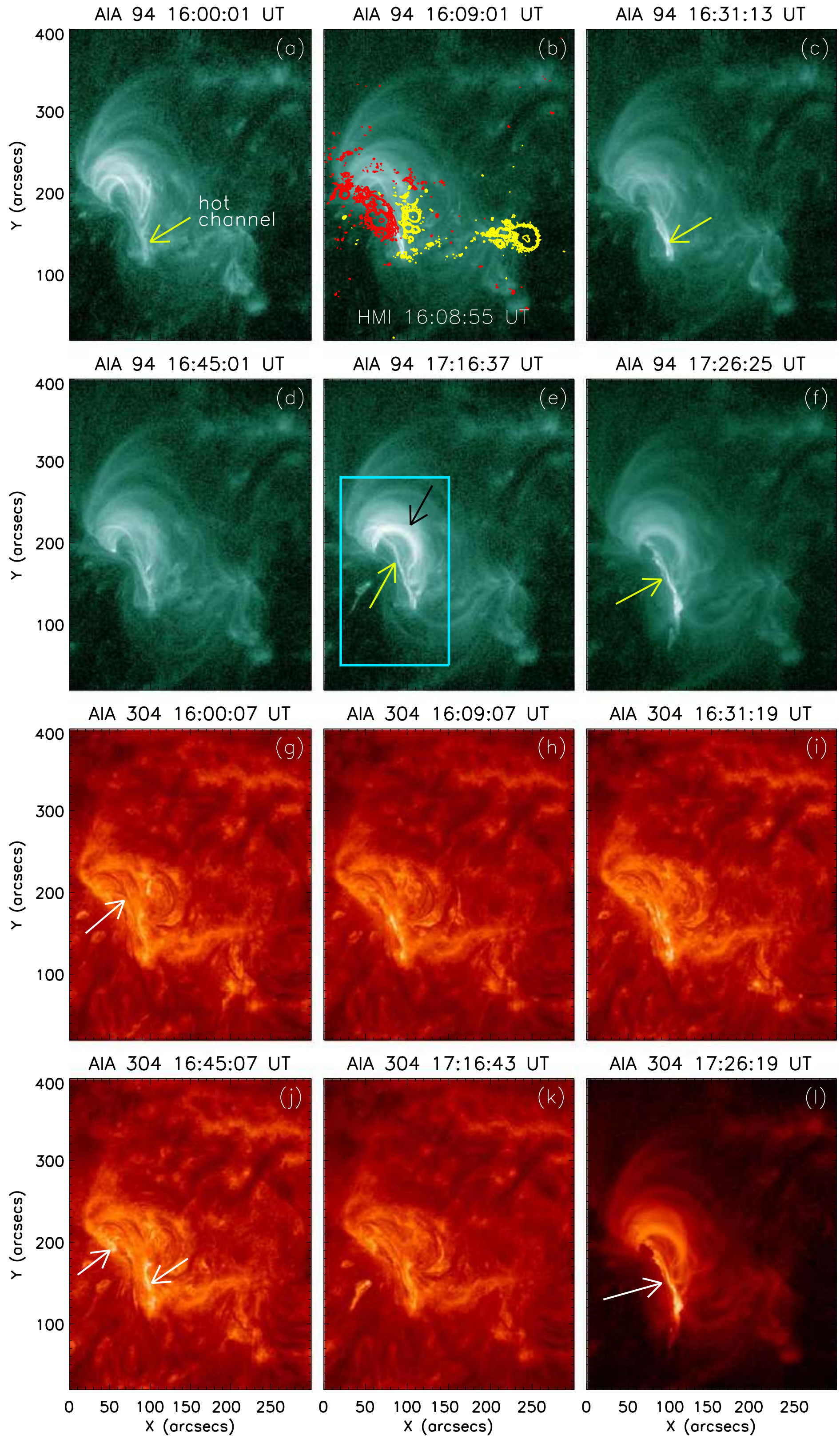

Figure 7. Pre-flare phase of the M6.6 flare shown in the AIA 94 and 304 Å image sequences. Panels (a)–(f): Sequence of AIA 94 Å images showing activation and pre-eruption stages of the hot channel (marked by yellow arrows in panels (a), (c), (e), and (f)) and overlying coronal loops (marked by the black arrow in panel (e)). Panel (b) shows the overplotted cotemporal HMI LOS magnetogram. The positive and negative polarities are shown by red and yellow contours, respectively, with contour levels set as ±[500, 800, 1000, 2000] G. The box in panel (e) indicates the field of view of the images plotted in Figure 8. Panels (g)–(l): simultaneous imaging in the AIA 304 Å channel. A filament structure is shown by the white arrow in panel (g). White arrows in panel (j) show the appearance of two brightenings on the two sides of the filament channel. The white arrow in panel (l) shows enhanced brightening from the filament channel.

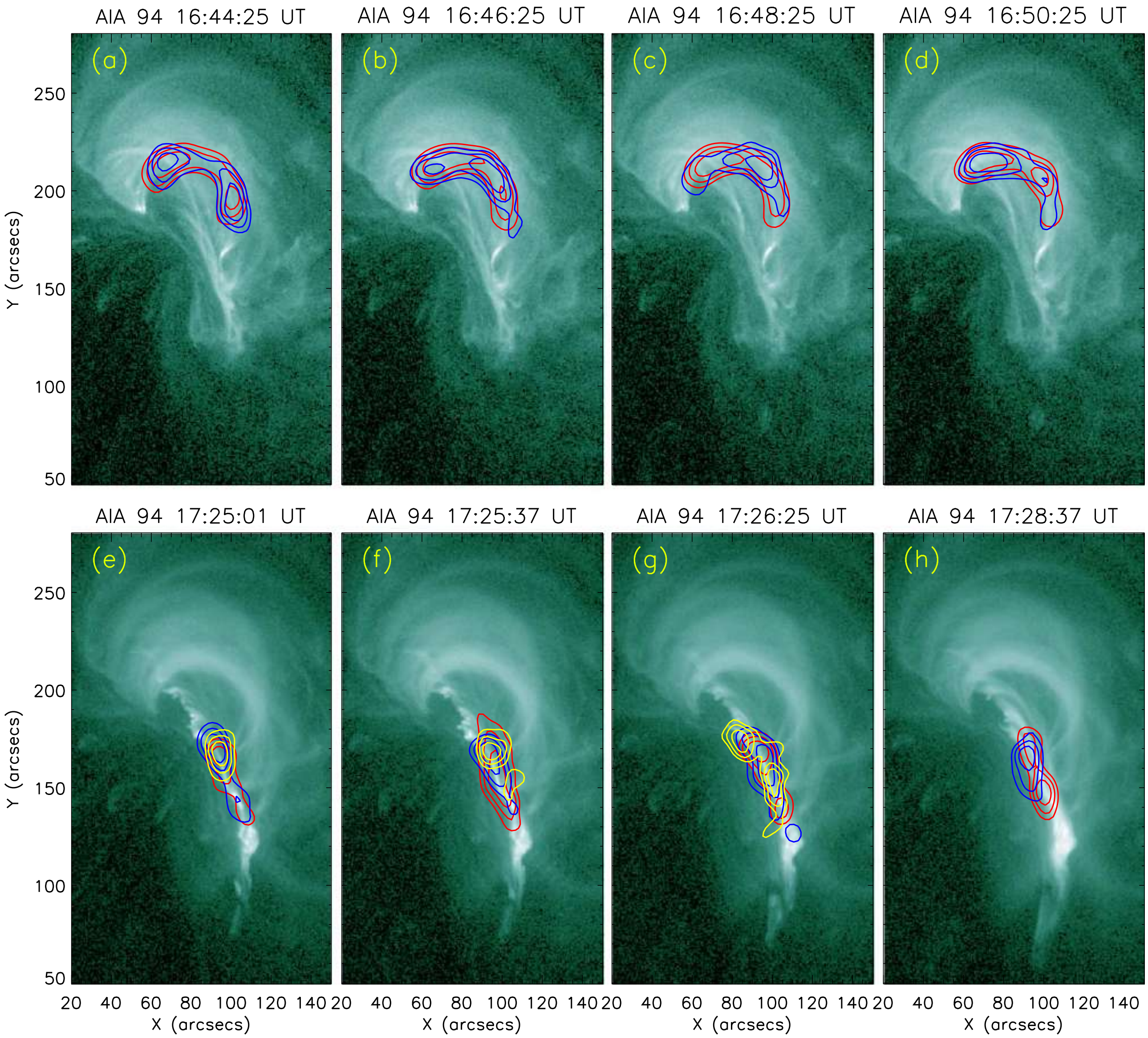

Figure 8. Sequence of RHESSI X-ray images in 5–10 keV (red contours), 10–15 keV (blue contours), and 15–25 keV (yellow contours) overplotted on cotemporal AIA 94 Å images. Panels (a)–(d): sequence of images for first stage (peaked at P1) of the pre-flare phase, where the X-ray sources are observed to be emitted from the overlying coronal loops. Panels (e)–(h): sequence of images for second stage (peaked at P2) of the pre-flare phase. In this period X-ray emissions are observed from the low-lying hot EUV channel below the coronal loops. The X-ray images are reconstructed by the CLEAN algorithm with integration time of 40 s. The contours drawn are at 70%, 80%, and 90% of the peak flux in each image.

the X-ray emitting sources in the 15–25 keV energy band show the appearance of multiple centroids (Figure 8(g)), which disappear afterwards (Figure 8(h)).

In Figure 9, we present spatially integrated, background subtracted RHESSI spectra along with their respective fits and residuals for a few selected intervals. Panels (a)–(c) of Figure 9 correspond to the spectra of pre-flare phase intervals. The RHESSI X-ray spectra during the first pre-flare phase (peaked at P1, see Figure 2(a)) show thermal emission only (Figures 9(a)–(b)). To estimate the characteristics of hot flaring plasma, namely temperature (T) and EM, the best spectral fit results are obtained with fitting in the energy range of 9–13 keV for this interval. At this stage, the plasma temperature is $\approx$19 MK and EM is $\approx 3 \times 10^{46}$ cm^{-3}. In the second pre-flare phase, which peaks at P2 (Figure 2(a)), we find rise in temperature ($\approx$24 MK) as well as EM ($\approx 7 \times 10^{46}$ cm^{-3}; Figure 9(c)), which suggests an increase of thermal emission along with volume of heated plasma. Notably, during this second phase of the pre-flare activity, the X-ray emission rises to $\approx$35 keV above the background level. Contrary to the first pre-flare phase, the second pre-flare phase shows distinct yet moderate nonthermal emission above 19 keV with a steep electron spectral index (δ) of $\approx$8.2. The spectral fit results obtained during the rise and main phase of the flare are presented in Figures 9(d)–(f), which are discussed at the end of Section 3.4.

3.4. Hot Channel Eruption and Further Consequences

The main phase of the M6.6 flare is illustrated by a few representative AIA 94 Å images in Figure 10. The activated hot channel (indicated by the yellow arrow in Figure 10(a)) starts to erupt upward, distending the overlying coronal loop system (indicated by the white arrow in Figure 10(a)). At this early stage, the X-ray emission originated at energies $\lesssim$25 keV

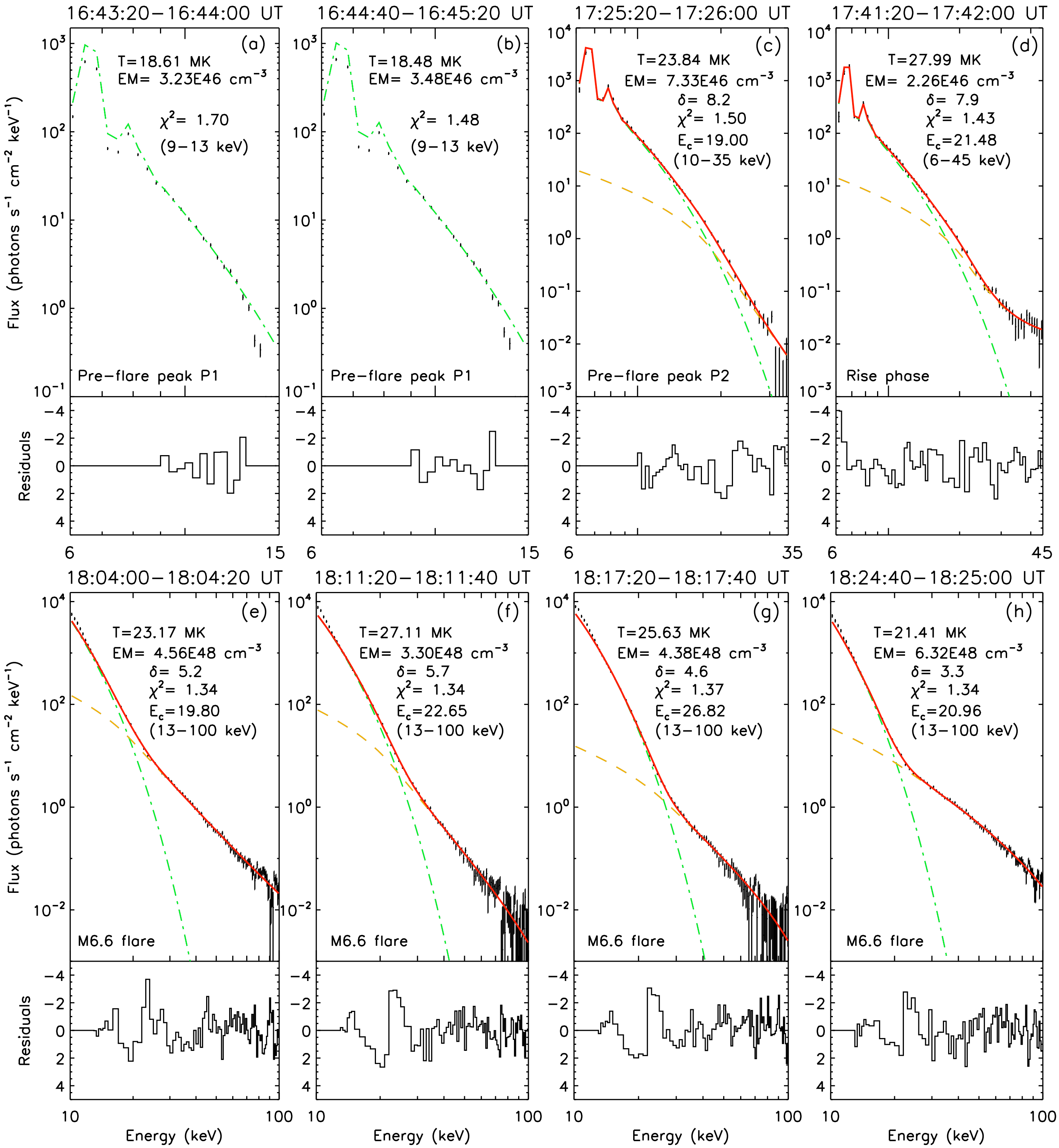

Figure 9. X-ray spectral fit of RHESSI data during various phases of the M6.6 flare. Panels (a) and (b) show spectral fit during the peak P1 (≈16:45 UT) and panel (c) shows spectral fit during the peak P2 (≈17:26 UT). We note that thermal emission is dominant during peak P1, whereas during peak P2, we observe the appearance of a nonthermal component in the spectral fit. Both temperature and EM rises during the peak P2 compared to P1. Temporal evolution of spectral fit parameters in the main phase of the M6.6 flare is shown in panels (e)–(h).

and the sources lie in a relatively compact region (Figure 10(a)). With the further upward expansion of the hot channel, we observe emission from conjugate HXR sources of 25–50 keV energies (green contours), which appears to be located near the anchored footpoints of the hot channel (Figure 10(b)). Importantly, the continuous rise of the GOES flux is superimposed with a distinct peak at ≈17:44 UT, which clearly appears in all the high energy RHESSI X-ray light curves up to 50 keV energies (Figure 3). The hot channel rises gradually with clear and intact structure visual in direct AIA 94 Å images. In Figures 10(c) and (d), we mark the leading front of the hot channel by white arrows. The GOES light

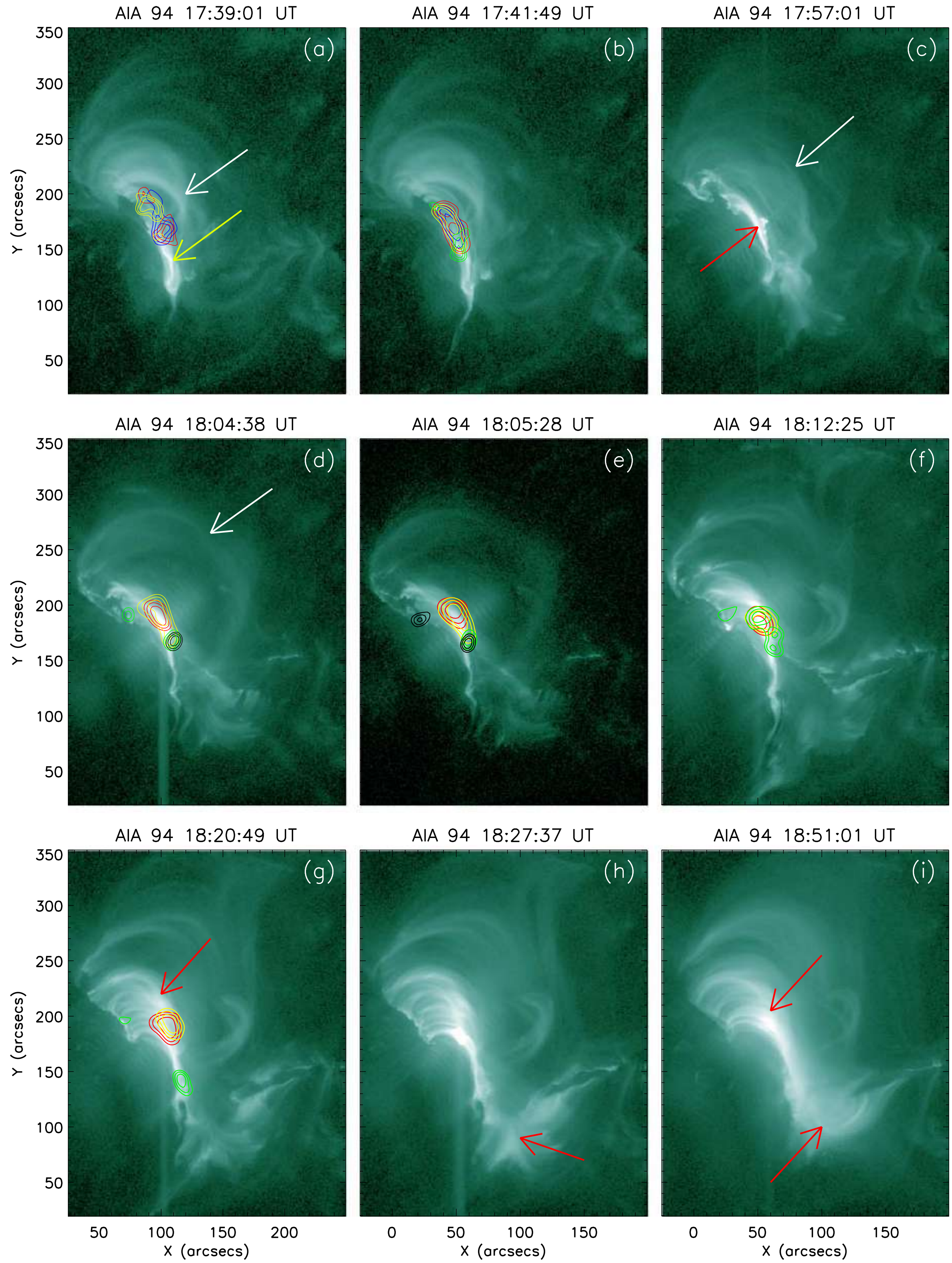

Figure 10. Sequence of AIA 94 Å images showing evolutionary phases of the eruption of the hot channel and associated M6.6 flare. Panel (a) shows the hot EUV channel (marked by the yellow arrow) and overlying coronal loops (marked by the white arrow). The erupting front of the hot channel is shown by white arrows in panels (c) and (d). The red arrow in panel (c) shows the start of formation of post-flare loops. RHESSI images in 5–10 keV (red contours), 10–15 keV (blue contours), 15–25 keV (yellow contours), 25–50 keV (green contours), and 50–100 keV (black contours) are reconstructed by the CLEAN algorithm with integration time of 32 s. The contour levels are set as 70%, 80%, and 90% of the peak flux in each image. Panels (g)–(i) show formation of post-flare loop arcades. The red arrow in panel (g) shows the post-flare loops in the northern part of the flaring region, which ultimately converts into dense post-flare loop arcades. The red arrow in panel (h) shows the start of formation of post-flare loops in the southern part of the flaring region. In panel (i), dense post-flare loop arcades in both northern and southern part of the flaring region are indicated by red arrows.

curves further suggest that the flare exhibits an extended maximum phase with dual peak structures at ≈18:00 UT and ≈18:13 UT. The comparison of AIA 94 Å with cotemporal multichannel RHESSI images clearly reveals two distinct regions of X-ray emission: the high energy HXR sources between 25 and 100 keV appear in a pair as conjugate sources while the low energy emission below $\lesssim$25 keV comes from the hotter region occupied with newly formed EUV coronal loops, in the wake of a hot channel eruption (Figures 10(d)–(g)). We also find an increase in separation of the HXR footpoint sources as the flare progresses. We note that the strength of HXR emission to be higher at the southern footpoint of post-flare loop arcades where the HXR emission up to 50 keV was observed (Figure 10(g)), which suggests an asymmetry in the deposition of energy at conjugate footpoint locations. Soon after the second peak, the flaring region starts to show the formation of dense, bright, gradually rising post-flare loop arcades in the northern part (shown by the red arrow in Figure 10(g)). Gradually the southern part of the flaring region also exhibits the build-up of post-flare loop arcades (indicated by the red arrow in Figure 10(h)). In Figure 10(i), we show well developed, dense post-flare loop arcades in both northern and southern parts of the flaring region by red arrows.

The comparison of evolution of HXR sources with respect to the AIA 304 Å images are shown in Figure 11. After the activation of the filament, the brightening started to appear in the form of flare ribbons (shown by green arrows in Figure 11(b)), which gradually move apart while exhibiting spatial expansion as well (see Figures 11(a)–(f)). Also, as expected, the high energy HXR sources of strength ≈25–100 keV show spatial consistency with the flare ribbons. The region marked by the white arrow in Figure 11(e) undergoes a gradual increase in the brightness (see Figures 11(e)–(i)). In the later stages, we observe distinct yet diffuse emission from post-flare coronal arcades, which is shown by black arrows in Figures 11(g)–(i).

As a comparison of phenomena occurring simultaneously in different heights of solar atmosphere, we have shown the flaring region in EUV (AIA 131 Å) and UV (AIA 1600 Å) channels during the first peak of the flare (Figure 12). The AIA 131 Å image clearly shows the erupting hot channel (i.e., MFR) structure (shown by the white arrow in Figure 12(a)). We observe simultaneous conjugate and sheared flare ribbon brightenings at the photospheric level in AIA 1600 Å image (marked by red arrows in Figure 12(b)).

To understand the activation and eruption of the hot channel, we plot a few AIA 94 Å running difference images (Figure 13). In various panels, we mark the expanding hot channel by yellow arrows. As discussed earlier, the eruption resulted into a fast halo CME (Figure 5). In Figure 13(g), we plot a time-slice diagram showing evolutionary phases of the hot channel. For the purpose, we have specified a narrow slit $\overline{B_1B_2}$, which is indicated in Figure 13(a). The time-slice diagram is constructed using the running difference images with a time gap of ≈4 minutes between the successive images. The plot reveals a slow rise (speed ≈14 km s^{-1}) phase of the hot channel between ≈17:37 UT and ≈17:49 UT (shown by the red dashed line), which is followed by another phase of its fast eruption. A second-order polynomial fit to the height-time measurement taken between ≈17:49 UT and ≈18:00 UT (shown by the yellow dashed line) yields the speed of the erupting hot channel as ≈37 km s^{-1} with an acceleration of ≈110 m s^{-2}. The speed of the erupting hot channel reaches ≈109 km s^{-1} at ≈18:00 UT. Notably, we observe formation of post-flare loops from ≈17:57 UT at a projected height of ≈4 Mm.

In Figures 9(d)–(h), we show RHESSI spectral fit results during the rise and main phase of the M6.6 flare. We find a steady rise in temperature as well as spectral hardening during the rise phase (Figure 9(d)). In the main phase of the event (Figures 9(e)–(h)) the spectra continued to become harder with $\delta \approx 3.3$ at ≈18:24 UT. The maximum plasma temperature (T ≈27 MK) was observed around the second peak of the M6.6 flare (see Figure 9(f)).

3.5. Nonlinear-force-free-field (NLFFF) Modeling of Active Region Corona

The coronal magnetic field lines (Figures 14(a)–(c)) are extrapolated using the NLFFF model of Wiegelmann (2008) to model the flux rope and associated coronal field lines. The lower boundary of the extrapolation is taken as a photospheric LOS magnetogram. The MFR, LLCLs, and HCLs are shown by arrows in Figure 14(b). Clear MFR is observed to form in between two opposite polarities of the trailing sunspot group (Figure 14(c)).

In Figures 14(d)–(e), AIA 171 and AIA 94 Å images of the pre-flare stage (at ≈17:25 UT) distinctly show the hot channel (i.e., MFR), LLCLs, and HCLs. In Figure 14(d), we present the 171 Å image overplotted with the photospheric LOS magnetogram with contour levels as ±[400, 800, 1000, 2000] G. The blue and red contours denote negative and positive polarities, respectively. The rectangular box in Figure 14(d) shows a region of hot core, which contains the LLCLs and MFR. The enlarged view of rectangular box is shown in Figure 14(e) overplotted with RHESSI contours in 5–10, 10–15, and 15–25 keV. The contours denote 70%, 80%, and 90% of peak flux in each image. Interestingly the X-ray contours are observed to be found along the length of the MFR.

4. Conclusions and Discussions

In this paper, we provide a comprehensive multiwavelength and multi-instrument study of a remarkable M-class major eruptive flare, which occurred in AR NOAA 12371 on 2015 June 22. The importance of the study lies in investigating the activities right from the early pre-flare phase until the decay of the flare with an aim of exploring the pre-flare processes in detail and the link between the pre-flare and main flare. The main observational results of the study are itemized below:

1. The eruption initiated from a magnetically bipolar region where a hot EUV channel (evidence of MFR) pre-existed (at least ≈5.5 hr before the eruptive M6.6 flare) that exhibited early signatures of activation during the pre-flare activities. The Hα observations reveal the presence of a filament in association with the coronal hot channel. Observations of the pre-flare phase clearly reveal activation of the filament with early eruption signatures, providing further credence of our interpretation of pre-flare activities.
2. The hot channel is found to be cospatial with an MFR detected in NLFFF model extrapolation. A very remarkable finding of the study lies in the detection of elongated as well as localized HXR sources of energies up to 25 keV that lie exactly over the extended central part of

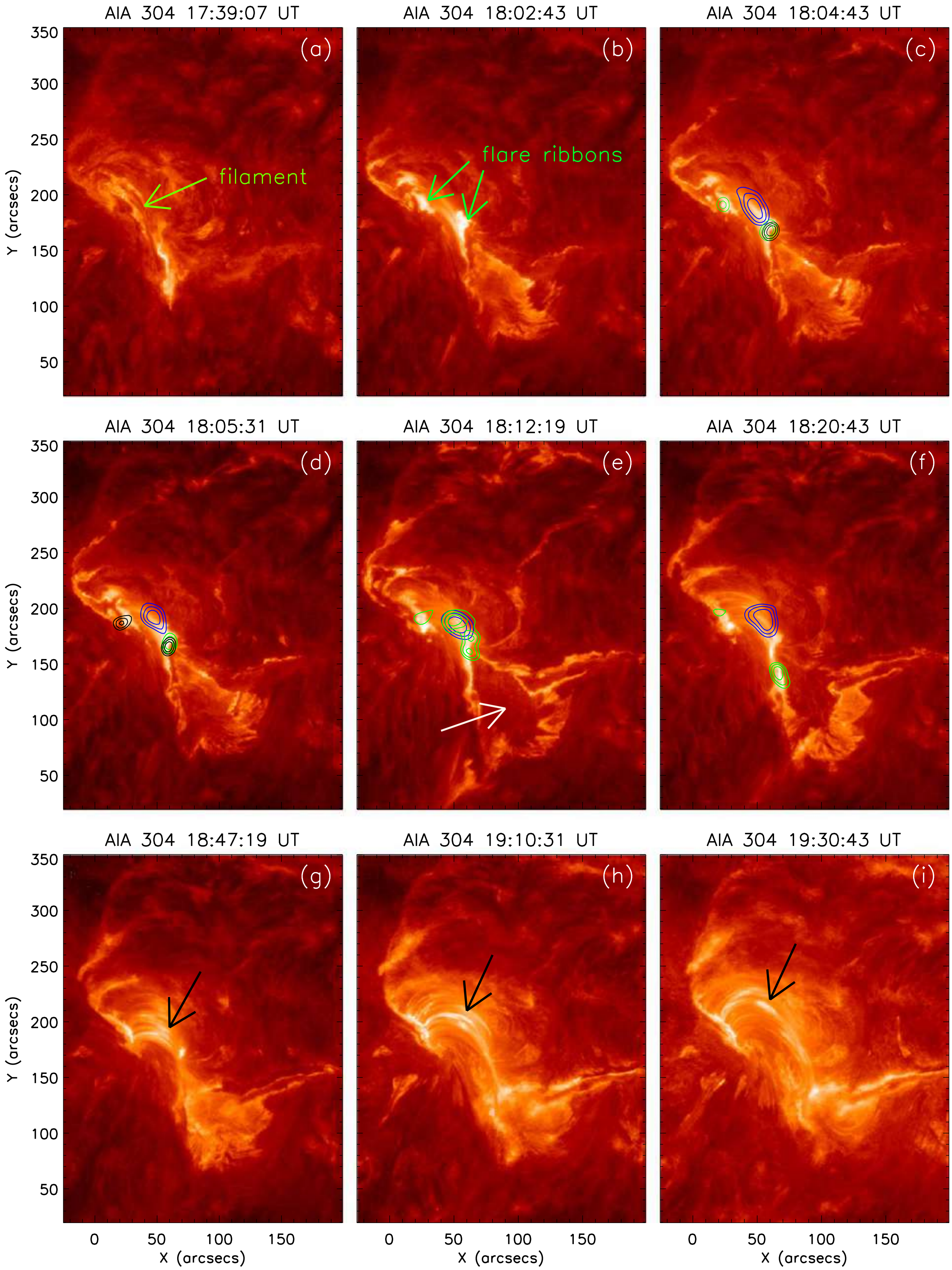

Figure 11. Sequence of AIA 304 Å images showing eruption of the flux rope (i.e., filament) and formation of post-flare loop arcades. The filament is shown by the green arrow in panel (a). Subsequently we observe parallel flare ribbons at the footpoints of the erupting filament at ≈18:02 UT (marked by green arrows in panel (b)). RHESSI images in 10–15 keV (blue contours), 25–50 keV (green contours), and 50–100 keV (black contours) are reconstructed by the CLEAN algorithm with integration time of 32 s. The contours denote 70%, 80%, and 90% of peak flux in each image. The white arrow in panel (e) marks a region that is gradually filled by chromospheric brightening (see panels (e)–(i)). We observe diffuse emission from post-flare coronal loops (shown by black arrows in panels (g)–(i)).

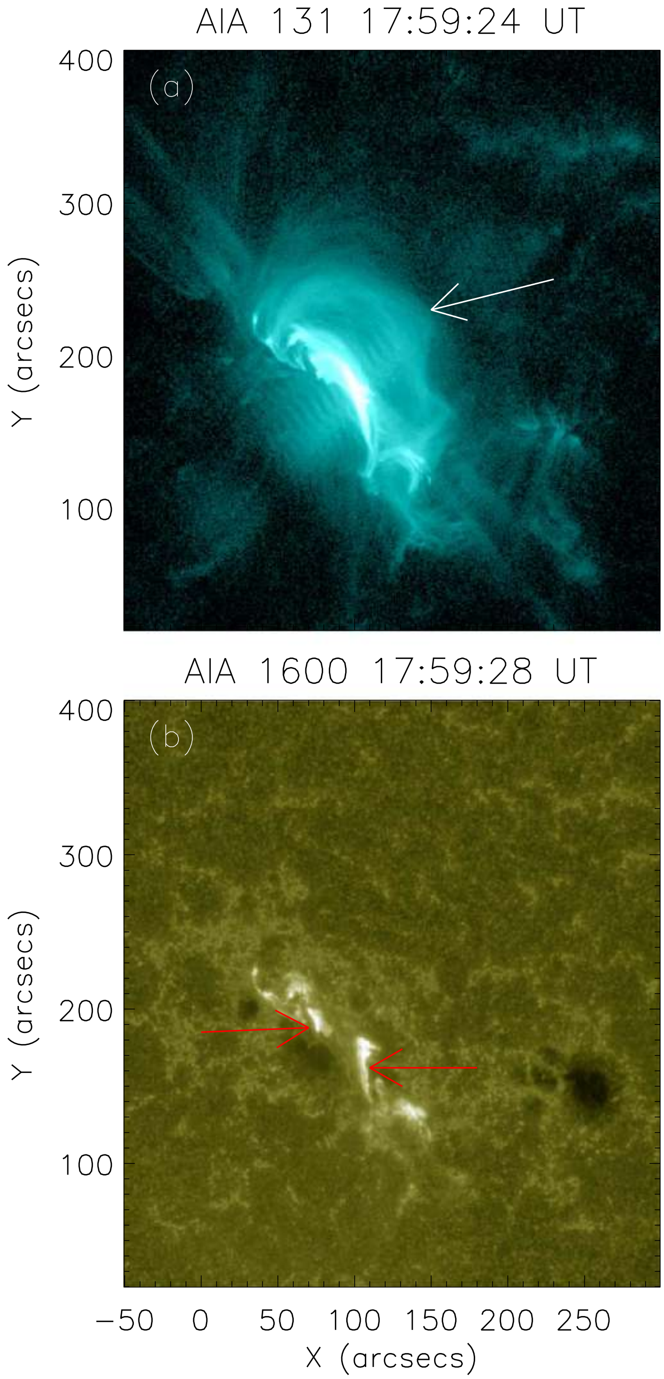

Figure 12. Structure of the solar corona and associated active region in EUV (AIA 131 Å) and UV (AIA 1600 Å) channels during the peak of the flare. In panel (a), we indicate the erupting hot flux rope structure in 131 Å image by the white arrow, while the cotemporal observation in AIA 1600 Å shows conjugate and sheared flare ribbon brightenings, which are shown by red arrows in panel (b).

the hot channel. To our knowledge, this is the first time an MFR has been detected in direct HXR observations.

3. An important yet realistic coincidence is the continued presence of X-ray sources during the whole pre-flare phase. In the early pre-flare phase, the X-ray emission came from the core region, which was comprised of a hot, dense bundle of LLCLs, just above the filament channel. On the other hand, during the late pre-flare phase, as explained in item 2 above, the X-ray emission extended up to higher energies and the sources are located in the region where the flux rope existed. These distinct pre-flare intensity enhancements, therefore, suggest build-up and activation of the MFR by magnetic reconnection involving interaction between the core field region and slowly evolving MFR.
4. The analysis of photospheric magnetograms during the extended period (≈42 hr) prior to the pre-flare phase of the eruptive flare categorically reveals clockwise rotation of mix polarity sunspot group along with remarkable moving magnetic features.
5. With the onset of the impulsive phase of M6.6 flare, we find a sudden transition of the MFR from the state of slow rise (≈14 km s^{-1}) to fast acceleration (≈110 m s^{-2} with the speed rises to ≈109 km s^{-1} within AIA field of view), which points toward a feedback relationship between source region CME dynamics and the strength of the large-scale magnetic reconnection powering the eruptive flare.
6. The classical signatures of large-scale magnetic reconnection are observed during the impulsive phase in terms of high energy (up to 100 keV) HXR conjugate sources that lie over the (E)UV flare ribbons. The Hα observations show the remaining structures of the filament thus confirming the event to be a partial filament eruption.

The analyses carried out reveal the appearance of EUV hot channels in the corresponding SDO/AIA observations, well before (≈5.5 hr) the eruptive flare. This finding is in agreement with the contemporary understanding that the presence of MFR is a prerequisite for a CME (Fan 2005; Li & Zhang 2013; Song et al. 2019). The correspondence between the spatial location of hot channel and MFR in coronal field modeling has been reported in several studies (Liu et al. 2018b; Mitra et al. 2018), which is further confirmed by our analysis. However, the build-up mechanism of the MFR is still an open question, which requires extensive observational and theoretical research. The present study is a step in this direction and suggests that the pre-flare activities play an important role in the process of MFR activation. The pre-flare activity could be related to evolution in the photospheric magnetic structure. However, photospheric magnetic field changes in the active regions occur gradually but eventually lead to the development of complex magnetic field configuration in the corona, which can also be seen in the present case. Our observation of rotation of sunspot group (in the clockwise direction) over several hours, which encloses the PIL and, in the later phases, overlying developing MFR is probably related to the transfer of twist from sub-photospheric level to the coronal field lines. This long-lasting process would store excess magnetic energy in the coronal flux rope. The brightening of the core field containing the MFR about 1.25 hr prior to the eruptive flare thus suggests the onset of heating, probably due to the magnetic reconnection, as the flux rope interacts with immediate low-lying arcades. Subsequently, the hot channel undergoes significant intensity enhancement and starts to appear in X-ray images up to 25 keV energies. Coronal pre-flare activity starts with the initiation of intense emission from the MFR and surrounding regions (an observational fact that has traditionally been observed in SXR as enhanced emission; see, e.g., Veronig et al. 2002; Chifor et al. 2007; Joshi et al. 2011, 2013; Hernandez-Perez et al. 2019).

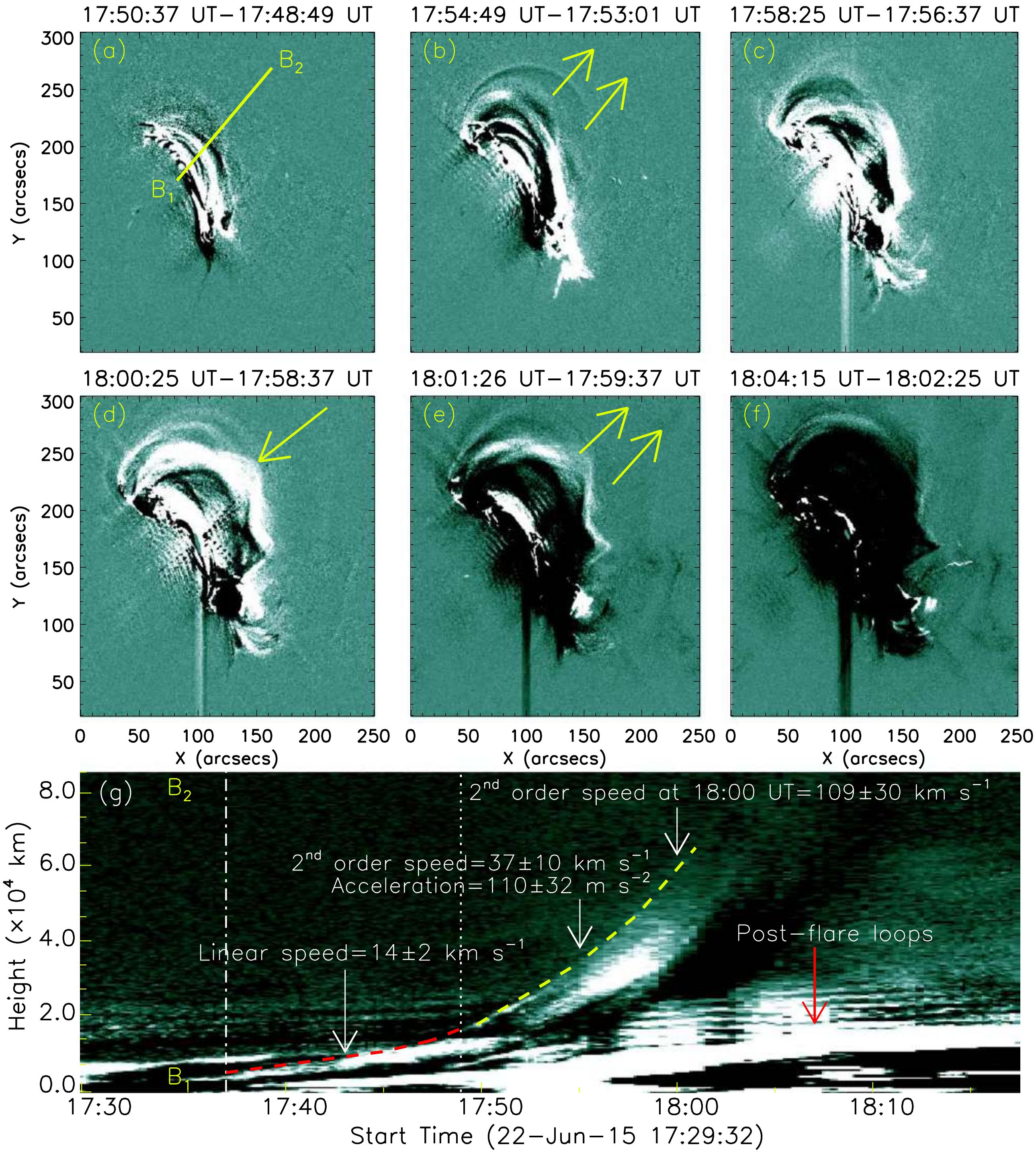

Figure 13. Sequence of AIA 94 Å running difference images showing the directions of eruption of the hot channel (shown by the yellow arrows in panels (b) and (e)). The arrow in panel (d) shows the erupting front. We plot a time-slice diagram of the erupting hot channel in panel (g). The direction, from B_1 to B_2, through which the time-slice plot is drawn, is shown as a yellow slit in panel (a).

We would like to highlight that, in our case, the regions of pre-flare activity and main M6.6 flare are cospatial. The statistical studies carried out with SXR images from Yohkoh, revealed three categories of pre-flare activities in terms of source locations: cospatial, adjacent, and remote (Fárník & Savy 1998; Kim et al. 2008). The cospatial and adjacent cases occurring within a few minutes before the main flare are supposed to have direct relevance for the triggering processes related to the main flare (Liu et al. 2009; Joshi et al. 2011; Mitra & Joshi 2019). Notably, EUV and X-ray images clearly show that the pre-flare brightenings are spatially distributed along the hot channel (i.e., MFR) and within the core field region. Furthermore, before the pre-flare emission, the region shows photospheric magnetic field changes along the PIL. These observations present consistency with the tether-cutting model of solar eruption (Moore & Roumeliotis 1992; Moore et al. 2001), where the build-up of MFR is a consequence of flux changes along the PIL and, therefore, early reconnection

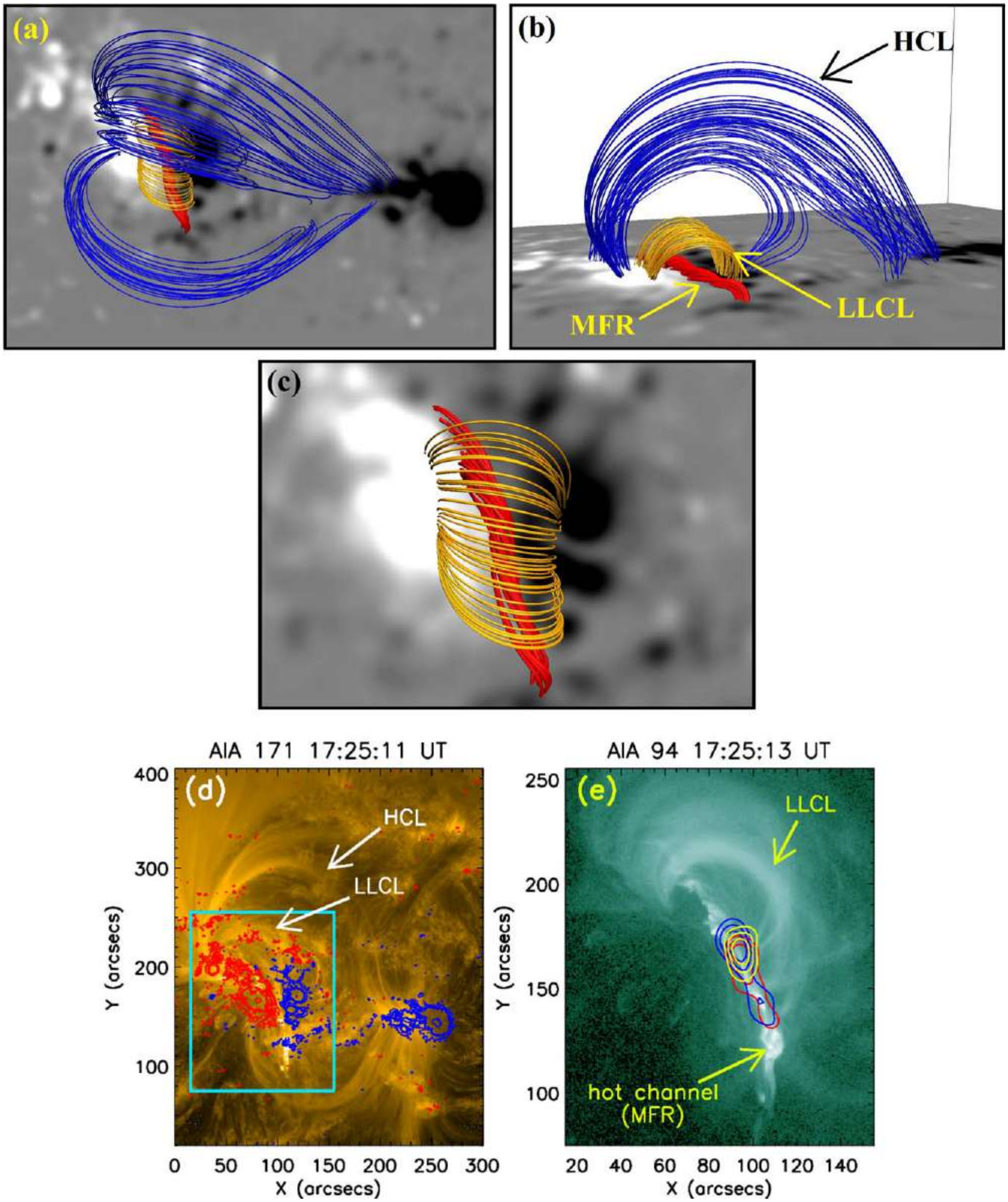

Figure 14. Coronal magnetic field lines obtained using NLFFF model of extrapolation are shown in panels (a), (b), and (c). The lower boundary of the extrapolation is the photospheric LOS magnetic field. Panels (a) and (b) show the top and side views of the extrapolated field lines, respectively. The MFR, LLCLs, and HCLs are clearly indicated in panel (b). The position of the MFR along the PIL of the active region and the LLCLs are shown in panel (c). AIA 171 Å image of the active region is shown in panel (d) in the pre-flare phase (at ≈17:25 UT), overplotted with the HMI LOS magnetogram. The positive and negative polarities of the magnetogram are shown by red and blue contours, respectively, with contour levels set as ±[400, 800, 1000, 2000] G. High and low coronal loops (HCL and LLCL, respectively) are shown by white arrows in panel (d). The rectangular box indicates a hot core region, whose enlarged view is shown in AIA 94 Å channel in panel (e) overplotted with RHESSI contours in 5–10 keV (red), 10–15 keV (blue), and 15–25 keV (yellow). The X-ray contours are reconstructed by the CLEAN algorithm with an integration time of 40 s. The contours denote 70%, 80%, and 90% of peak flux in each image. LLCLs are also clearly visible above the hot channel/MFR, which is cospatial with X-ray sources.

signatures (causing the pre-flare activity) are expected to occur close to PIL and nearby core regions (Yurchyshyn et al. 2006; Chen et al. 2014; Dhara et al. 2017).

We find direct evidence of pre-flare tether-cutting reconnection in HXR imaging observations at lower energies (up to 25 keV). The HXR emission signifies intense heating of the core region. With the progress of pre-flare activity, the strength of HXR emission increases and a subtle yet clear nonthermal component starts to appear, which we identify as second pre-flare enhancement. The comparison of imaging and spectroscopic observations suggests that both thermal and nonthermal components originated from the EUV hot channel in the late pre-flare phase. Importantly, the HXR source at lower energies presents an elongated morphology and the X-ray sources lie exactly over the EUV hot channel. These observations provide direct support of tether-cutting reconnection. To our knowledge, the observation of extended HXR sources from a developing MFR during the pre-flare phase is a new observational finding. As expected, during this phase the hot channel rises slowly, an important feature of a CME precursor (Sterling & Moore 2005; Nagashima et al. 2007; Sterling et al. 2007; Song et al. 2015). In Hα observations, the partial filament eruption begins at this time, further supporting the physical link between the pre-flare activity and initiation of solar eruption. Importantly, the slowly rising MFR transitioned to a phase of eruptive expansion with the onset of the impulsive phase of the M6.6 flare. Now, the appearance of "classical" flare signatures, viz., distinct coronal and footpoint HXR sources along with inner flare ribbons formed at both sides of PIL, provide evidence of large-scale magnetic reconnection, which are attributed to the reconnection-opening of overlying field lines (i.e., progression of reconnection in higher coronal fields of the envelope region) stretched by the erupting MFR. The sudden transition in the kinematic evolution of MFR from the phase of slow to fast rise precisely divides the pre-flare and impulsive phase of the flare, which we attribute to the feedback relationship between the early CME dynamics and the strength of the large-scale magnetic reconnection (Temmer et al. 2008; Vršnak 2016; Song et al. 2018; Mitra & Joshi 2019).

The authors would like to thank the SDO, RHESSI, and SOHO teams for their open data policy. SDO is NASA's mission under the Living With a Star (LWS) program. RHESSI was NASA's mission under the SMall EXplorer (SMEX) program. SOHO is a joint project of international cooperation between the ESA and NASA. This work is supported by the Indo-Austrian joint research project No. INT/AUSTRIA/BMWF/ P-05/2017 and OeAD project No. IN 03/2017. A. M.V. acknowledges the Austrian Science Find (FWF): P27292-N20. BBSO operation is supported by NJIT and US NSF AGS-1821294 grants. V.Y. acknowledges support from NSF AST-1614457, AFOSR FA9550-19-1-0040 and NASA 80NSSC17K0016, 80NSSC19K0257, and 80NSSC20K0025 grants. The authors sincerely thank the anonymous referee for providing useful suggestions and constructive comments, which enhanced the presentation and overall quality of the article.

ORCID iDs

Suraj Sahu https://orcid.org/0000-0001-8377-8640
Bhuwan joshi https://orcid.org/0000-0001-5042-2170
Prabir K. Mitra https://orcid.org/0000-0002-0341-7886
Astrid M. Veronig https://orcid.org/0000-0003-2073-002X
V. Yurchyshyn https://orcid.org/0000-0001-9982-2175

References

Archontis, V., & Vlahos, L. 2019, RSPTA, 377, 20190152
Awasthi, A. K., Liu, R., Wang, H., Wang, Y., & Shen, C. 2018, ApJ, 857, 124
Benz, A. O. 2017, LRSP, 14, 2
Bisoi, S. K., Chakrabarty, D., Janardhan, P., et al. 2016, JGRA, 121, 3882
Brueckner, G. E., Howard, R. A., Koomen, M. J., et al. 1995, SoPh, 162, 357
Burlaga, L., Fitzenreiter, R., Lepping, R., et al. 1998, JGR, 103, 277
Burlaga, L., Sittler, E., Mariani, F., & Schwenn, R. 1981, JGR, 86, 6673
Burlaga, L. F., Skoug, R. M., Smith, C. W., et al. 2001, JGR, 106, 20957
Canou, A., & Amari, T. 2010, ApJ, 715, 1566
Carmichael, H. 1964, in Proc. AAS-NASA Symp., Vol. 50, The Physics of Solar Flares, ed. W. N. Hess (Washington, DC: NASA), 451
Chen, H., Zhang, J., Cheng, X., et al. 2014, ApJL, 797, L15
Cheng, X., Guo, Y., & Ding, M. 2017, ScChD, 60, 1383
Cheng, X., Zhang, J., Liu, Y., & Ding, M. D. 2011, ApJL, 732, L25
Chifor, C., Mason, H. E., Tripathi, D., Isobe, H., & Asai, A. 2006, A&A, 458, 965
Chifor, C., Tripathi, D., Mason, H. E., & Dennis, B. R. 2007, A&A, 472, 967
Clyne, J., Gruchalla, K., & Rast, M. 2010, in ASP Conf. Ser. 429, Numerical Modeling of Space Plasma Flows, Astronum-2009, ed. N. V. Pogorelov, E. Audit, & G. P. Zank (San Francisco, CA: ASP), 323
Denker, C., Johannesson, A., Marquette, W., et al. 1999, SoPh, 184, 87
Dhara, S. K., Belur, R., Kumar, P., et al. 2017, SoPh, 292, 145
Domingo, V., Fleck, B., & Poland, A. I. 1995, SSRv, 72, 81
Fan, Y. 2005, ApJ, 630, 543
Fárník, F., Hudson, H., & Watanabe, T. 1996, SoPh, 165, 169
Fárník, F., & Savy, S. K. 1998, SoPh, 183, 339
Filippov, B., Martsenyuk, O., Srivastava, A. K., & Uddin, W. 2015, JApA, 36, 157
Fletcher, L., Dennis, B. R., Hudson, H. S., et al. 2011, SSRv, 159, 19
Gibson, S. E., & Fan, Y. 2006, JGRA, 111, A12103
Gopalswamy, N., Lara, A., Kaiser, M. L., & Bougeret, J. L. 2001, JGR, 106, 25261
Green, L. M., Török, T., Vršnak, B., Manchester, W., & Veronig, A. 2018, SSRv, 214, 46
Hernandez-Perez, A., Su, Y., Veronig, A. M., et al. 2019, ApJ, 874, 122
Hirayama, T. 1974, SoPh, 34, 323
Holman, G. D., Aschwanden, M. J., Aurass, H., et al. 2011, SSRv, 159, 107
Holman, G. D., Sui, L., Schwartz, R. A., & Emslie, A. G. 2003, ApJL, 595, L97
Hurford, G. J., Schmahl, E. J., Schwartz, R. A., et al. 2002, SoPh, 210, 61
Jing, J., Liu, R., Cheung, M. C. M., et al. 2017, ApJL, 842, L18
Joshi, B., Ibrahim, M. S., Shanmugaraju, A., & Chakrabarty, D. 2018, SoPh, 293, 107
Joshi, B., Kushwaha, U., Cho, K. S., & Veronig, A. M. 2013, ApJ, 771, 1
Joshi, B., Kushwaha, U., Veronig, A. M., et al. 2017, ApJ, 834, 42
Joshi, B., Veronig, A., Manoharan, P. K., & Somov, B. V. 2012, ASSP, 33, 29
Joshi, B., Veronig, A. M., Lee, J., et al. 2011, ApJ, 743, 195
Kang, J., Inoue, S., Kusano, K., Park, S.-H., & Moon, Y.-J. 2019, ApJ, 887, 263
Kim, S., Moon, Y. J., Kim, Y. H., et al. 2008, ApJ, 683, 510
Klein, L. W., & Burlaga, L. F. 1982, JGR, 87, 613
Kopp, R. A., & Pneuman, G. W. 1976, SoPh, 50, 85
Koskinen, H. E. J., Baker, D. N., Balogh, A., et al. 2017, SSRv, 212, 1137
Kundu, M. R., Garaimov, V. I., White, S. M., & Krucker, S. 2004, ApJ, 600, 1052
Lemen, J. R., Title, A. M., Akin, D. J., et al. 2012, SoPh, 275, 17
Li, L. P., & Zhang, J. 2013, A&A, 552, L11
Lin, R. P., Dennis, B. R., Hurford, G. J., et al. 2002, SoPh, 210, 3
Liu, C., Cao, W., Chae, J., et al. 2018a, ApJ, 869, 21
Liu, T., Su, Y., Cheng, X., van Ballegooijen, A., & Ji, H. 2018b, ApJ, 868, 59
Liu, W., Wang, T.-J., Dennis, B. R., & Holman, G. D. 2009, ApJ, 698, 632
Mitra, P. K., & Joshi, B. 2019, ApJ, 884, 46
Mitra, P. K., Joshi, B., & Prasad, A. 2020, SoPh, 295, 29
Mitra, P. K., Joshi, B., Prasad, A., Veronig, A. M., & Bhattacharyya, R. 2018, ApJ, 869, 69
Moore, R. L., & Roumeliotis, G. 1992, in Eruptive Solar Flares, ed. Z. Svestka, B. V. Jackson, & M. E. Machado, Vol. 399 (New York: Springer), 69
Moore, R. L., Sterling, A. C., Hudson, H. S., & Lemen, J. R. 2001, ApJ, 552, 833
Möstl, C., Farrugia, C. J., Miklenic, C., et al. 2009, JGRA, 114, A04102

Nagashima, K., Isobe, H., Yokoyama, T., et al. 2007, ApJ, 668, 533
Patsourakos, S., Vourlidas, A., & Stenborg, G. 2013, ApJ, 764, 125
Pesnell, W. D., Thompson, B. J., & Chamberlin, P. C. 2012, SoPh, 275, 3
Priest, E. R., & Forbes, T. G. 2002, A&ARv, 10, 313
Schou, J., Scherrer, P. H., Bush, R. I., et al. 2012, SoPh, 275, 229
Smith, D. M., Lin, R. P., Turin, P., et al. 2002, SoPh, 210, 33
Song, H. Q., Chen, Y., Qiu, J., et al. 2018, ApJL, 857, L21
Song, H. Q., Chen, Y., Zhang, J., et al. 2015, ApJL, 804, L38
Song, H. Q., Zhang, J., Cheng, X., et al. 2019, ApJ, 883, 43
Sterling, A. C., Harra, L. K., & Moore, R. L. 2007, ApJ, 669, 1359
Sterling, A. C., & Moore, R. L. 2005, ApJ, 630, 1148
Sturrock, P. A. 1966, Natur, 211, 695
Sui, L., Holman, G. D., & Dennis, B. R. 2004, ApJ, 612, 546
Sun, X. 2013, arXiv:1309.2392
Syed Ibrahim, M., Joshi, B., Cho, K. S., Kim, R. S., & Moon, Y. J. 2019, SoPh, 294, 54
Temmer, M., Veronig, A. M., Vršnak, B., et al. 2008, ApJL, 673, L95
Veronig, A., Vršnak, B., Temmer, M., & Hanslmeier, A. 2002, SoPh, 208, 297
Veronig, A. M., & Brown, J. C. 2004, ApJL, 603, L117
Veronig, A. M., Podladchikova, T., Dissauer, K., et al. 2018, ApJ, 868, 107
Vršnak, B. 2016, AN, 337, 1002
Wang, J., Liu, C., Deng, N., & Wang, H. 2018, ApJ, 853, 143
Webb, D. F., & Howard, T. A. 2012, LRSP, 9, 3
Wiegelmann, T. 2008, JGRA, 113, A03S02
Yashiro, S., Gopalswamy, N., Michalek, G., et al. 2004, JGRA, 109, A07105
Yurchyshyn, V., Karlický, M., Hu, Q., & Wang, H. 2006, SoPh, 235, 147
Zhang, G., & Burlaga, L. F. 1988, JGR, 93, 2511
Zurbuchen, T. H., & Richardson, I. G. 2006, SSRv, 123, 31

The Astrophysical Journal, 930:41 (16pp), 2022 May 1 https://doi.org/10.3847/1538-4357/ac5cc1

Homologous Compact Major Blowout-eruption Solar Flares and their Production of Broad CMEs

Suraj Sahu[1,2], Bhuwan Joshi[1], Alphonse C. Sterling[3], Prabir K. Mitra[1], and Ronald L. Moore[3,4]
[1] Udaipur Solar Observatory, Physical Research Laboratory, Dewali, Badi Road, Udaipur-313001, Rajasthan, India; suraj@prl.res.in
[2] Discipline of Physics, Indian Institute of Technology Gandhinagar, Palaj, Gandhinagar-382355, Gujarat, India
[3] NASA/Marshall Space Flight Center, Huntsville, AL 35812, USA
[4] Center for Space Plasma and Aeronomic Research, University of Alabama in Huntsville, Huntsville, AL 35805, USA
Received 2021 October 6; revised 2022 February 23; accepted 2022 March 7; published 2022 May 3

Abstract

We analyze the formation mechanism of three homologous broad coronal mass ejections (CMEs) resulting from a series of solar blowout-eruption flares with successively increasing intensities (M2.0, M2.6, and X1.0). The flares originated from NOAA Active Region 12017 during 2014 March 28–29 within an interval of ≈24 hr. Coronal magnetic field modeling based on nonlinear force-free field extrapolation helps to identify low-lying closed bipolar loops within the flaring region enclosing magnetic flux ropes. We obtain a double flux rope system under closed bipolar fields for all the events. The sequential eruption of the flux ropes led to homologous flares, each followed by a CME. Each of the three CMEs formed from the eruptions gradually attained a large angular width, after expanding from the compact eruption-source site. We find these eruptions and CMEs to be consistent with the "magnetic-arch-blowout" scenario: each compact-flare blowout eruption was seated in one foot of a far-reaching magnetic arch, exploded up the encasing leg of the arch, and blew out the arch to make a broad CME.

Unified Astronomy Thesaurus concepts: Solar flares (1496); Solar coronal mass ejections (310)

Supporting material: animations

1. Introduction

Solar flares are identified as transient, energetic phenomena occurring in the localized region of the Sun and are responsible for the release of a huge amount of magnetic energy into interplanetary space. Decades of studies about these phenomena have revealed that solar flares, filament/prominence eruptions, and coronal mass ejections (CMEs) are different observational manifestations of a single physical process occurring in the solar atmosphere, and that their origin is controlled by local coronal magnetic field topology (Vršnak 2003; Longcope 2005; Benz 2008; Shibata & Magara 2011; Green et al. 2018). These various forms of plasma ejections from the Sun play an important role in determining the state of space weather.

Traditionally, solar flares were identified by the manifestation of parallel brightenings (i.e., flare ribbons) on the two sides of a magnetic polarity inversion line (PIL) in an active region (AR) of the Sun. Historically, the flare ribbons have been extensively observed in traditional Hα observations of the Sun. In the case of an eruptive flare, typically a rising filament-carrying flux rope stretches the overlying field lines creating a current sheet underneath. Magnetic reconnection sets in at this current sheet and the field lines successively reconnect to form apparently expanding postflare loops and separating Hα ribbons at their footpoints, as the reconnection site achieves successively greater heights in the corona (e.g., Shibata 1999). To explain the appearance of the flaring loops, two ribbons, and their connection with filament eruptions, a "standard flare model" was developed by combining the pioneering works of Carmichael (1964), Sturrock (1966), Hirayama (1974), and Kopp & Pneuman (1976), which is collectively called the "CSHKP model." The CSHKP model deals with a 2D configuration of solar flares with a translational symmetry along the reconnecting X-line (the third dimension) (Jing et al. 2008), hence it can also be called a "standard 2D model" of solar flares.

In the recent past, there has been significant improvement in our understanding of solar flares owing to sophisticated space-borne satellites and numerical developments, which resulted in the formulation of a 3D model of solar flares (e.g., Aulanier et al. 2012). Importantly, this 3D model not only considers the third dimension, but it also includes the strong-to-weak transition of shear from preflare magnetic configuration to postflare loops. The interpretation of solar flares in the 3D regime is based upon several complex characteristics: coronal sigmoids (Sterling & Hudson 1997; Moore et al. 2001; Aulanier et al. 2010; Green et al. 2011; Joshi et al. 2017a, 2018; Mitra et al. 2018), systematic HXR footpoint motions along flare ribbons (Fletcher & Hudson 2002; Joshi et al. 2009), and sheared flare loops (Asai et al. 2003; Warren et al. 2011). In addition to these complex magnetic features, some new aspects of the flare ribbons in the 3D domain have been identified, such as photospheric current ribbons (Janvier et al. 2014), three flare ribbons (Wang et al. 2014), circular flare ribbons (Masson et al. 2009; Sun et al. 2013; Devi et al. 2020; Joshi et al. 2021; Mitra & Joshi 2021), J-shaped ribbons (Chandra et al. 2009; Schrijver et al. 2011; Savcheva et al. 2015; Joshi et al. 2017b), etc. Since the nature of solar flares is intrinsically 3D, the energy release processes via magnetic reconnection are supposed to be 3D in nature. In view of this idea, there have been several intriguing concepts regarding 3D magnetic reconnection: slipping and slip-running reconnection (Aulanier et al. 2006), null-point reconnection (Priest & Pontin 2009; Wang & Liu 2012; Prasad et al. 2020), interchange reconnection (Fisk 2005; Rappazzo et al. 2012; Owens et al. 2020), interchange slip-running reconnection (Masson et al. 2012), etc. All these reconnection processes proceed with the large-scale restructuring of coronal magnetic fields. Coronal field lines are rooted in the photosphere and are continuously shuffled by the steady convective motion below the photosphere. This shuffling process interlaces the field lines to generate complex magnetic field topologies, such as magnetic null points and their associated separatrix surfaces, separator lines, quasi-separatrix layers, etc. (Demoulin et al. 1997; Aulanier et al. 2005; Pontin et al. 2007; Jiang et al. 2021). These intriguing coronal structures act as preferential sites for current accumulation and subsequent magnetic reconnection. In view of this, in our analysis, we synthesize the multiwavelength measurements of solar atmospheric layers vis-à-vis the topological rearrangement in the coronal magnetic field configuration.

Right from the start of the era of direct soft X-ray (SXR) imaging of the Sun, there has been consensus about the classification of solar flares into two types: eruptive and confined (Pallavicini et al. 1977; Švestka & Cliver 1992; Moore et al. 2001). An eruptive flare is one that is accompanied by a CME, whereas a confined flare occurs without a CME. In general, an eruptive flare is characterized by the appearance of two ribbons on both sides of the PIL that spread apart with time as observed in Hα images and at other wavelengths. They have large-scale hot postflare loops observed in SXR and are of long duration (e.g., tens of minutes to a few hours), whereas a confined flare occurs in a relatively compact region and lasts for a short period (e.g., less than an hour) (Kushwaha et al. 2014; Cai et al. 2021). Although infrequent, even some large X-class flares have been found to belong to the confined category (Green et al. 2002; Wang & Zhang 2007). It is worth mentioning that, although flares and CMEs have a strongly coupled relationship, it is not a cause-and-effect one (Zhang et al. 2001; Temmer et al. 2010; Kharayat et al. 2021).

CMEs are designated as "homologous" when they originate from the same location of an AR with a similar morphological resemblance in coronagraphic observations (Liu et al. 2017). The cause of occurrence of these homologous CMEs was explored by several authors; Zhang & Wang (2002) have stated that repeated flare-CME activities are triggered by the continuous emergence of moving magnetic features in the vicinity of the main polarity of the AR. The study of a series of eruptions by Chertok et al. (2004) has revealed that the homology tendency appears to be due to repeated transient perturbation of the global coronal structure, partial eruption, and relatively fast restoration of the same large-scale structures involved in the repeating CME events. In a magnetohydrodynamic simulation of the development of homologous CMEs by Chatterjee & Fan (2013), the repeated CME activities originate from the repeated formations and partial eruptions of kink-unstable flux ropes as a result of the continued emergence of twisted flux ropes into a pre-existing coronal potential arcade.

Morphologically, CMEs are complex structures that exhibit a range of shapes and sizes (Schwenn 2006; Webb & Howard 2012). Recently, it has been recognized that there is a broad class of CMEs, called "over-and-out" CMEs, which come from flare-producing magnetic explosions of various sizes and are laterally far offset from the flares. A subclass of CMEs of this particular variety was originally identified by Bemporad et al. (2005), where the authors reported observations of a series of narrow ejections that occurred at the solar limb. These ejections originated from homologous compact flares, whose source was an island of included polarity located just inside the base of a coronal streamer. These ejections resulted in narrow CMEs that moved out along the streamer. It was inferred that each CME was produced by means of the transient inflation or blowing open of an outer loop of the streamer arcade by ejecta, hence they were termed as "streamer puff" CMEs. Later Moore & Sterling (2007) presented new evidence that strengthened the conclusion of Bemporad et al. (2005) and it was inferred that the "streamer puff" CMEs are essentially a subgroup of "over-and-out" CMEs. For an "over-and-out" CME, there would be a laterally far-offset ejective flare or filament eruption and no discernible flare arcade directly under the CME. Together with the work of Bemporad et al. (2005), Moore & Sterling (2007) put forward the concept of "magnetic-arch blowout" (MAB) to provide a plausible explanation for the production of "over-and-out" CMEs. First, a compact magnetic explosion located in a streamer arcade produces a compact ejective flare. This generates an escaping plasmoid, which becomes the core of the ensuing CME. Second, the source of the explosion, being compact relative to the streamer arcade, should blow out only a short section of the arcade. Observationally, the erupting plasmoid would be laterally deflected by the guiding leg of the streamer arcade and would overpower the arcade near its top, where the arcade field is weaker than its legs. Third, the blowing out of an outer loop of the streamer arcade could result in coronal dimming at the feet of the loop. The lateral extent of the dimming would demarcate the extent of the opened section of the arcade, which participated in the eruption process. Later, Sterling et al. (2011) presented a more generalized concept of the MAB scenario, applicable for CMEs that are not produced from streamer regions (see Figure 6 of Sterling et al. 2011). They investigated two precursor eruptions leading to an X-class flare, where the first precursor was a MAB event. In this case, an initial standard-model eruption of the AR's core field blew out an east-lobe loop of the core region, leading to a CME displaced toward the east of the flaring region. We note that in all the above cases, the basic physical process of the eruption remains the same, whereby they differ only in terms of different coronal magnetic environments hosting the compact blowout-eruption flares.

In this paper, we analyze three compact homologous eruptive flares, the eruptions of which result in CMEs of large angular width that resemble the "over-and-out" CMEs discussed above. The eruptions originated from NOAA Active Region 12017 within a span of $\approx$24 hr during 2014 March 28–29. In this case, each successive eruption is of increasing intensity (M2.0, M2.6, and X1.0, respectively) and results from the sequential eruption of low coronal flux ropes lying over the same location of the AR. The third event presented in our analysis (i.e., X1.0 flare) was well observed by a suite of ground- and space-based observatories (Kleint et al. 2015; Li et al. 2015; Liu et al. 2015; Young et al. 2015; Woods et al. 2018). The study by Kleint et al. (2015) revealed that a filament eruption was observed above a region of previous flux emergence, which possibly led to a change in magnetic field configuration, causing the X-flare. Liu et al. (2015) discussed a scenario of asymmetric filament eruption due to nonuniform filament confinement and an MHD instability. This disturbed the fan-spine-like field encompassing the filament leading to breakout-type reconnection at the coronal quasi-null region. Subsequently, the filament eruption triggered intense reconnection at the quasi-null, producing a circular flare ribbon. These studies mainly concentrated on a single event (X1.0 flare), which is the strongest among the three major flares. The scope of our study is much broader in that we study the evolution of all three successive major eruptions, all of which originated at the same location of mixed polarity under a dense compact arcade. Importantly, all the compact magnetic explosions produced an initial perturbation in the system that ultimately resulted in the formation of a broad CME. Furthermore, in all three cases, the source region of the CMEs, marked by coronal dimming, exhibits lateral offset from the flaring location—a typical characteristic of "over-and-out" CMEs. Although the eruptions of compact flux ropes are progenitors of the CMEs, the actual large-scale structure of the CMEs is linked to the configuration and topological changes in the large-scale magnetic field connecting to magnetic flux far from the flare site. In Section 2, we discuss the observational data sources and techniques. The details of the analysis and results are provided in Section 3. The interpretations and conclusions of our analysis are given in Section 4.

2. Observations and Data Sources

We have extensively used data taken from the Atmospheric Imaging Assembly (AIA; Lemen et al. 2012) on board the Solar Dynamics Observatory (SDO; Pesnell et al. 2012) for extreme-ultraviolet (EUV) imaging. AIA observes the full disk of the Sun and produces images in seven EUV (94, 131, 171, 193, 211, 304, and 335 Å) and two ultraviolet (UV) (1600 and 1700 Å) passbands. The images produced by AIA have a cadence of 12 s and 24 s for EUV and UV filters, respectively, and a pixel size of 0.″6, while the resolution of AIA is 1.″5.

We have used line-of-sight (LOS) magnetic field, intensity, and vector magnetic field measurements at the solar photosphere recorded by the Helioseismic and Magnetic Imager (HMI; Schou et al. 2012) on board SDO. The cadence of the LOS magnetic field and intensity measurement is 45 s, whereas the vector magnetic field has a cadence of 720 s. The data obtained from HMI have a pixel size of 0.″5. We employ the SolarSoftWare (SSW;[5] Freeland & Handy 2012) routine *hmi_prep.pro*, which converts the resolution to 0.″6 pixel^{-1} to compare the HMI data with the AIA data. The resolution of HMI is 1.″0.

The CMEs of the events under analysis were observed by the C2 coronagraph of the Large Angle and Spectrometric Coronagraph (LASCO; Brueckner et al. 1995) on board the Solar and Heliospheric Observatory (SOHO; Domingo et al. 1995). The C2 coronagraph observes the solar corona in white light images with a field of view (FOV) of 1.5–6 $R_\odot$.

To understand the small-scale coronal magnetic configurations in the preflare stages, we employ the nonlinear force-free field (NLFFF) method developed by Wiegelmann (2008), which utilizes the "optimization approach" (Wheatland et al. 2000; Wiegelmann 2004). We use the HMI.sharp_cea_720s series vector magnetograms for the photospheric boundary condition as inputs of the extrapolation. Our extrapolation volume extends up to 385, 316, and 252 pixels in x, y, and z directions, respectively, taking the photosphere as the x–y plane. These correspond to a physical volume of ($280 \times 229 \times 183$) Mm^3 above the AR under consideration. For visualization of the extrapolated magnetic field lines in 3D, we use the Visualization and Analysis Platform for Ocean, Atmosphere, and Solar Researchers (VAPOR;[6] Clyne et al. 2007) software.

[5] https://www.lmsal.com/solarsoft/
[6] https://www.vapor.ucar.edu/

The large-scale coronal magnetic field lines surrounding the activity site are determined using the potential field source surface (PFSS) extrapolation method (Schrijver & De Rosa 2003). PFSS is an IDL-based algorithm that is available in the SSW package.

3. Analysis and Results

3.1. Relationship between Coronal Mass Ejections and their Source Region

In Figure 1(a), we provide the GOES light curve in the 1–8 Å channel from ≈14:30 UT on 2014 March 28 to ≈19:00 UT on 2014 March 29. The light curve clearly indicates the occurrence of three large flares of class M2.0, M2.6, and X1.0 (the flare intervals are marked by vertical shaded regions in different colors). All these flares were of the eruptive category and produced spectacular, large-scale structures of CMEs observed in the white light coronagraphic images from LASCO.[7] We find that the eruptive flares show successively increasing intensities (viz., M2.0, M2.6, and X1.0). We also note that there had been no significant flaring activities (of class $>M$) at least one day before and after the events under analysis. These events occurred in NOAA AR 12017, which presented a $\beta\gamma$ type photospheric magnetic configuration during the reported activities. This AR is typical in the sense that it exhibited multiple flaring episodes within a short span of ≈2 days during 2014 March 28–29, and it has been the subject of several studies. Yang et al. (2016) investigated the magnetic field of the AR during the aforementioned period and found the presence of a magnetic flux rope (MFR) in an NLFFF extrapolation, which was prone to kink instability. Furthermore, the closed quasi-separatrix layer structure surrounding the MFR became smaller as a consequence of the eruption. Chintzoglou et al. (2019) revealed that NOAA AR 12017 hosted a "collisional PIL," which developed owing to the collision between two emerging flux tubes nested within the AR. Also, during the entire evolution over the visible solar disk, the AR showed significant cancellation (up to 40%) of the unsigned magnetic flux of the smallest emerging bipolar magnetic region.

In Figure 1(b), we plot the EUV light curves based on AIA imaging observations in 94, 171, and 304 Å channels. The AIA light curves are obtained from intensity variation over the whole NOAA AR 12017 (marked by a red rectangle in Figure 3(b)). We note that the EUV 94 Å light curve resembles the GOES 1–8 Å light curve fairly well. A summary of the flaring events is given in Table 1, which is based on the GOES flare catalog.[8]

In Figure 2, we provide LASCO C2 images of three CMEs (marked as Event I, II, and III). The CMEs associated with events I and II are non-halo (with angular sizes of 103° and 111°, respectively), whereas the CME associated with event III is a halo CME. We note that the linear speed of the CMEs increases gradually from event I to event III, with values of 420, 503, and 528 km s^{-1}, respectively. Several parameters of these CMEs are listed in Table 2.

The large-scale coronal connectivities are thought to play a major role in the development of broad CME structures. In

[7] https://cdaw.gsfc.nasa.gov/CME_list/UNIVERSAL/2014_03/univ2014_03.html
[8] https://www.ngdc.noaa.gov/stp/space-weather/solar-data/solar-features/solar-flares/x-rays/goes/xrs/goes-xrs-report_2014.txt

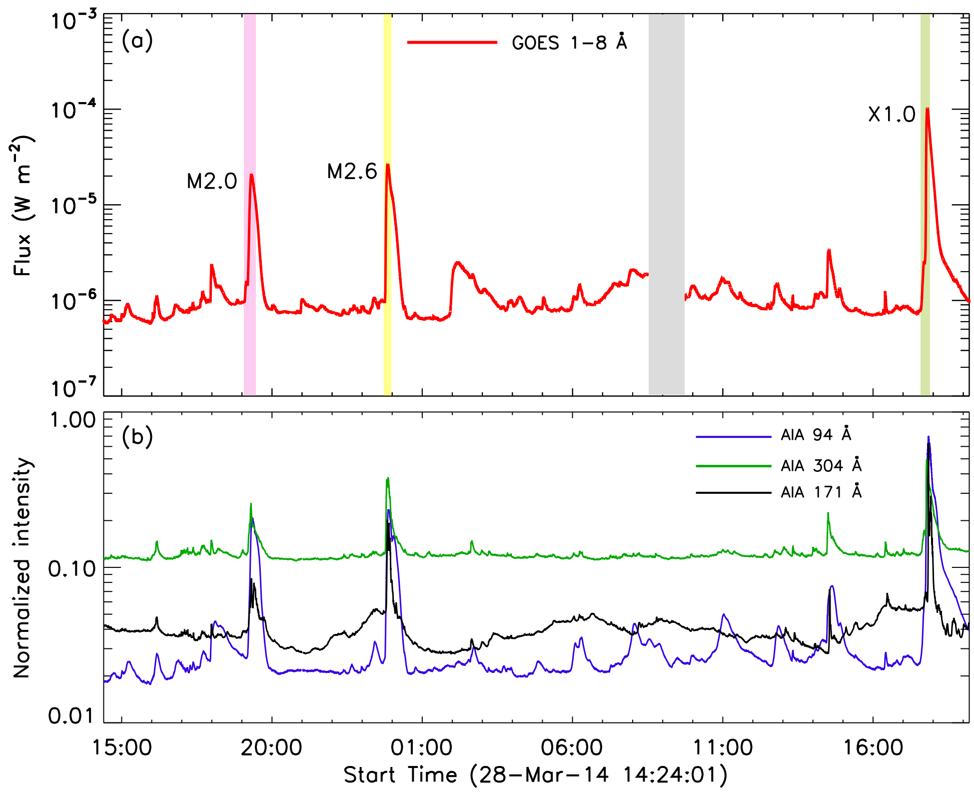

Figure 1. Panel (a): GOES soft X-ray flux in 1–8 Å channel indicating the three flare events of intensities M2.0, M2.6, and X1.0. The shaded regions in purple, yellow, and olive green represent the flare durations according to the GOES flare catalog. The gray shaded region indicates a period over which GOES data were unavailable. Panel (b): normalized intensity light curves of AIA passbands 94 Å [$\log(T) = 6.8$], 304 Å [$\log(T) = 4.7$], and 171 Å [$\log(T) = 5.7$] multiplied by factors of 0.7, 0.5, and 1.2, respectively, for clear visualization. The light curves denote the variation of intensity over the AR under analysis. An animation showing the temporal variation of GOES SXR light curves (top) and the flare evolution in 94, 304, and 171 Å channels (bottom) is available. The animation runs from 18:45 UT on 2014 March 28 to 18:20 UT on 2014 March 29. The real-time duration is 30 s.

(An animation of this figure is available.)

order to visualize large-scale coronal magnetic field lines, we carry out PFSS extrapolation for a few representative instances (see Figures 3(a), (c), and 4(b)–(c)). In Figure 3(a), we show the extrapolated field lines in and around the AR before event I. To show the detailed magnetic structure on the photosphere, the region marked within the yellow dashed box in Figure 3(a) has been shown in Figures 3(b)–(c). In Figure 3(b), NOAA AR 12017 and 12018 are marked by red rectangles. NOAA AR 12017 is the AR of our interest. The flaring region lies in the leading part of the AR, which is marked by a sky-blue box. In all three cases, the eruption begins with a compact blowout eruption of a flux rope from a small region of mixed polarity within the flaring region. We term this small region as the "core," and mark it with a green box (see also Figure 8). Notably, the size (i.e., area under the green box) of the core region is significantly smaller ($\approx$19 times) than the extent of the AR (i.e., the area under the red rectangle denoting NOAA AR 12017). A careful examination of the magnetogram reveals the presence of extended and dispersed magnetic flux of positive polarity, located toward the northwest of the flaring site, substantially away from the AR boundaries. This distant positive-polarity region (DPR) extends like an arc, which we manually mark by a green dashed line in Figure 3(b). Importantly, we note clear magnetic connectivities between the negative polarity of the flaring region and the DPR, which we denote as white field lines in Figure 3(c), adjacent to open field lines (shown in pink), originating from the flaring region. The DPR acts as a proxy for the remote footpoints of large-scale coronal field lines (i.e., a magnetic arch; MA), which is involved in the formation of large-scale CMEs. To explore the fine details of the flaring region, we show zoomed images of this region in Figures 3(d)–(g). Panels (d) and (e) represent the magnetic configuration before events I and II, whereas panels (f) and (g) represent the magnetic structure of the flaring region before event III. Comparison of panels (d)–(g) of Figure 3 clearly reveals substantial small-scale changes (i.e., various epochs of emergence and cancellation) in the photospheric magnetic field of the flaring region over the time period spanning the three events.

Each of the eruptive flares is followed by collimated surges of cool material from the flaring region. In Figure 4(a), we show a representative image of the surge from the flaring region observed after event II. We choose this particular observation because of its clear visibility. In Figures 4(b)–(c), we show the large-scale coronal field lines, demonstrated by PFSS extrapolation, connecting the flaring region with the DPR (shown as white field lines). The epochs in these panels denote instances a few hours after event II and a few hours before event III, respectively. The pink lines represent open field lines emanating from the flaring region. We note that the large-scale coronal magnetic field configuration remains unchanged during the course of the events (see Figures 3(c) and 4(b)–(c)). Interestingly, the surge nearly follows the open field lines (see Figures 4(a)–(c)).

Table 1
The Flares in NOAA AR 12017 during 2014 March 28–29

Event Number	Flare Class	Date	Start	Time (UT) Peak	End	Heliographic Coordinate
I	M2.0	2014 Mar 28	19:04	19:18	19:27	N11W21
II	M2.6	2014 Mar 28	23:44	23:51	23:58	N11W23
III	X1.0	2014 Mar 29	17:35	17:48	17:54	N11W32

3.2. Trio of Blowout-eruption Flares and Associated Magnetic Environment

The temporal and morphological analysis of the eruptive flares is presented in Figures 5–7. Panel (a) in these figures show the GOES light curves of the events in the 1–8 and 0.5–4 Å channels, along with the AIA light curves in 94 and 171 Å, while panels (b)–(i) provide a few representative AIA images. For imaging analysis, we examine AIA observations taken in the 94 and 171 Å channels. The AIA 94 Å [$\log(T) = 6.8$] channel is apt for imaging the flaring coronal structures while AIA 171 Å [$\log(T) = 5.7$] channel is useful to infer the low-temperature structures formed in the corona and transition region. The selected FOV of the AIA images encompasses the flaring region (see Figures 3(d)–(g)) and surrounding regions into which the eruption evolves.

Figure 5 reveals several temporal and spatial aspects of the first (M2.0 flare) event. A comparison of LOS photospheric magnetic flux with the EUV images (see panels (b) and (f)) during the preflare stage reveals small-scale connectivities (marked by white arrows in panel (f)) between opposite magnetic polarities within the core region. In the 171 Å image in panel (f), we note several structures that extend outward (marked by a green arrow), suggestive of either large-scale or quasi-open field lines. The presence of open field lines is well supported by the global PFSS extrapolation presented in Figures 3 and 4 (see also Section 3.1). The sequence of AIA images (see also the animation attached with Figure 1) reveals two stages of eruptions, which we term as ejecta I and II. Ejecta I originates from the eastern part of the core at ≈19:03 UT (marked as “ejecta I” in panels (c) and (g)). Ejecta II starts at ≈19:18 UT from the western part of the core (marked as “ejecta II” in panels (d) and (h)). The onset times of the two ejecta are indicated in the GOES light curves in panel (a). We observe that ejecta I precedes the flare while ejecta II occurs during the impulsive phase, shortly before the peak. In panels (d) and (h), we mark a wide circular ribbon structure by sky-blue arrows, situated north of the mixed-polarity core region. The compact postflare loops, formed as a result of standard flare reconnection between the legs of the field lines stretched by the erupting flux rope, are indicated by a red arrow (panel (d)). We explain the formation of the circular ribbon and the compact postflare loops with the help of a schematic diagram (Figure 11) in Section 4. After the peak, we observe a gradual decline in the light curves, indicating the decay phase, which is marked by the growth of dense postflare loop arcades (shown in panels (e) and (i)). Multiple eruptions in close succession like this have been observed before, and it is plausible that the first eruption leads to a destabilization of nearby fields in the same region leading to the second eruption (e.g., Török et al. 2011; Sterling et al. 2014; Joshi et al. 2020).

In Figure 6(a), we show the temporal variation of the second (M2.6 flare) event. In the following panels, we demonstrate the structural changes associated with the eruption’s evolution in EUV 94 and 171 Å images. During the preflare stage, the coronal configuration of the flaring region shows similarity to that of event I in the form of small-scale connectivities and the existence of quasi-open-type field lines (see panels (b) and (f)). Similar to event I, here also we observe two discrete eruptions in association with the flaring activities. The first eruption starts in the eastern part of the core region just after the beginning of the impulsive phase at ≈23:46 UT. We mark this eruption as “ejecta I” (panels (c) and (g)). The second eruption originates from the western part of the core just after the ejecta I at ≈23:48 UT, which we term as “ejecta II” (shown in panels (d) and (h)). These successive eruptions show similar morphological behavior to that of event I with respect to their origin and the subsequent path followed by them. The flare reaches its peak at ≈23:51 UT (see panel (a)). Thereafter, the postflare loops are observed to form (shown in panels (e) and (i)).

The temporal and spatial evolutionary phases of the third (X1.0 flare) event are depicted in Figure 7. During the pre-eruptive stage of the eruption, we note the existence of a null-point-like structure connecting the opposite magnetic polarities of the flaring region, which is evident in the 171 Å image in panel (g). Unlike the two previous events, both of which consisted of two ejective episodes, in this case there is only a single eruption from the core region, which starts at ≈17:45 UT, as marked in panel (a). The eruption apparently destroys the null-point-like structure during the buildup to the maximum phase of the X1.0 flare. The flare peaks at ≈17:48 UT (indicated in panel (a)). After that, the dense postflare arcades are formed (shown in panels (e) and (i)).

Notably, we observe circular ribbon structures during the peak of all the events (see panels (d) and (h) of Figures 5–7).

To understand the magnetic complexities of the core region on the size scale of the AR, we employ coronal magnetic field modeling using the NLFFF extrapolation technique. We demonstrate the results of the extrapolation carried out during the preflare stages of the events in Figure 8. The extrapolation results clearly demonstrate the existence of two adjacent flux rope systems for each of the three events. We note that the compact flux ropes lie over the compact region of strong mixed polarity within the core region (marked by a green box in Figure 3(b)). The flux ropes lying on the eastern and western parts of the core are shown as red and yellow field lines, respectively. We note a system of low-lying closed field lines (shown in green) connecting the negative and positive polarities of the core that constrain the two flux ropes. A comparison of modeled coronal field structure (Figure 8) with the corresponding imaging observations (Figures 5–7) suggests sequential eruptions of the eastern and western flux ropes during events I and II, whereas, only a single flux rope erupts for the case of event III. For event III, observational results suggest the eruption of western flux rope (shown as yellow field lines in Figure 8(c)) from the core region.

Even though the third eruption does not have two “ejecta” as in the first two events, there is nonetheless enhanced activity in

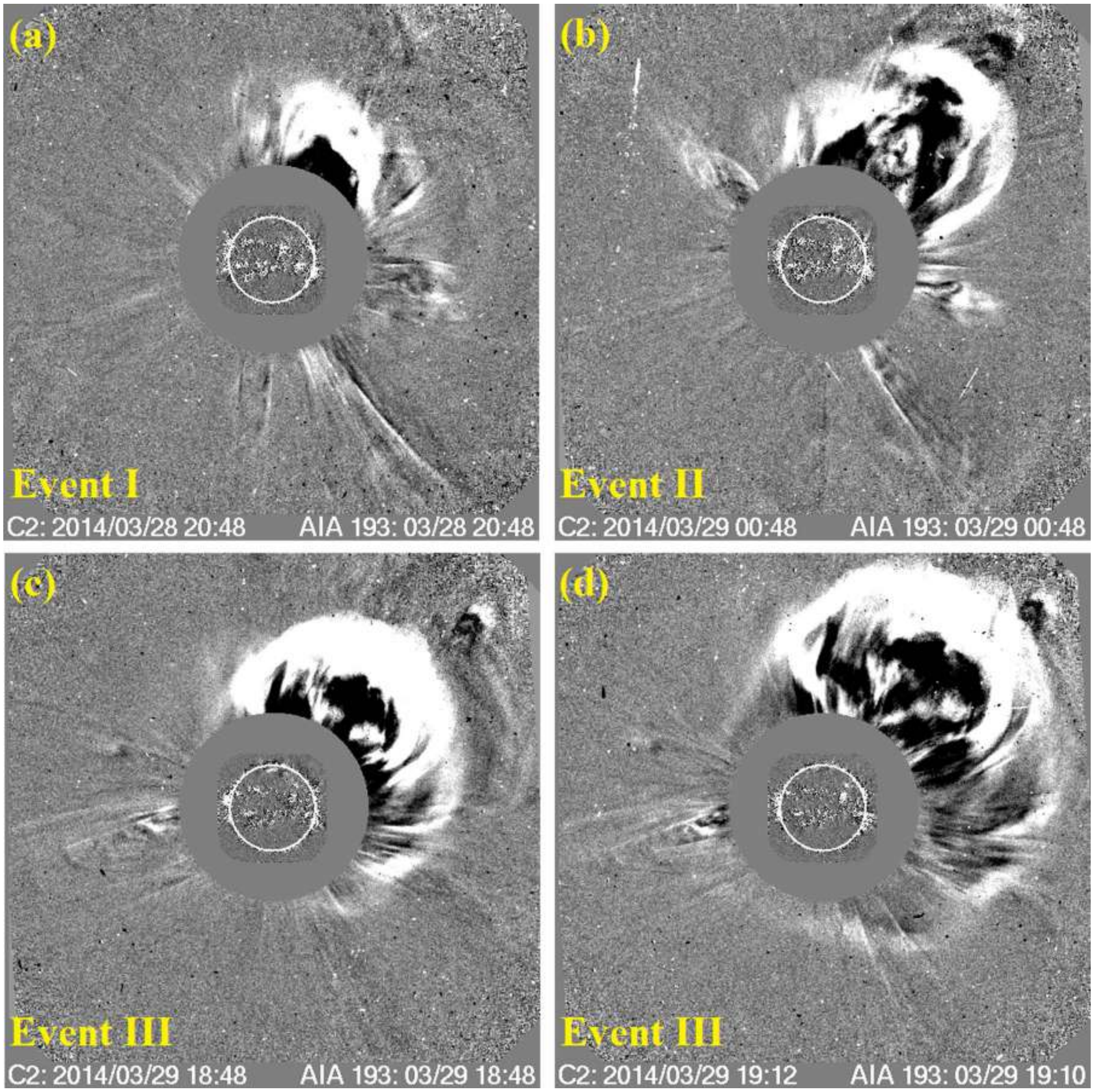

Figure 2. Depiction of the wide CMEs formed due to the large-scale eruptions associated with the events under analysis. Panels (a) and (b) show the CMEs associated with events I and II and the CME produced in the aftermath of event III is shown in panels (c) and (d). In all panels, the CME images are from the LASCO C2 coronagraph and the coronagraph occulter is overplotted by an AIA 193 Å image.

Table 2
Some Parameters of the CMEs Produced by the Events under Investigation

CME	Speed (km s^{-1}) V_L	V_S	Angular Width (°)	Mass ($\times 10^{15}$ gram)	Kinetic Energy ($\times 10^{30}$ erg)
CME 1	420	464	103	2.6	2.3
CME 2	503	327	111	2.3	2.9
CME 3	528	505	360	5.0	7.0

Note. CME 1, CME 2, and CME 3 are made by events I, II, and III, respectively. V_L and V_S are linear speed and second-order speed at 20 solar radii, respectively. The various parameters of CMEs are obtained from the SOHO/LASCO CME catalog (https://cdaw.gsfc.nasa.gov/CME_list/UNIVERSAL/2014_03/univ2014_03.html).

this third event prior to the main eruption. It is visible in the GOES plot of Figure 7(a) peaking shortly after 17:40 UT, and it corresponds to an initial movement of the filament prior to eruption, with accompanying brightenings (visible in 94, 304, and 171 Å images; see the animation attached with Figure 1). The difference for this third event from those first two is that in this case the preflare motions and brightenings are along the same main magnetic neutral line (or along the same portion of that neutral line) from which the main eruption occurs, rather than manifesting as an earlier "ejecta" event at a different location in the AR. This is similar to the stop-and-start "slow-rise" evolution seen in other filament eruption events (e.g., Sterling & Moore 2005). For each of these three cases, the erupting flux ropes act as a "seed" toward the formation of large-scale CME structures.

3.3. Magnetic-arch Blowout and Coronal Dimming

All the events analyzed in this study are eruptive in nature, and each of the three eruptions led to the formation of broad CMEs. Although the CMEs possessed large-scale structures with wide angular width (>100° to halo; Figure 2), the corresponding source ARs of flare blowout eruptions were

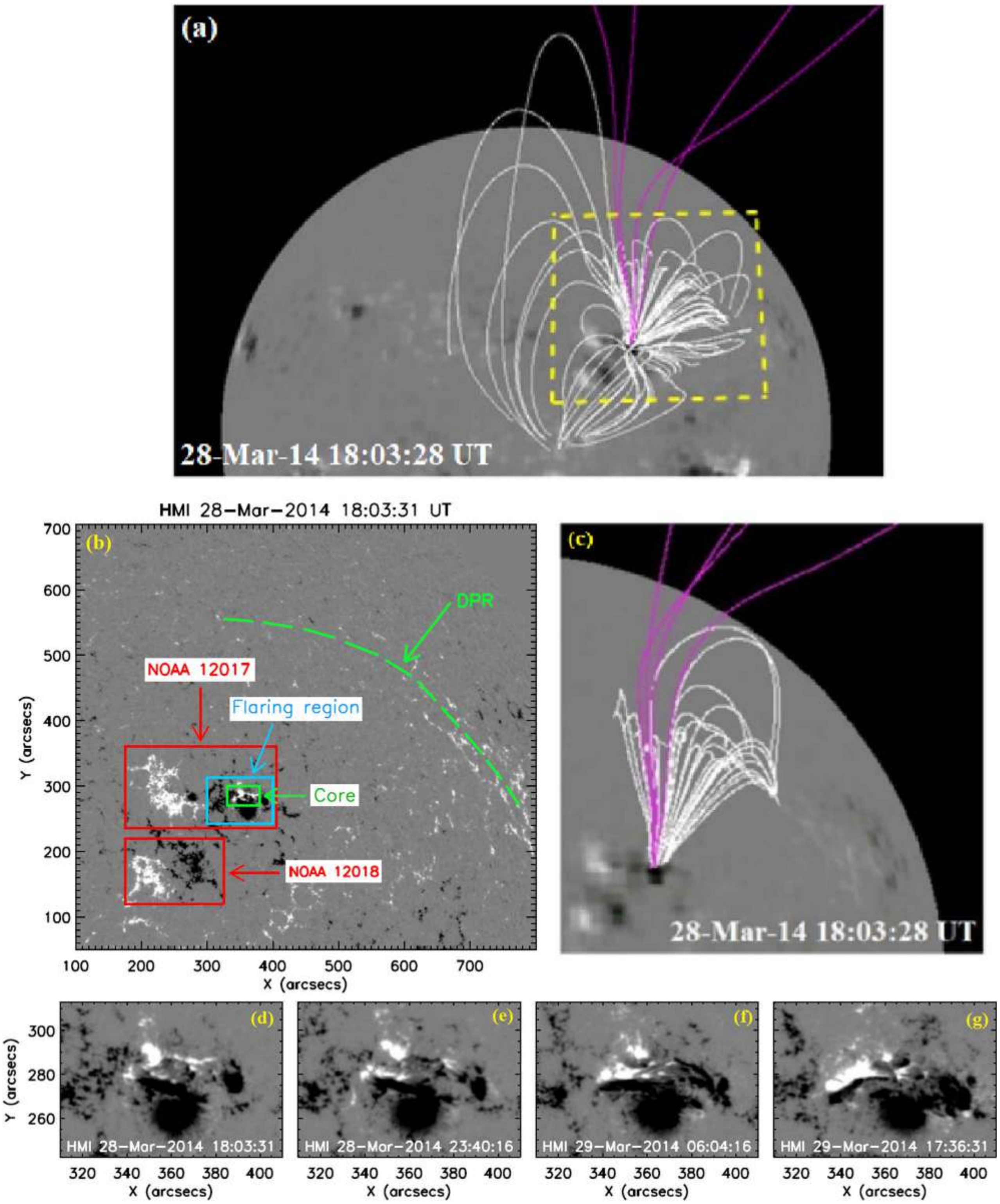

Figure 3. Panel (a): the large-scale field surrounding the AR from which the eruptions occur. The white and pink lines denote closed and open field lines, respectively, overlaid onto the LOS magnetogram. The yellow dashed box is enlarged in panels (b)–(c). In panel (b), we show the photospheric LOS magnetogram. NOAA AR 12017 and 12018 are indicated by the red rectangles. We note that NOAA AR 12017, the AR of our interest, displays an approximate spatial extension of $230'' \times 125''$. We mark the flaring region within this AR with a sky-blue box. Inside this, we mark the "core" location of the mixed-polarity magnetic field with a green box. The spatial extension of the core is $\approx 50'' \times 30''$, and it is the source of all the compact blowout-eruption flares. Notably, the core region is much smaller ($\approx$19 times) than the size of the AR. We show the DPR as a green dashed line. In panel (c), we show the large-scale connectivity between the negative polarity of the flaring region and the DPR as white field lines (see panels (b) and (c)) before the time of event I. The pink lines are open field lines originating from the flaring region. In panels (d)–(g), we show the evolution of the flaring region. In panels (d) and (e), we show the morphology of this region before events I and II, respectively, whereas, the magnetic configuration before event III is shown in panels (f) and (g).

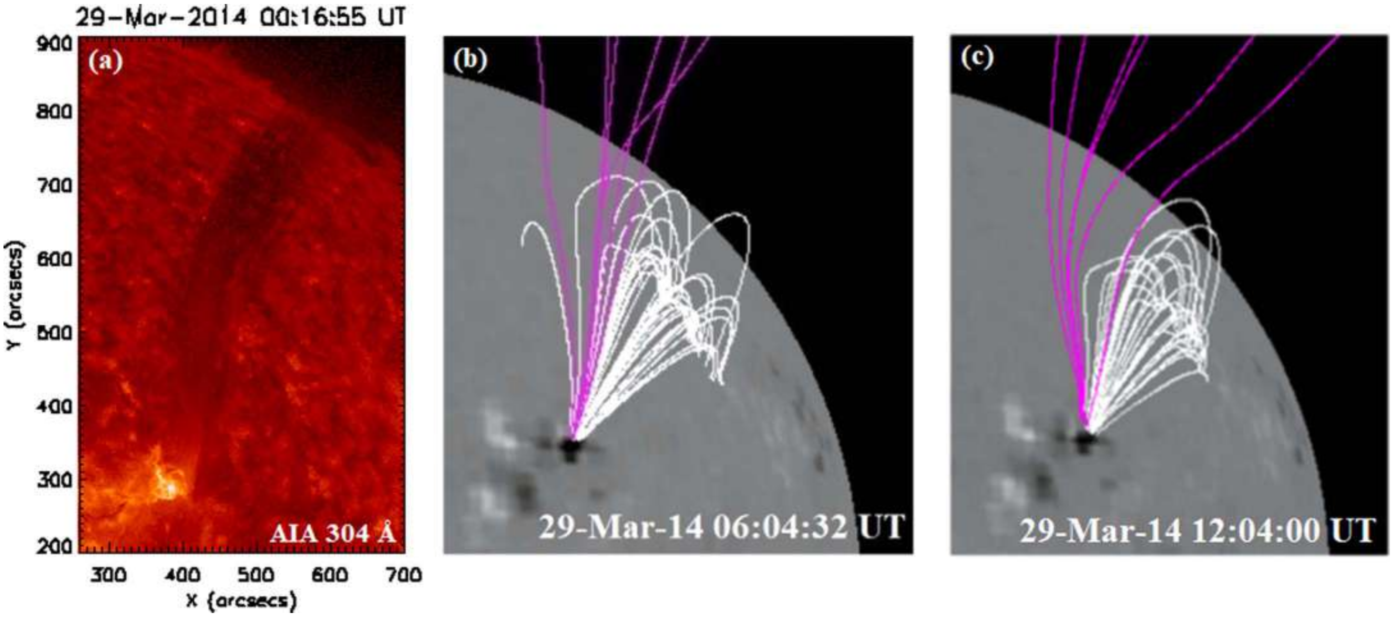

Figure 4. In panel (a), we show a surge consisting of cool material expelled from the flaring region, observed to occur after event II. Panels (b) and (c) show the large-scale connectivity, revealed by PFSS model extrapolation, between the flaring region and the DPR at instances shortly after event II and shortly before event III, respectively. The surge nearly follows the open pink field lines (see panels (a)–(c)). The large-scale connectivity between the flaring region and the DPR remains unchanged before event I, after event II, and before event III (see panels (b) and (c) with Figure 3(c)). The surges are too large to see in the FOV of animation 1 (attached with Figure 1).

much more compact (see the spatial comparison shown in Figure 3(b)). This phenomenon of the CME being much wider than the source region has been recognized for some time (e.g., Harrison 1995; Dere et al. 1997; Gopalswamy & Thompson 2000). Moore et al. (2007) argue that such a widening between the source region and the CME is a consequence of the magnetic pressure of the exploding field coming into pressure balance with the interplanetary field in the solar wind, which is far weaker than the AR coronal field surrounding the source region, meaning that the CME field has to expand substantially for that new pressure balance to ensue. We show with AIA 193 Å fixed-difference images the large-scale coronal changes accompanying the early evolution and subsequent development of the broad CMEs during our three events. Some snapshots of these observations during the course of event I are represented in Figure 9. Note that the FOV chosen in Figures 9(a)–(f) represents a much larger area compared to the FOV shown in Figures 5–7. For comparison, in Figure 9(a), we indicate the flaring region (see the sky-blue box in Figure 3(b)). The saturated pixels in and around the flaring region in panel (c) approximately mark the start of the flare. The eruption of flux ropes from the core region is followed by EUV dimming. The onset of the dimming can be realized in the form of a slight dark region adjacent to the flaring region which is manifested as a result of sudden plasma depletion (see Figure 9(d)). The dimming region expanded gradually, indicated by an arrow in Figure 9(e), spreading out as an “EIT Wave” (or “EUV Wave”) (e.g., Thompson & Myers 2009; Gallagher & Long 2011; Long et al. 2014). In the following panel (f), we show a widespread dimming formed northward of the AR (see also the attached animation).

The morphological features observed during the course of the eruptions for events II and III are shown in the upper and lower panels of Figure 10, respectively. Following the flux rope eruptions, the EUV coronal dimming is observed subsequently to grow to cover a large area (marked by sky-blue arrows in Figures 10(b)–(c)).

Event III presents much more pronounced large-scale structures compared to events I and II. However, it shows morphological similarities with the previous events in terms of the development of coronal dimming and the resulting broad CME, which actually becomes a halo CME for event III. The dimmings are indicated by sky-blue arrows in Figures 10(e)–(f). In Figures 9(e), 10(b), and (e), we mark the location of the flaring region and a part of the DPR with red and green stars, respectively. These locations actually denote the footpoints of the large-scale field lines (i.e., MA), whose blowout eruption resulted in the formation of the broad CMEs and accompanying EUV dimming.

4. Discussion

In this study, we explored the formation process of three homologous, broad CMEs resulting from eruptive flares in the compact bipolar region of NOAA AR 12017 over 2014 March 28–29. All the events were identified as flux rope eruptions, formed over the same PIL of the AR. Our work presents a clear example of a large-scale coronal magnetic configuration that is repeatedly blown out by compact flux rope eruptions leading to a series of broad CMEs.

The EUV imaging observations of NOAA AR 12017 clearly reveal filaments at the core of the AR near the polarity inversion lines. The magnetic field holding the filaments along the PIL erupts successively three times within a time span of ≈24 hr. Our NLFFF extrapolation results reveal the existence of twisted magnetic structures that would envelop the filaments and are capable of storing the magnetic free energy (e.g., Fan & Gibson 2007; Zhang et al. 2012; Toriumi & Wang 2019; Mitra et al. 2020; Sahu et al. 2020) required for the subsequent multiple eruptions. For events I and II, the flux rope containing the filament near the eastern part of the core erupted first

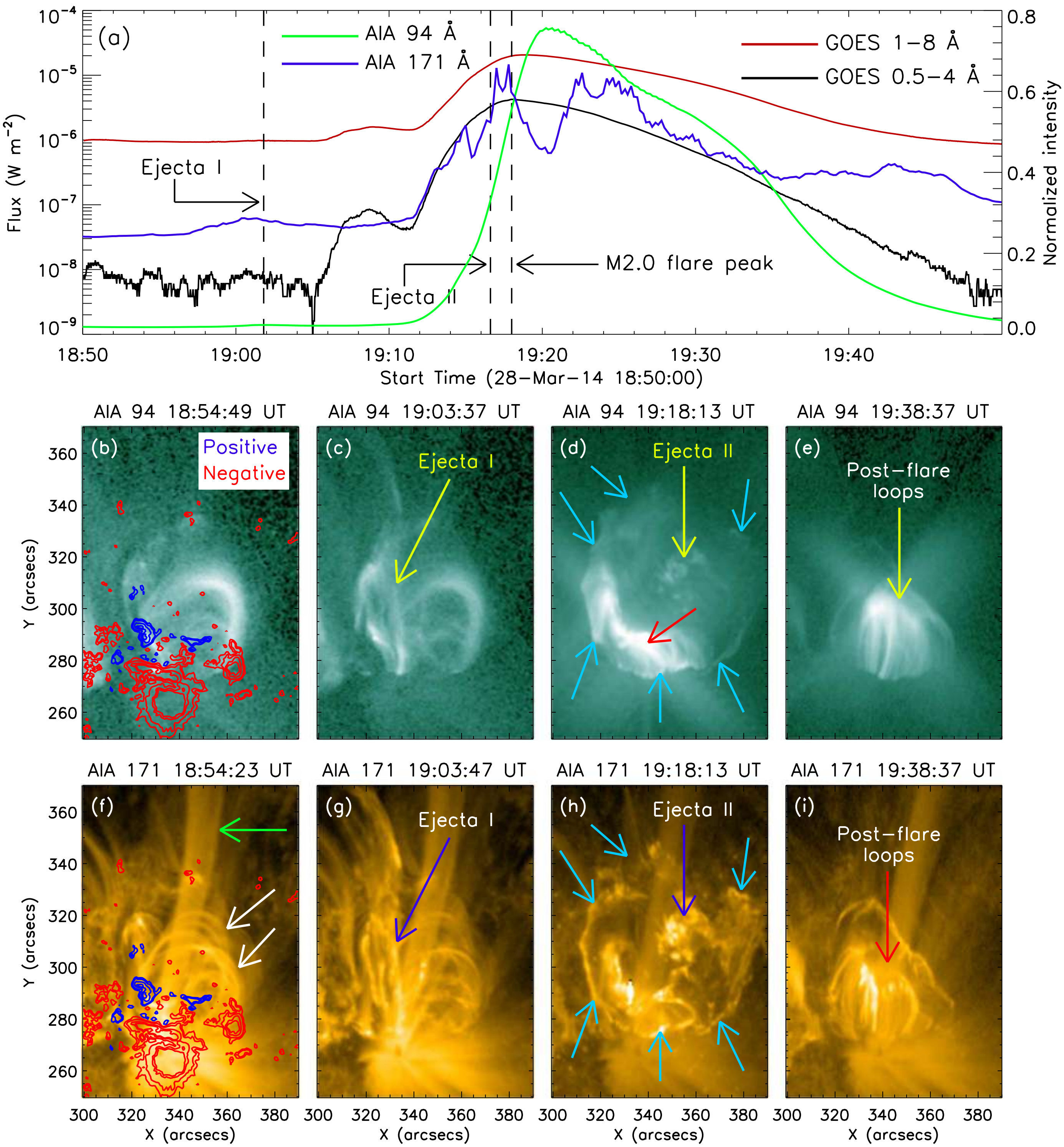

Figure 5. Panel (a): the GOES light curves in 1–8 and 0.5–4 Å channels and the intensity curves for event I, obtained from the flaring region recorded in AIA 94 and 171 Å channels. The light curves span from 18:50 UT to 19:50 UT on 2014 March 28 showing the epochs of the first event, which had the M2.0 flare and two associated ejecta. Panels (b)–(e): evolution of the eruption in the AIA 94 Å channel. In panel (b), we overlay the LOS magnetic contours with red and blue, representing negative and positive magnetic polarities, respectively. Panels (c) and (d) indicate ejecta I and II, respectively. In panels (d) and (h), we demarcate a wide circular ribbon structure north of the core region by sky-blue arrows. The compact postflare loops result from the standard flare reconnection between the legs of the field lines stretched by the erupting flux rope are indicated by a red arrow in panel (d). In panel (e), we show the growing postflare loop arcades. Panels (f)–(i) show the flare evolution in the AIA 171 Å channel. The same magnetic contours as in panel (b) are also shown in panel (f). The magnetic contour levels are set at ±[200, 400, 800, 1000, 2000] G. In panel (f), the two white arrows indicate small-scale connectivities within the flaring region, whereas the green arrow shows several structures that extend outward. Ejecta I, ejecta II, and the postflare arcades are indicated in panels (g), (h), and (i), respectively. The peak of the flare occurs just after the eruption of ejecta II (see panel (a)).

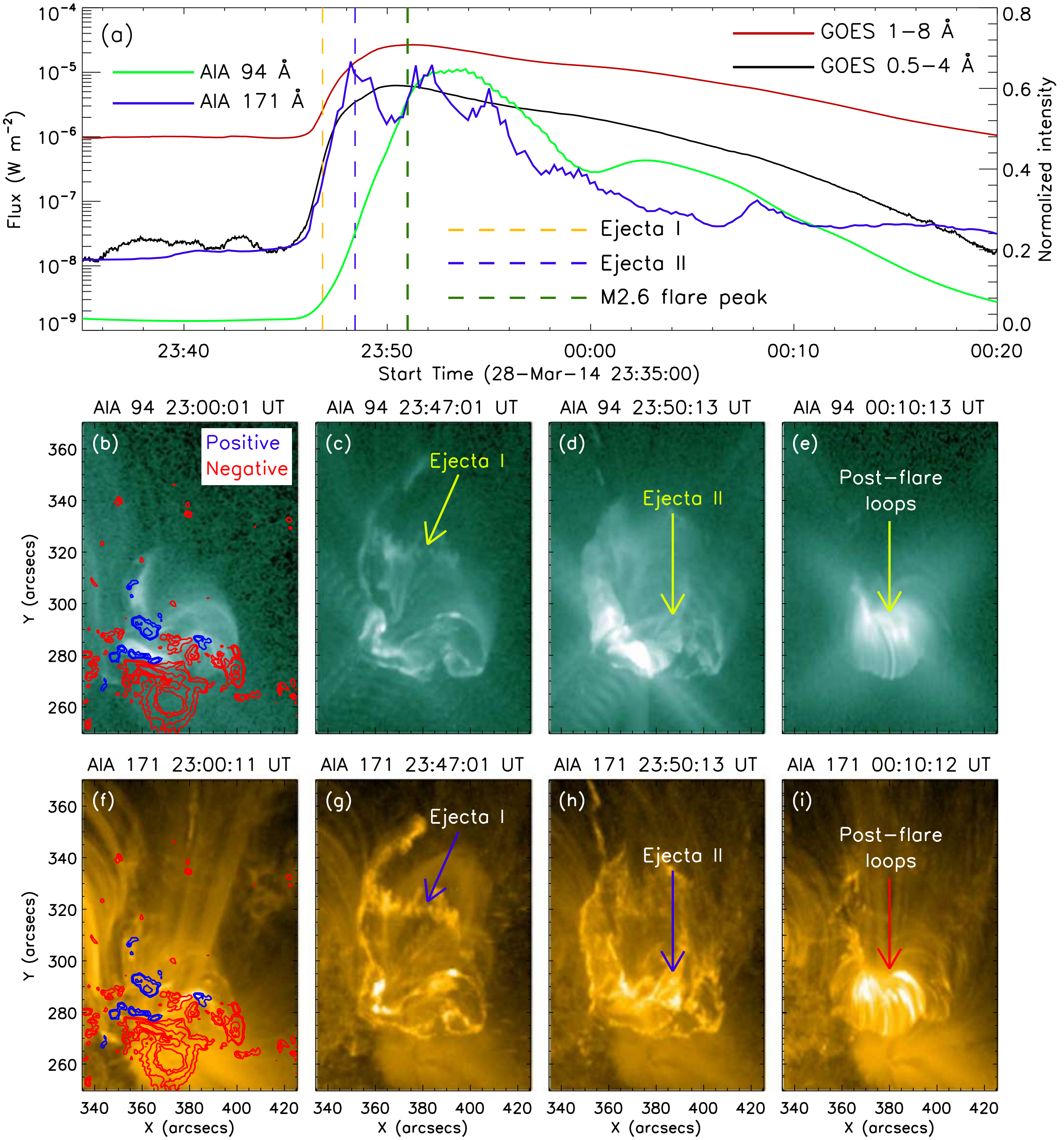

Figure 6. Panel (a): the GOES light curves in 1–8 and 0.5–4 Å channels along with the intensity curves obtained from the flaring region in AIA 94 and 171 Å channels for event II. The time range of the light curves spans between 23:35 UT on 2014 March 28 and 00:20 UT on March 29. The flare peak and the two ejecta are indicated by dashed lines in different colors. Panels (b)–(e): evolution of the flare shown in the AIA 94 Å channel. The LOS magnetogram is overplotted as contours on the 94 Å image in panel (a). Ejecta I and II are shown in panels (c) and (d), respectively. The postflare loops are shown in panel (e). In panels (f)–(i), we show the flare evolution in AIA 171 Å observations. The LOS magnetogram is overplotted on the 171 Å image in panel (f). The magnetic contour levels are ±[200, 400, 800, 1000, 2000] G in all the panels. Panels (g) and (h) show ejecta I and II, respectively. The formation of bright postflare loops is shown in panel (i).

(obtained in modeling as the red flux rope structure in Figures 8(a)–(b)) followed by the eruption of flux rope containing the filament from the western part (indicated by yellow flux rope structure in Figures 8(a)–(b)). For event III, we observe a single filament/flux rope eruption from the western part of the core region; the extrapolation results indicate that this is likely triggered by the eruption of the yellow flux rope shown in Figure 8(c). The sequential eruption of filaments led to homologous flares followed by CMEs. The eruptions occurred from a very compact site (i.e., core) within

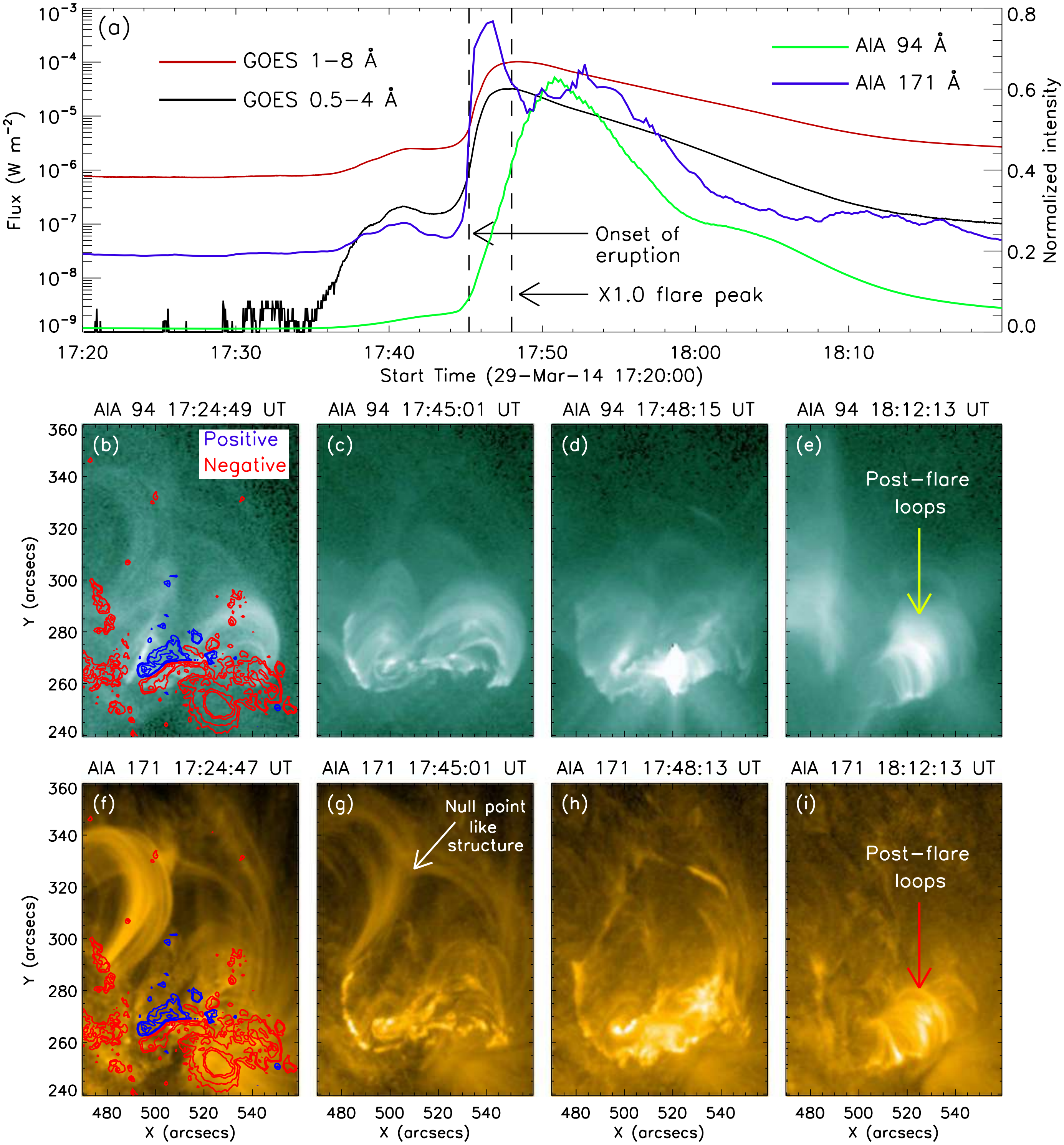

Figure 7. In panel (a), we plot the GOES light curves in 1–8 and 0.5–4 Å channels for the case of event III, along with the intensity curves from the AIA 94 and 171 Å channels recorded from the flaring region. The time interval chosen for this panel runs from 17:20 UT to 18:20 UT on 2014 March 29. We indicate the onset of eruption and the flare peak by dashed lines. In this case, we observe a single eruption from the core region, unlike events I and II where we observed two successive eruptions denoted as ejecta I and II in Figures 5 and 6. Panels (b)–(e) show the evolution of the flare in AIA 94 Å images. In panel (b), we overplot the magnetic contours onto the 94 Å image. In panel (e), we show the postflare loop arcades. In panels (f)–(i), we show the flare evolution in the AIA 171 Å channel. The magnetic contours drawn in panel (f) are the same as in panel (b). The contour levels are set at ±[200, 400, 800, 1000, 2000] G. We observe an inverted Y-shaped null-point-like structure in the pre-eruptive stage, indicated in panel (g). The formation of postflare loop arcades is shown in panel (i).

the flaring region (see Figure 3(b)), while the resulting CMEs are of wide angular width (>100° to halo) (see Figure 2). Woods et al. (2018) explored the triggering mechanism of the filament eruption that occurred with the X-class flare of our study (event III). The authors confirmed the existence of two flux ropes present within the AR prior to flaring. Interestingly, only one of these two flux ropes erupts during the flare. Woods et al. (2018) interpreted that tether-cutting reconnection

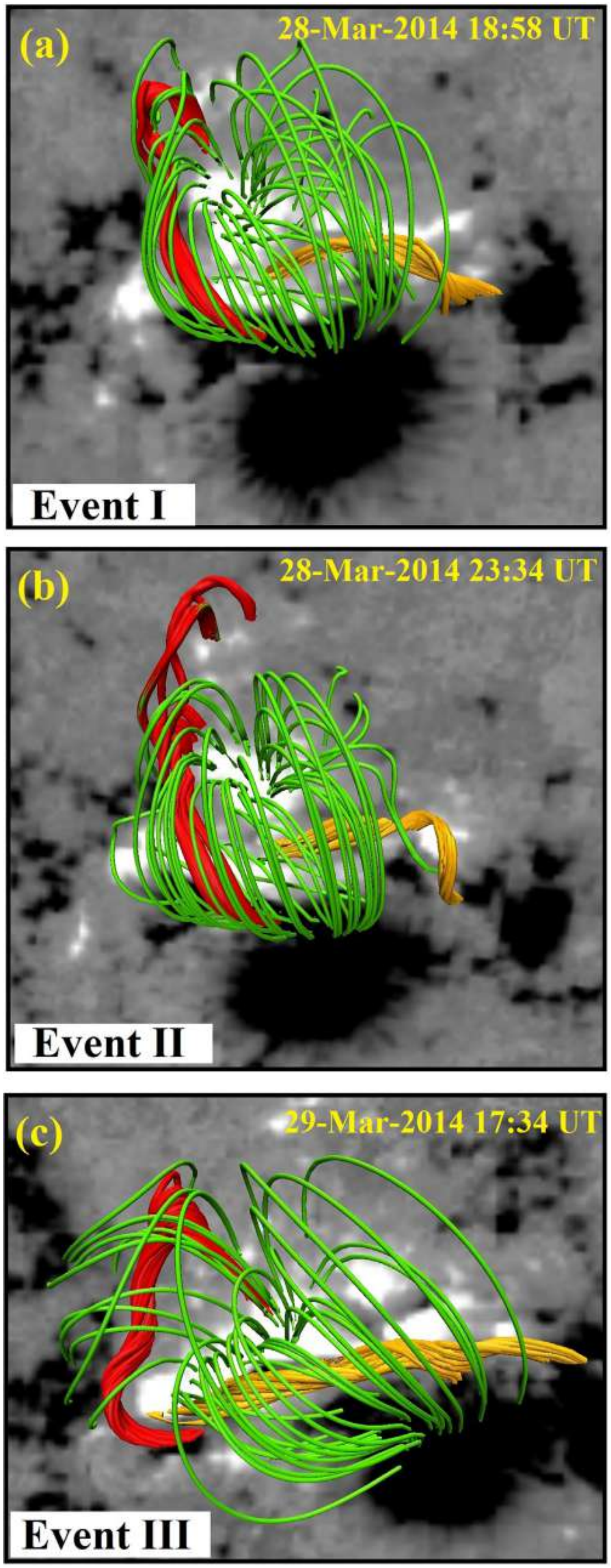

Figure 8. Pre-eruptive configurations of the core region in zoomed view, obtained from the NLFFF extrapolations using HMI vector magnetograms. The core consists of closed bipolar field lines (shown in green) constraining the underlying flux ropes. The flux ropes form over the strong mixed-polarity region within the core. We show the flux ropes lying over the eastern and western parts of the core region as red and yellow field lines, respectively.

allowed one of the flux ropes to rise to a torus-unstable region prior to flaring, resulting in its successful eruption.

For exploring the large-scale coronal magnetic field changes causing broad CMEs, we conduct PFSS extrapolation to visualize global potential coronal loops in and around the AR (shown in Figures 3(a), (c), and 4(b)–(c)). We observe large-scale field lines connecting the DPR with the flaring region. In view of the generation of broad CMEs, we propose a scenario in which the erupting magnetic flux ropes disrupt these large-scale coronal loops to evolve into broad CMEs. We note that the open field lines (shown in pink) originating from the flaring region can act as a "runway" for the successful successive eruption of the flux ropes. The influence of large-scale open field lines in the kinematic and dynamic evolution of CMEs has also been investigated in some other recent studies (e.g., Chen 2013; Georgoulis et al. 2019; Gou et al. 2019).

We examine the AIA 193 Å fixed-difference images during the course of the events over an extended neighborhood of the flaring region. We observe that the eruptions are followed by substantial coronal dimming (Sterling & Hudson 1997; Reinard & Biesecker 2008; Mason et al. 2014) which gradually expanded (see Figures 9 and 10). Previous studies have shown that coronal dimming corresponds to the temporary regions of strongly reduced coronal emission in EUV and SXRs that form in the wake of CMEs. In general, their formation is interpreted as density depletion due to the expansion and expulsion of plasma during the early CME evolution. The presence of large-scale open field lines, as demonstrated in the present study, would further support the growth of dimming regions as open field lines act as conduits for outward plasma flow.

The blowout eruptions of compact flux ropes from the core region and their sequential interactions with the overlying large-scale coronal field resulted in broad CMEs. The present observations exhibit excellent conformity with the MAB scenario originally proposed by Moore & Sterling (2007). In essence, the erupting compact flux ropes explode up the large-scale field lines connecting the flaring region of the AR and the DPR (see Figures 3(b)–(c)). In a feedback process, the activated flux rope blows out the large-scale field lines which in turn strengthens the magnetic field of the erupting CME-flux rope.

In Figure 11, we show a schematic representation (viewed from solar west) of the MAB scenario for the production of the broad CMEs resulting from our three homologous compact major blowout-eruption solar flares. In Figure 11(a), we show the large-scale field (see white field lines in Figures 3(c) and 4(b)–(c)), which has one end rooted in the DPR, while the other end terminates at a part of the large leading negative sunspot of the AR and at a negative flux region situated north of the compact mixed-polarity region (labeled as "core" in Figure 3(b)). The large leading negative sunspot of the AR is denoted by circles with double negative signs. The large field lines connecting the DPR and the AR essentially form an MA. The open field lines (see pink field lines in Figures 3(a), (c), and 4(b)–(c)) originate from the large negative sunspot in the adjacent neighborhood of the MA. In Figure 11(a), on the right of the large negative sunspot, we show the positive polarity of the compact region, which hosts the compact arcade (CA; see green field lines in Figure 8) enveloping the flux rope. On the right of the CA we show another set of field lines; these connect to a distant dispersed negative polarity region, situated north of the compact mixed-polarity region (see panels (b) and

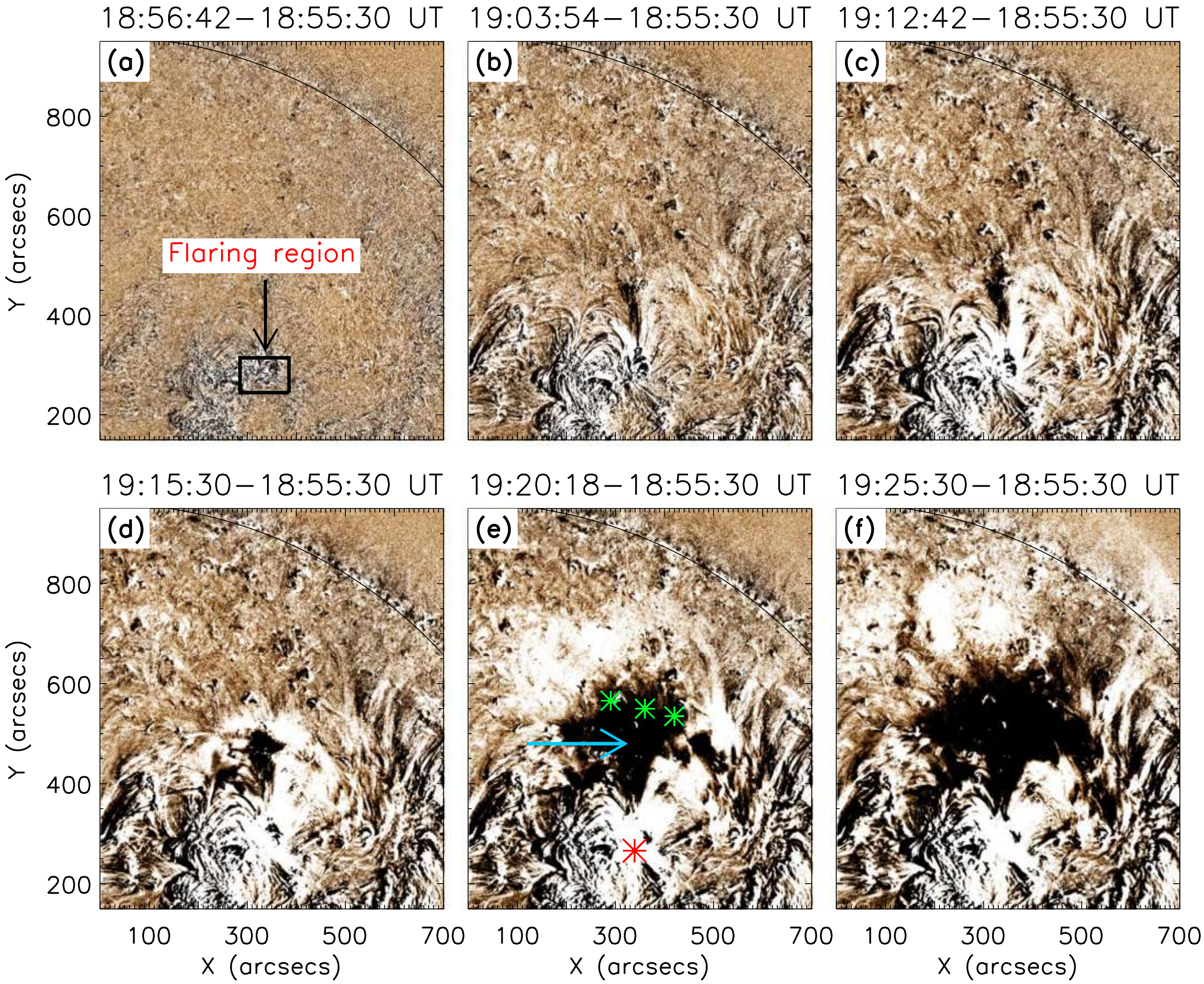

Figure 9. Panels (a)–(f): a sequence of AIA 193 Å fixed-difference images showing the coronal dimming accompanying the large-scale eruptions for the case of event I. An image before the start of the flare (at 18:55:30 UT) is subtracted from all the subsequent images. In panel (a), we mark the flaring region by a box. Panel (c) approximately denotes the start of the flare (see Figure 5(a)). In panel (d), we observe the appearance of slight dimming adjacent to the flaring region. Panel (e) shows the subsequent growth of the dimming, which is marked by an arrow. We indicate the center of the flaring region with a red star and a part of the DPR with green stars. These marked locations denote the footpoints of the large-scale field lines (i.e., MA) involved in the formation of broad CMEs (see Figures 3(b)–(c)). Panel (f) shows a later image, in which the dimming has expanded. An animation of this figure is available. The animation shows the eruptions in AIA 193 Å fixed-difference images along with the GOES light curves for all the events. The animation runs from 18:33 UT on 2014 March 28 to 18:33 UT on 2014 March 29. The real-time duration is 20 s.

(An animation of this figure is available.)

(f) of Figures 5–7). The eruption of the flux rope induces reconnection (i.e., external reconnection) between the CA and MA field lines. Another reconnection, which is standard flare reconnection (i.e., internal reconnection) will ensue between the legs of the field lines stretched by the erupting flux rope. The plausible reconnection sites are marked by cross signs (Figures 11(a)–(b)) and the post-reconnection loops are drawn in red in Figures 11(b)–(c). The reconnection weakens the MA field lines gradually and creates a "pathway" for the subsequent eruption of the flux rope. The eruption of the flux rope continues along the curve of the large MA loops. As this process continues, the flux rope eventually blows out the large MA loops, making the strong dimming region (indicated in Figure 11(c)) extend from the AR up to the DPR (observed to form northward of the AR; see Figures 9–10). The extent of the dimming region demarcates the lateral section of the MA that gets blown out and results in the broad CME structure. In Figure 11(c), we indicate two sets (S1 and S2) of post-reconnection field lines, where the observations indicate that S1 is larger in size than S2, since the negative footpoint of S1 connects to a relatively distant region compared to S2 (see panels (b) and (f) of Figures 5–7). The brightness along the outer footpoints of the S1 field lines is observationally confirmed by a wide circular ribbon structure that is clearly visible during the peak of the flares (see panels (d) and (h) of Figures 5–7). The S2 field lines exhibit themselves as relatively compact postflare loop arcades (indicated by the red arrow in Figure 5(d); see also Figure 5(h), and panels (d) and (h) of

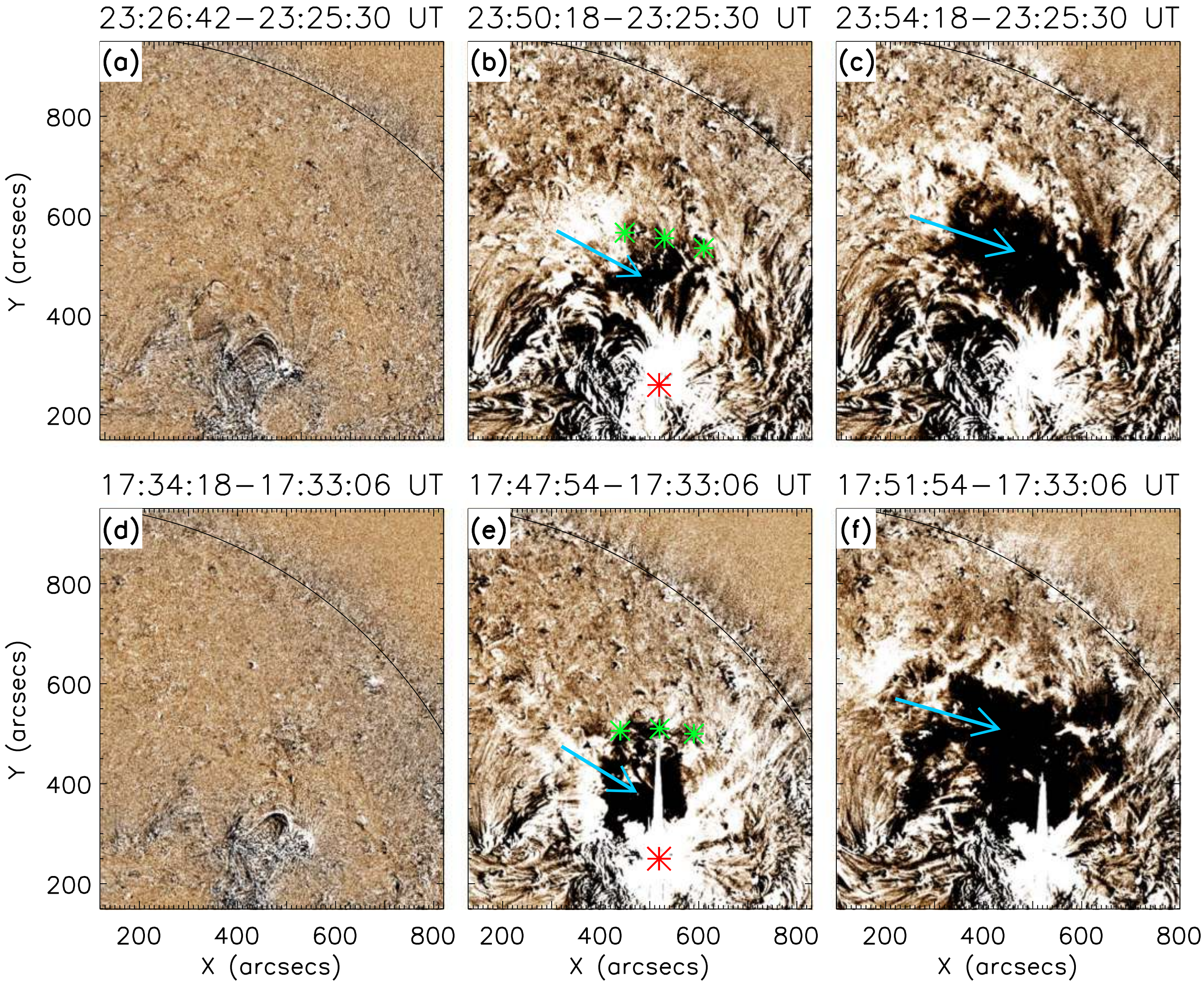

Figure 10. Panels (a)–(c): the eruptions from the core region and subsequent appearance of coronal dimming for event II, observed in 193 Å fixed-difference images. The dimmings are indicated in panels (b)–(c) by arrows. Panels (d)–(f): the post-eruption coronal features are depicted in 193 Å fixed-difference images for event III. The dimmings are indicated in panels (e)–(f) by arrows. In panels (b) and (e), we mark the center of the flaring region with red stars and a part of the DPR with green stars. These marked locations are essentially the footpoints of the large-scale field lines (i.e., MA), whose blowout eruption resulted in the formation of broad CMEs.

Figures 6–7), appearing within the circular ribbon periphery. As the eruption of the flux rope continues, it is channeled along the MA structure. Thus, the flux rope experiences substantial deviation from its original path, as the eruption proceeds. This kind of lateral deflection during the eruption was also observed in previous studies of "over-and-out" type CMEs (Jiang et al. 2009; Yang et al. 2011, 2012a, 2012b). We observe large surges from the flaring region after the eruption of the flux ropes in all the events. The surges, consisting of cool plasma expelled from the flaring region, nearly follow the open field lines shown in Figures 3(c), 4, and 11. Notably, a significant portion of the surge erupted from the eastern part of the flaring region for event I and from the western part for the subsequent events, which is likely due to the changes in the magnetic configurations of the flaring region.

Between our study and the study of Moore & Sterling (2007), there are some similarities as well as dissimilarities in terms of the pre-eruptive configuration of different observational features detected, but in both cases the central idea involving the physics of eruption remains the same. Unlike the eruption in Moore & Sterling (2007), the eruptions in our analysis do not occur in the foot of one leg of a large MA in the base of a large streamer; another difference is that our CMEs have greater angular widths than did the Moore & Sterling (2007) CME. On the other hand, our case and the Moore & Sterling (2007) paper have critical similarities, e.g., both studies have compact ejective flares seated at one foot of a large MA, and in both cases the origin of the CMEs occurred laterally far offset from the flare site. In view of this, we note that our analysis presents important observational evidence of the MAB scenario for CME formation resulting from homologous compact major blowout-eruption solar flares. Our work essentially generalizes the MAB mechanism formulated in Moore & Sterling (2007) to more general cases, including cases with homologous flares.

To summarize, our study incorporates a comprehensive analysis of three homologous ejective eruptive events triggered by a sequence of three compact flux rope eruptions and

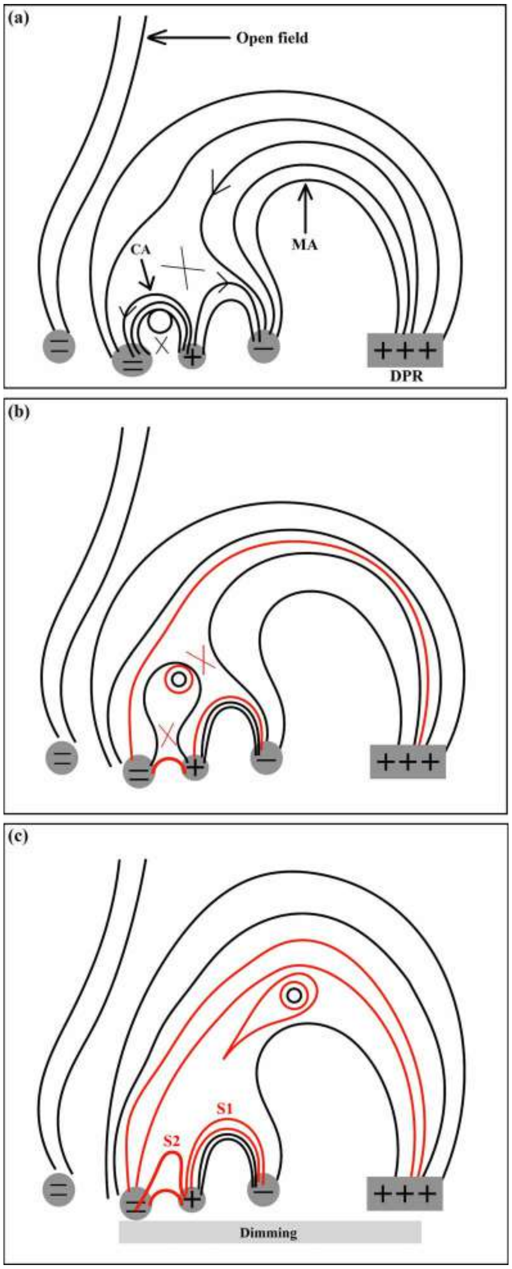

Figure 11. Schematic representation of the MAB scenario for the production of broad CMEs resulting from homologous compact major blowout eruptions, viewed from solar west. Panel (a): the large MA connects the DPR and the negative flux region of the AR. The large negative sunspot of the AR is denoted by circles with double negative signs, from where the open field lines also originate. On the right of the large sunspot, we show a compact bipolar region hosting the compact arcade (CA), enveloping the flux rope. On the right of CA, we show another set of field lines, which connect the compact region and a larger negative flux region, situated north of the compact region (see panels (b) and (f) of Figures 5–7). The plausible reconnection sites are marked by cross signs. Panel (b): the reconnection between CA and MA, weakens the MA field lines and creates a pathway for the eruption of the flux rope. Panel (c): the external reconnection between CA and MA produces the set of field lines labeled S1, and the internal reconnection between the legs of the field lines stretched by the erupting flux rope creates the set of field lines labeled S2. The brightening in the outer footpoints of the S1 field lines is observationally confirmed by the wide circular ribbon structure, whereas the S2 field lines exhibit themselves as compact postflare loop arcades (see panels (d) and (h) of Figures 5–7). The extent of the dimming resulting from the blowout eruption of MA is also indicated in panel (c).

subsequent blowout of three broad CMEs. The eruptions produce flares of successively increasing intensities (M2.0, M2.6, and X1.0), and generate large-scale EUV dimmings. The occurrence of homologous and broad CMEs has important consequences for space weather conditions. A comprehensive understanding of such events and their generation mechanism is vital as the space age progresses.

A.C.S. and R.L.M. acknowledge support from the NASA HGI and HSR programs. The authors would like to thank the SDO and SOHO teams for their open data policy. SDO (2010–present) is NASA's mission under the Living With a Star (LWS) program. SOHO (1995–present) is a joint project of international cooperation between the ESA and NASA. We thank the anonymous referee for providing insightful comments and suggestions, which improved the presentation and overall quality of the article.

Software: SolarSoftWare (Freeland & Handy 2012), VAPOR (Clyne et al. 2007).

ORCID iDs

Suraj Sahu https://orcid.org/0000-0001-8377-8640
Bhuwan Joshi https://orcid.org/0000-0001-5042-2170
Alphonse C. Sterling https://orcid.org/0000-0003-1281-897X
Prabir K. Mitra https://orcid.org/0000-0002-0341-7886
Ronald L. Moore https://orcid.org/0000-0002-5691-6152

References

Asai, A., Ishii, T. T., Kurokawa, H., Yokoyama, T., & Shimojo, M. 2003, ApJ, 586, 624
Aulanier, G., Janvier, M., & Schmieder, B. 2012, A&A, 543, A110
Aulanier, G., Pariat, E., & Démoulin, P. 2005, A&A, 444, 961
Aulanier, G., Pariat, E., Démoulin, P., & DeVore, C. R. 2006, SoPh, 238, 347
Aulanier, G., Török, T., Démoulin, P., & DeLuca, E. E. 2010, ApJ, 708, 314
Bemporad, A., Sterling, A. C., Moore, R. L., & Poletto, G. 2005, ApJL, 635, L189
Benz, A. O. 2008, LRSP, 5, 1
Brueckner, G. E., Howard, R. A., Koomen, M. J., et al. 1995, SoPh, 162, 357
Cai, Z. M., Zhang, Q. M., Ning, Z. J., Su, Y. N., & Ji, H. S. 2021, SoPh, 296, 61
Carmichael, H. 1964, in Proc. AAS-NASA Symp. 50, The Physics of Solar Flares, ed. W. M. Hess, Vol. 50 (Washington, DC: NASA), 451
Chandra, R., Schmieder, B., Aulanier, G., & Malherbe, J. M. 2009, SoPh, 258, 53
Chatterjee, P., & Fan, Y. 2013, ApJL, 778, L8
Chen, Y. 2013, ChSBu, 58, 1599
Chertok, I. M., Grechnev, V. V., Hudson, H. S., & Nitta, N. V. 2004, JGRA, 109, A02112
Chintzoglou, G., Zhang, J., Cheung, M. C. M., & Kazachenko, M. 2019, ApJ, 871, 67
Clyne, J., Mininni, P., Norton, A., & Rast, M. 2007, NJPh, 9, 301
Demoulin, P., Bagala, L. G., Mandrini, C. H., Henoux, J. C., & Rovira, M. G. 1997, A&A, 325, 305
Dere, K. P., Brueckner, G. E., Howard, R. A., et al. 1997, SoPh, 175, 601
Devi, P., Joshi, B., Chandra, R., et al. 2020, SoPh, 295, 75
Domingo, V., Fleck, B., & Poland, A. I. 1995, SSRv, 72, 81
Fan, Y., & Gibson, S. E. 2007, ApJ, 668, 1232
Fisk, L. A. 2005, ApJ, 626, 563
Fletcher, L., & Hudson, H. S. 2002, SoPh, 210, 307
Freeland, S. L., & Handy, B. N. 2012, SolarSoft: Programming and Data Analysis Environment for Solar Physics, Astrophysics Source Code Library, ascl:1208.013
Gallagher, P. T., & Long, D. M. 2011, SSRv, 158, 365
Georgoulis, M. K., Nindos, A., & Zhang, H. 2019, RSPTA, 377, 20180094

Gopalswamy, N., & Thompson, B. J. 2000, JASTP, 62, 1457
Gou, T., Liu, R., Kliem, B., Wang, Y., & Veronig, A. M. 2019, SciA, 5, 7004
Green, L. M., Kliem, B., & Wallace, A. J. 2011, A&A, 526, A2
Green, L. M., Matthews, S. A., van Driel-Gesztelyi, L., Harra, L. K., & Culhane, J. L. 2002, SoPh, 205, 325
Green, L. M., Török, T., Vršnak, B., Manchester, W., & Veronig, A. 2018, SSRv, 214, 46
Harrison, R. A. 1995, A&A, 304, 585
Hirayama, T. 1974, SoPh, 34, 323
Janvier, M., Aulanier, G., Bommier, V., et al. 2014, ApJ, 788, 60
Jiang, C., Feng, X., Liu, R., et al. 2021, NatAs, 5, 1126
Jiang, Y., Yang, J., Zheng, R., Bi, Y., & Yang, X. 2009, ApJ, 693, 1851
Jing, J., Chae, J., & Wang, H. 2008, ApJL, 672, L73
Joshi, B., Ibrahim, M. S., Shanmugaraju, A., & Chakrabarty, D. 2018, SoPh, 293, 107
Joshi, B., Kushwaha, U., Veronig, A. M., et al. 2017a, ApJ, 834, 42
Joshi, B., Veronig, A., Cho, K. S., et al. 2009, ApJ, 706, 1438
Joshi, N. C., Joshi, B., & Mitra, P. K. 2021, MNRAS, 501, 4703
Joshi, N. C., Sterling, A. C., Moore, R. L., & Joshi, B. 2020, ApJ, 901, 38
Joshi, N. C., Sterling, A. C., Moore, R. L., Magara, T., & Moon, Y.-J. 2017b, ApJ, 845, 26
Kharayat, H., Joshi, B., Mitra, P. K., Manoharan, P. K., & Monstein, C. 2021, SoPh, 296, 99
Kleint, L., Battaglia, M., Reardon, K., et al. 2015, ApJ, 806, 9
Kopp, R. A., & Pneuman, G. W. 1976, SoPh, 50, 85
Kushwaha, U., Joshi, B., Cho, K.-S., et al. 2014, ApJ, 791, 23
Lemen, J. R., Title, A. M., Akin, D. J., et al. 2012, SoPh, 275, 17
Li, Y., Ding, M. D., Qiu, J., & Cheng, J. X. 2015, ApJ, 811, 7
Liu, C., Deng, N., Liu, R., et al. 2015, ApJL, 812, L19
Liu, L., Wang, Y., Liu, R., et al. 2017, ApJ, 844, 141
Long, D. M., Bloomfield, D. S., Gallagher, P. T., & Pérez-Suárez, D. 2014, SoPh, 289, 3279
Longcope, D. W. 2005, LRSP, 2, 7
Mason, J. P., Woods, T. N., Caspi, A., Thompson, B. J., & Hock, R. A. 2014, ApJ, 789, 61
Masson, S., Aulanier, G., Pariat, E., & Klein, K. L. 2012, SoPh, 276, 199
Masson, S., Pariat, E., Aulanier, G., & Schrijver, C. J. 2009, ApJ, 700, 559
Mitra, P. K., & Joshi, B. 2021, MNRAS, 503, 1017
Mitra, P. K., Joshi, B., & Prasad, A. 2020, SoPh, 295, 29
Mitra, P. K., Joshi, B., Prasad, A., Veronig, A. M., & Bhattacharyya, R. 2018, ApJ, 869, 69
Moore, R. L., & Sterling, A. C. 2007, ApJ, 661, 543
Moore, R. L., Sterling, A. C., Hudson, H. S., & Lemen, J. R. 2001, ApJ, 552, 833
Moore, R. L., Sterling, A. C., & Suess, S. T. 2007, ApJ, 668, 1221
Owens, M., Lockwood, M., Macneil, A., & Stansby, D. 2020, SoPh, 295, 37
Pallavicini, R., Serio, S., & Vaiana, G. S. 1977, ApJ, 216, 108
Pesnell, W. D., Thompson, B. J., & Chamberlin, P. C. 2012, SoPh, 275, 3
Pontin, D. I., Bhattacharjee, A., & Galsgaard, K. 2007, PhPl, 14, 052106
Prasad, A., Dissauer, K., Hu, Q., et al. 2020, ApJ, 903, 129
Priest, E. R., & Pontin, D. I. 2009, PhPl, 16, 122101
Rappazzo, A. F., Matthaeus, W. H., Ruffolo, D., Servidio, S., & Velli, M. 2012, ApJL, 758, L14
Reinard, A. A., & Biesecker, D. A. 2008, ApJ, 674, 576
Sahu, S., Joshi, B., Mitra, P. K., Veronig, A. M., & Yurchyshyn, V. 2020, ApJ, 897, 157
Savcheva, A., Pariat, E., McKillop, S., et al. 2015, ApJ, 810, 96
Schou, J., Scherrer, P. H., Bush, R. I., et al. 2012, SoPh, 275, 229
Schrijver, C. J., Aulanier, G., Title, A. M., Pariat, E., & Delannée, C. 2011, ApJ, 738, 167
Schrijver, C. J., & De Rosa, M. L. 2003, SoPh, 212, 165
Schwenn, R. 2006, LRSP, 3, 2
Shibata, K. 1999, in Proc. Nobeyama Symp., Solar Physics with Radio Observations, ed. T. S. Bastian, N. Gopalswamy, & K. Shibasaki, 381
Shibata, K., & Magara, T. 2011, LRSP, 8, 6
Sterling, A. C., & Hudson, H. S. 1997, ApJL, 491, L55
Sterling, A. C., & Moore, R. L. 2005, ApJ, 630, 1148
Sterling, A. C., Moore, R. L., Falconer, D. A., & Knox, J. M. 2014, ApJL, 788, L20
Sterling, A. C., Moore, R. L., & Harra, L. K. 2011, ApJ, 743, 63
Sturrock, P. A. 1966, Natur, 211, 695
Sun, X., Hoeksema, J. T., Liu, Y., et al. 2013, ApJ, 778, 139
Švestka, Z., & Cliver, E. W. 1992, in IAU Colloq. 133, Eruptive Solar Flares, ed. Z. Švestka, B. V. Jackson, & M. E. Machado (New York: Springer), 1
Temmer, M., Veronig, A. M., Kontar, E. P., Krucker, S., & Vršnak, B. 2010, ApJ, 712, 1410
Thompson, B. J., & Myers, D. C. 2009, ApJS, 183, 225
Toriumi, S., & Wang, H. 2019, LRSP, 16, 3
Török, T., Panasenco, O., Titov, V. S., et al. 2011, ApJL, 739, L63
Vršnak, B. 2003, in Energy Conversion and Particle Acceleration in the Solar Corona, ed. L. Klein, Vol. 612 (New York: Springer), 28
Wang, H., & Liu, C. 2012, ApJ, 760, 101
Wang, H., Liu, C., Deng, N., et al. 2014, ApJL, 781, L23
Wang, Y., & Zhang, J. 2007, ApJ, 665, 1428
Warren, H. P., O'Brien, C. M., & Sheeley, N. R. J. 2011, ApJ, 742, 92
Webb, D. F., & Howard, T. A. 2012, LRSP, 9, 3
Wheatland, M. S., Sturrock, P. A., & Roumeliotis, G. 2000, ApJ, 540, 1150
Wiegelmann, T. 2004, SoPh, 219, 87
Wiegelmann, T. 2008, JGRA, 113, A03S02
Woods, M. M., Inoue, S., Harra, L. K., et al. 2018, ApJ, 860, 163
Yang, J., Jiang, Y., Bi, Y., et al. 2012a, ApJ, 749, 12
Yang, J., Jiang, Y., Zheng, R., et al. 2011, SoPh, 270, 551
Yang, J., Jiang, Y., Zheng, R., et al. 2012b, ApJ, 745, 9
Yang, K., Guo, Y., & Ding, M. D. 2016, ApJ, 824, 148
Young, P. R., Tian, H., & Jaeggli, S. 2015, ApJ, 799, 218
Zhang, J., Cheng, X., & Ding, M.-D. 2012, NatCo, 3, 747
Zhang, J., Dere, K. P., Howard, R. A., Kundu, M. R., & White, S. M. 2001, ApJ, 559, 452
Zhang, J., & Wang, J. 2002, ApJL, 566, L117

The Astrophysical Journal, 943:70 (16pp), 2023 February 1 https://doi.org/10.3847/1538-4357/acac2d

Evolution of Magnetic Fields and Energy Release Processes during Homologous Eruptive Flares

Suraj Sahu[1,2], Bhuwan Joshi[1], Avijeet Prasad[3,4], and Kyung-Suk Cho[5,6]
[1] Udaipur Solar Observatory, Physical Research Laboratory, Dewali, Badi Road, Udaipur-313 001, Rajasthan, India; suraj@prl.res.in, sahusuraj419@gmail.com
[2] Discipline of Physics, Indian Institute of Technology Gandhinagar, Palaj, Gandhinagar-382 355, Gujarat, India
[3] Rosseland Centre for Solar Physics, University of Oslo, Postboks 1029, Blindern NO-0315, Oslo, Norway
[4] Institute of Theoretical Astrophysics, University of Oslo, Postboks 1029, Blindern NO-0315, Oslo, Norway
[5] Space Science Division, Korea Astronomy and Space Science Institute, Daejeon 305-348, Republic of Korea
[6] Department of Astronomy and Space Science, University of Science and Technology, Daejeon 305-348, Republic of Korea
Received 2022 July 15; revised 2022 November 30; accepted 2022 December 7; published 2023 January 27

Abstract

We explore the processes of the repetitive buildup and the explosive release of magnetic energy, together with the formation of magnetic flux ropes, which eventually resulted in three homologous eruptive flares of successively increasing intensities (i.e., M2.0, M2.6, and X1.0). The flares originated from NOAA active region 12017 between 2014 March 28 and 29. EUV observations and magnetogram measurements, together with coronal magnetic field modeling, suggest that the flares were triggered by the eruption of flux ropes that were embedded in a densely packed system of loops within a small part of the active region. In X-rays, the first and second events show similar evolutions, with single compact sources, while the third event exhibits multiple emission centroids, with a set of strong nonthermal conjugate sources at 50–100 keV during the hard X-ray peak. Over an interval of $\approx$ 44 hr, the photospheric magnetic field encompassing the three flares undergoes important phases of emergence and cancellation, together with significant changes near the polarity inversion lines within the flaring region. Our observations point toward the tether-cutting mechanism being the plausible triggering process of the eruptions. Between the second and third events, we observe a prominent phase of flux emergence that temporally correlates with the buildup phase of free magnetic energy in the active region corona. In conclusion, our analysis reveals efficient coupling between the rapidly evolving photospheric and coronal magnetic fields in the active region, leading to a continued phase of the buildup of free energy, which results in the homologous flares of successively increasing intensities.

Unified Astronomy Thesaurus concepts: Solar coronal mass ejections (310); Solar flares (1496); Solar magnetic flux emergence (2000); Solar x-ray emission (1536)

Supporting material: animations

1. Introduction

Solar flares are sudden explosive events in the solar atmosphere that release huge amounts of energy, in the form of heat, radiation, and bulk plasma motion, and produce highly accelerated charged particles (Fletcher et al. 2011; Benz 2017). It is widely believed that the fundamental processes that drive an eruptive event—the buildup/storage of free magnetic energy and its explosive release via magnetic reconnection—are inherently guided by the complexity of the solar magnetic fields (Priest & Forbes 2002). Therefore, in order to understand the drivers of solar flares and their associated processes, it is important to analyze the variability in the buildup and release of magnetic energy. Solar eruptive phenomena involve the expulsion of magnetized plasma out into the heliosphere. Hence, in order to understand the dynamics of the magnetized plasma during and after the explosive energy release, we need to explore multiwavelength and multi-instrument data, together with coronal magnetic field modeling.

The regions of the Sun with the strongest magnetic fields are known as solar active regions (ARs). These ARs present diverse natures in terms of their morphology, depending upon the distribution and strength of the underlying photospheric magnetic fields (Toriumi & Wang 2019). Typically, during the growth phase, as an AR expands and evolves, the complexity of the photospheric magnetic fields increases. A complex AR may produce several energetic events—such as flares, coronal mass ejections (CMEs), jets, prominence eruptions, etc.—over its whole lifetime (Joshi et al. 2018; Mitra et al. 2018, 2020b; Sahu et al. 2020; Zuccarello et al. 2021).

Solar eruptions may originate in a repetitive manner from the same location of the AR, and sometimes they can show morphological resemblances in their multiwavelength imaging and coronagraphic observations. Such repetitive activities are known as "homologous eruptions" (Woodgate et al. 1984; Zhang & Wang 2002). Exploring homologous eruptions is extremely important for understanding the role of the photospheric magnetic field variations and associated coronal changes in determining the eruptivity. In this way, by assessing the homology tendency of an AR, we can provide important inputs for understanding the onset of CMEs and subsequent space weather consequences. In the past, several studies of different features of homologous eruptions have been carried out, revealing the following aspects to be responsible for the occurrence of homologous activity: flux emergence (Nitta & Hudson 2001; Chatterjee & Fan 2013), shearing motions and magnetic flux cancellation (Li et al. 2010; Vemareddy 2017), the persistent photospheric horizontal motion of the magnetic structure along the polarity inversion line (PIL; Romano et al. 2015, 2018), and the coronal null point configuration (DeVore & Antiochos 2008), among others. Homologous solar eruptions form a contemporary topic of research in solar physics, and the present study aims to provide additional observational inputs in this direction.

In this study, we present detailed evolutions of the photospheric magnetic fields that were associated with three homologous eruptive flares that occurred between 2014 March 28 and 29 in the NOAA AR 12017. Interestingly, these three homologous events are of successively increasing intensities (M2.0, M2.6, and X1.0). In our previous study (Sahu et al. 2022), we explored the formation processes of three homologous broad CMEs that resulted from these three eruptive flares. We have identified the events as flux rope eruptions originating from the same compact flaring region (FR) of the AR. Our work has presented a clear example of a large-scale coronal magnetic configuration that has been repeatedly blown out by compact flux rope eruptions, leading to a series of broad CMEs. The flaring activities in AR 12017, especially the X-class event on 2014 March 29, have been subjected to various studies involving observational and modeling analyses (Kleint et al. 2015; Li et al. 2015; Liu et al. 2015; Young et al. 2015; Yang et al. 2016; Woods et al. 2017, 2018; Cheung et al. 2019). Liu et al. (2015) discussed a scenario of asymmetric filament eruption, in the context of nonuniform filament confinement and an MHD instability prior to the X-flare. The study by Yang et al. (2016) comprised all the flaring activities in the AR between 2014 March 28 and 29. They concluded that the flares were mainly triggered by the kink instability of the associated filaments. Woods et al. (2018) investigated the triggering mechanism of the third event (the X1.0 flare) and the associated filament eruption. Their study confirmed the existence of two flux ropes within the AR prior to the flaring. Interestingly, one of these two flux ropes erupted, which may have been due to the tether-cutting reconnection (Moore et al. 2001), allowing the flux rope to rise to a torus unstable region. In this paper, our motivation is to conduct a detailed study in order to understand the repetitive buildup of magnetic energy and flux ropes that eventually drive the three homologous eruptive flares. Toward this, we provide a quantitative estimation of the temporal evolution of the free magnetic energy in the AR, and we examine precisely the changes in photospheric magnetic flux over the entire period of the homologous flaring activity. We further present a detailed multiwavelength investigation of the temporal, spatial, and spectral characteristics of each event. In Section 2, we provide a brief discussion of the data sources and analysis techniques. Section 3 gives the details of the EUV and X-ray observations of the flares. In Section 4, we describe the evolutions of the photospheric magnetic fields during the events, as well as the associated coronal magnetic configuration. The buildup of the photospheric current in relation to the triggering of the eruptions is presented in Section 5. The evolutionary stages of the eruptive hot plasma structures are presented in Section 6. The details of the storage and release processes of the free magnetic energy are described in Section 7. We discuss and interpret our results in the final section.

2. Observational Data Sources and Techniques

We use data from the Atmospheric Imaging Assembly (AIA; Lemen et al. 2012) on board the Solar Dynamics Observatory (SDO; Pesnell et al. 2012) for EUV imaging and analysis. AIA observes the full disk of the Sun in seven EUV (94 Å, 131 Å, 171 Å, 193 Å, 211 Å, 304 Å, and 335 Å), two UV (1600 Å and 1700 Å), and one visible (4500 Å) channels. For our analysis, we use the EUV 304 Å [$\log(T) \approx 4.7$] and 193 Å [$\log(T) \approx 6.2$, 7.3] observations. The 304 Å images provide information about the chromosphere and transition region of the Sun, while the 193 Å images are used to analyze the corona and hot flare plasma. In order to investigate the evolution of the photosphere through line-of-sight (LOS) magnetogram and continuum observations, we obtain data from the Helioseismic Magnetic Imager (HMI; Schou et al. 2012) on board the SDO.

Table 1
The Flares in NOAA AR 12017 between 2014 March 28 and 29

Flare	Flare Class	Date	Time (UT) Start	Peak	End
F1	M2.0	2014 March 28	19:05	19:18	19:27
F2	M2.6	2014 March 28	23:44	23:51	23:58
F3	X1.0	2014 March 29	17:35	17:48	17:54

To visualize the X-ray sources and to quantify the parameters that are associated with the X-ray emission processes, we use data obtained from the Reuven Ramaty High Energy Solar Spectroscopic Imager (RHESSI; Lin et al. 2002). RHESSI observes full-disk solar X-ray sources in the energy range of 3 keV to 17 MeV. We use the CLEAN algorithm (Hurford et al. 2002) to reconstruct the X-ray images in different energy bands (i.e., 3–6, 6–12, 12–25, 25–50, and 50–100 keV). For image reconstruction, we use the front segments of detectors 3–8, with a 20 s integration time. We also carry out X-ray spectroscopy using the RHESSI data. The details of the spectroscopy are given in Section 3.3.

For the calculation of the free magnetic energy associated with the AR in the coronal volume, we need 3D information about the magnetic field above the photosphere. For this purpose, we use the nonlinear force-free field (NLFFF) extrapolation technique, which was originally formulated by Wiegelmann (2008), then further developed by Wiegelmann & Inhester (2010) and Wiegelmann et al. (2012). We use the vector magnetograms (HMI.sharp_cea_720s series) as the photospheric input boundary conditions for the extrapolation. The extrapolation volume extends up to 280, 229, and 183 Mm in the *X*, *Y*, and *Z* directions, respectively, considering the photosphere as the *X*–*Y* plane.

3. Multiwavelength Analysis of Flare Evolution

3.1. Multiwavelength Overview of AR 12017

Our study focuses on three homologous flaring events of successively increasing intensities (M2.0, M2.6, and X1.0). The flares occurred in NOAA AR 12017 between 2014 March 28 and 29. A summary of the flares is given in Table 1, which is based on the GOES flare catalog.[7] The three flares are indicated along with the GOES light curves (in the 1–8 and 0.5–4 Å channels) in Figure 1. The durations of the three flares are marked by the vertical pink stripes. The gray shaded region indicates an interval, when the GOES data were unavailable.

[7] https://www.ngdc.noaa.gov/stp/space-weather/solar-data/solar-features/solar-flares/x-rays/goes/xrs/goes-xrs-report_2014.txt

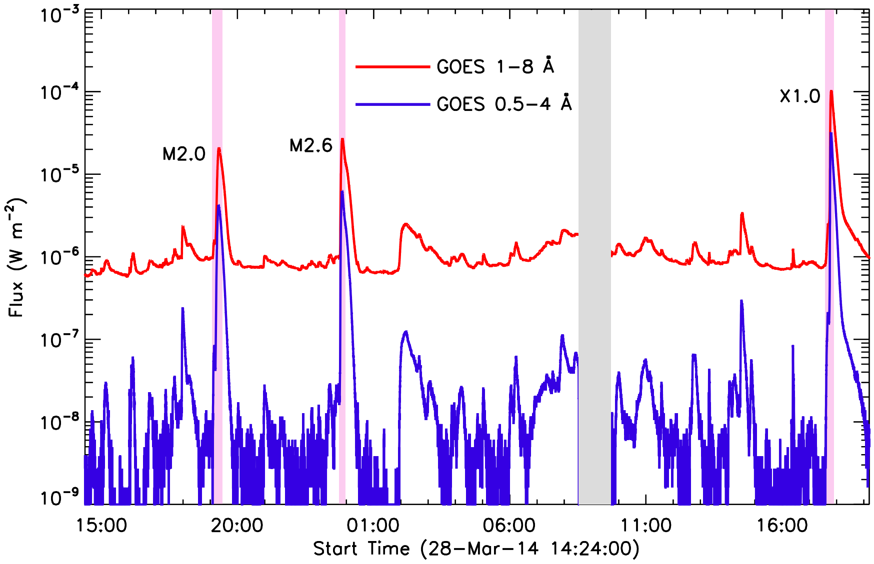

Figure 1. GOES light curves in the 1–8 and 0.5–4 Å channels, showing the three flares (M2.0, M2.6, and X1.0) under analysis. The intervals of the three flares are shown by the pink vertical stripes. The gray shaded region indicates an interval when the GOES data were unavailable.

In Figure 2, we provide a multiwavelength view of AR 12017, by plotting simultaneous white-light continuum, magnetogram, and EUV images, prior to the onset of the first event of M2.0 intensity. By comparing the different panels of Figure 2, one can note many interesting features of the AR and the FR. A comparison of the continuum and magnetogram images (Figures 2(a) and (b)) suggests that the leading part of the AR consists of sunspots of predominantly negative polarity (see the regions enclosed by the boxes in the various panels of Figure 2), which happen to be the source of the eruptive flares under analysis. Hence, we term the region inside the box the FR. On the trailing part of the AR, we observe sparsely located small sunspots with dispersed fluxes of predominantly positive polarity (Figures 2(a) and (b)). The EUV images at 171 and 193 Å readily suggest the existence of large coronal loops connecting the leading and trailing parts of the AR (Figures 2(c) and (d)). The presence of a compact closed-loop configuration in the FR is also clearly visible. In Figure 2(e), we provide a preflare 304 Å image of AR 12017. Here, we can clearly distinguish the dominance of the brighter emission from the FR over the other parts of the AR.

3.2. Temporal and Spatial Aspects

The temporal and spatial evolutions in the EUV 304 Å observations of the M2.0 (F1), M2.6 (F2), and X1.0 (F3) flares are presented in Figures 3, 5, and 6, respectively. In all these figures, panel (a) presents the light curves of the flares, while panels (b)–(g) show their spatial evolutions. The temporal evolutions of the flares have been studied with GOES 1–8 Å, AIA 304 Å, and RHESSI X-ray light curves. We have reconstructed the RHESSI X-ray light curves in various energy bands, viz, 3–6, 6–12, 12–25, 25–50, and 50–100 keV. For F1, we do not show the 50–100 keV light curve, due to the lack of significant X-ray flux above 50 keV. To explore the spatial structures in the FRs and their evolutions at the upper chromospheric level, we plot a few representative AIA 304 Å images, which are overplotted by the RHESSI X-ray sources at various energy bands. We note that the X-ray emission sources at 6–12 keV are exactly cospatial with the lower-energy sources at 3–6 keV, hence they are not shown in these figures. To understand the evolutions of the spatial structures at the flaring corona, we show the EUV 193 Å images in Figures 4(a) to (d) and (e) to (h) and Figure 7 for F1, F2, and F3, respectively.

3.2.1. M2.0 Flare

Before the beginning of the rise phase of F1, we observe a preflare enhancement in the X-ray light curves at ≈19:08 UT. We note that this preflare hump is absent from the AIA 304 Å light curve, which exclusively represents emission from the FR. This observation suggests that this preflare emission is not associated with the flaring event under analysis. We observe plasma eruption from the eastern part of the FR in the form of a collimated stream (as indicated by the arrows in Figures 3(b) and (c)) at the outset of F1 (see the animation attached to Figure 3). At the base of the collimated structure, we note X-ray emission up to 25 keV, as shown by the contours of the different energy bands. During the peak of the flare (≈19:18 UT), the hard X-ray (HXR) source of 25–50 keV appears at the flaring core (shown by the black contours in Figure 3(d)). After the flare's peak, we observe the eruption of cool (i.e., dark) plasma from the western part of the core region (shown by the arrows in Figures 3(e) and (g); see also the attached animation). During this period, the X-ray sources up to 25 keV are observed as a single source, suggesting X-ray production from a compact and dense system of coronal loops. The X-ray sources in the decay phase (Figures 3(f) and (g)) further confirm this scenario, as the X-ray emission is observed to originate above the closely packed postflare loop system.

The evolutionary stages of F1 in the EUV 193 Å images are shown in Figures 4(a) and (d). Prior to the flare, we detect an activated filament (indicated by the arrow in Figure 4(a)), with a clear signature of activity in the form of the brightening at its base. Subsequently, the filament erupts in a jet-like manner (marked by the arrow in Figure 4(b)), with a morphological similarity to the collimated stream observed in the EUV 304 Å images (see Figures 3(b) and (c)). The start of the impulsive rise phase of the flare can be discerned in the form of the extended brightening over

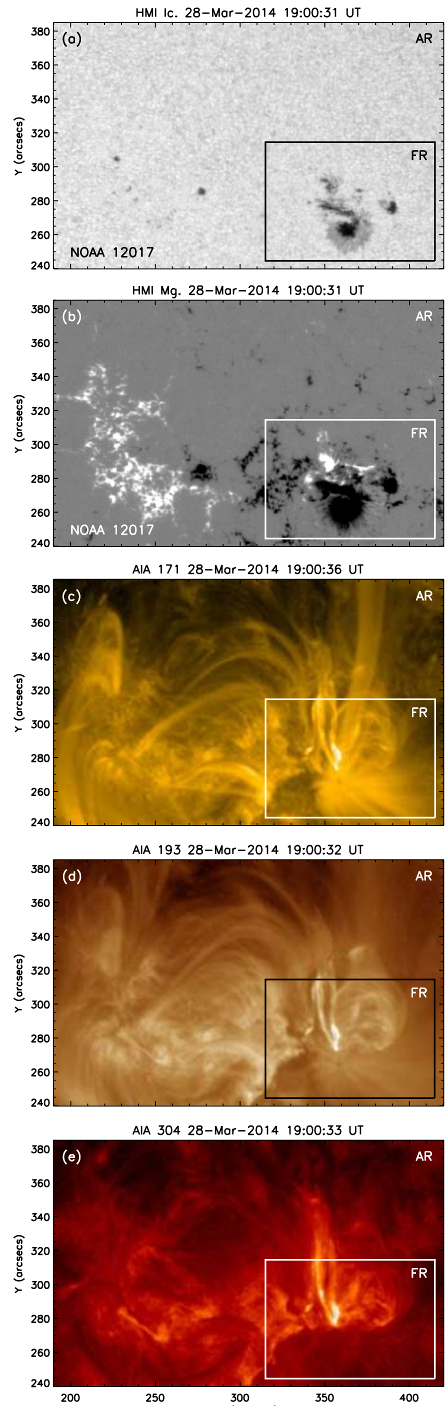

Figure 2. Multiwavelength view of AR 12017 on 2014 March 28 at ≈ 19:00 UT (i.e., 5 minutes before the start of the first flare, according to the GOES data). (a) HMI continuum image of the AR. We observe a large sunspot in the leading part of the AR, which we mark with the black box. The flares in our study occurred within this marked area of the AR, which we term the FR. We indicate the FR with the boxes in all the subsequent panels. (b) HMI LOS magnetogram of the AR. The FR consists of a strong negative-polarity region, together with relatively weaker compact positive polarities, which are located north of it. (c) and (d) AIA 171 Å [$\log(T) \approx 5.7$] and 193 Å [$\log(T) \approx 6.2, 7.3$] images showing the connectivity of the different loop systems between the leading and trailing parts of the AR, along with compact loops within the FR. (e) AIA 304 Å [$\log(T) \approx 4.7$] image displaying the much brighter emission from the FR in comparison to the other parts of the AR.

the FR (Figure 4(c); see also Figure 3(a)). Afterward, we observe the formation of compact postflare loop arcades in the core region (shown by the arrow in Figure 4(d)).

3.2.2. M2.6 Flare

The evolutionary stages of F2 are shown in Figure 5 through the EUV 304 Å image sequences. As with F1, in this case we also observe a single X-ray source throughout the flare evolution. Furthermore, the X-ray sources from lower to higher energies (e.g., 6–12, 12–25, 25–50, and 50–100 keV) are observed to be cospatial. During the peak of the flare (≈ 23:50 UT), the X-ray sources in the energy band of 50–100 keV are observed to appear in the core region (Figure 5(d)). Thereafter, the 50–100 keV source disappears, while the X-ray emission in the lower-energy bands persists (Figures 5(e) and (g)). We note a double-peak structure in the AIA 304 Å light curve during the peak time of the flare (see Figure 5(a)). This double-peak structure suggests two successive episodes of intense brightening, which accompany the eruptions from the eastern and western parts of the FR, respectively (indicated by the arrows in Figures 5(c) and (d); see also the animation attached to Figure 5), which ultimately result in the flaring intensity of the M2.6 class. Notably, the eruptions in this case are not jet-like ejections, as in the case of F1.

In Figures 4(e) to (h), we show the EUV 193 Å images that present the evolutionary stages of F2. Prior to the flare, we observe a bright activated loop system in the core region (indicated by the arrow in Figure 4(e)). This loop structure subsequently erupts (marked by the arrow in Figure 4(f)) in a nearly coherent manner, which also marks the beginning of the impulsive phase of the flare (see Figure 5(a)). Thereafter, the erupting loop system loses its coherency, and we use an arrow to mark its bright eastern part in Figure 4(g). Later on, dense and compact postflare loop arcades are observed to form in the core region (indicated by the arrow in Figure 4(h)).

3.2.3. X1.0 Flare

The evolution of the X1.0 flare (F3) is shown by a few representative AIA 304 Å images in Figures 6(b) to (g). Prior to the impulsive phase of the event, starting at ≈ 17:44 UT, we observe a clear signature of preflare activity persisting for ≈8 minutes (≈17:36–17:44 UT). This preflare phase is discernible in all the X-ray and EUV light curves (Figure 6(a)), and the preflare activity is observed in the AIA images as enhanced brightening, from the western part of the core region, which also emits X-ray sources up to 25 keV (Figures 6(b) and (c)). Thereafter, the X-ray sources evolve at two separate locations, and we observe emission up to 25 keV from both the eastern and western parts of the flaring core region (Figure 6(d)). The X-ray emission in the 6–12 keV energy range persists in the eastern part of the core, whereas the strong emission in the energy range of 25–50 keV is observed as appearing in the western part of the flaring core (Figure 6(e)). During the peak of the HXR light curves, we observe clear X-ray sources in the 50–100 keV energy band. Importantly, this high-energy source presents an elongated structure with two distinct centroids (Figure 6(f)). Subsequently, the X-ray emission up to 50 keV persists, which is observed as a single-source structure in multiple energy bands (Figure 6(g)).

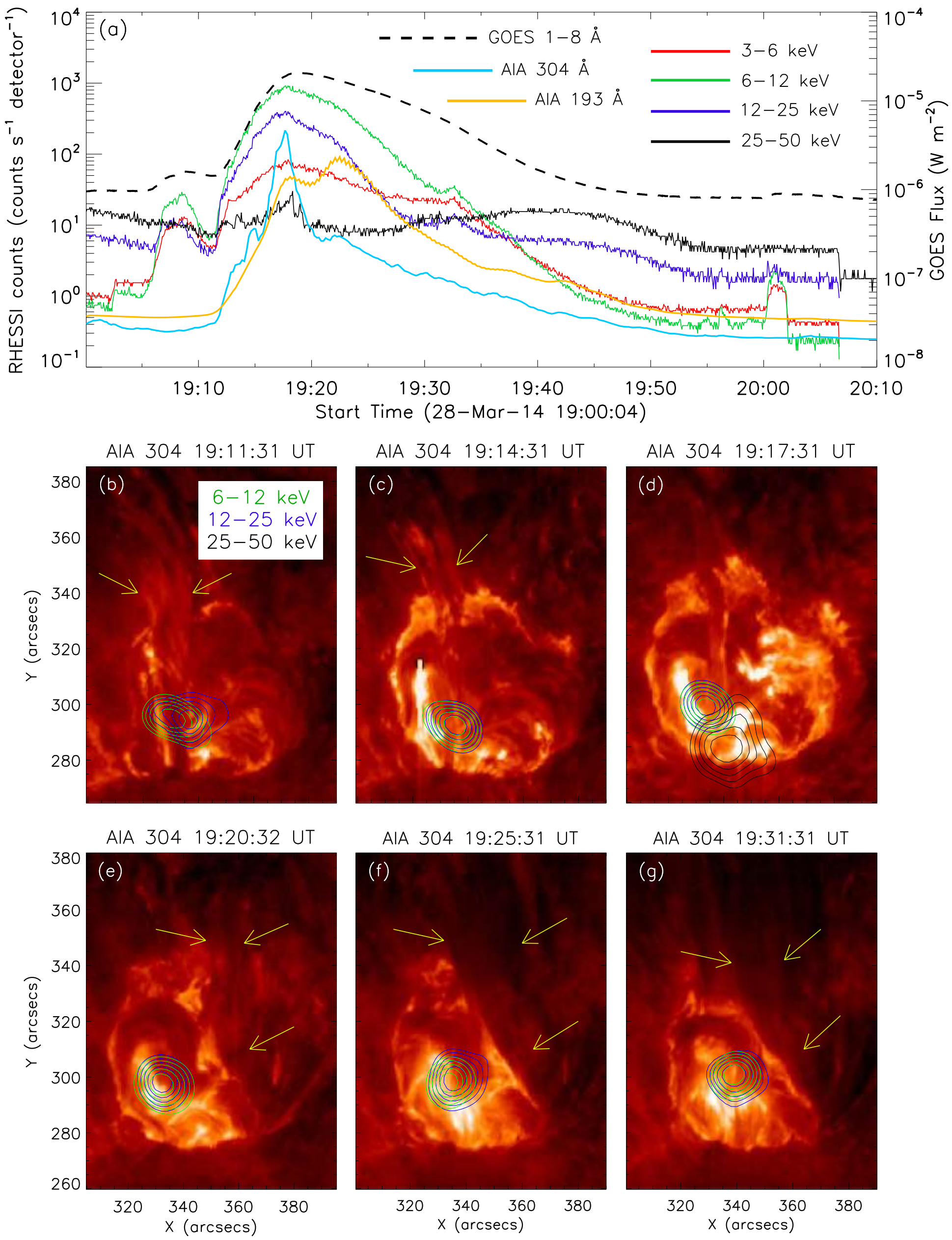

Figure 3. (a) RHESSI X-ray count rates in different energy bands between 3 and 50 keV during the M2.0 event. The GOES flux profile in the 1–8 Å channel and the AIA 193 and 304 Å light curves of the FR are also overplotted. (b)–(g) The evolution of the flare, as shown in AIA 304 Å images. The X-ray contours in 6–12, 12–25, and 25–50 keV are overplotted on the EUV images. The X-ray images are reconstructed by the CLEAN algorithm, with an integration time of 20 s. The contours are drawn at 50%, 60%, 70%, 80%, and 90% of the peak flux in each image. The yellow arrows—except in (d)—indicate the plasma eruptions originating from the core region. An animation is associated with this figure, showing the evolutionary stages of the flare in the AIA 304 Å observations.

(An animation of this figure is available.)

The evolution of F3 in the EUV 193 Å images is presented in Figure 7. Similar to the EUV 304 Å observations, in these images we also observe a clear signature of enhanced brightening, from the western part of the core, revealing the preflare activity (indicated by the arrows in Figures 7(a) and (b)). Subsequently, this preflare enhancement spreads over the whole core region (Figures 7(c) and (d)). During the main phase of the flare, intense widespread flare emissions are observed from the core (Figures 7(e) and (f)). Thereafter, the postflare loop arcades are observed to form (shown by the arrow in Figure 7(g)), which gradually get denser and brighter, before they are observed extending over a large area of the core (marked by the arrow in Figure 7(h)).

3.3. RHESSI X-Ray Spectroscopy

To quantify the thermal and nonthermal components of the X-ray emission during these three flares, we conduct X-ray spectroscopic analysis using RHESSI observations. We generate RHESSI spectra with an energy binning of 1/3 keV from 6 to 15 keV, 1 keV from 15 to 100 keV, and 5 keV from 100 keV onward. We use the front segments of detectors 1–9 (except for detectors 2 and 7, which have a lower energy

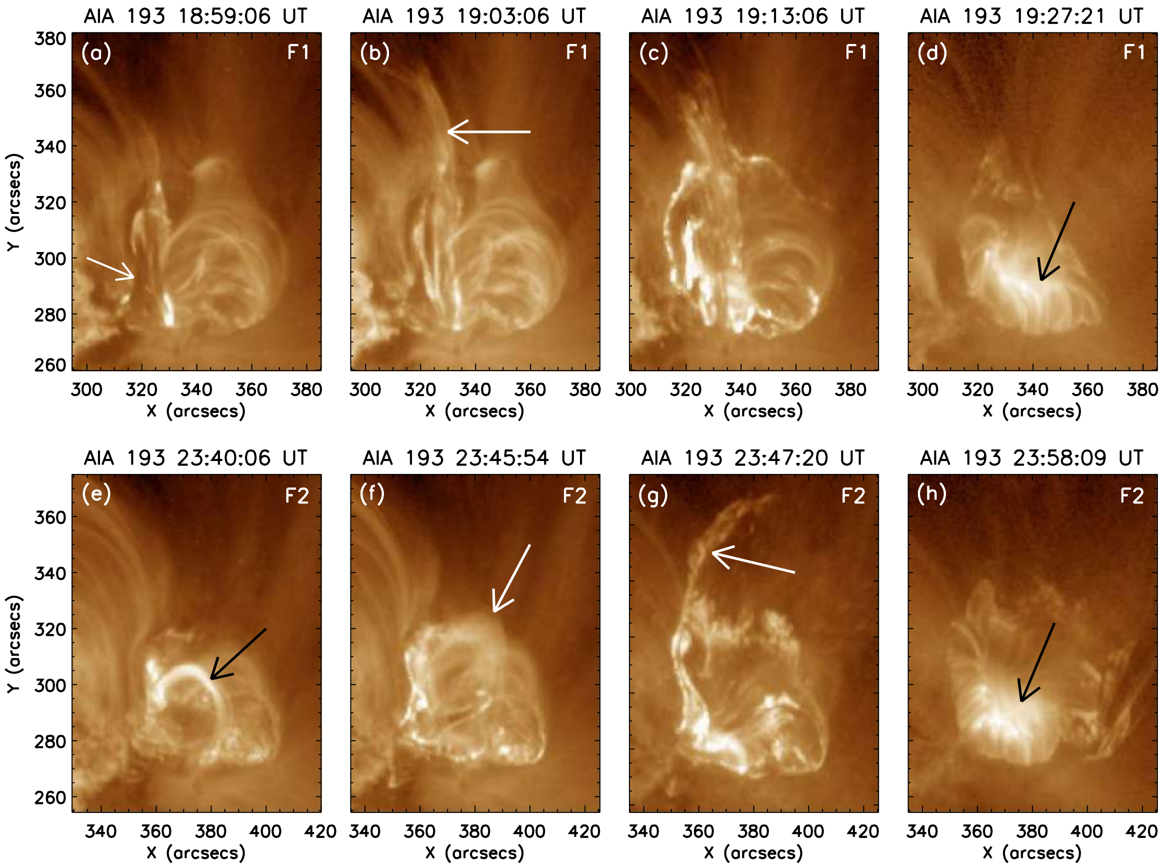

Figure 4. (a)–(d) The evolution of the M2.0 flare (F1) in the AIA 193 Å images. In (a), we use an arrow to indicate an activated filament with clear brightening at its base. (b) The subsequent jet-like eruption of the filament. (c) The extended brightening within the FR, which marks the start of the impulsive phase of the flare. In (d), we use an arrow to indicate the compact postflare loop system. (e)–(h) The evolution of the M2.6 flare (F2) in the AIA 193 Å images. In (e), we use an arrow to mark a bright loop system in the core region observed prior to the flare. This loop system subsequently erupts in a coherent manner, which we indicate with the arrow in (f). Thereafter, the erupting structure evolves noncoherently. We use an arrow to mark the bright eastern part of the erupting structure in (g). In (h), we use an arrow to indicate the compact bright postflare loop arcades.

resolution and a higher threshold energy, respectively). The spectra are deconvolved with the full detector response matrix (i.e., offdiagonal elements are included; Smith et al. 2002). For the thermal fitting, we use an isothermal model constructed using the line spectrum. The nonthermal spectra are fitted using the thick-target bremsstrahlung model (Holman et al. 2003). We derive the temperature (T) and the emission measure (EM) of the hot flaring plasma from the thermal fit, and we derive the electron spectral index (δ) from the nonthermal component.

The results obtained from the spectral fit of the X-ray emission from the FR are presented in Figures 8(a), (b), and (c), for F1, F2, and F3, respectively. For F1, the GOES flare peak ($\approx$ 19:18 UT on 2014 March 28) coincides with the HXR (25–50 keV) peak. A high value of the electron spectral index (i.e., $\delta = 8.7$) indicates a mild nonthermal component of the flaring X-ray emission. During the F2 peak, the electron spectral index decreases to 3.3, indicating a much harder nonthermal spectrum compared to F1. From the thermal spectral fit, we obtain the temperature of the FR as $\approx$25.6 MK, which is higher than the temperature ($\approx$20.9 MK) during the peak of F1. During F3, the hardness of the spectrum remains almost the same as that of F2. However, the EM ($\approx 61 \times 10^{47}$ cm^{-3}) increases by an order of magnitude during F3, as compared to the previous two events (see Figures 8(a) to (c)). This indicates a significant enhancement in the electron density of the hot ($T \approx 26$ MK) plasma within the flaring volume.

4. Structure and Evolution of Magnetic Fields

4.1. Photospheric Magnetic Fields

We analyze the structural and temporal evolutions of the photospheric magnetic fields of the FR in Figure 9. To examine the magnetic flux changes quantitatively, we plot spatial variations of the positive and negative magnetic flux of the region of interest (shown in Figures 9(b) to (m)). In Figure 9(a), we provide the time profiles of the integrated magnetic fluxes through the selected area (see Figures 9(b) to (m)), together with the GOES 1–8 Å soft X-ray (SXR) light curve. The time profiles of the magnetic fluxes are for the period from 00:00 UT on 2014 March 28 to 20:00 UT on 2014 March 29 ($\approx$44 hr), covering all the flare events under analysis. Also, the chosen interval includes a time span of $\approx$19 hr before F1, to examine the buildup of the preflare photospheric flux in detail.

In Figure 9(a), we select six different epochs ($t1$, $t2$, $t3$, $t4$, $t5$, and $t6$) to explore the spatial changes in the photospheric magnetic field distribution. Among these epochs $t3$, $t4$, and $t6$ are selected at the peak time of the flares under analysis. The continuum and LOS magnetogram images during the epochs ($t1$–$t6$) are presented in Figures 9(b)–(m). We observe substantial structural changes in the photospheric magnetic field of the FR over the selected interval of $\approx$44 hr (see Figures 9(b)–(m) and the attached animation).

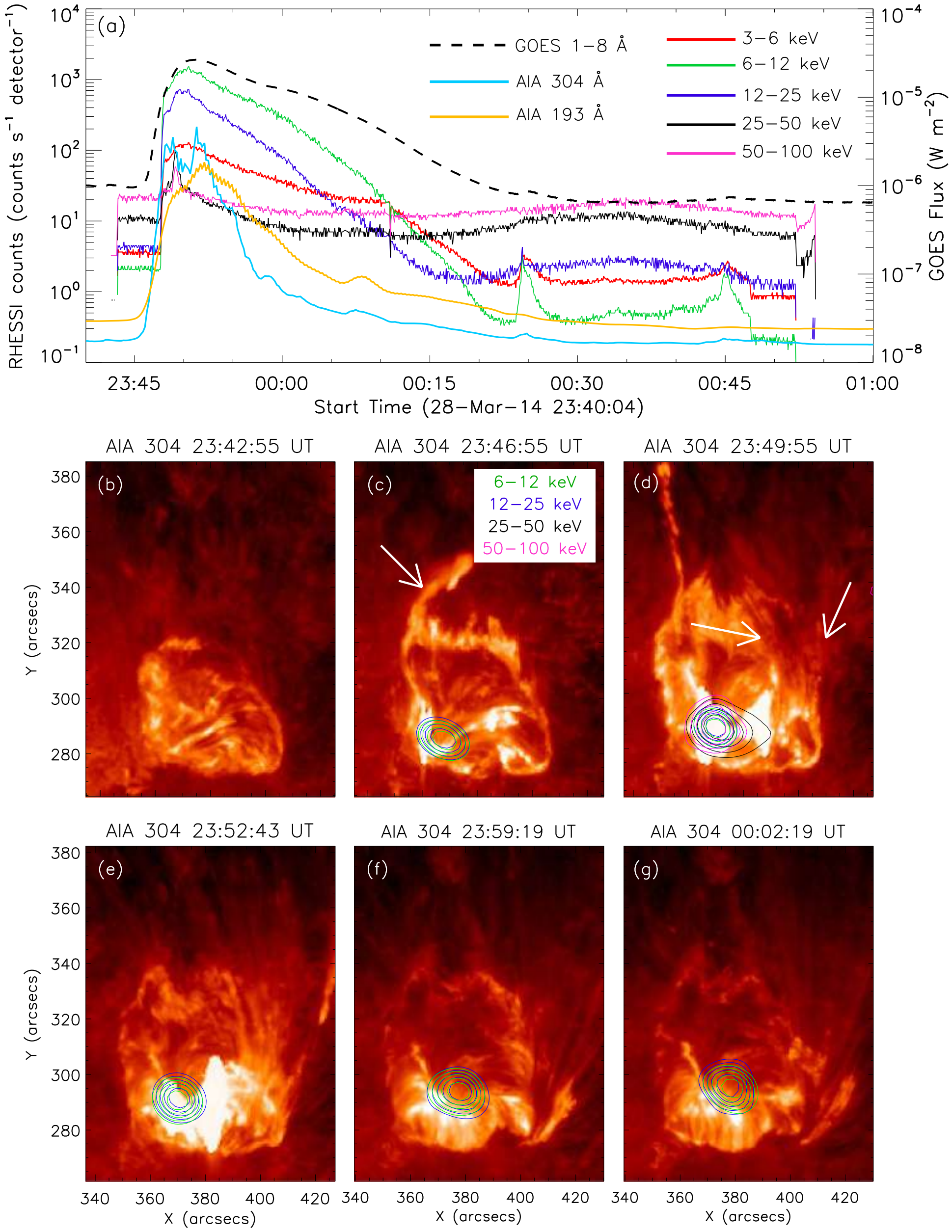

Figure 5. (a) RHESSI X-ray count rates in different energy bands between 3 and 100 keV during the M2.6 event. The GOES flux profile in the 1–8 Å channel and the AIA 193 and 304 Å light curves of the FR are also overplotted, for comparison with the X-ray light curves. (b) The preflare configuration of the FR observed in AIA 304 Å, devoid of significant X-ray emissions. (c)–(g) The evolution of the flare in the AIA 304 Å observations, with the RHESSI X-ray sources overplotted on the EUV images. In (c)–(d), we indicate the plasma structures erupting from the eastern and western parts of the FR, respectively. The X-ray contours in 6–12, 12–25, 25–50, and 50–100 keV are overplotted on the EUV images. The X-ray images are reconstructed by the CLEAN algorithm, with an integration time of 20 s. The contours are drawn at 50%, 60%, 70%, 80%, and 90% of the peak flux in each image. An animation of this figure is available, which shows the various phases of the flare in the AIA 304 Å observations.

(An animation of this figure is available.)

In Figures 9(b) to (g), we show the evolution of the FR using cotemporal continuum and magnetogram observations for three epochs—*t*1, *t*2, and *t*3—that present magnetic field changes prior to F1. The inspection of these images reveals an increase followed by a decrease of the sunspot area of the northern sunspot group (shown by the black arrows in Figures 9(b) to (d)). We also observe the growth of the compact sunspot groups on the western side of the main sunspot group (indicated by the dark blue arrows in Figures 9(b) to (d)). Figures 9(e) to (g) show cotemporal LOS magnetogram observations corresponding to the continuum images in Figures 9(b) to (d). In Figures 9(e) and (g), we focus on the eastern and western PILs, marked by the red and sky blue dotted lines, respectively. The yellow arrows indicate the gradual decrease of the positive flux near the eastern PIL (Figures 9(e) to (g)), whereas the red arrows indicate the subsequent decrease of the negative flux (see Figures 9(g) and (k)). We further note that the orientation of the western PIL has changed from *t*1 to *t*3 (see the sky blue dotted lines in Figures 9(e) and (g)).

In Figures 9(h) to (m), we present the continuum and LOS magnetogram observations showing the evolution of the FR

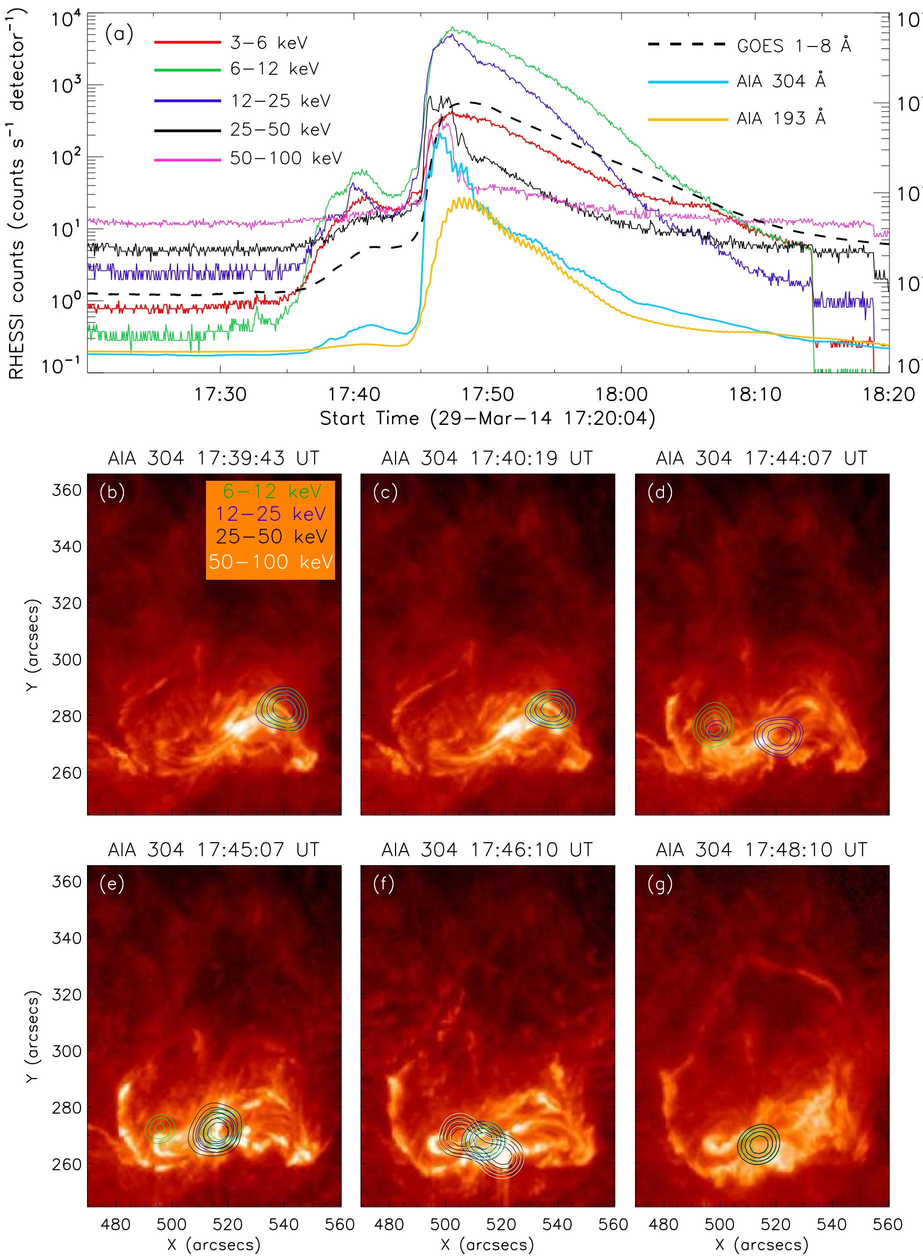

Figure 6. (a) RHESSI X-ray count rates in different energy bands between 3 and 100 keV during the X1.0 event. The GOES flux profile in the 1–8 Å channel and the AIA 193 and 304 Å light curves of the FR are overplotted. (b)–(g) AIA 304 Å observations, showing the evolution of the flare. The X-ray contours in 6–12, 12–25, 25–50, and 50–100 keV are overplotted on the EUV images. The X-ray images are reconstructed by the CLEAN algorithm, with an integration time of 20 s. The contours are drawn at 60%, 70%, 80%, and 90% of the peak flux in each image. An animation is associated with this figure, showing the different evolutionary stages of the flare in the AIA 304 Å observations.

(An animation of this figure is available.)

during epochs *t*4, *t*5, and *t*6, which are used to explore the changes in the photospheric magnetic field structures that are associated with F2 and F3. Notably, after F2, the photospheric configurations of the sunspot groups and associated magnetic fields in the northern region exhibit striking changes (see Figures 9(h) and (j); see also the attached animation). During the interval between F2 and F3, we observe that the northern sunspot group, with a relatively compact configuration, undergoes a rapid expansion, resulting in its fragmentation into three distinct parts (indicated by the arrows in Figure 9(j)). The magnetogram images that are cotemporal with the continuum observations are shown in Figures 9(k) to (m). The eastern and western PILs are indicated by the red and sky blue dotted lines, respectively, in Figure 9(k). We observe clear features of flux cancellation and emergence. The sky blue arrows indicate the substantial cancellation of the negative flux near the western PIL, whereas the green arrows indicate the gradual increase of the positive flux near the same PIL. These observations showing the flux emergence and cancellation are in agreement with the qualitative estimation shown in Figure 9(a).

4.2. Magnetic Configuration of Flaring Corona

In Figure 10, we represent the preflare coronal magnetic structures in and around the FR, obtained through NLFFF extrapolation. The first, second, and third columns denote the

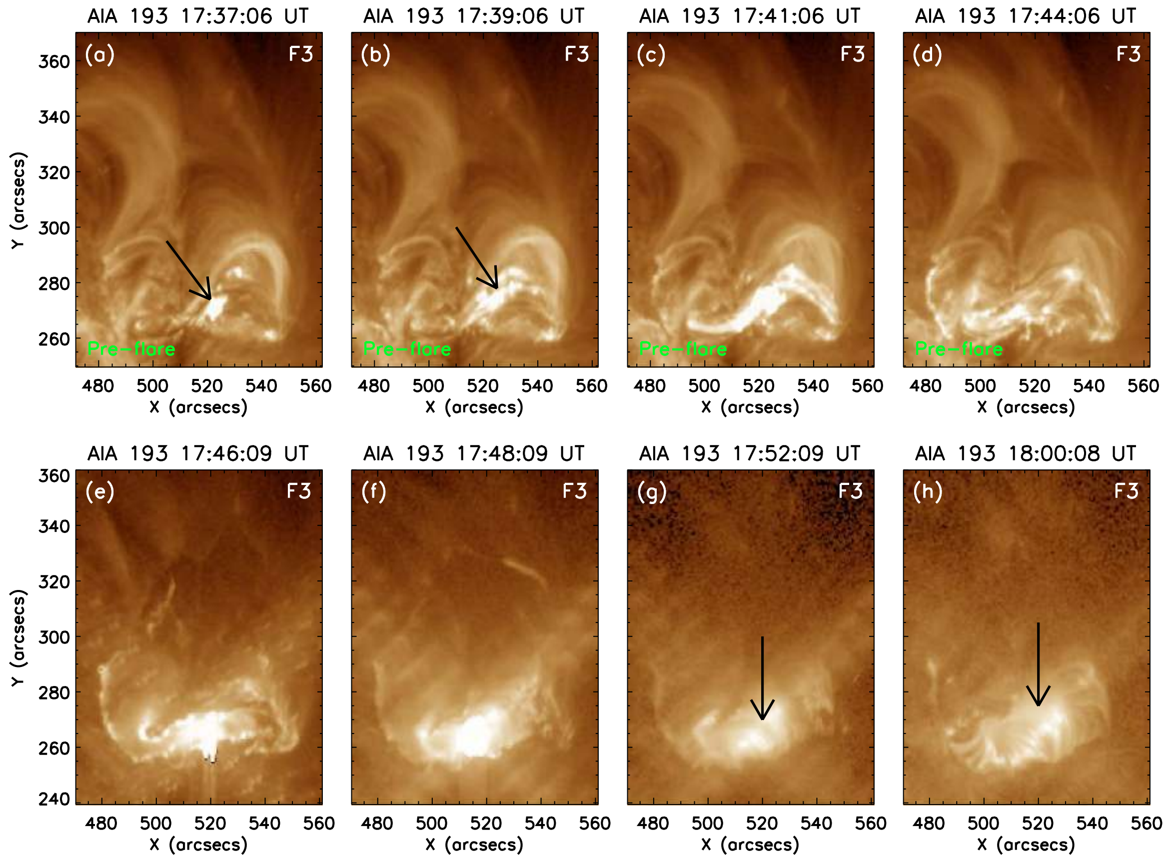

Figure 7. The evolution of the X1.0 flare (F3) in the AIA 193 Å images. (a)–(d) The morphological changes during the preflare phase of the flare. (e)–(h) The main phase of the flare. We note preflare activity, in the form of intense brightening from the western part of the core, which we indicate with the arrows in (a) and (b). This preflare intensity enhancement subsequently spreads over a large area within the core region ((c) and (d)). During the main phase of the flare, enhanced intensity is observed from an extended part of the core region ((e) and (f)). Afterward, dense postflare loop arcades are observed to form, which gradually elongate over a broad area of the core, as indicated by the arrows in (g) and (h).

epochs corresponding to F1, F2, and F3, respectively. In the top panels, we show the extrapolated coronal field lines, taking the HMI SHARP CEA radial magnetic fields as the background, whereas in the bottom panels, we show the AIA 304 Å images in the background, using the visualization software VAPOR (Li et al. 2019). In all cases, we find the existence of two flux ropes lying over the compact eastern and western PILs of the FR (see Figure 9), shown by yellow and blue field lines, respectively. The flux ropes are encompassed by the low-lying bipolar field lines (shown in green). The sequential eruptions of the flux ropes and the neighboring core field give rise to the eruptive flares under analysis. We observe filaments in the AIA 304 Å images, which are indicated by the arrows in the bottom panels. A detailed investigation into the modeling of the coronal magnetic fields during the three events is in progress, and will be presented in a subsequent study.

5. Morphology and Evolution of Photospheric Longitudinal Currents

We show the morphological changes associated with the photospheric longitudinal current in response to the magnetic field changes in Figure 11. In the photosphere, the vertical component of the electric current density (i.e., J_z) can be obtained from the horizontal magnetic field components (i.e., B_x and B_y), using Ampere's law (Kontogiannis et al. 2017; Fleishman & Pevtsov 2018; Fursyak et al. 2020):

$$J_z = \frac{1}{\mu_0}\left(\frac{dB_y}{dB_x} - \frac{dB_x}{dB_y}\right). \tag{1}$$

The magnetic field components (B_z, -B_y, B_x) in heliographic Cartesian coordinates can be approximately obtained from the corresponding field components (B_r, B_θ, B_ϕ) in heliocentric spherical coordinates (Gary & Hagyard 1990). In order to calculate the longitudinal current (I_z) from the longitudinal current density (J_z), we need to multiply J_z by the area of one pixel, i.e., 13.14×10^{10} m^2. In Figure 11, we present the distribution of the current (i.e., I_z), along with the structure of the radial component of the magnetic field (i.e., B_r), within the FR, before the start of the flares. The top, middle, and bottom panels of Figure 11 correspond to F1, F2, and F3, respectively. For better visualizations, we saturate the current values at $\pm\, 0.5 \times 10^{10}$ A in all panels. The color code for the I_z maps (Figures 11(a), (c), and (e)) is shown by a colorbar in Figure 11(a). We observe a significant amount of current concentration along the western PIL (see the sky blue dotted lines in Figures 9(e), (g), and (k)) of the FR for all events. Notably, the negative current largely dominates the positive current in all cases. Between F2 and F3, the western PIL undergoes elongation (Figure 11(f); see also Figures 9(k) to (m)). In a similar way, the region of strong photospheric currents that predominantly exists at the flaring core region is

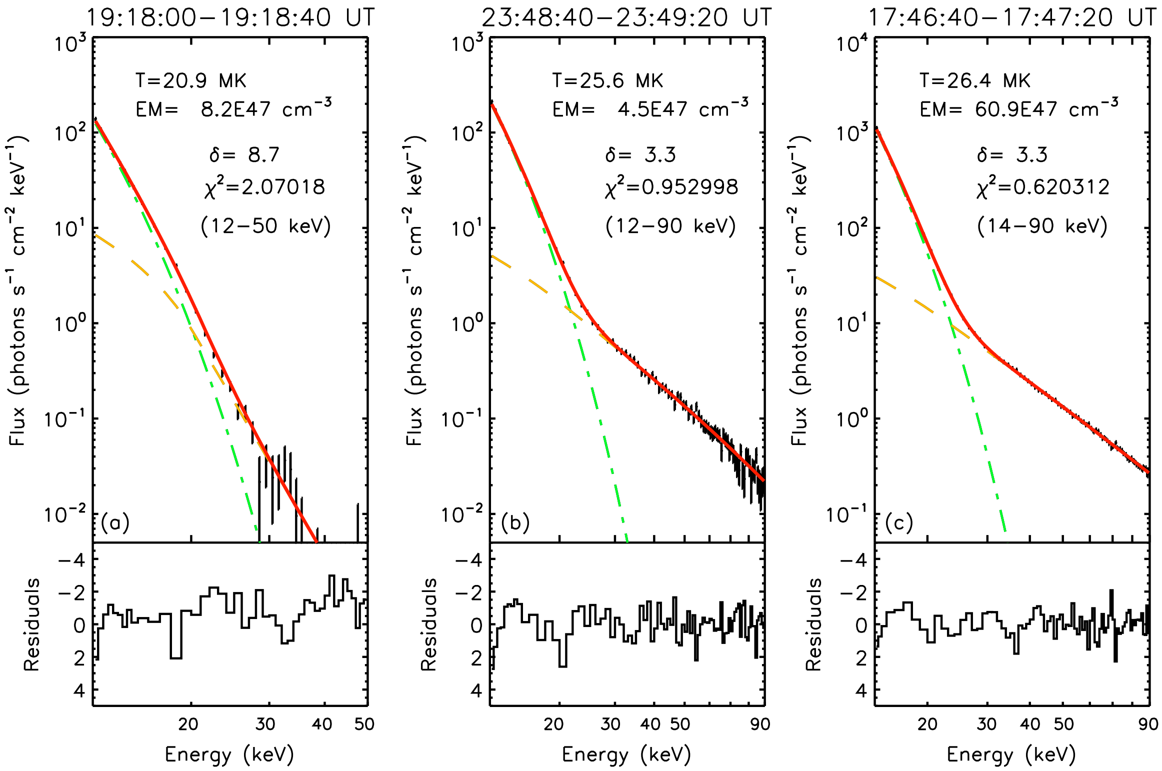

Figure 8. Results of the RHESSI X-ray spectral fit, along with their residuals, for all the events under analysis. We use an isothermal model (shown by the green dashed–dotted line) for the thermal fit and a thick-target Bremsstrahlung model (shown by the yellow dashed line) for nonthermal fit of the observed spectra. The solid red line indicates the sum of the two components. Each spectrum was accumulated with an integration time of 40 s, using the front segments of detectors 1–9 (except for detectors 2 and 7). The energy ranges that we select for the spectral fit are annotated in the respective panels. In (a), (b), and (c), we show the spectra at the peak of the HXR emissions during the M2.0, M2.6, and X1.0 flares, respectively.

observed to show an extended morphological structure prior to F3 (see Figures 11(a), (c), and (e)).

6. Onset of Eruption

For a quantitative understanding of the eruption from the flaring core, we present time slice diagrams in Figure 12. Figures 12(a)–(b), (c)–(d), and (e)–(f) correspond to F1, F2, and F3, respectively. In the left column of this figure, we show the directions of the slits along which we observe significant eruptive features. In the right column, we show the corresponding time slice diagrams in AIA 94 Å running difference images, constructed by tracking the eruptive signatures along the slits. We mark the erupting hot plasma structures with the red dots in Figures 12(b), (d), and (f). We note that the speeds of the hot plasma ejections show an increasing trend from F1 to F3 (i.e., ≈296, 581, and 955 km s^{-1}). Following the hot plasma eruption, an eruption of dark (i.e., cool) material ensues, which we indicate with the white arrows. To compare the eruption of the plasma structure with the temporal evolution of the flare, we overplot the AIA 94 Å flare light curves in all panels. We note that the rise of the 94 Å intensity is near simultaneous with the onset of the hot plasma eruption from the flaring core. Subsequently, the eruptions from the source region turn into CMEs. According to the Large Angle and Spectromeric Coronagraph Experiment (LASCO) CME catalog,[8] the linear speeds of the CMEs within the LASCO field of view (FOV) that are associated with F1, F2, and F3 are 420, 503, and 528 km s^{-1}, respectively.

7. Evolution of Free Magnetic Energy

Our analysis is comprised of homologous eruptive flares, which show gradually increasing SXR intensities (M2.0, M2.6, and X1.0). To investigate the scenario in the framework of the storage and release process of the free magnetic energy associated with the complex magnetic configuration of the AR, we calculate the temporal evolution of the free energy over an interval of ≈30 hr, which is demonstrated in Figure 13. The free magnetic energy (E_F) is defined as the difference between the nonpotential (E_{NP}) and potential (E_P) magnetic energies, i.e.:

$$E_F = E_{NP} - E_P, \tag{2}$$

where E_{NP} is calculated from the magnetic fields obtained from the NLFFF extrapolation. The different forms of energies can be calculated from the magnetic field information using the following relation:

$$E = \int_V \frac{B^2}{8\pi}\, dV. \tag{3}$$

We observe that there is a prominent decrease of the free magnetic energy due to the occurrence of the flaring events. We calculate the decreases to be 17%, 9.5%, and 38% for the events M2.0, M2.6, and X1.0, respectively. There is a data gap in the GOES light curve (in the 1–8 Å channel) from 08:30 UT to 09:40 UT on 2014 March 29, which is indicated by the hatched region. To confirm whether the GOES SXR flux

[8] https://cdaw.gsfc.nasa.gov/CME_list/UNIVERSAL/2014_03/univ2014_03.html

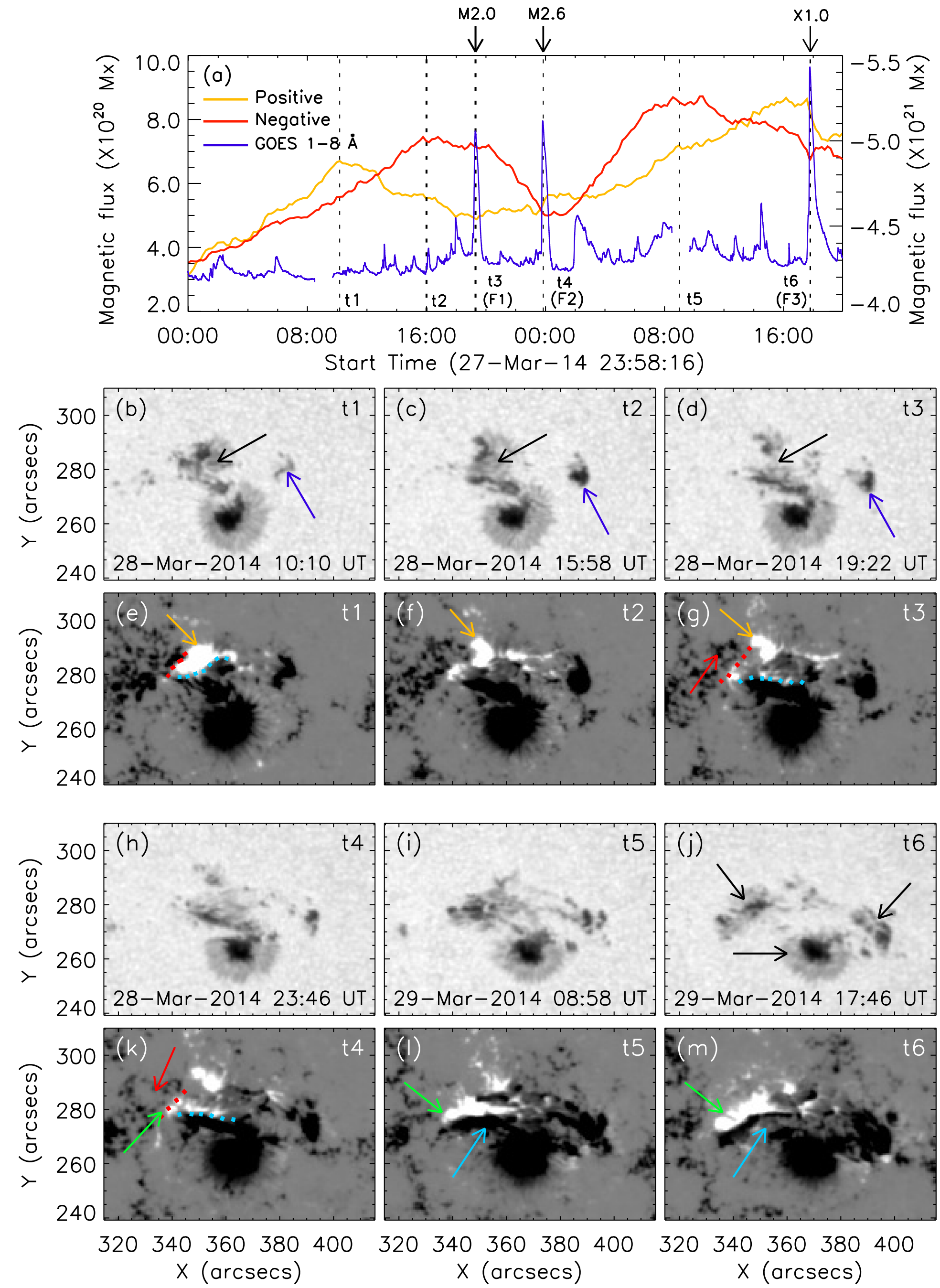

Figure 9. (a) The temporal evolution of the magnetic flux obtained from the FR, along with the GOES SXR light curve in the 1–8 Å channel. (b)–(d) Intensity images of the FR at three instances—*t*1, *t*2, and *t*3—as marked in (a). The black arrows denote small-scale changes in the northern sunspot group, while the blue arrows indicate the growth of a compact sunspot group. (e)–(g) LOS magnetogram images that are cotemporal with the continuum observations (shown in the row above) at times *t*1, *t*2, and *t*3, respectively. The yellow and red arrows are used to indicate the changes in the positive and negative fluxes, respectively. (h)–(j) Intensity images of the FR at *t*4, *t*5, and *t*6, as marked in (a). The arrows in panel (j) indicate three distinct sunspot groups. (k)–(m) LOS magnetogram images for *t*4, *t*5, and *t*6 that are cotemporal with the corresponding continuum observations (shown in the row above). The yellow (see panels (e)–(g)) and red (see panels (g) and (k)) arrows are used to indicate the changes in the positive and negative fluxes, respectively. The green and sky blue arrows are used to indicate the changes in positive and negative fluxes, respectively. The red and sky blue dotted lines in (e), (g), and (k) denote the PILs in the eastern and western parts of the FR, respectively. An animation representing the continuum (top panel) and LOS magnetogram (bottom panel) observations of the AR is available in the online material. It runs from 00:00 UT on 2014 March 28 to 20:00 UT on 2014 March 29. The region marked by the black and white boxes in the top and bottom panels of the animation represents the FR (see Figure 2).

(An animation of this figure is available.)

enhancements are associated with the flaring activity in AR 12017, in which we are interested, we have shown the AIA 94 Å light curve deduced exclusively from the AR. It is observed that, in general, the EUV light curve matches well with the GOES light curve, and the prominent SXR peaks represent the activity in the AR.

8. Discussion

In this study, we explore the multiwavelength evolution of three homologous flaring events of successively increasing intensities and their associated energy release processes. The events occurred between 2014 March 28 and 29, in NOAA AR

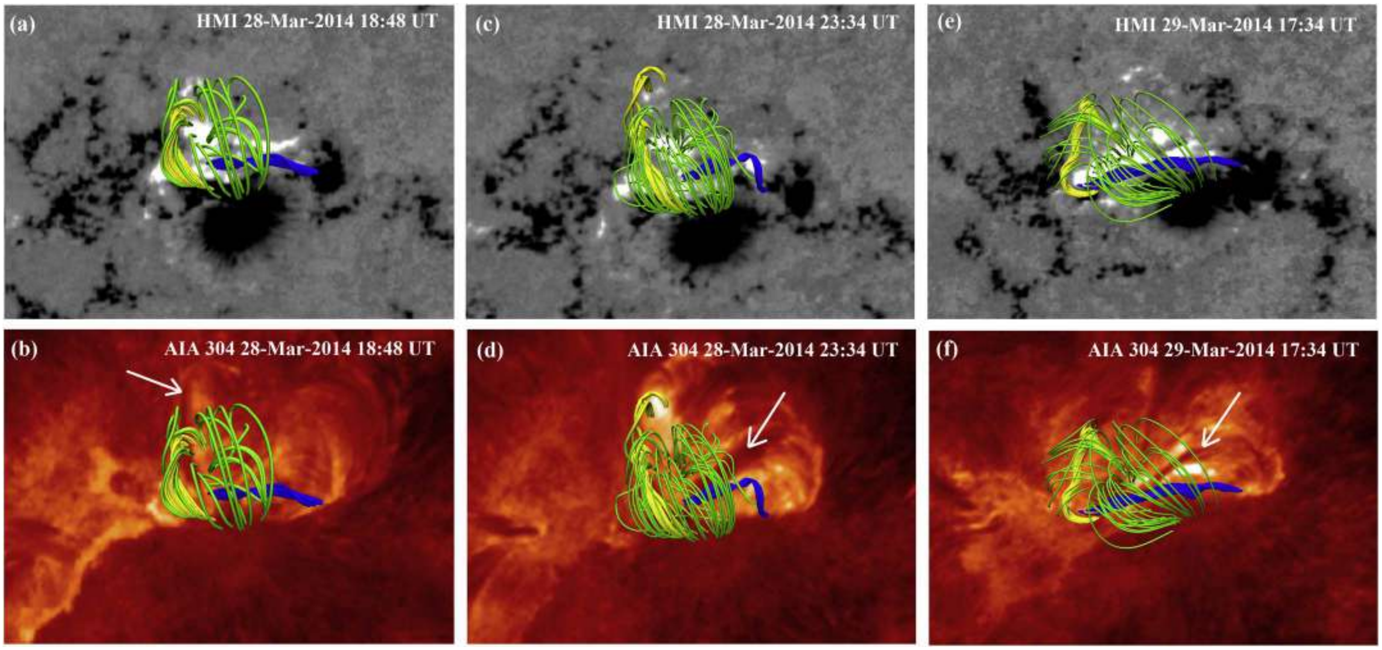

Figure 10. The preflare coronal magnetic structures obtained through NLFFF modeling, presented over the photospheric radial magnetic fields (top) and the AIA 304 Å observations (bottom), in and around the FR for all the events. (a)–(b), (c)–(d), and (e)–(f) denote the epochs corresponding to F1, F2, and F3, respectively. We note the existence of two flux ropes, shown by the yellow and blue field lines, residing over the eastern and western PILs of the FR (top panels; see also Figure 9), respectively. The flux ropes are enveloped by the low-lying bipolar field lines (green). In the bottom panels, we mark the filaments with arrows, observed through EUV imaging.

12017, over an interval of ≈24 hr. The flares were triggered by eruptions of flux ropes from the core of the AR. The importance of this study lies in its investigation of the intrinsic coupling of magnetic fields and associated processes, from the photosphere to the corona, which resulted in the repetitive buildup of compact magnetic flux ropes and their subsequent eruptions, observed in the form of homologous eruptive flares of successively increasing intensities. The important observational aspects of this study are summarized as follows:

1. According to the GOES observations, the durations of the flares of our analysis are 22, 14, and 19 minutes, for the M2.0 (F1), M2.6 (F2), and X1.0 (F3) flares, respectively (see Table 1). A statistical analysis of almost 50,000 GOES SXR flares over the period from 1976 to 2000 is presented in Veronig et al. (2002). Their analysis reveals that the average values of the durations of M- and X-class flares are 24 and 30 minutes, respectively. In view of this, the duration of F1 is close to the value as suggested by the study of Veronig et al. (2002), while F2 and F3 have shorter durations. Notably, although F1 and F2 are of comparable intensity, and are homologous in nature, the duration of F2 is significantly shorter than that of F1. On the other hand, F3, despite being a large X-class flare, exhibits a shorter duration as compared to F1.
2. The inspection of the RHESSI X-ray images in multiple energy bands within the energy range 3–100 keV during the evolution of F1 and F2 reveals a single X-ray source persisting throughout the flaring intervals. In both events, the X-ray emissions are observed to come from the dense and closely packed coronal loop system. The X-ray observations during the third event reveal emissions from different spatial locations within the FR (see Figure 6). During the onset of the impulsive phase of the third flare, we observe X-ray emissions from both the eastern and western parts of the FR (Figures 6(d) and (e)). Notably, conjugate X-ray sources with two distinct centroids in the 50–100 keV energy range are observed within the core region during the peak of the X1.0 flare (Figure 6(f)). These conjugate X-ray sources likely originate from the deposition of energy by energetic electrons at the footpoints of the post-reconnected loop system, as depicted in the standard flare model (see, e.g., Joshi et al. 2009).
3. We observe significant cancellations of magnetic fluxes (both positive and negative) within a bipolar flaring core region, near the eastern and western PILs (see Figure 9 and Section 4.1). A detailed comparison of the HMI magnetograms and EUV images (see Figures 3–7 and Figure 9) reveals that the source region of the eruptions is spatially well correlated with the compact PILs (see Figure 10). Notably, we observe significant flux changes near the eastern PIL before F1 and F2, whereas the change of flux is at its maximum near the western PIL before F3 (see Figure 9). Thus, our observations imply a precise link between each flux rope eruption and magnetic flux cancellation in the photosphere. The observations of extended phases of flux cancellation, together with the prominent flux canceling features near the PIL, have important implications for understanding the repetitive buildup of the flux ropes and the triggering mechanism of the homologous eruptions. Contextually, from the EUV imaging observations, we note that the eruptions were initiated from the eastern PIL, during F1 and F2, whereas during F3, the eruption was triggered from the western PIL. These observations show conformity with the tether-cutting model of solar eruption (Moore & Roumeliotis 1992; Moore et al. 2001), where the buildup process of a flux rope along the PIL is

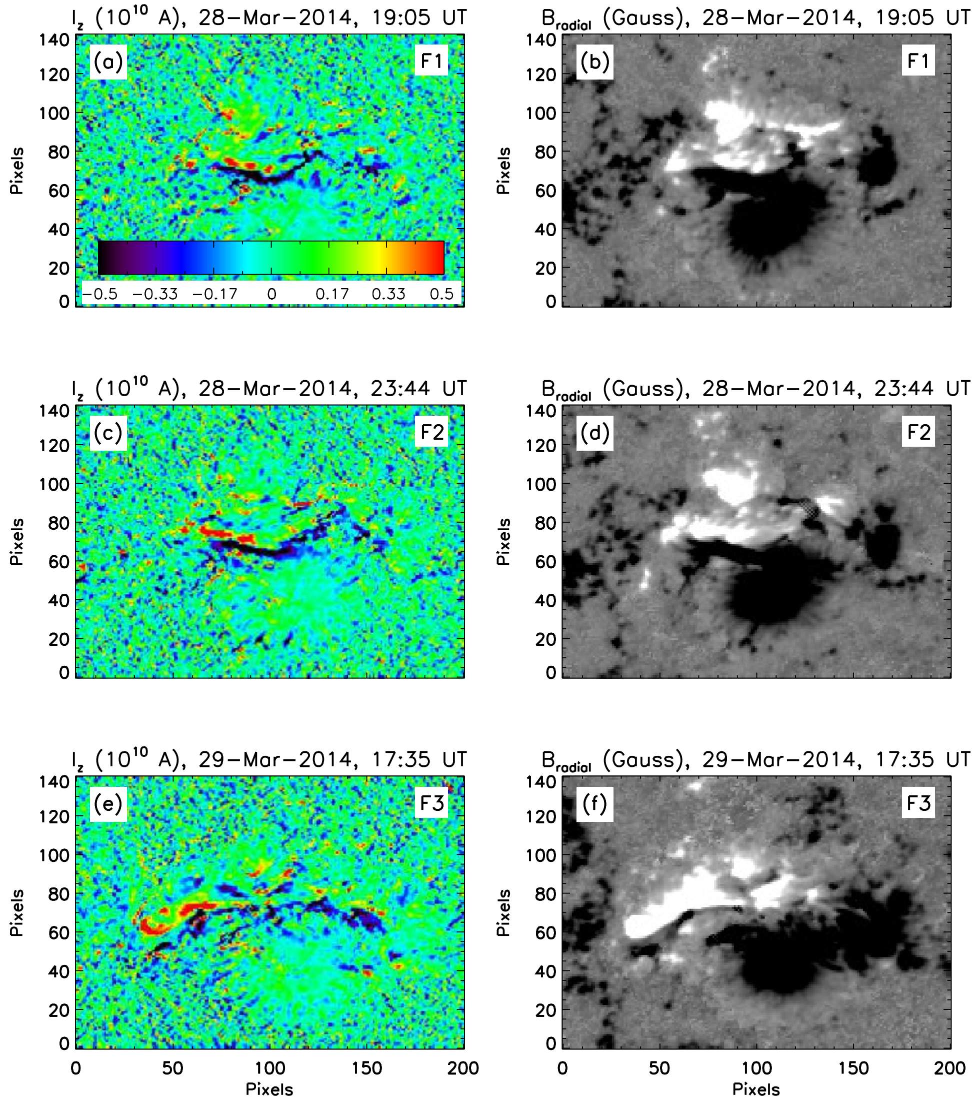

Figure 11. Comparisons of the photospheric longitudinal current (I_z; first column) and the radial component of the magnetic field (B_{radial}; second column) before the onset of the flares. (a)–(b), (c)–(d), and (e)–(f) correspond to F1, F2, and F3, respectively. In (a), we denote a colorbar corresponding to the distribution of I_z in (a), (c), and (e). We saturate the I_z and B_{radial} values to $\pm$ 0.5 $\times$ 10^{10} A and $\pm$ 500 G, respectively, in all panels. We note that the current distribution is strong near the western PIL of the FR (see Figure 9), and that it elongates along the PIL before F3. The morphological changes in the longitudinal current distribution are similar to the structural changes in the distribution of the radial magnetic field component (see (e) and (f)).

governed by flux cancellation, which extends over a much longer interval as compared to the flare timescales. The preexistence of magnetic flux ropes in ARs in relation to eruptive flares and CMEs has been well recognized (see, e.g., Shibata 1999). Several contemporary observations have also confirmed the slow activation of a magnetic flux rope, prior to the flare's impulsive phase (e.g., Joshi et al. 2016; Mitra & Joshi 2019; Sahu et al. 2020; Kharayat et al. 2021). In our work, for each eruption, the NLFFF extrapolation results reveal the presence of two flux ropes, corresponding to the eastern and western PILs. The synthesis of EUV imaging, magnetogram observations, and NLFFF modeling suggests that the formed flux rope was likely destabilized by rapidly evolving localized magnetic field structures near the PIL, indicating the role of small-scale tether-cutting reconnection in the triggering process. This scenario is further confirmed by the location of the X-ray sources during the early phase, when the emission only originates at lower energies (below 25 keV; see Figures 3(b), 5(c), and 6(b)), as these sources are well correlated with the locations of prominent flux cancellation.

4. We further highlight the results of NLFFF extrapolation, which reveal the presence of two magnetic flux ropes, formed over the eastern and western PILs, prior to each eruptive flare. In this context, it is relevant to discuss and compare the different aspects relating to the magnetic flux rope manifestations in this AR, as studied in detail by Yang et al. (2016) and Woods et al. (2018), in association with the flaring activity of March 28–29. Using an NLFFF model, Yang et al. (2016) showed a magnetic flux rope in the region, for which the twist number and decay index of the constraining field were calculated. Their analysis revealed that the decay index lies below the critical value for torus instability to be operational. Therefore, the authors favored the role of twist instability toward the CME onset, although they could not find a common critical value for the twist number over which

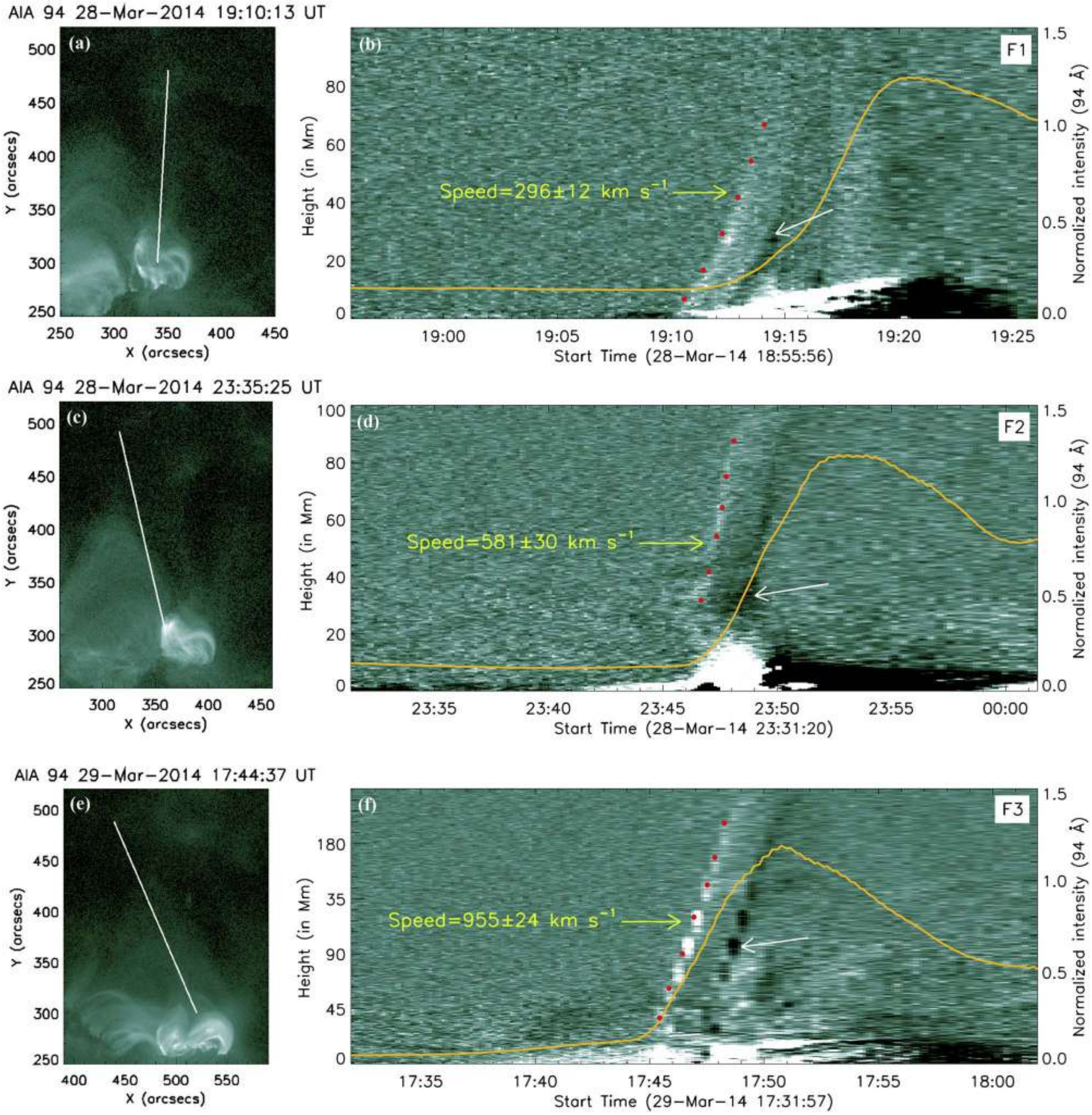

Figure 12. The evolutionary stages of the eruption of the hot plasma structures from the core FR. (a)–(b), (c)–(d), and (e)–(f) correspond to F1, F2, and F3, respectively. The left column shows the directions of the slits over the AIA 94 Å direct images along which we calculate the height–time profiles of the eruptions. In the right column, we show time slice diagrams obtained from the AIA 94 Å running difference images, by tracking the intensity variation along the slits. The erupting hot plasma structures are indicated by the red dots in (b), (d), and (f). The speeds of the erupting structures are annotated in these panels, with the corresponding uncertainties in the measurements. We note that the speeds gradually increase from F1 to F3. Following the hot plasma eruption, we observe the eruption of a dark (i.e., cool) structure, which we mark with the white arrows in these panels. The flare intensity profiles in the AIA 94 Å channel are also overplotted with the orange curves.

the flux rope tends to erupt. Nevertheless, their work points toward the fact that the twist number is a sensitive parameter in relation to flare occurrence. In a subsequent work, Woods et al. (2018) studied the most energetic flare (the X1.0 event) from this AR, which is the third event in our study. They found that the flux rope actually comprised two flux ropes, only one of which erupted during the X1.0 flare. The detailed EUV and X-ray imaging observations presented in our work also reveal the destabilization of the flux rope formed at the western PIL, in agreement with the work of Woods et al. (2018). Due to the presence of the magnetic flux cancellation and the brightening below the flux rope, Woods et al. (2018) concluded that the tether-cutting mechanism was responsible for the rising of the western flux rope to a torus unstable region prior to the flare. From the flare light curves, together with the corresponding EUV imaging observations, we clearly find preflare brightening for the X1.0 flare (see Figures 6(a) to (d)), which further points toward the role of tether-cutting reconnection for the

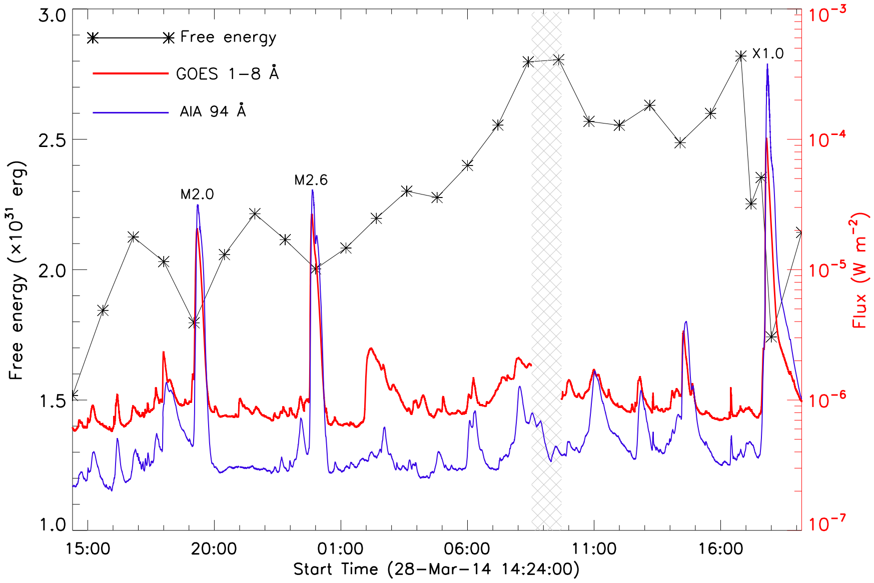

Figure 13. The evolution of the free magnetic energy over an interval of ≈30 hr, encompassing all the flares in the study. The free energy was calculated for the coronal volume encompassing the AR, taking the HMI SHARP CEA cutout as the photospheric boundary. We also plot the full-disk GOES light curve in the 1–8 Å channel. The hatched region shows an interval during which the GOES data are not available. To complement the data gap, we plot an EUV 94 Å intensity curve, obtained from AIA, recorded for the AR.

activation of the flux rope to the torus unstable region. For a series of four eruptive events, similar results were obtained by Mitra & Joshi (2021), who proposed the combined roles of ideal (torus) and resistive (tether-cutting) instability for the onsets of CMEs.

5. The sequential eruptions of the flux ropes from the flaring core give rise to corresponding CMEs. The inspection of the series of AIA 94 Å running difference images reveals eruptions of hot coherent plasma structures (i.e., heated flux ropes) from the core region (Figure 12). We note that the speeds of the flux rope eruptions in the source region significantly increase from F1 to F3. A comparison of the speeds of the eruptive flux ropes at the source region with the corresponding CMEs in the LASCO FOV (see Section 6) reveals that the first flux rope undergoes acceleration (296 versus 420 km s^{-1}), the second one moves with approximately constant speed (581 versus 503 km s^{-1}), while the final eruption exhibits deceleration (955 versus 528 km s^{-1}).
6. The buildup of the electric current in the photosphere is directly associated with the emergence of current-carrying flux (Tan et al. 2006; Török et al. 2014). The photospheric currents prior to the flare onset signify the buildup of nonpotentiality in the AR corona (Schrijver et al. 2005; Dalmasse et al. 2015). Our study reveals that a strong current accumulation occurs near the western PIL of the FR (Figure 11), where one of the two flux ropes lies (Figure 10). Furthermore, before F3, the magnetic flux near the western PIL is observed to undergo expansion, showing an extended morphology (Figure 11(f)). In response to this, the longitudinal current distribution is elongated along the same PIL before F3 (Figure 11(e)). In general, photospheric currents have important consequences in terms of triggering solar eruptive events. Mitra et al. (2020a) studied the role of precursor flare activity in triggering a dual-peak M-class flare. Their study revealed the presence of strong localized regions of photospheric currents of opposite polarities at the precursor location, making the region susceptible to small-scale magnetic reconnection.
7. The photospheric flux emergence and shearing motion introduce strong electric currents and inject energy into the AR corona. The coronal fields is reconfigured in this process, resulting in the accumulation of free magnetic energy in the coronal volume (Régnier 2012; Vekstein 2016). This stored free energy is regarded as a prime factor that is responsible for the explosive phenomena. The successively increasing intensities of the homologous flares of our analysis point toward a complex "storage and release" process of magnetic energies in the AR. For a quantitative understanding of the energy storage and release process, we study the evolution of the free magnetic energy over a time span covering the three homologous events (Figure 13). We find that the maximum release of the free magnetic energy (i.e., 38%) is observed during the strongest event (i.e., the F3/X1.0 flare). It is also remarkable to observe that the third event has a prolonged period for the storage of the free magnetic energy (i.e., a period of ≈ 17 hr between F2 and F3), during which no major flare above class C occurs in the AR. Interestingly, this "storage phase" largely overlaps with a persistent phase of flux emergence (see Figure 9(a); the interval between *t*4 and *t*5). In conclusion, our analysis reveals that the dominant variation in the magnetic flux (both at a large scale, involving the full FR, as well as at small scales, close to the compact PILs) and the buildup of free magnetic energy in and around the FR is the root cause for the homologous eruptive flares of successively increasing intensities.

In summary, our paper provides a detailed investigation of the multiwavelength evolutions of three homologous eruptive flares, by combining HXR, EUV, white-light, and magnetogram observations. We provide a quantitative estimation of the evolution of the free magnetic energy in the corona associated with the AR, and we explore its links with the ongoing photospheric and coronal processes. Thus, our study brings out the connection between the photospheric developments and the resulting rapid buildup and subsequent eruption of coronal magnetic structures.

The authors would like to thank the SDO and RHESSI teams for their open data policy. SDO is NASA's mission under the Living With a Star (LWS) program. RHESSI was NASA's mission under the SMall EXplorer (SMEX) program. HMI data are courtesy of NASA/SDO and the HMI science team. A.P. would like to acknowledge the support from the Research Council of Norway, through its Centres of Excellence scheme, project No. 262622, as well as through Synergy grant No. 810218 459 (ERC-2018-SyG) of the European Research Council. A.P. would also like to acknowledge partial support from NSF award AGS-2020703. K.S.C. was support by the R&D program (2023-1-800-04) of the Korea Astronomy and Space Science Institute. The authors thank the anonymous referee for providing constructive comments and suggestions, which improved the overall quality of the article.

ORCID iDs

Suraj Sahu https://orcid.org/0000-0001-8377-8640
Bhuwan Joshi https://orcid.org/0000-0001-5042-2170
Avijeet Prasad https://orcid.org/0000-0003-0819-464X
Kyung-Suk Cho https://orcid.org/0000-0003-2161-9606

References

Benz, A. O. 2017, LRSP, 14, 2
Chatterjee, P., & Fan, Y. 2013, ApJL, 778, L8
Cheung, M. C. M., Rempel, M., Chintzoglou, G., et al. 2019, NatAs, 3, 160
Dalmasse, K., Aulanier, G., Demoulin, P., et al. 2015, ApJ, 810, 17
DeVore, C. R., & Antiochos, S. K. 2008, ApJ, 680, 740
Fleishman, G. D., & Pevtsov, A. A. 2018, in Electric Currents in Geospace and Beyond, ed. A. Keiling, O. Marghitu, & M. Wheatland, Vol. 235 (Washington, DC: American Geophysical Union), 43
Fletcher, L., Dennis, B. R., Hudson, H. S., et al. 2011, SSRv, 159, 19
Fursyak, Y. A., Kutsenko, A. S., & Abramenko, V. I. 2020, SoPh, 295, 19
Gary, G. A., & Hagyard, M. J. 1990, SoPh, 126, 21
Holman, G. D., Sui, L., Schwartz, R. A., & Emslie, A. G. 2003, ApJL, 595, L97
Hurford, G. J., Schmahl, E. J., Schwartz, R. A., et al. 2002, SoPh, 210, 61
Joshi, B., Ibrahim, M. S., Shanmugaraju, A., & Chakrabarty, D. 2018, SoPh, 293, 107
Joshi, B., Kushwaha, U., Veronig, A. M., & Cho, K.-S. 2016, ApJ, 832, 130
Joshi, B., Veronig, A., Cho, K.-S., et al. 2009, ApJ, 706, 1438
Kharayat, H., Joshi, B., Mitra, P. K., Manoharan, P. K., & Monstein, C. 2021, SoPh, 296, 99
Kleint, L., Battaglia, M., Reardon, K., et al. 2015, ApJ, 806, 9
Kontogiannis, I., Georgoulis, M. K., Park, S.-H., & Guerra, J. A. 2017, SoPh, 292, 159
Lemen, J. R., Title, A. M., Akin, D. J., et al. 2012, SoPh, 275, 17
Li, S., Jaroszynski, S., Pearse, S., Orf, L., & Clyne, J. 2019, Atmos, 10, 488
Li, Y., Ding, M. D., Qiu, J., & Cheng, J. X. 2015, ApJ, 811, 7
Li, Y., Lynch, B. J., Welsch, B. T., et al. 2010, SoPh, 264, 149
Lin, R. P., Dennis, B. R., Hurford, G. J., et al. 2002, SoPh, 210, 3
Liu, C., Deng, N., Liu, R., et al. 2015, ApJL, 812, L19
Mitra, P. K., & Joshi, B. 2019, ApJ, 884, 46
Mitra, P. K., & Joshi, B. 2021, MNRAS, 503, 1017
Mitra, P. K., Joshi, B., & Prasad, A. 2020a, SoPh, 295, 29
Mitra, P. K., Joshi, B., Prasad, A., Veronig, A. M., & Bhattacharyya, R. 2018, ApJ, 869, 69
Mitra, P. K., Joshi, B., Veronig, A. M., et al. 2020b, ApJ, 900, 23
Moore, R. L., & Roumeliotis, G. 1992, in Triggering of Eruptive Flares—Destabilization of the Preflare Magnetic Field Configuration, ed. Z. Svestka, B. V. Jackson, & M. E. Machado, Vol. 399 (New York: Springer), 69
Moore, R. L., Sterling, A. C., Hudson, H. S., & Lemen, J. R. 2001, ApJ, 552, 833
Nitta, N. V., & Hudson, H. S. 2001, GeoRL, 28, 3801
Pesnell, W. D., Thompson, B. J., & Chamberlin, P. C. 2012, SoPh, 275, 3
Priest, E. R., & Forbes, T. G. 2002, A&ARv, 10, 313
Régnier, S. 2012, SoPh, 277, 131
Romano, P., Elmhamdi, A., Falco, M., et al. 2018, ApJL, 852, L10
Romano, P., Zuccarello, F., Guglielmino, S. L., et al. 2015, A&A, 582, A55
Sahu, S., joshi, B., Mitra, P. K., Veronig, A. M., & Yurchyshyn, V. 2020, ApJ, 897, 157
Sahu, S., Joshi, B., Sterling, A. C., Mitra, P. K., & Moore, R. L. 2022, ApJ, 930, 41
Schou, J., Scherrer, P. H., Bush, R. I., et al. 2012, SoPh, 275, 229
Schrijver, C. J., DeRosa, M. L., Title, A. M., & Metcalf, T. R. 2005, ApJ, 628, 501
Shibata, K. 1999, Ap&SS, 264, 129
Smith, D. M., Lin, R. P., Turin, P., et al. 2002, SoPh, 210, 33
Tan, B., Ji, H., Huang, G., et al. 2006, SoPh, 239, 137
Toriumi, S., & Wang, H. 2019, LRSP, 16, 3
Török, T., Leake, J. E., Titov, V. S., et al. 2014, ApJL, 782, L10
Vekstein, G. 2016, JPlPh, 82, 925820401
Vemareddy, P. 2017, ApJ, 845, 59
Veronig, A., Temmer, M., Hanslmeier, A., Otruba, W., & Messerotti, M. 2002, A&A, 382, 1070
Wiegelmann, T. 2008, JGRA, 113, A03S02
Wiegelmann, T., & Inhester, B. 2010, A&A, 516, A107
Wiegelmann, T., Thalmann, J. K., Inhester, B., et al. 2012, SoPh, 281, 37
Woodgate, B. E., Martres, M.-J., Smith, J. B., Jr., et al. 1984, AdSpR, 4, 11
Woods, M. M., Harra, L. K., Matthews, S. A., et al. 2017, SoPh, 292, 38
Woods, M. M., Inoue, S., Harra, L. K., et al. 2018, ApJ, 860, 163
Yang, K., Guo, Y., & Ding, M. D. 2016, ApJ, 824, 148
Young, P. R., Tian, H., & Jaeggli, S. 2015, ApJ, 799, 218
Zhang, J., & Wang, J. 2002, ApJL, 566, L117
Zuccarello, F., Ermolli, I., Korsos, M. B., et al. 2021, RAA, 21, 313